Measurement of neutrino Neutral-Current Quasi-Elastic interactions in the T2K experiment and application to Diffuse Supernovae Neutrino Background searches

Licheng Feng

Thesis Supervisor:
Prof. Roger Wendell

Kyoto University
Graduate School of Science
Department of Physics
Physics and Astrophysics

This PhD journey is a reconciliation with my past,
for the little boy who wanted to become an astrophysicist.

Abstract

The cumulative history of core-collapse supernovae and cosmic star formation is encoded in the Diffuse Supernova Neutrino Background (DSNB). Detecting this faint, constant flux of neutrinos is a major goal of modern astrophysics, as it would provide a complete timeline of stellar death beyond the singular observation of SN1987A. However, searching for the DSNB in water Cherenkov detectors, such as Super-Kamiokande (SK), is hindered by atmospheric neutral-current quasielastic (NCQE) interactions. To detect the DSNB, NCQE processes must be understood and modeled with high precision. This thesis presents a systematic study of NCQE interactions using accelerator data from the T2K experiment to constrain this background and improve DSNB sensitivity.

We report measurements of the three critical components of the NCQE background: neutron multiplicity, interaction cross sections, and Cherenkov-ring features. First, because DSNB signals are accompanied by a single neutron while atmospheric backgrounds often produce multiple neutron, neutron multiplicity is a key discriminator. Using T2K data corresponding to 1.76×10^{20} protons on target (POT), we measured the mean neutron multiplicity for ν-^{16}O NCQE-like interactions to be

$$\bar{\mathrm{M}} = 1.37 \pm 0.33\ (\mathrm{stat.})^{+0.17}_{-0.27}\ (\mathrm{syst.}).$$

This can be contrasted with predictions from neutrino generators, such as NEUT with the Bertni-base cascade model for secondary interactions, of (2.24 ± 0.01 (stat.)). Using the INCL++ and BIC models instead give 1.84±0.01 (stat.) and 1.87±0.01 (stat.), which give better agreement.

Second, to determine the absolute scale of the background, we measured NCQE-like flux-averaged cross sections using 21.42×10^{20} POT for neutrinos and 16.35×10^{20} POT for antineutrinos. The resulting flux-averaged cross sections are

$$\langle \sigma_{\nu\mathrm{NCQE}} \rangle = \left(1.75 \pm 0.15\ (\mathrm{stat.})^{+0.43}_{-0.23}\ (\mathrm{syst.})\right) \times 10^{-38}\ \mathrm{cm}^2/\mathrm{oxygen},$$

$$\langle \sigma_{\bar{\nu}\mathrm{NCQE}} \rangle = \left(0.97 \pm 0.16\ (\mathrm{stat.})^{+0.19}_{-0.13}\ (\mathrm{syst.})\right) \times 10^{-38}\ \mathrm{cm}^2/\mathrm{oxygen}.$$

Third, the Cherenkov rings features of NCQE are also crucial beacause they determins how well the atmospheric NCQE background can be separated from DSNB signal. We evaluate the uncertainty of the DNSB event selection at Super-Kamiokande based on these Cherenkov ring features. A Neural Network-based classifier was developed and tested using 21.42×10^{20} POT for neutrinos and 16.35×10^{20} POT for antineutrinos, demonstrating a superior efficiency over the existing cut while maintaining similar uncertainties.

Finally, these T2K results were utilized in a DSNB sensitivity study for Super-Kamiokande, assuming a 0.01% Gadolinium loading and an exposure of 552.1 days. The inclusion of these measurements successfully reduced the uncertainty on the atmospheric NCQE background from 71.0% to 43.4%. We show that this suppression of background uncertainty improves overall sensitivity. We discussed the projection to the projected end of Super-Kamiokande in 2032, and show that this enhanced sensitivity has the potential to achieve a 3σ detection of the DSNB flux. The techniques and constraints developed in this work are directly applicable to future searches at Super-Kamiokande and Hyper-Kamiokande.

Acknowledgements

I express my sincere gratitude to my supervisor, Prof. Roger Wendell. This journey could never have begun without your support. I still recall a dinner conversation with lab young members where we discussed whether, if we had the fortune to become supervisors, we would accept a student whose research interest does not lies perfectly with our own field. Most of us, including myself, said no. Yet, you make it happen and set this journey in motion. You truly are a Good Samaritan. I might not be your ideal student, but you will always be the teacher I respect the most.

I would like to thank Prof. Yasuhiro Nishimura for being a Good Samaritan. Your kindness is deeply appreciated.

I would like to extend my appreciation to Prof. Yasuhiro Nakajima. Thank you for introducing me to Super-K, T2K, SAMURAI, and the US–Japan project. Those experiences helped me identify the research area that suits me best, and I'm truly grateful.

I am honored to be part of the NCQE study at T2K. My heartfelt thanks go to Ashida Yosuke. Your energy has broadened the impact of NCQE research beyond T2K and greatly increased the value of T2K data. I am grateful for the expert guidance of Abe Seisho, Yota Hino, Han Seungh, Takatomi Yano, Kamil Skwarczynski, Tairafune Seidai, Xia Junjie, Fabio Icabo, and Mehta Pruthvi, whose insights into physics have been truly invaluable. The wonderful people in T2K are a treasure to me. Thank you to Prof. Kendall Mahn, Ryosuke Akutsu, Nobuyuki Yoshimura, Noguchi Yohei, and Xingyu Zhao, for your support in collaboration procedures, shift work, and the lunches gathered during meetings.

I consider it a privilege to collaborate with the outstanding members of the DSNB study at SuperK, including Saki Fujita, Andrew Santos, and Masayuki Harada. It's always a pleasure to observe how such exceptional individuals make decisions. I enjoyed my time at SuperK. My gratitude goes to Soniya Samani, Prof. Masayuki Nakahata, Prof. Hiroyuki Sekiya, Prof. Koshio Yuseke, Prof. Patrick De Perio, Prof. Michael Smy, Masataka Shinoki, Shota Izumiyama, and Maekawa Yuto for our

discussions on physics.

Kyoto University's High-Energy Laboratory, especially room 304, will always be special to me. Hu Zhoujun, Hu Jianrun, Zhenxiong Xie, and Feng Jiahui created a warm niche there, while Fujimoto Naoki, Nakata Hironobu, and Hanimura Keigo were extremely friendly. I am grateful to Adachi Shunsuke, Kikawa Tatsuya, Chen Shion, and Tajima Osamu for keeping the lab running smoothly, and I owe special thanks to Prof. Tsuyoshi Nakaya for his generous support and mentorship of young researchers.

I feel a special connection with Koshio Lab in Okayama and Yokoyama-Nakajima Lab in Tokyo, including Tada Tomoaki, Seiya Sakai, Koyo Takeya, Prof. Masashi Yokoyama, Prof. Nakagiri Kota, Yoshimi Yoshimoto, Shoma Kodama, Shima Shizuka, Eguchi Aoi, Vincent Gousy-Leblanc, and Rhea Gaur. Thank you for all the conversations.

I would like to thank my parents, Tao-An Feng and Mei-Shueh Yun, for their encouragement and support, and I am grateful to my wife, Shih-Han Lee, and our cat, Aoi, for taking this leap of faith with me.

Yes, I neglected part of my life, but that was the good old days.
This was the magic and we were making it happen.

Contents

Abstract ii

Acknowledgements iv

List of Figures . . . xxii

List of Tables . . . xxvi

I Introduction 1

1 Introduction 2

1.1 Neutrinos from Core-Collapse Supernovae . . . 2

1.2 Diffuse Supernova Neutrino Background and Current Search Status . 5

1.3 DSNB Search Methodology . . . 7

1.4 Neutrino–nucleus interactions . . . 9

1.4.1 NCQE signals in particle physics detectors . . . 11

1.4.2 NCQE formalism on a free nucleon . . . 12

1.4.3 Neutrino oscillations . . . 13

1.5 Current DSNB search status . . . 15

1.6 Previous NCQE Measurements . . . 18

1.7 Thesis Outline . . . 19

II Neutron measurement of Neutrino-Oxygen Neutral-Current Quasielastic-like Interactions 21

2 Measurement motivation 22

3 Experimental Setup 24

3.1 J-PARC Accelerator and Neutrino Beamline . . . 24

3.1.1 Primary neutrino beamline . . . 25

3.1.2 Secondary neutrino beamline . . . 26

3.2 Near detectors . . . 27

3.3 Super-Kamiokande detector . . . 29
3.3.1 SK Phases and the SK-Gd Experiment . . . 30
3.3.2 Detector Principle . . . 32
3.3.3 Photo-Multiplier Tubes . . . 33
3.3.4 Data Acquisition System . . . 34
3.3.5 Water Purification System . . . 34
3.3.6 PMT Calibration . . . 36
3.3.7 Water Calibration . . . 39
3.3.8 Energy Calibration . . . 45

4 Event simulation and reconstruction **51**
4.1 Event simulation . . . 51
4.1.1 Neutrino interaction . . . 51
4.1.2 Detector simulation . . . 54
4.2 Event reconstruction . . . 65
4.2.1 BONSAI fitter . . . 65
4.2.2 Energy Reconstruction . . . 67
4.2.3 Cherenkov angle reconstruction . . . 69
4.2.4 Multiple Scattering Goodness . . . 69
4.2.5 Neutron tagging algorithm . . . 71

5 Event Analysis **77**
5.1 prompt signal selection . . . 77
5.2 prompt signal selection results . . . 81
5.3 The delayed signal selection . . . 84
5.3.1 Definition of neutron tagging efficiency . . . 85
5.3.2 `NTag` configuration . . . 86
5.4 Observable difference between `bonsai_keras` and `lowe_tmva` . . . 89
5.5 Delayed signal results with `bonsai_keras` . . . 91
5.6 Delayed signal results with `lowe_tmva` . . . 95

6 Systematic **105**
6.1 Statistical uncertainty . . . 106
6.2 Gd concentration . . . 106
6.3 Nucleon SI . . . 107
6.4 Detector Response for Neutron Signal . . . 110
6.5 Discussions about Other Systematic Uncertainties . . . 113
6.5.1 ν beam flux . . . 113
6.5.2 ν oscillation . . . 113
6.5.3 Nucleon FSI . . . 113
6.5.4 π FSI/SI . . . 113

6.5.5 μ and π capture on ^{16}O . . . 114
6.5.6 Prompt signal selection . . . 114
6.5.7 PMT gain . . . 115
6.5.8 Water status . . . 115
6.6 Total Systematic Uncertainties . . . 116

7 Mean neutron multiplicity result 118
7.1 Discussion . . . 119
7.1.1 NC 2p2h interaction . . . 121
7.1.2 Strange axial coupling constant . . . 122
7.1.3 De-excitation models in NEUT . . . 123
7.1.4 Short Range Correlation . . . 124
7.1.5 Pauli Blocking and Random Phase Approximation . . . 126
7.2 Conclusion . . . 128
7.3 Future prospect . . . 128
7.3.1 Insights from Other Neutrino-induced Neutron Measurements 128
7.3.2 Insights from Other NCQE Related Measurements . . . 129
7.3.3 Application to DSNB search at SK . . . 130

III Validation of DSNB Feature Classifiers Against atmospheric NCQE Using the T2K NCQE sample 133

8 Measurement motivation 134
8.1 Measurement goal . . . 134

9 T2K NCQE Run 1-11 MC production and Data sample 136
9.1 T2K NCQE MC production . . . 136
9.1.1 Neutrino flux (`21bv2` relative to `13av4`) . . . 136
9.1.2 Neutrino interaction (NEUT 5.9.0 relative to 5.6.3) . . . 137
9.1.3 Detector simulation . . . 140

10 Event Analysis 144
10.1 prompt signal selection . . . 146
10.2 prompt signal selection results . . . 147
10.2.1 Features among runs and MC settings . . . 147
10.3 NCQE cross-section related systematic uncertainty . . . 156
10.3.1 T2K flux . . . 156
10.3.2 Neutrino interaction . . . 157
10.3.3 Primary-γ . . . 159
10.3.4 Secondary-γ . . . 160
10.3.5 Summary of uncertainty . . . 160

10.4 NCQE cross-section measurement result . . . 161
10.4.1 Systematic uncertainty improves other than SI models . . . 166
10.4.2 Prospect of T2K NCQE Cross-section measurements . . . 167

11 The DSNB selection in SK **168**
11.1 Improving the 3rd cuts . . . 171
11.1.1 MC samples for DSNB and atmospheric NCQE . . . 173
11.1.2 Cut strategies for DSNB and atmospheric NCQE . . . 173
11.1.3 Neural network for feature classification . . . 176
11.2 Performance and benchmarking . . . 180

12 LINAC validation **183**
12.1 Features from LINAC . . . 184
12.2 Neural network validation . . . 184
12.3 Discrete MSG cut strategy validation . . . 195
12.4 Linear MSG cut strategy validation . . . 195

13 T2K validation **201**
13.1 Feature difference between T2K and atmospheric neutrino flux. . . . 202
13.2 The three cut strategies validation . . . 204
13.3 Summary of systematic uncertainty . . . 215
13.3.1 Updated 3rd cuts uncertainty for DSNB . . . 215
13.3.2 Updated 3rd cut uncertainty for atmospheric NCQE . . . 220

14 Other background Estimation **224**
14.1 Atmospheric CCQE Interactions . . . 224
14.2 Lithium-9 . . . 224
14.3 Reactor Neutrinos . . . 225
14.4 Accidental Coincidences . . . 225

15 DSNB sensitivity with new cuts **226**
15.1 Expected Spectrum and Upper Limit Extraction . . . 226
15.2 Future Prospect . . . 229

IV Conclusion **233**

16 Conclusion **234**
References . . . 251

List of Figures

1.1 Schematic of the delayed neutrino-heating mechanism in core-collapse supernovae, adapted from Ref. [4]. 3
1.2 Evolution of CCSN neutrino luminosities and mean energies. Black, red, and blue lines correspond to ν_e, $\bar{\nu}_e$, and ν_x, respectively. The right panels illustrate the relative hemispheric differences following core bounce. Figure adapted from Ref. [2] 4
1.3 Neutrino burst from SN1987A (1987 February 23) as recorded by Kamiokande-II[7] and IMB [8]. Plotted are the reconstructed event energies and arrival times (relative to the first event) for each detector [10]. 5
1.4 Predictions for the DSNB $\bar{\nu}_e$ flux, spanning roughly an order of magnitude across the detection window. [23]. 7
1.5 DSNB spectrum with background components. Hatched bands denote total systematic uncertainty [23]. 10
1.6 NCQE cross-section from Ref. [26]: total (dashed) and γ (solid) NCQE cross sections, with red for ν and blue for $\bar{\nu}$. 13
1.7 Per-bin 90% C.L. upper limits on the DSNB $\bar{\nu}_e$ flux. Red: SK-VI+VII observed (solid) and expected (dashed). Blue: SK-IV observed and expected [35]. Green: KamLAND observed limit [38]. Gray bands: range of DSNB flux predictions. Figure adapted from Ref. [36]. . . . 17

3.1 Schematic view of the T2K experiment [55]. 24
3.2 The structure of the neutrino beamline at J-PARC [55] 25
3.3 The arrangement of proton beam monitors at the final focusing section of the primary beamline upstream the target [55] 26
3.4 Schematic view of the J-PARC neutrino secondary beamline [55]. . . 27
3.5 Oscillation probabilities for $\nu_\mu \rightarrow \nu_e$ (top) and $\nu_\mu \rightarrow \nu_\mu$ (middle), alongside T2K flux predictions at the far detector for various off-axis angles (bottom) [55]. 28
3.6 Predicted neutrino flux for T2K Run 11 at SK without oscillations. . 28
3.7 Schematic view of the Near Detectors [55]. 29
3.8 SK schematic [68]. 30

3.9 Gd loading scheme. Taken from [55]. Colder and higher Gd concentration water is heavier than tank water. 32
3.10 Inner-detector PMT schematic and quantum efficiency versus wavelength [68]. 33
3.11 A schematic view of the water purification system [68]. 36
3.12 A schematic view of the Gd loaded water purification system [77]. . . 37
3.13 A schematic view of the relative PMT gain calibration (left) and the relative PMT gain distribution in SK-IV (right) [85]. 39
3.14 A typical TQ map for a readout channel in SK-IV [85]. 40
3.15 Water-laser schematic (left), representative timing distributions (center), and MC fit results (right) used by SK to determine wavelength-dependent absorption and scattering parameters in SK-IV. [85]. . . . 41
3.16 Decay-electron for water transparency monitoring in SK: schematic (left), analysis parameters (center), and N_{eff} versus PMT distance (right) used to extract the effective water attenuation length. [85]. . . 43
3.17 Left: schematic of the Cherenkov-ring selection at $\theta = 42^\circ \pm 10^\circ$ (red) and $\theta = 42^\circ \pm 15^\circ$ (blue). Right: N_{eff} as a function of distance for the (n,γ)Gd sample. 44
3.18 Comparison of water transparency from decay electrons and (n,γ)Gd. Left: example (n,γ)Gd fit with linear using a fixed intercept ("y-fixed, yellow) and a free intercept ("y-free, purple). Right: SK-VI to early SK-VII trends from both methods. (n,γ)Gd gives about 30m larger transparency, with attenuation-length differences < 50 m. Correlations between methods are 0.66 (y-free) and 0.82 (y-fixed). 45
3.19 Fit-window comparison for water-transparency extraction. N_{eff} vs distance for decay electrons (Left) and (n,γ)Gd (Right) with their respective fit ranges. The (n,γ)Gd window is broad, excluding only edge bins. 46
3.20 Impact of fit range on the inferred attenuation length. Left: overlay of decay-electron and (n,γ)Gd N_{eff} vs distance, showing agreement for $r \gtrsim 2200$ cm. Right: attenuation lengths from (n,γ)Gd using 700–3400 cm (yellow) and 2200–3400 cm (purple), compared with decay electrons (red). Differences relative to decay electrons are shown below, highlighting the fit-range dependence. 46
3.21 Angular dependence of the water-transparency calibration for decay electrons and (n,γ)Gd. Left: definitions of θ and ϕ. Upper right: variation in θ within $\pm 1.0\%$. Lower right: variation in ϕ within $\pm 0.75\%$. 47
3.22 A schematic view of the LINAC calibration [88]. 49
3.23 A schematic view of the DT calibration (left) and angle distribution results (right) [85]. 50

4.1 MC-truth neutron multiplicities for ν-^{16}O (left) and hadron-^{16}O (right) interactions predicted by NEUT using its de-excitation model options. 54
4.2 Illustration of various "physics lists" used for neutron inelastic scattering in SKDETSIM and SKG4. The horizontal axis indicates the kinetic energy of the incoming neutron. A physics list in GEANT4 defines which interaction models and cross sections are used over different energy ranges. In this study, SKDETSIM (based on GEANT3) employs GCALOR [107], while SKG4 (based on GEANT4) can choose from multiple physics lists [106]. Examples include FTFP_BERT_HP (Fritiof Parton & Precompound + Bertini Cascade + High Precision neutron model), QGSP_BIC_HP (Quark-Gluon String & Precompound + BInary Cascade + High Precision neutron model), and INCL++_HP (Liège INtranuclear Cascade + High Precision neutron model). . . . 57
4.3 MC-truth neutron multiplicity across SI models. Upper Left: NEUT 5.6.3 primary vs. SKG4–INCL secondary. Upper Right: BERT vs. INCL. Lower Left: INCL and BERT with a common de-excitation (G4PreCompound). Lower Right: BERT with G4Cascade (default) vs. G4PreCompound. Consistent with the SK-Gd atmospheric NCQE study [105], using G4PreCompound for BERT brings the multiplicity closer to INCL/BIC, indicating de-excitation modeling drives the original BERT discrepancy. 62
4.4 The relationship between the effective hits N_{eff} and the reconstructed visible energy for electrons simulated in Monte Carlo analysis, along with the result of a linear fitting (top), and the ratio of the MC to the fitted values (bottom). This Figure is taken Ref. [4]. 68
4.5 Schematic view of Cherenkov angle definitation (Left). Distributions of opening angles from all PMT triplets for electron events (upper right), and events with multiple γ rays (lower right). Blue lines mark the reconstructed Cherenkov angles. Figure adapted from Ref. [4]. 70
4.6 Steps to compute MSG value. **Left:** Start with one pair of PMT hits (black dots). From the reconstructed prompt vertex, draw any 42° cones whose edges (black, dashed) pass through both hits. The cone axis is marked by the red cross. **Middle:** Repeat for every PMT pair. Each pair yields zero, one, or two candidate cones. **Right:** Identify the largest cluster of candidate cones whose axes fall within 50° of a single direction (red, solid). Clustering is iterated to maximize the magnitude of the summed axis vectors in the largest cluster. Figure taken from Ref. [36] 71
4.7 Concept of the pre-selection. 72

4.8 Normalized 14 feature variables before neural network classification. Green and blue lines are Gd(n,γ) and H(n,γ) signal, respectively. The gray line is the mis-tagged neutrons from the background noise. . . . 75
4.9 Normalized 14 feature variables after neural network classification. Green and blue lines are Gd(n,γ) and H(n,γ) signal, respectively. The gray line is the mis-tagged neutrons from the background noise. . . . 76

5.1 Residual-time distributions for various Δt_0 settings in the Run 11 NCQE study. 79
5.2 Gaussian-fit results from scanning Δt_0 in the Run 11 NCQE study, showing an optimal range near 190 ns. 79
5.3 Linear fits for the ambient low-energy background cuts. The events above the red lines were kept. 81
5.4 Two-dimensional E_{rec}–θ_C distributions of NCQE and CCQE MC with the optimized cut. The region above the line is NCQE-enriched and selected. The lower region is CCQE-dominated and rejected. 81
5.5 Distributions of E_{rec}, θ_C, `dwall`, `effwall`, `OvaQ`, and $\cos\theta_{\mathrm{beam}}$. The SKDETSIM MC is shown as stacked histograms by interaction channel. SKG4 predictions with INCL and BIC are overlaid as red and black lines. The T2K Run 11 data are consistent with the MC within statistical uncertainties. 83
5.6 Vertex distributions X_v, Y_v, Z_v, and R_v^2 for MC and T2K Run 11 data. 84
5.7 Two-dimensional vertex distributions for MC and T2K Run 11 data: X_v–Y_v (top-down) and R_v^2–Z_v (side view). 85
5.8 The left plot illustrates how the delayed neutron tagging efficiency varies with distance in `prompt_keras` (blue), `bonsai_keras` (green), and `lowe_tmva` (brown) settings. The right plot demonstrates the delayed neutron tagging efficiency varies with noise rate. 88
5.9 The NN output values for `bonsai_keras` (left plot) and `lowe_tmva` (right plot). The `lowe_tmva` performs better in tagging $H(n,\gamma)$ events, as shown in a more prominent blue region in the right plot compared to the left plot. 89
5.10 NHits comparison for delayed signals between `bonsai_keras` and `lowe_tmva`. 90
5.11 Comparison between `bonsai_keras` and `lowe_tmva`: neutron multiplicity, capture time, and travel distance. 90
5.12 Neutron candidate features before NN classification. Stacked components: accidental noise (grey), $H(n,\gamma)$ (blue), and $Gd(n,\gamma)$ (green). . 92
5.13 Neutron candidate features after NN classification. Stacked components: accidental noise (grey), $H(n,\gamma)$ (blue), and $Gd(n,\gamma)$ (green). . 93

5.14 NN output values for $Gd(n,\gamma)$ (green), $H(n,\gamma)$ (blue), and accidental noise (grey). Run 11 data are consistent with the MC prediction, indicating stable NN performance. 94
5.15 Delayed–signal features: neutron multiplicity (left), capture time (middle), and travel distance (right). SKDETSIM is shown as colored histograms by interaction channel. INCL and BIC SI variants are dashed overlays. 94
5.16 Neutron–kinematic distributions: $\cos\theta_{\mathrm{nb}}$, $\cos\theta_{\mathrm{n}\gamma}$, longitudinal distance, and transverse distance. 96
5.17 Delayed signal vertex geometry: X_n, Y_n, Z_n, R_n^2, and the 2D projections Y_n–X_n and Z_n–R_n^2. 97
5.18 NN input–feature distributions of neutron candidates before the NN selection (pre-selection only). 98
5.19 Features of candidates that pass the NN selection, defining the delayed–signal sample (pre-selection plus NN classification). 99
5.20 NN output score distributions for $\mathrm{Gd}(n,\gamma)$, $\mathrm{H}(n,\gamma)$, and accidental noise in MC and T2K Run 11. Data agree with MC, indicating stable NN performance with `lowe_tmva`, the DSNB selection using in SK6&7 [36]. 100
5.21 Neutron multiplicity, capture time, and travel-distance distributions with `lowe_tmva` setting. 101
5.22 Neutron kinematics features distribution with `lowe_tmva` setting. . . 102
5.23 Delayed signal vertex distributions in X_n, Y_n, Z_n, and R_n^2. Lower panels: top view (X_n, Y_n) and side view (R_n^2, Z_n). The blue region shows the fiducial volume. The gray region indicates the inner detector region. 103

6.1 Neutron multiplicity (left), neutron-capture time (center), and neutron travel distance (right) for $Gd_2(SO_4)_3{\cdot}8H_2O$ concentrations of 0.0263% (black) and 0.0251% (purple). Upper row: `bonsai_keras`. Lower row: `lowe_tmva`. 108
6.2 Delayed–signal observables for SKDETSIM and SKG4 under several SI models. Columns show capture time, travel distance, and tagging efficiency versus travel distance. Rows are, in order: `bonsai_keras` with SKDETSIM/INCL/BIC, `bonsai_keras` with SKDETSIM/BERT, and `lowe_tmva` with the same framework comparisons. 109

6.3 Comparison of NHits distributions for Am/Be data (black) and MC simulations (red) across different source positions, with r_H set to 50% (left) and 56% (right). The simulation components are color-coded: true Gd(n,γ) (pink), H(n,γ) (cyan), 4.438 MeV γ-rays (green), and background PMT hits (gray). All histograms are normalized by the number of events. Figure adapted from Ref. [129] 112
6.4 PMT gain variation within the T2K Run 11 period. 115
6.5 Water transparency and PMT dark-rate trends during the T2K Run 11 period. 116

7.1 Mean neutron multiplicity for different neutrino generators. MC predictions use SKDETSIM with the Bertini-style SI model. 119
7.2 Mean neutron multiplicity for different SI models. MC predictions use NEUT 5.6.3. 120
7.3 The neutron multiplicity with NC 2p2h simulation with TEM. The left plot compares the 2p2h simulation in NEUT (black), NuWro with Nieves (blue), and NuWro with TEM (red). The center plot presents interaction channels for NEUT. The right plot highlights the NC 2p2h interactions in NuWro with a light blue histogram. 121
7.4 Summary of experimental constraints on the strange axial coupling g_A^s. Orange points: δs from polarized lepton deep inelastic scattering (EMC [134, 135], HERMES [136], COMPASS [137]). Green points: ν–NCQE measurements (BNL E734 [46], MiniBooNE [138], KamLAND [44]). Adapted from Ref. [44]. 122
7.5 Left: MC predictions of neutron multiplicity for several g_A^s choices. The solid black curve uses the NEUT default $g_A^s = -0.08$. The dashed blue curve shows the NuWro default $g_A^s = 0.0$. The dashed red curve uses $g_A^s = -0.3$, following the KamLAND analysis, which is the neutron multiplicity result from KamLAND is shown in the right panel [44]. Lower g_A^s reduces the predicted neutron yield in both cases. Although g_A^s shifts the prediction, changes of the SI model produce a larger reduction, indicating a smaller relative impact from g_A^s. 123
7.6 Fractional difference in NEUT+NucDeEx relative to NEUT only. The gray region marks the reconstructed energy region below 3.5 MeV, which will be filtered out in the prompt NCQE event selection. 125
7.7 Neutron multiplicity with NucDeEx (red) and without (black) for pure NCQE interaction events. NEUT+NucDeEx yields slight more neutrons, shifting the distribution to higher multiplicities as expected. . . 125

7.8 Neutron multiplicity for the NEUT default (black) and an SRC-modified configuration (red). Left: NEUT vs. NuWro. Right: NEUT with SFCORRNNFRAC varied from 0.3 to 0.6. 126
7.9 Impact of Pauli blocking (left) and RPA (right) on the Q^2 distribution (top) and neutron multiplicity (bottom). Pauli blocking causes a $\sim$ 0.5% reduction in neutrons with minimal shape change, while RPA produces a noticeable low-Q^2 suppression and a $\sim$ 13% reduction in neutrons. 127
7.10 For both panels, events in the full energy range [3.49, 29.49] MeV are shown. Left panel: *MSG* distributions for prompt events, comparing data set with MC using the BERT SI model (histogram), INCL++ (dotted red), and BIC (dashed black). Right panel: Correlation between Cherenkov angle and *MSG*, with $MSG \sim 0.5$ indicating coherent patterns. Delayed signal multiplicity for each prompt event is categorized as zero (blue squares), one (red circles), or more than one (orange triangles). 131
7.11 Comparisons of data and MC predictions for NCQE-like events within the reconstructed energy range of [3.49, 7.49] MeV, showing *MSG* distributions alongside θ_C. 132
7.12 Same as Figure 7.11, but for the higher-energy range of [7.49, 29.49] MeV, which overlaps with the DSNB search window. In the left plot, an $MSG > 0.38$ selection yields an efficiency of 21.4% $\pm$ 17.1 (stat.), while the right plot highlights (in gray) the naive DSNB cut region ($38° < \theta_C < 53°$, $MSG > 0.37$). 132

9.1 The primary γ multiplicity (left) and total energy (right) between NEUT 5.9.0 and 5.6.4 of all interactions. The error bars indicate the statistical uncertainty of the MC sample. 139
9.2 The primary γ multiplicity (left) and total energy (right) for NEUT 5.9.0 with default de-excitation model and NucDeEx. 139
9.3 The physics list used in SKDETSIM and SKG4 140
9.4 Secondary gamma difference between G4Cascade and G4PreCompound with BERT with T2K flux of all interactions. 141
9.5 Secondary γ difference between G4PreCompound and NucDeEx. Also shown the secondary γ difference between BERT and INCL with same de-excitation model (G4PreCompound) 142

10.1 NCQE event overview and MC comparisons. **Left:** schematic of an NCQE interaction on ^{16}O showing a primary and secondary γ production. **Right:** total (primary + secondary) energy distributions for γ's, electrons, and positrons. γ's dominate in the analysis range of $[3.5, 29.5]$ MeV. 146
10.2 The Run 10a linear fitting result of ambient low energy background cuts. 147
10.3 The Run 10b linear fitting result of ambient low energy background cuts. 147
10.4 The features of T2K NCQE events (FHC) for Run 1-9. 149
10.5 The features of T2K NCQE events (FHC) for Run 10. 149
10.6 The features of T2K NCQE events (FHC) for Run 11. 150
10.7 The features of T2K NCQE events (FHC) among Runs 1-9, 10, and 11. 150
10.8 The features of T2K NCQE events (FHC, Run1-11) among NEUT 5.9.0 with default de-excitation model (gray) and NucDeEx (magenta). 153
10.9 The features of T2K NCQE events (FHC, Run1-11) among BERT-G4Cas(red), BERT-G4Pre(blue), and INCL-G4Pre(black). 154
10.10 The features of T2K NCQE events (FHC, Run 1-11) among BERT-Pre, INCL-G4Pre, INCL-NucDeEx, and NEUT(564)-INCL-G4Pre. 154
10.11 The features of T2K NCQE events (FHC) among Runs 1-11. 155
10.12 The features of T2K NCQE events (RHC) among Runs 1-9. 155
10.13 The features of T2K NCQE events (FHC+RHC) among Runs 1-11. . 156
10.14 The previous (dashed black) T2K neutrino beam uncertainty and the updated one (solid black) in this study. 157
10.15 The Q^2 distributions of ν-NCQE in FHC (left) and $\bar{\nu}$-NCQE in RHC (right) each selection stage. Figure were taken from Ref. [4] 158
10.16 Comparison of NC inelastic (left) and NCQE cross sections on oxygen (right). 159
10.17 Scale factor results from pseudo-experiments, where observed event counts were fluctuated according to statistical uncertainties. The extracted values are $f_{\nu\text{-NCQE}} = 0.82 \pm 0.07$ and $f_{\bar{\nu}\text{-NCQE}} = 1.10 \pm 0.20$. . 164
10.18 Systematic uncertainty evaluation of the scale factors via pseudo-experiment variations. The resulting values are $f_{\nu\text{-NCQE}} = 0.82^{+0.20}_{-0.11}$ and $f_{\bar{\nu}\text{-NCQE}} = 1.10^{+0.22}_{-0.15}$, with the secondary-$\gamma$ emission model identified as the primary source of uncertainty. 165
10.19 Measured Run 1-11 NCQE-like cross sections on ν–^{16}O (left) and $\bar{\nu}$–^{16}O (right), compared with the NEUT NCQE predictions. Data points are placed at the flux-mean energies: 0.82 GeV for neutrinos and 0.68 GeV for antineutrinos. Vertical bars show statistical uncertainties (shorter) and the total uncertainties (longer). Horizontal bars indicate the $\pm 1\sigma$ ranges for the T2K flux spectra. 166

11.1 The T2K (blue) and atmospheric (yellow) neutrino fluxes, specifically for NCQE interactions. 172
11.2 The T2K (blue) and atmospheric (yellow) neutrino NCQE event features, together with DSNB event feature (red). 174
11.3 Feature distribution before and after applying the θ_C cut [38°, 53°]. Brown and blue lines mark the 95% containment for atmospheric NCQE and DSNB events, respectively. 175
11.4 MSG cut strategy applied bin-by-bin in energy during the SK-VII DSNB search. 175
11.5 Comparison of different cut strategies using MSG and N50 distributions. The plots illustrate how the proposed linear and NN cuts perform relative to the traditional discrete approach. 177
11.6 Schematic of the neural network structure used in this analysis. . . . 177
11.7 Training loss (left) and accuracy (right) versus epoch. 180
11.8 Optimization of the NN output threshold (left) and corresponding ROC curves (right). 181
11.9 ROC comparison of the θ_C-only cut, discrete MSG, linear MSG, and NN classifier. 182

12.1 LINAC features (purple) overlays with DSNB (dash blue) and Atm. NCQE (dash brown). Rows indicate 8, 12, 15 MeV LINAC e^- beams. Columns plot θ_C-N50, N50-MSG, and N50-θ_C. 185
12.2 NN-output distributions for LINAC electrons in SK6 (Run 11). Rows: 8, 12, 15 MeV. Columns: injection positions. LINAC Data (purple) vs. LINAC MC (blue). DSNB (black dashed) and Atm. NCQE (red dashed) overlaid. 187
12.3 NN-output distributions for LINAC electrons in SK-IV (pure water), "edge" injections. Rows: 8, 12, 15 MeV. Columns: injection positions. LINAC Data (purple) vs. LINAC MC (blue). DSNB (black dashed) and Atm. NCQE (red dashed) templates overlaid. 188
12.4 NN-output distributions for LINAC electrons in SK-IV (pure water), "center" injections. Rows: 8, 12, 15 MeV. columns: injection positions. LINAC Data (purple) vs. LINAC MC (blue). DSNB (black dashed) and Atm. NCQE (red dashed) templates overlaid. 189
12.5 SK-VI, 8 MeV LINAC run: comparison of NN output and related features for data and MC, shown both all and with NN output higher than 0.9. The data (purple dashed) have a sub-cluster at $N50 \approx 100$, whereas the MC (magenta solid) confines at $N50 \approx 75$. 190

12.6 SK-VI period, 8 MeV LINAC run. For events with a high NN output larger than 0.9, the LINAC data (purple dashed) show a clear excess over MC (magenta) across the detector's top, center, and bottom regions. 191
12.7 SK-IV period, 8 MeV LINAC run. For events with a high NN output larger than 0.9, the LINAC data (purple dashed) show a clear excess over MC (magenta) across the detector's top, center, and bottom regions. The LINAC data excess is weaker than in SK-IV but remains visible at the lower-edge position for events with NN output larger than 0.9. 192
12.8 SK-VI period, 8 MeV LINAC run. For events with a high NN output larger than 0.52, the LINAC data (purple dashed) show a clear excess over MC (magenta) across the detector's top, center, and bottom regions. Also a 15 MeV LINAC run for reference. 193
12.9 Cumulative NN-output distributions for single-electron LINAC events. The LINAC data (purple dot) and LINAC MC (blue line) are integrated from high to low NN score. The largest difference between them is adopted as the systematic uncertainty on the NN cut for DSNB (single electron-like) source. 194
12.10 LINAC MC–data separation in cumulative NN-output curves for LINAC runs across SK periods and injection positions. The maximum gap, 2.72%, occurs for the 8 MeV lower-edge sample in SK-VI period and is taken as the NN-cut systematic uncertainty. 194
12.11 LINAC calibration of the discrete MSG cut employed in the SK-VI/VII DSNB analyses. LINAC data (blue) and MC (orange) for the 8, 12, and 15 MeV SK-IV period sample are shown. The green band denotes the accepted MSG range used, providing a baseline for comparison with the NN multivariate selection. 196
12.12 MC–data efficiency differences for the discrete MSG cut, evaluated with LINAC calibration runs at 8, 12, and 15 MeV during SK4 and SK6. The largest discrepancy (2.76%) occurs for the 8 MeV lower-edge sample in SK6 and is adopted as the systematic uncertainty for the discrete MSG cut on DSNB (single electron-like). 197
12.13 SK-IV LINAC calibration for linear MSG cut. LINAC data (blue) and MC (orange) for the 8, 12, and 15 MeV LINAC sample are shown. The green band denotes the linearly defined acceptance region, showing a simplified alternative to the discrete MSG selection. 198

12.14 LINAC MC–data efficiency differences for the linear MSG cut, evaluated with LINAC runs at 8, 12, and 15 MeV among SK-IV and SK-VI period. The largest discrepancy, 3.22%, occurs for the 8 MeV sample in SK-VI period and is taken as the systematic uncertainty for the linear-MSG selection for DSNB (single electron-like source). 199

13.1 T2K FHC (blue) vs atmospheric NCQE (orange or green) neutrino flux after the 1st–3rd DSNB cuts. T2K's narrower, higher flux yields a slightly high energy tail and larger Cherenkov angles with lower MSG. 203
13.2 Cherenkov angle reweighting of T2K to atmospheric NCQE. Reweighted T2K (light blue) matches the atmospheric E_{vis} and MSG. Ratio panels show residuals (at most ∼8% on the energy spectrum). 203
13.3 T2K FHC: visible energy E_{vis} after each cumulative cut (SKDETSIM histograms, SKG4 with BERT-G4Cascade (blue) and INCL-NucDeEx (red) overlays.). 206
13.4 T2K FHC: N_{50} after each cumulative cut (SKDETSIM histograms, SKG4 with BERT-G4Cascade (blue) and INCL-NucDeEx (red) overlays.) 207
13.5 T2K FHC: θ_C after each cumulative cut (SKDETSIM histograms, SKG4 with BERT-G4Cascade (blue) and INCL-NucDeEx (red) overlays.) 207
13.6 T2K FHC: MSG after each cumulative cut (SKDETSIM histograms, SKG4 with BERT-G4Cascade (blue) and INCL-NucDeEx (red) overlays.) 208
13.7 T2K FHC: OvaQ after each cumulative cut (SKDETSIM histograms, SKG4 with BERT-G4Cascade (blue) and INCL-NucDeEx (red) overlays.) 208
13.8 T2K RHC: visible energy E_{vis} after each cumulative cut (SKDETSIM histograms, SKG4 with BERT-G4Cascade (blue) and INCL-NucDeEx (red) overlays.) 209
13.9 T2K RHC: N_{50} after each cumulative cut (SKDETSIM histograms, SKG4 with BERT-G4Cascade (blue) and INCL-NucDeEx (red) overlays.) 209
13.10 T2K RHC: Cherenkov angle θ_C after each cumulative cut (SKDETSIM histograms, SKG4 with BERT-G4Cascade (blue) and INCL-NucDeEx (red) overlays.) 210
13.11 T2K RHC: MSG after each cumulative cut (SKDETSIM histograms, SKG4 with BERT-G4Cascade (blue) and INCL-NucDeEx (red) overlays.) 210
13.12 T2K RHC: OvaQ after each cumulative cut (SKDETSIM histograms, SKG4 with BERT-G4Cascade (blue) and INCL-NucDeEx (red) overlays.) 211
13.13 T2K NCQE (FHC+RHC, Runs 1–11): visible energy E_{vis} after each cumulative cut. SKDETSIM histograms. SKG4 overlays in blue(BERT-G4Cascade) / red(INCL-NucDeEx)). 215

13.14 T2K NCQE (FHC+RHC): PMT hits N_{50} after each cumulative cut. SKDETSIM histograms, SKG4 with BERT-G4Cascade (blue) and INCL-NucDeEx (red) overlays. 216
13.15 T2K NCQE (FHC+RHC): Cherenkov angle θ_C after each cumulative cut. SKDETSIM histograms, SKG4 with BERT-G4Cascade (blue) and INCL-NucDeEx (red) overlays. 216
13.16 T2K NCQE (FHC+RHC): MSG after each cumulative cut. SKDETSIM histograms, SKG4 with BERT-G4Cascade (blue) and INCL-NucDeEx (red) overlays. 217
13.17 T2K NCQE (FHC+RHC): OvaQ after each cumulative cut. SKDETSIM histograms, SKG4 with BERT-G4Cascade (blue) and INCL-NucDeEx (red) overlays. 217
13.18 Distributions of θ_C–N50 (left), N50–MSG (center), and θ_C–MSG (right). The top row shows events passing only the E_{vis} $[7.5, , 29.5]$ MeV cut. The bottom row shows MC after applying the E_{vis} and θ_C cuts, with events selected by the MSG_{dis} cut highlighted. T2K MC is shown as a brown heatmap. T2K data are plotted in black (non-selected) and red (selected). FHC points are circles, and RHC points are triangles. The selected region (MSG_{dis}) is shaded light green. 218
13.19 Distributions of θ_c–N50 (left), N50–MSG (center), and θ_c–MSG (right). The top row shows events after the MSG_{lin} selection. The bottom row shows events after the NN selection. T2K MC is shown as a brown heatmap. T2K data are plotted in black (non-selected) and red (selected). FHC points are circles and RHC points are triangles. Selected regions are shaded light green. 218
13.20 Distributions of θ_c–N50 (left), N50–MSG (center), and θ_c–MSG (right) with visible-energy selection. T2K MC (brown) and DSNB MC (blue) are rendered as heatmaps. The 95% contours are shown for both samples. T2K MC are further categorized by γ multiplicity: single (red), double (orange), and ≥ 3 (green). 219
13.21 Distributions of θ_c–N50 (left), N50–MSG (center), and θ_c–MSG (right) with visible-energy and cherenkov angle selection. T2K MC (brown) and DSNB MC (blue) are rendered as heatmaps. The 95% contours are shown for both samples. T2K MC are further categorized by γ multiplicity: single (red), double (orange), and ≥ 3 (green). 219

13.22 Neutron tagging efficiency calibration with a ^{241}Am-Be source. Top panel shows pre-correction results [129]. Bottom left shows the corrected calibration, and bottom-right shows the data/MC ratio. Fixing the MC H–Gd capture ratio achieves ∼6% data–MC agreement and reduces the neutron tagging uncertainty on NCQE events from 21% to 7.5%. 222
13.23 Update to the neutron-multiplicity systematic. **Left:** mean neutron multiplicity form T2K NCQE [161]. **Center:** atmospheric-neutrino CCQE with different de-excitation models at SK [129]. **Right:** Comparison of BERT and INCL with the same de-excitation model to SK data. The ratio to data spread between "INCL + BERT_PC" and "INCL + INCL_PC" is ∼15%, which is adopted as the revised neutron multiplicity uncertainty, replacing the previous 40% estimate [50]. . . 222

15.1 Expected background spectra for the DSNB search under four selection settings: θ_C only, $\mathrm{MSG_{dis}}$, $\mathrm{MSG_{lin}}$, and NN. The DSNB signal shape is modeled assuming the flux predictions of Horiuchi+09 [17]. 228
15.2 Distribution of background subtracted distributions from 10^6 pseudo-experiments in each energy bin using the NN selection. The vertical marker indicates the 90% C.L. upper limit on the signal yield, $N^{\mathrm{sig}}_{90\%}$. 229
15.3 90% C.L. upper limits on the DSNB $\bar{\nu}_e$ flux versus energy for selections θ_C (black dashed), $\mathrm{MSG_{dis}}$ (blue), $\mathrm{MSG_{lin}}$ (green), and NN (red). The KamLAND limit (cyan) [38] is shown for comparison. 230
15.4 Projected DSNB significance versus time [23] up to 2032. Curves show 5% background efficiency with 68% (blue soild) and 43% (red soild) systematics, and a 2% background efficiency enabled by additional T2K data (purple dashed). Under the the most optimistic DSNB flux model (Kaplinghat+00), all scenarios reach 3σ before SK ends. 231
15.5 DSNB 3σ flux sensitivity compared with modern model predictions. . 232

List of Tables

3.1 Summary of the Super-Kamiokande phases SK-I to SK-VII. 31
3.2 Cherenkov thresholds for charged particles of interest. The particle masses are taken from Ref. [81], and the threshold values are computed from Eq. 3.5. 33
3.3 Summary of the SK triggers. The numbers in the second column are the number of hit PMTs within a 200 ns window (N_{200}). 35
3.4 Selection summary, where Δt is the time between the parent muon and the decay–electron candidate. 42
3.5 Event selections for water-transparency calibration with decay electrons and (n, γ)Gd. 43
3.6 Comparison of analysis settings between Decay-e and (n,γ)Gd. 44
3.7 Summary of water-transparency (attenuation-length) and directional uncertainties. 46

4.1 Model configuration in NEUT. 52
4.2 Transition probabilities to nucleon-hole and others states for the considered models. 53
4.3 Excited states and γ-ray emission modes of ^{16}O proton hole $(p_{3/2})^{-1}$ and neutron hole $(p_{1/2})^{-1}$. 53
4.4 Excitation energies and branching ratios for residual nuclei of ^{16}O proton hole $(s_{1/2})^{-1}$. Table adapted from Ref. [105]. 55
4.5 Natural abundances and thermal neutron-capture cross sections of gadolinium isotopes. 61
4.6 Summary of the configuration parameters used in the SKDETSIM and SKG4 simulations. 63
4.7 Oscillation parameters used in Eq. 4.18, with the reactor constraint [124]. 65
4.8 Summary of parameter values for pre-selection. 72

5.1 Run-by-run timing shifts relative to Runs 1–3 and to the preceding run. 78
5.2 Parameters for `dwall`, `effwall`, and `OvaQ` in T2K Run 11. 80
5.3 Expected number of neutrino events for Run 11 (MC) that passing each NCQE selection criteria for each interaction mode. 82

5.4 Expected number of neutrino events for Run 11 (MC) that pass all NCQE selections using SKSETSIM and SKG4, with the choice of secondary model indicated in parentheses. 82
5.5 Number of events passing each NCQE selection criteria for data and MC. For MC, the nominal SKDETSIM and prediction from three SI models with SKG4 are provided, where the selection efficiency is also shown in the parentheses. 82
5.6 Summary of NTag settings used in this analysis. 87
5.7 Summary of NTag parameters adopted in this analysis. 87
5.8 Summary of neutron tagging efficiencies for `bonsai_keras` and `lowe_tmva` settings. 88
5.9 Neutron event numbers from the MC sample and dataset with `bonsai_keras` are presented. SKDETSIM and SKG4 are provided, and ratios of each interaction channel to total events are shown in parentheses. Datasets are categorized into On-Beam and Off-Beam, where Off-Beam assesses beam-unrelated noise. There is slight overprediction with the BERT model, while the dataset is more consistent with the INCL model. . . 91
5.10 Neutron event numbers from the MC sample and dataset with LOWE ntag setting are presented. SKDETSIM and SKG4 are provided, and ratios of each interaction channel to total events are shown in parentheses. Datasets are categorized into On-Beam and Off-Beam, where Off-Beam assesses beam-unrelated noise. There is slight overprediction with the BERT model, while the dataset is more consistent with the INCL model. 100
5.11 EventID Summary 104

6.1 Summary of Gd concentration settings used in this uncertainty evaluation. 107
6.2 Variations of delayed signal selection performance by nucleon SI. These numbers are normalized by Run 11, 1.76×10^{20} POT. 110
6.3 Detector response uncertainties on tagging efficiency. 112
6.4 ν cross-section parameters. Figure taken from Ref. [52]. 114
6.5 Uncertainties for non-positional selection parameters. 115
6.6 Summary of systematic uncertainties on the overall neutron tagging efficiency. Sources between the dashed lines are those that were taken from AmBe calibration results [129]. 117
6.7 Total uncertainties on overall neutron tagging efficiency and background rate for Run 11. 117

7.1 Summary of the delayed signal variations under different conditions beyond the SI models. 120

7.2 Stage-by-stage delayed signals for NEUT and NEUT+NucDeEx after NCQE cuts. NucDeEx increases delayed singal by 0.9% while slightly reducing overall tagging efficiency (−0.5%). The overall effect is small. 124

8.1 The total uncertainty of the atmospheric NCQE spectrum used in the SK-VI DSNB study [23]. 135

9.1 Model configuration of NEUT 5.9.0 in this study. 137
9.2 MC generator–detector configurations and their abbreviations. 142
9.3 Summary of MC-setting comparisons 143

10.1 Summary on T2K Run 1–11 with the operation mode, MR Run, SK DAQ Run, and POT for the SK good spills used in this analysis. . . . 145
10.2 Summary on parameters for `dwall`, `effwall`, and `OvaQ` in each T2K run. 148
10.3 Summary on parameters for a_{opt} and b_{opt} in each T2K run. 151
10.4 Summary on Run 1-9, 10, and 11 NCQE event 151
10.5 Summary on FHC and RHC NCQE event (Run 1-11) 152
10.6 Probabilities for nucleon–hole configurations in ^{16}O. 152
10.7 Flux originated systematic uncertainties [%] for each interaction. . . . 157
10.8 Neutrino interaction related systematic uncertainties [%] for each interaction. 158
10.9 Primary-γ originated systematic errors [%] for each interaction. . . . 159
10.10 Secondary-γ originated systematic errors [%] for each interaction. . . 160
10.11 Summary of systematic uncertainties (%) and event composition fractions (%) for the NCQE cross section. Struck-out entries indicate the values used in the Run 1–9 measurement [50]; updated values are given here. 161

11.1 Cut based neutron selection variables. 171
11.2 Neural-network configuration and training settings. 179
11.3 Selection methods on DSNB and atmospheric NCQE efficiency. . . . 181

12.1 LINAC Runs by Period and Position 183
12.2 NN Systematic uncertainty from LINAC for SK6 and SK4. 195
12.3 Discrete MSG Systematic uncertainty from LINAC for SK6 and SK4. 197
12.4 Linear MSG Systematic uncertainty from LINAC for SK6 and SK4. . 200

13.1 Relative ratios of flux-averaged events from T2K to atmospheric flux for six models, normalized to NEUT. Table taken from Ref. [50] . . . 204

13.2 Expected event yields after successive selection cuts for NCQE Runs 1–11 FHC and RHC modes. Percentages in parentheses give the fractional contribution of each component to the total MC expectation at the corresponding stage. 205
13.3 Summary of Run 1–11 event predictions for FHC and RHC. Columns correspond to cuts; rows correspond to different MC settings. Numbers in parentheses indicate the fraction relative to the "NCQE selection" sample. 206
13.4 Summary of NCQE event predictions combining Run 1–11 FHC and Run 1–9 RHC (FHC+RHC). Columns correspond to cuts; rows correspond to different MC settings. Numbers in parentheses indicate the fraction relative to the combined "NCQE selection" sample. 213
13.5 Summary of MC systematic uncertainties for FHC and RHC from different sources. 214
13.6 Systematic uncertainties on the DSNB signal due to event reduction cuts (mentioned in Chapter 11) as estimated with LINAC data and MC. 220
13.7 Each uncertainty value from the original table divided by 43.1 and reported in percent. 221
13.8 Systematic uncertainties on the atmospheric NCQE for DSNB search. 223

15.1 Background by energy bin for the θ_C cut, including systematic uncertainties and 90% C.L. limits. 227
15.2 Background by energy bin for the MSG_{dis} cut, including systematic uncertainties and 90% C.L. limits. 227
15.3 Background by energy bin for the MSG_{lin} cut, including systematic uncertainties and 90% C.L. limits. 227
15.4 Background by energy bin for the NN cut, including systematic uncertainties and 90% C.L. limits. 228

Part I

Introduction

Chapter 1

Introduction

The Diffuse Supernova Neutrino Background (DSNB) acts as a cosmic archive, preserving the integrated history of star formation and core-collapse supernovae. Detecting this continuous, faint flux is a primary objective in modern astrophysics, as it would provide a comprehensive timeline of stellar death that far exceeds the isolated data point of SN1987A. However, identifying the DSNB within neutrino detectors is complicated by the noise of atmospheric neutral-current quasielastic (NCQE) interactions. To successfully isolate the DSNB signal, these background processes must be modeled with exceptional precision. Accordingly, this thesis utilizes accelerator data from the T2K experiment to measure NCQE interactions, aiming to constrain this background effectively and enhance the sensitivity required for DSNB detection.

1.1 Neutrinos from Core-Collapse Supernovae

A supernova is a stellar explosion caused by either the core collapse of a massive star or the thermonuclear disruption of a white dwarf. Supernovae are sorted by their optical spectra. If hydrogen (Balmer) lines are absent, the event is Type I. If they are present, it is Type II. Within Type I, prominent silicon features define Type Ia. When silicon is absent, the class splits into Type Ib (helium lines detected) and Type Ic (no helium). Physically, Type Ia result from the thermonuclear disruption of carbon–oxygen white dwarfs, whereas all non-Ia types are core-collapse supernovae (CCSNe) driven by the gravitational collapse of a stellar core and accompanied by an intense neutrino flux [1].

In CCSN progenitors, successive burning stages culminate in an iron core, the terminal point of energy-releasing fusion because iron is the most tightly bound nucleus. Beyond this point, fusion no longer provides pressure support. Instead, the core is supported by electron degeneracy pressure, a quantum mechanical effect

arising from the Pauli exclusion principle that prevents electrons from occupying the same state. The core contracts to higher densities, and electron captures on heavy nuclei (e.g., Mg, Na, Ne) lower the electron fraction, weakening electron-degeneracy pressure. At temperatures $T \sim 5 \times 10^9$ K, photodisintegration of iron and α particles removes additional support and accelerates the collapse [2].

Infall proceeds until the core density approaches nuclear values, $\rho \sim 10^{14}\,\mathrm{g\,cm^{-3}}$. There, short-range repulsive nuclear forces abruptly halt the collapse and launch an outward shock. The shock heats and dissociates the inflowing material. With continued accretion, it loses energy and stalls. A proto–neutron star of radius ~ 10 km forms at the center, supported by neutron degeneracy [3].

Neutrino heating can revive the stalled shock: material behind the shock absorbs neutrinos streaming from the proto–neutron star, re-energizing the shock and ejecting the stellar envelope. A successful explosion leaves behind a neutron star. If the progenitor is massive enough, ongoing accretion can instead drive collapse to a black hole [2]. Figure 1.1 shows the schematic of the delayed neutrino-heating mechanism in core-collapse supernovae.

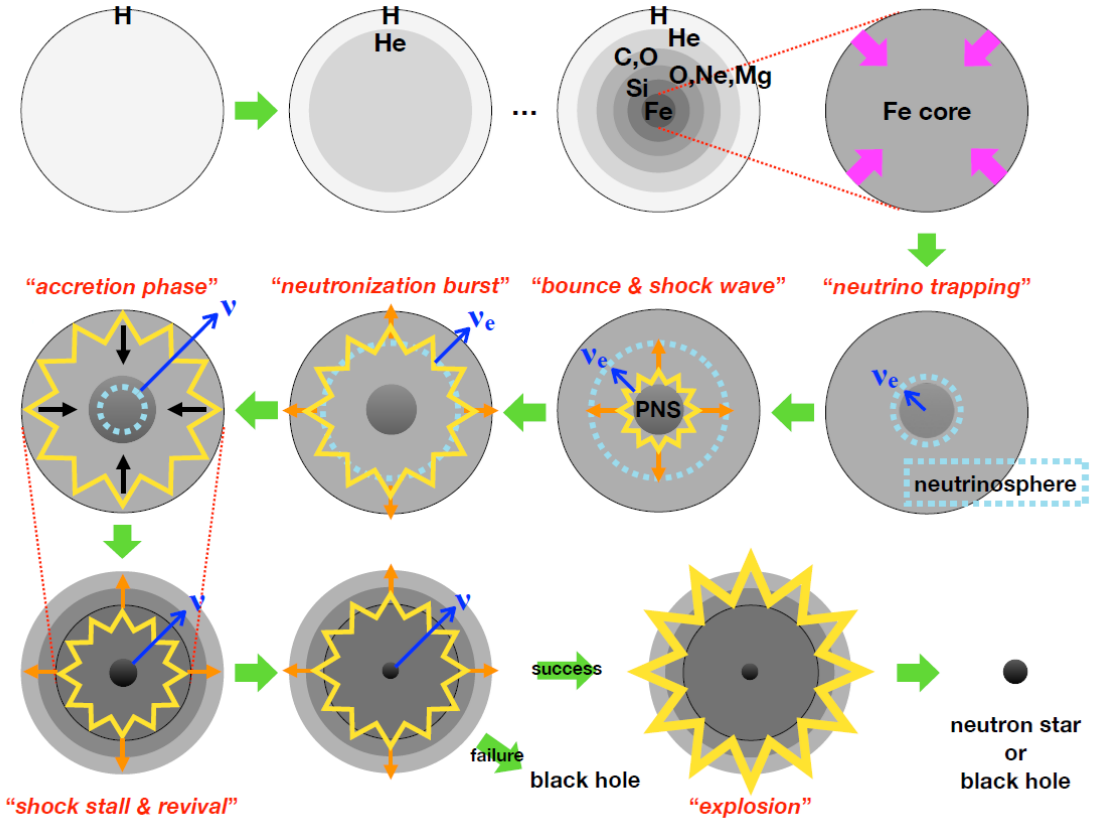

Figure 1.1: Schematic of the delayed neutrino-heating mechanism in core-collapse supernovae, adapted from Ref. [4].

The neutrino emission is both intense and flavor dependent because interac-

tion cross sections in dense matter vary by flavor. Electron (anti)neutrinos undergo charged-current reactions with nucleons and nuclei, while muon and tau (anti)neutrinos interact only through neutral currents and decouple deeper within the proto–neutron star, emerging with higher characteristic energies. Theoretical predicted that CCSNe release a total energy of $\sim 10^{53}$ ergs, with about 99% carried away by neutrinos over $\mathcal{O}(10)$ s. Each event emits roughly 10^{58} neutrinos with characteristic energies of ~ 10 MeV [5]. Figure 1.2 shows the evolution of CCSN neutrino luminosities and mean energies.

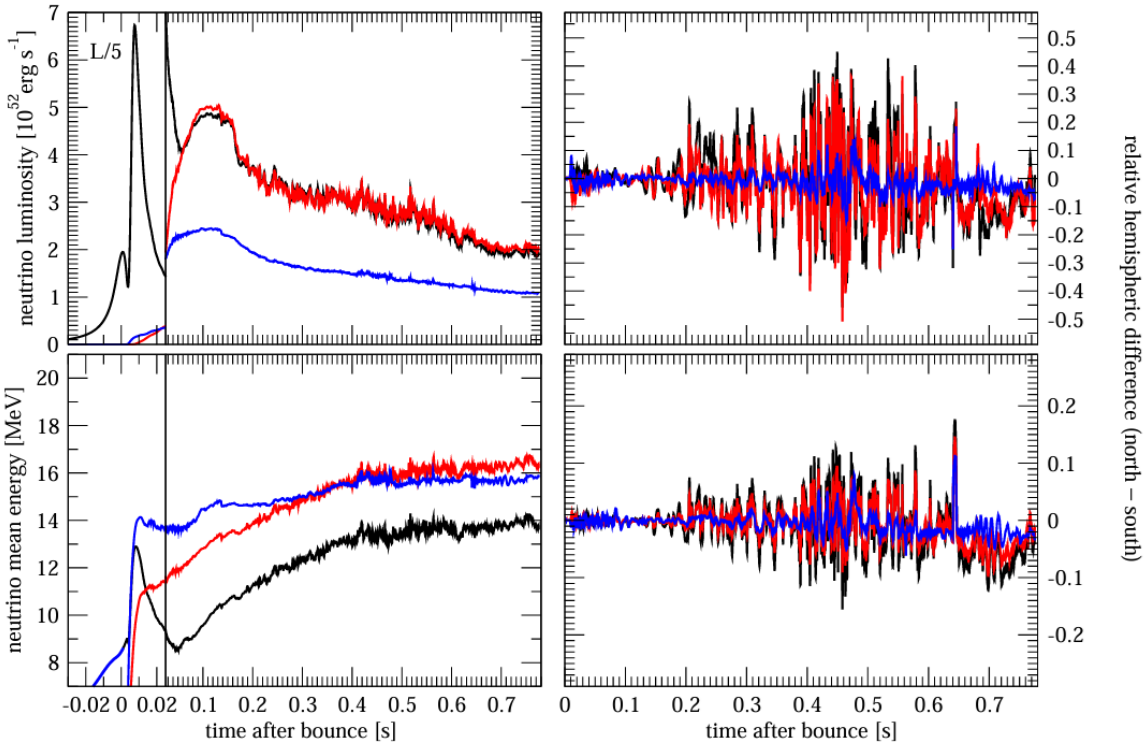

Figure 1.2: Evolution of CCSN neutrino luminosities and mean energies. Black, red, and blue lines correspond to ν_e, $\bar{\nu}_e$, and ν_x, respectively. The right panels illustrate the relative hemispheric differences following core bounce. Figure adapted from Ref. [2]

Although CCSNe are rare, occurring only a few times per century in a typical galaxy [6], humanity has observed a supernova neutrino burst once to date: from SN 1987A in the Large Magellanic Cloud, detected on February 23rd 1987 by Kamiokande-II [7], IMB [8], and Baksan [9]. Figure 1.3 shows the distributions of event energies and arrival times measured by Kamiokande-II and IMB. This detection validated the basic core-collapse framework, although the limited statistics made detailed tests of collapse models difficult. The total neutrino energy inferred for SN 1987A is consistent with theoretical expectations. The exact explosion mechanism remains an open question. Several theoretical models for shock revival are currently under investigation, most notably the delayed neutrino-heating mechanism and the magnetorotational mechanism.

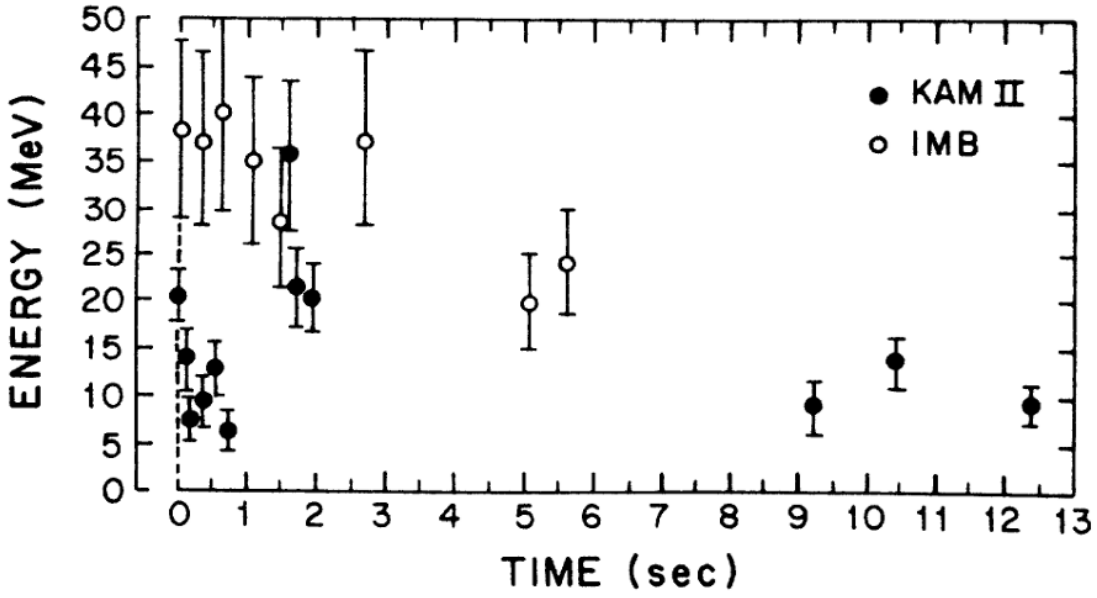

Figure 1.3: Neutrino burst from SN1987A (1987 February 23) as recorded by Kamiokande-II[7] and IMB [8]. Plotted are the reconstructed event energies and arrival times (relative to the first event) for each detector [10].

1.2 Diffuse Supernova Neutrino Background and Current Search Status

Neutrinos from all past CCSNe, however, are expected to accumulate and form a diffuse, all–sky flux known as the Diffuse Supernova Neutrino Background (DSNB) or the Supernova Relic Neutrinos (SRNs). Measuring neutrino flux from DSNB would constrain both the cosmic CCSN rate and the physics of neutrino emission. Below we summarize a standard prediction of the DSNB flux following Refs. [11].

Consider supernovae neutrinos produced at redshift $z \to z + dz$ with emission energies $E'_\nu \to E'_\nu + dE'_\nu$. Their differential number density at emission is

$$dn'(E'_\nu) = R_{\rm CCSN}(z)\,(1+z)^3 \frac{dt}{dz}\,dz\,\frac{dN(E'_\nu)}{dE'_\nu}\,dE'_\nu, \tag{1.1}$$

where $R_{\rm CCSN}(z)$ is the CCSN rate per comoving volume at redshift z (and t denotes cosmic time). A prime indicates quantities evaluated at the emission epoch. The factor $(1+z)^3$ accounts for the physical volume at emission, and $dN(E'_\nu)/dE'_\nu$ is the neutrino number spectrum per CCSN. The present day number density follows as

$$dn(E_\nu) = \frac{dn'(E'_\nu)}{(1+z)^3}. \tag{1.2}$$

Because of redshift, $E'_\nu = (1+z)E_\nu$. Hence the number density today of DSNB

neutrinos produced between z and $z + dz$ with observed energies $E_\nu \to E_\nu + dE_\nu$ is

$$dn(E_\nu) = R_{\rm CCSN}(z)\,\frac{dt}{dz}\,dz\,\frac{dN(E'_\nu)}{dE'_\nu}\,(1+z)\,dE_\nu. \tag{1.3}$$

Redshift and time are related by the Friedmann equation,

$$\frac{dt}{dz} = \frac{1}{H_0(1+z)\sqrt{\Omega_m(1+z)^3+\Omega_\Lambda}}, \tag{1.4}$$

with H_0 the Hubble constant and Ω_m and Ω_Λ the present–day matter and cosmological constant density parameters, respectively. Using $d\Phi(E_\nu)/dE_\nu = c\cdot\, dn(E_\nu)/dE_\nu$, the DSNB flux becomes

$$\frac{d\Phi(E_\nu)}{dE_\nu} = c\int_0^\infty \frac{dz}{H_0\sqrt{\Omega_m(1+z)^3+\Omega_\Lambda}}\,R_{\rm CCSN}(z)\,\frac{dN(E'_\nu)}{dE'_\nu}. \tag{1.5}$$

The DSNB flux can depend on the progenitor's initial mass M and metallicity Z. Including the initial mass function $\Psi_{\rm IMF}(M)$ and the metallicity distribution $\Psi_{\rm ZF}(z,Z)$ yields

$$\begin{aligned}\frac{d\Phi(E_\nu)}{dE_\nu} = c\int_0^\infty \frac{dz}{H_0\sqrt{\Omega_m(1+z)^3+\Omega_\Lambda}}\Bigg[R_{\rm CCSN}(z)\int_0^{z_{\rm max}}\Psi_{\rm ZF}(z,Z)\\ \times\left\{\int_{M_{\rm min}}^{M_{\rm max}}\Psi_{\rm IMF}(M)\,\frac{dN(M,Z,E'_\nu)}{dE'_\nu}\,dM\right\}dZ\Bigg].\end{aligned} \tag{1.6}$$

Calculating this integral requires specific choices for the astrophysical inputs and the neutrino emission spectrum $\frac{dN}{dE}$, the latter of which introduces the largest theoretical uncertainties due to the complex physics of core collapse and black hole formation. Here we discuss features of some common DSNB models.

The earliest studies (Hartmann+97 [12]; Malaney+97 [13]; Kaplinghat+00 [14]) established baseline expectations by deriving the cosmic star formation rate from chemical evolution constraints and adopting deliberately conservative parameters, such as lower neutrino effective temperatures, which kept the predicted flux estimates within roughly one order of magnitude. Ando+03 [15] first treated realistic neutrino oscillations with a numerical spectrum, and Lunardini+09 [16] emphasized the harder high-energy tail produced by massive stars collapsing directly into black holes (so-called failed supernovae). Horiuchi+09 [17] anchored the supernova rate to the observed cosmic star-formation history and adopted standard spectral parameters ($\langle E_{\bar\nu_e}\rangle \approx 15$ MeV) consistent with SN 1987A observations. Galais+10 [18] showed that shockwave propagation can reduce the flux compared with static profiles.

More recent work examines the diversity of progenitor stars and their underlying explosion mechanisms, including Nakazato+15 [11] (black-hole-forming SNe and the equation of state), Horiuchi+18 [19] (critical compactness), Kresse+20 [20] (helium-star and black-hole contributions), Tabrizi+20 [21] (neutrino decay beyond standard oscillations), and Horiuchi+21 [22] (envelope physics from binary interactions), which together identify the assumptions that most strongly alter the overall rate and spectral shape. Figure 1.4 presents a comparison of DSNB flux predictions from the models discussed above. We focus on the $\bar{\nu}_e$ flux because it represents the dominant detection channel, Inverse Beta Decay (IBD), whereas interactions for other channels are subdominant and experimentally challenging in water Cherenkov detectors to isolate.

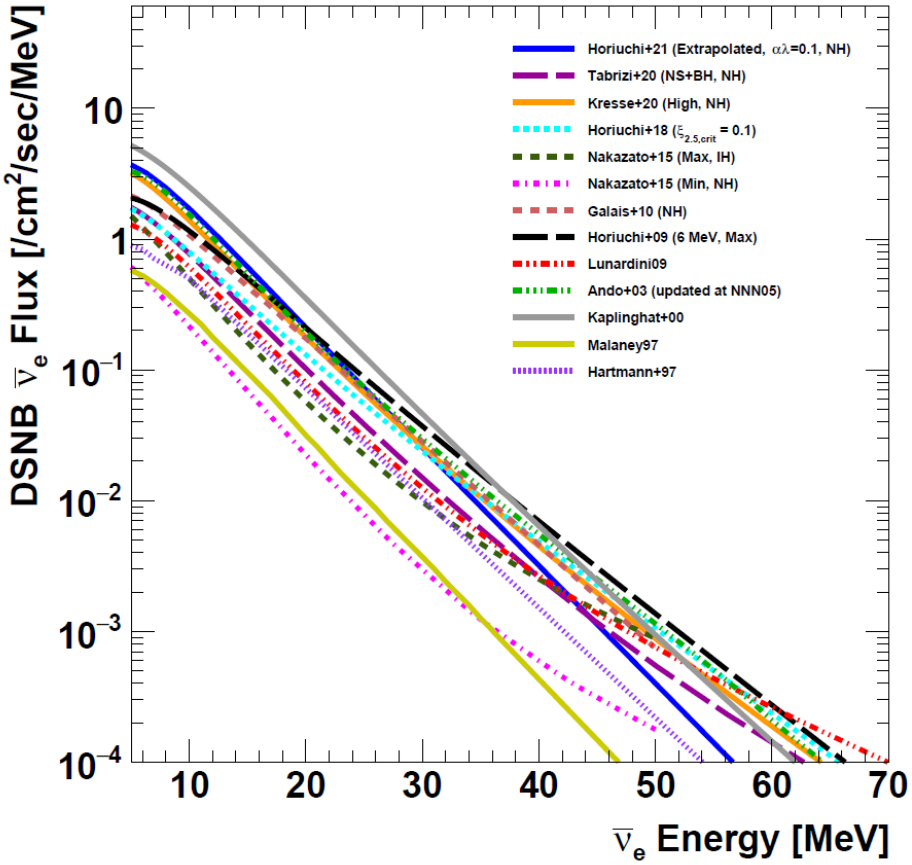

Figure 1.4: Predictions for the DSNB $\bar{\nu}_e$ flux, spanning roughly an order of magnitude across the detection window. [23].

1.3 DSNB Search Methodology

To distinguish DSNB signals from dominant backgrounds, current detectors (e.g., Super-Kamiokande and Jiangmen Underground Neutrino Observatory) rely on the IBD channel. IBD serves as the primary probe due to its relatively large cross-section and unique experimental prompt-delay pair signature.

Signal : The IBD interaction involves an $\bar{\nu}_e$ (from DSNB) interacting with a free proton (from detector), described by:

$$\bar{\nu}_e + p \rightarrow e^+ + n \tag{1.7}$$

This process yields a distinctive coincidence signature comprising a prompt positron signal followed by a delayed neutron capture signal. Crucially, the IBD cross section is known with high precision [24]. Consequently, the predicted DSNB signal rate depends almost exclusively on the astrophysical flux model and the detector response. This stands in sharp contrast to the background contributions, which suffer from large uncertainties driven by the complex modeling of neutrino-nucleus interactions.

- **Prompt Signal:** Photomultiplier tubes detect the signal produced when the outgoing positron deposits energy in liquid scintillator or emits Cherenkov radiation in water. The visible energy correlates directly with the incident neutrino energy and is approximated as $E_{\text{vis}} \approx E_\nu - 1.3\,\text{MeV}$ after correcting for the neutron-proton mass difference.

- **Delayed Signal:** The neutron thermalizes before being captured by a nucleus such as Hydrogen or Gadolinium to produce delayed gamma-rays. This capture event occurs on a timescale of $\sim \mathcal{O}(100)\,\mu$s and is useful for discriminating against backgrounds like solar neutrinos or spallation products that yield single-event signatures without associated neutrons.

Backgrounds : The DSNB search targets the flux peak (∼8–30 MeV), making background estimation and suppression in this energy window crucial.

- **Reactor Neutrinos:** Electron antineutrinos emitted from nuclear power plants interact via IBD ($\bar{\nu}_e + p \rightarrow e^+ + n$). While physically identical to the DSNB signal, their flux falls off steeply with energy, confining them primarily to the region below ~ 10 MeV.

- **Spallation Muon Products :** Cosmic ray muons interacting with oxygen nuclei can produce unstable isotopes like ^{9}Li. This isotope undergoes β-decay accompanied by neutron emission ($^9\text{Li} \rightarrow e^- + \bar{\nu}_e + n + 2\alpha$), perfectly mimicking the positron+neutron IBD signature.

- **Atmospheric Charged-Current (CC) Interactions :** These interactions involve atmospheric neutrinos producing charged leptons that mimic the DSNB signal. This category includes:

  - **$\nu_\mu(\bar{\nu_\mu})$ CC interaction :** Atmospheric $\nu_\mu(\bar{\nu_\mu})$ CC interactions can produce muons with energies below the Cherenkov threshold. These "invisi-

ble" muons then decay to Michel electrons ($\mu^{\pm} \to e^{\pm} + \nu + \bar{\nu}$), yielding a prompt signal. The same CC interaction ejects primary nucleons that trigger an intranuclear cascade, generating multiple neutrons. Taken together, these prompt and delayed signals can mimic an IBD event.

  - $\nu_e(\bar{\nu}_e)$ **CC interactions:** Atmospheric $\bar{\nu}_e$ can undergo IBD on free protons in water, producing a prompt positron signal followed by a delayed neutron-capture signal. CC interactions of ν_e or $\bar{\nu}_e$ on ^{16}O yield an $e^{\pm}$ accompanied neutron from primary hadrons, allowing these events to mimic the IBD event.

- **Atmospheric Neutral Current (NC) Interactions:** Atmospheric NC interactions, predominantly NCQE of ν_x on ^{16}O, can produce backgrounds in which deexcitation γ rays and neutrons induced from primary hadrons mimic the IBD prompt and delayed signals. However, these events can be differentiated from the standard IBD topology (one positron, one neutron) by leveraging features such as multiple γ emissions and a generally higher neutron multiplicity.

Dominant Background Systematic Uncertainties The DSNB sensitivity is limited by background suppression and systematics, with atmospheric NCQE on ^{16}O as the dominant background. Uncertainty in the NCQE cross section sets the overall background rate, while uncertainties in de-excitation γ observables and neutron multiplicity directly determine the suppression performance.

Figure 1.5 presents the DSNB spectrum. The atmospheric charged current (CC) component is shown in yellow, spallation ^{9}Li in green, reactor in magenta, accidental coincidences in gray, and atmospheric NCQE in cyan. Hatched bands indicate the total systematic uncertainty.

1.4 Neutrino–nucleus interactions

In what follows, we discuss neutrino–nucleus interactions relevant to the NCQE cross-section measurement, which constitute key systematic uncertainties and directly affect DSNB sensitivity.

Elastic and Quasi-elastic (QE) scattering For $E_\nu \lesssim 1\,\text{GeV}$, QE processes dominate: the (anti)neutrino scatters from a single bound nucleon and no hadron heavier than a nucleon is produced. CCQE interactions, such as inverse beta decay, are mediated by $W^{\pm}$, while NC interactions proceed via Z^0.

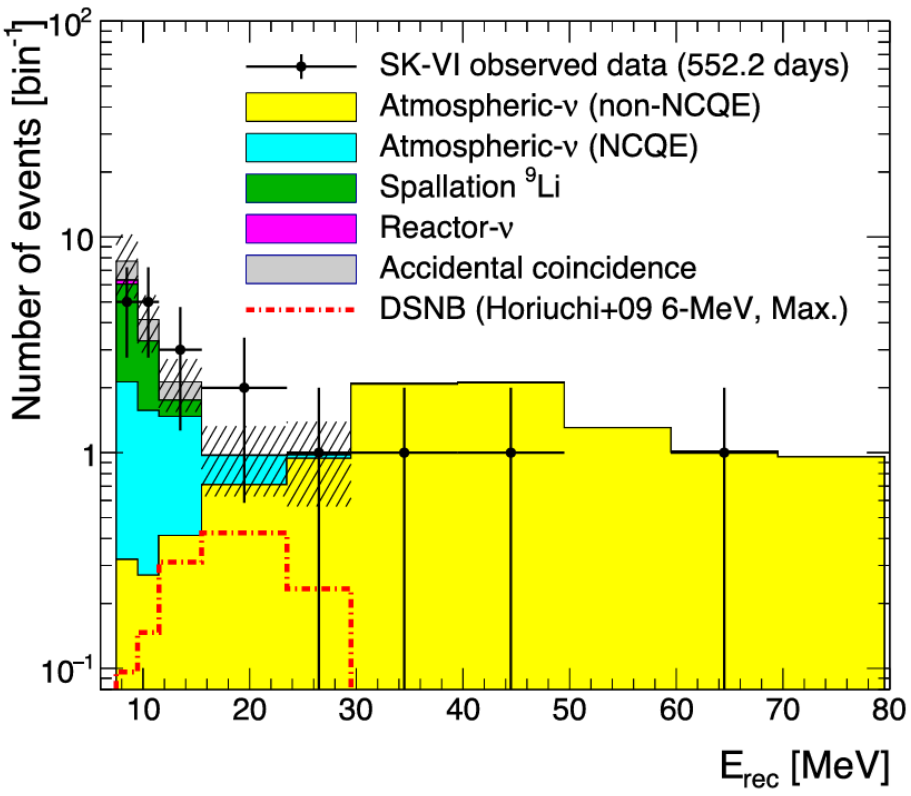

Figure 1.5: DSNB spectrum with background components. Hatched bands denote total systematic uncertainty [23].

$$\begin{aligned}
\text{CC(QE):} \quad & \overset{(-)}{\nu}_\ell + N \longrightarrow \ell^\mp + N', \\
\text{NC elastic:} \quad & \overset{(-)}{\nu} + N \longrightarrow \overset{(-)}{\nu} + N^*, \\
\text{NCQE:} \quad & \overset{(-)}{\nu} + N \longrightarrow \overset{(-)}{\nu} + (N-1)^* + A, \qquad A \in \{n, p\}.
\end{aligned}$$

In CCQE, a charged lepton is produced and the nucleon flavor flips ($n \leftrightarrow p$). NC elastic is neutrino scattering off a free nucleon with a two-body final state, whereas NCQE is the analogous process on a bound nucleon inside a nucleus, ejecting the nucleon and leaving an excited residual nucleus. Experimentally one can observes NCQE interaction with hadron knock-out and possible nuclear de-excitation γ rays and hadrons.

Multi-nucleon (2p2h) processes Meson-exchange currents [25] and short-range correlations enable scattering from correlated nucleon pairs, yielding two-particle–two-hole (2p2h) final states. These events could happends both in CC or NC and mimic QE topologies but exhibit different kinematics. Accurate modeling is essential to avoid biases in oscillation and cross-section measurements.

Resonant pion production For $E_\nu \gtrsim 300, \mathrm{MeV}$ the excitation of a baryon resonance (most notably $\Delta(1232)$) occurs, followed by its decay into a nucleon and a pion.

$$\begin{aligned} &\text{CC:} \quad \nu_\ell + N \to \ell^- + \Delta \to \ell^- + N' + \pi\,, \\ &\text{NC:} \quad \nu + N \to \nu + \Delta \to \nu + N' + \pi\,. \end{aligned}$$

Inside nuclei, final state interaction can absorb the pion or eject additional hadrons, and produce γ_s that may resemble NCQE-like signals.

Coherent pion production The neutrino scatters coherently from the entire nucleus, which remains in its ground state, producing a very forward pion:

$$\begin{aligned} &\text{CC:} \quad \nu_\ell + A \to \ell^- + A + \pi^\pm\,, \\ &\text{NC:} \quad \nu + A \to \nu + A + \pi^0\,. \end{aligned}$$

The intact nucleus yields a characteristically clean, forward-peaked sample.

1.4.1 NCQE signals in particle physics detectors

In realistic detectors, neutrinos interact with nucleons bound inside nuclei. In water targets, common NCQE interactions are:

$$\begin{aligned} \nu(\bar{\nu}) + {}^{16}\mathrm{O} &\to \nu(\bar{\nu}) + {}^{15}\mathrm{O}^* + n, \\ \nu(\bar{\nu}) + {}^{16}\mathrm{O} &\to \nu(\bar{\nu}) + {}^{15}\mathrm{N}^* + p. \end{aligned}$$

The residual nucleus is left excited, and the knocked neutron or proton final state (multiplicity and momentum) is reshaped by nuclear binding, Fermi motion, Pauli blocking, short-range correlations, and final-state interactions (FSI) between the produced hadrons and the remnant nucleus, which will be explained later. De-excitation γ rays provide a clean NCQE interaction tag. Any neutron induced from NCQE interaction can subsequently capture on hydrogen, emitting a 2.2 MeV γ, or on gadolinium (if present), yielding an ~ 8 MeV γ-ray cascade. These delayed capture γ signals, separated from the prompt activity by $\mathcal{O}(100)\,\mu$s, enable studies of NCQE interactions and their associated neutron production.

1.4.2 NCQE formalism on a free nucleon

For neutral-current elastic scattering on a free nucleon, the Llewellyn-Smith form [26] of the differential cross section can be written as

$$\frac{d\sigma^{\nu(\bar{\nu})}}{dQ^2} = \frac{G_F^2\, M^2}{8\pi\, E_\nu^2}\left[A(Q^2) \;\pm\; B(Q^2)\,\frac{s-u}{M^2} \;+\; C(Q^2)\left(\frac{s-u}{M^2}\right)^2\right], \tag{1.8}$$

where G_F is the Fermi constant, $M = 0.938$ GeV the nucleon mass, E_ν the incident (anti)neutrino energy, and $Q^2 \equiv -q^2 \geq 0$ the squared four-momentum transfer. For a nucleon at rest the Mandelstam variables satisfy

$$s - u \;=\; 4ME_\nu - Q^2\,. \tag{1.9}$$

Defining $\tau \equiv Q^2/(4M^2)$, the functions A, B, C in Eq. (1.8) are expressed in terms of the NC form factors $\tilde{F}_{1,2}$ (Dirac/Pauli), $\tilde{F}_A$ (axial), and $\tilde{F}_P$ (pseudoscalar) as

$$A(Q^2) = 4\tau\Big[(1+\tau)\,|\tilde{F}_A|^2 - (1-\tau)\,|\tilde{F}_1|^2 + \tau(1-\tau)\,|\tilde{F}_2|^2 + 4\tau\,\Re(\tilde{F}_1\tilde{F}_2)\Big]\,, \tag{1.10}$$

$$B(Q^2) = 4\tau\,\tilde{F}_A\left(\tilde{F}_1 + \tilde{F}_2\right), \tag{1.11}$$

$$C(Q^2) = \tfrac{1}{4}\Big(|\tilde{F}_A|^2 + |\tilde{F}_1|^2 + \tau\,|\tilde{F}_2|^2\Big)\,. \tag{1.12}$$

In NC scattering, contributions proportional to the final-lepton mass vanish.

The NC nucleon form factors are related to the electromagnetic (vector), axial, and strange-quark contributions. A convenient decomposition [26] is

$$\tilde{F}_{1,2}^N(Q^2) = \left(\tfrac{1}{2} - 2\sin^2\theta_W\right)F_{1,2}^N(Q^2) \;-\; \tfrac{1}{2}\,F_{1,2}^s(Q^2) \;+\; \tfrac{1}{2}\,\tau_3^N\left[F_{1,2}^p(Q^2) - F_{1,2}^n(Q^2)\right], \tag{1.13}$$

$$\tilde{F}_A^N(Q^2) = -\,\tfrac{1}{2}\,g_A\,\tau_3^N\left(1 + \frac{Q^2}{M_A^2}\right)^{-2} \;+\; \tfrac{1}{2}\,F_A^s(Q^2), \tag{1.14}$$

$$\tilde{F}_P^N(Q^2) = \frac{2M^2}{m_\pi^2 + Q^2}\,\tilde{F}_A^N(Q^2)\,, \tag{1.15}$$

where $N \in \{p, n\}$, $\tau_3^p = +1$ and $\tau_3^n = -1$, $\sin^2\theta_W = 0.2312$ (numerical value used in this work), g_A is the axial weak coupling, M_A the axial mass, $m_\pi = 0.1395$ GeV the charged-pion mass, and $F_{1,2}^{p,n}$ are the proton/neutron vector form factors (e.g. BBBA05 parametrization [27]). Possible strange-quark contributions $F_{1,2}^s$ and F_A^s enter only in NC processes and can differ between protons and neutrons through the τ_3^N term. The Figure 1.6 below shows the NCQE cross section computed using the formalism outlined above.

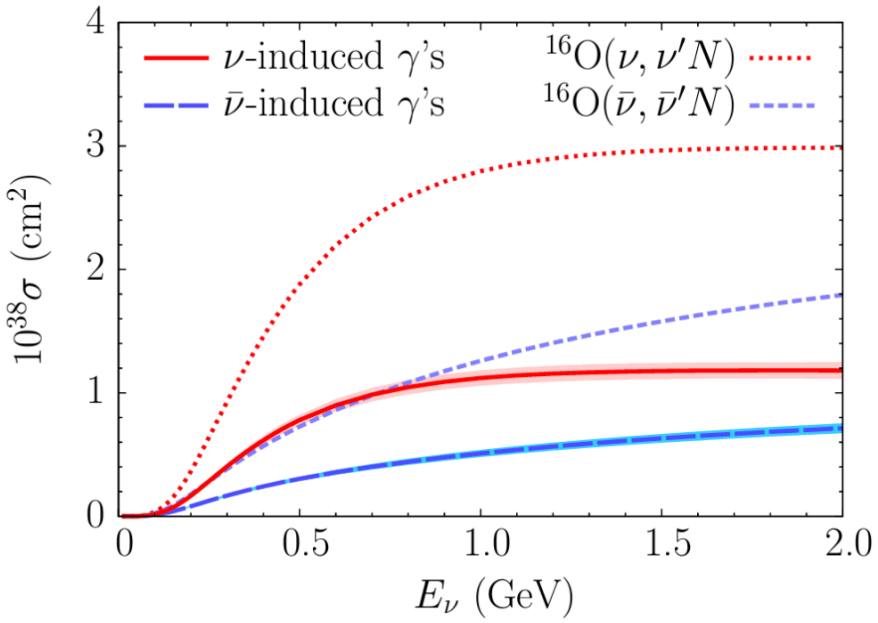

Figure 1.6: NCQE cross-section from Ref. [26]: total (dashed) and γ (solid) NCQE cross sections, with red for ν and blue for $\bar{\nu}$.

1.4.3 Neutrino oscillations

We introduce neutrino oscillations because our analysis includes oscillation effects for the CC interaction in the T2K NCQE measurement and in the DSNB search using atmospheric neutrinos. In 1957, Bruno Pontecorvo proposed that neutrinos might convert into antineutrinos and back again [28]. Five years later, Maki, Nakagawa, and Sakata developed the framework of neutrino flavor mixing (MNS), together with Pontecorvo's insight is now covered in the PMNS (Pontecorvo–Maki–Nakagawa–Sakata) matrix [29]. It relates flavor and mass eigenstates as shown in Equation 1.16: for a neutrino of definite flavor α and mass index i,

$$|\nu_\alpha\rangle = \sum_i U^*_{\alpha i} |\nu_i\rangle, \qquad |\nu_i\rangle = \sum_\alpha U_{\alpha i} |\nu_\alpha\rangle. \tag{1.16}$$

In Equation 1.16, $U_{\alpha i}$ are the elements of the PMNS matrix (the star denotes complex conjugation). A standard 3×3 parameterisation of U is given in Equation 1.17, where $c_{ij} \equiv \cos\theta_{ij}$ and $s_{ij} \equiv \sin\theta_{ij}$:

$$
\begin{aligned}
U &= \begin{pmatrix} 1 & 0 & 0 \\ 0 & c_{23} & s_{23} \\ 0 & -s_{23} & c_{23} \end{pmatrix} \begin{pmatrix} c_{13} & 0 & s_{13}e^{-i\delta_{\mathrm{CP}}} \\ 0 & 1 & 0 \\ -s_{13}e^{i\delta_{\mathrm{CP}}} & 0 & c_{13} \end{pmatrix} \begin{pmatrix} c_{12} & s_{12} & 0 \\ -s_{12} & c_{12} & 0 \\ 0 & 0 & 1 \end{pmatrix} \\
&= \begin{pmatrix} c_{12}c_{13} & s_{12}c_{13} & s_{13}e^{-i\delta_{\mathrm{CP}}} \\ -s_{12}c_{23} - c_{12}s_{13}s_{23}e^{i\delta_{\mathrm{CP}}} & c_{12}c_{23} - s_{12}s_{13}s_{23}e^{i\delta_{\mathrm{CP}}} & c_{13}s_{23} \\ s_{12}s_{23} - c_{12}s_{13}c_{23}e^{i\delta_{\mathrm{CP}}} & -c_{12}s_{23} - s_{12}s_{13}c_{23}e^{i\delta_{\mathrm{CP}}} & c_{13}c_{23} \end{pmatrix}.
\end{aligned} \tag{1.17}
$$

The parameters θ_{12}, θ_{23}, and θ_{13} are the mixing angles [30], and if $\delta_{\mathrm{CP}} \neq 0$, U contains irreducible complex phases that can lead to CP violation [31].

Suppose a neutrino is produced in flavor state $|\nu_\alpha\rangle$ in vacuum. Using Equation 1.16 and propagating mass eigenstates with the time-dependent Schrödinger equation,

$$
i\,\frac{\partial}{\partial t}\,|\nu_i(x,t)\rangle = E_i\,|\nu_i(x,t)\rangle = -\frac{1}{2m_i}\frac{\partial^2}{\partial x^2}|\nu_i(x,t)\rangle, \tag{1.18}
$$

one obtains the plane-wave solution

$$
|\nu_\alpha(t)\rangle = \sum_k U^*_{\alpha k}\, e^{-iE_k t}\,|\nu_k(t{=}0)\rangle. \tag{1.19}
$$

Because U is unitary, the mass eigenstates can be expanded in the flavor basis,

$$
|\nu_k\rangle = \sum_\beta U_{\beta k}\,|\nu_\beta\rangle, \tag{1.20}
$$

which leads to the transition amplitude

$$
\langle\nu_\beta|\nu_\alpha(t)\rangle = \sum_k U^*_{\alpha k}\,U_{\beta k}\,e^{-iE_k t}\,, \tag{1.21}
$$

and hence the oscillation probability

$$
P(\nu_\alpha \to \nu_\beta;\, t) = \left|\langle\nu_\beta|\nu_\alpha(t)\rangle\right|^2 = \sum_{j,k} U^*_{\alpha j}U_{\beta j}\,U_{\alpha k}U^*_{\beta k}\,e^{-i(E_j - E_k)t}\,. \tag{1.22}
$$

For ultra-relativistic neutrinos ($m_k \ll E$), the energies satisfy

$$
E_k = \sqrt{p^2 + m_k^2} \simeq E + \frac{m_k^2}{2E}\,, \tag{1.23}
$$

so that

$$P_{\alpha\to\beta}(t) = \sum_{j,k} U^*_{\alpha j} U_{\beta j}\, U_{\alpha k} U^*_{\beta k} \exp\left[-\,i\,\frac{\Delta m^2_{jk}}{2E}\,t\right], \qquad \Delta m^2_{jk} \equiv m^2_j - m^2_k. \tag{1.24}$$

Since highly relativistic neutrinos travel nearly at the speed of light, one may replace $t \simeq L$ (setting $c = 1$) to obtain

$$P_{\alpha\to\beta}(L, E) = \sum_{j,k} U^*_{\alpha j} U_{\beta j}\, U_{\alpha k} U^*_{\beta k} \exp\left[-\,i\,\frac{\Delta m^2_{jk} L}{2E}\right]. \tag{1.25}$$

Separating the diagonal ($j = k$) and interference ($j \neq k$) pieces and using unitarity yields the standard form,

$$P_{\alpha\to\beta}(L, E) = \delta_{\alpha\beta} - 4\,\mathrm{Re}\sum_{j>k}\left[U^*_{\alpha j} U_{\beta j}\, U_{\alpha k} U^*_{\beta k}\right] \sin^2\left(\frac{\Delta m^2_{jk} L}{4E}\right) \tag{1.26}$$

$$+\,2\,\mathrm{Im}\sum_{j>k}\left[U^*_{\alpha j} U_{\beta j}\, U_{\alpha k} U^*_{\beta k}\right] \sin\left(\frac{\Delta m^2_{jk} L}{2E}\right). \tag{1.27}$$

This expression makes explicit the roles of mixing angles, mass-squared differences, and the CP-violating phase in governing neutrino flavor oscillations.

1.5 Current DSNB search status

To date, no DSNB signal has been detected. Underground experiments, including SK [32, 33, 34, 35, 23, 36], KamLAND [37, 38], SNO [39, 40], and Borexino [41], have reported only upper limits. Among published searches, SK and KamLAND set the strongest bounds on the DSNB flux for $E_\nu > 8$ MeV, whereas Borexino provides the tightest constraints for $E_\nu < 8$ MeV. As members of the SK Collaboration, we summarize below the hardware and analysis improvements implemented at SK.

SK has operated in eight phases: SK-I (1996–2001), SK-II (2003–2005), SK-III (2006–2008), SK-IV (2008–2018), and SK-V (2019–2020), after which pure-water running ended and the SK with Gd loaded began with SK-VI (0.01% Gd from 2020), SK-VII (0.03% Gd from 2022), and SK-VIII (2024–present).

(1) **SK I (1496 days) [32]**: The first DSNB search at SK.
The first dedicated DSNB search at SK used 1496 days of SK-I data and targeted inverse beta decay prompt signal only with energy threshold above 18 MeV. The analysis constructed a reduction pipeline that employed a spallation veto, Cherenkov angle, and solar direction selections to control irreducible backgrounds for a spectral fit. The resulting limits were model-dependent 90%

C.L. flux bounds of 20 to 130 $\mathrm{cm^{-2}\,s^{-1}}$.

(2) **SK I-III (2853 days)** [33]: Revised full prompt signal DSNB search.
This study combines SK-I/II/III data for a total of 2853 days, doubling the statistics relative to the previous SK-I result. The analysis threshold is lowered to a positron energy of 16 MeV. Methodologically, this updated study performs a simultaneous unbinned maximum-likelihood fit across three Cherenkov-angle regions, with sidebands constraining NC-elastic and μ/π backgrounds. Improved background rejection and higher efficiency open the 16–18 MeV window and enhance the DSNB sensitivity. Consequently, this study set model-dependent 90% C.L. flux limits of 2.8–3.1 $\mathrm{cm^{-2}\,s^{-1}}$ above 16 MeV.

(3) **SK IV (960 days)** [34]: First use of delayed signal in a DSNB search.
This work reports the first DSNB search at SK that employs (n,γ)H via the delayed neutron capture signal, enabling an inverse-beta-decay (IBD) analysis with a lower energy threshold. The neutron tagging efficiency is measured to be 17.7% with an accidental-tag rate of 1.1%. Using 960 days data set, this study identified 13 candidates in the range 13.3–31.3 MeV, consistent with background expectations. This study set model-independent upper limits down to 13.3 MeV.

(4) **SK I-IV (2790 days)** [35]: The full SK pure-water DSNB search.
This study increases the statistics and expands the energy window to 9.3–81.3 MeV through a model-independent search combined with a spectral fit, with explicit treatment of reactor and solar neutrino backgrounds near threshold. This search analyzes the full SK-IV period totaling 2970.1 days and performs a spectral fit on the combined SK-I–IV exposure of 5823 days, enabling world-leading sensitivity. Methodologically, it tightens spallation rejection and applies a sophisticated boosted decision-tree neutron-tagging algorithm, achieving a higher neutron tagging efficiency and more precise background estimates, which assist with T2K results. These advances yield combined SK-I–IV 90% C.L. flux limits of $\sim$ 2.6–2.7 $\mathrm{cm^{-2}\,s^{-1}}$ above 17.3 MeV across many DSNB models, improving on previous SK constraints.

(5) **SK VI (552 days)** [23]: First Gd-loaded DSNB search.
This search presents the first SK-Gd (SK-VI, 0.01% Gd) DSNB search using both (n,γ)H and (n,γ_s)Gd delayed signal, achieving a total neutron-tagging efficiency of 35.6% with a misidentification probability of 2.8×10^{-4} per event, roughly twice the tagging efficiency of the SK-IV BDT-based method [35]. With only 552.2 days ($\approx$ one fifth of the SK-IV exposure [35]), SK-Gd attains per-bin sensitivities below 31.3 MeV that are already comparable to that result, owing to the higher neutron tagging efficiency and the reduced accidental background.

(6) **SK VI-VII (956 days)** [36]: Revised IBD selection algorithm.
This DSNB search adds SK-VII data at 0.03% Gd and brings the total SK-Gd livetime to 956.2 days, enabling both a spectrum-independent search over 7.5–29.5 MeV and an extended spectrum-dependent fit up to 79.5 MeV. It introduces two updated neutron-tagging algorithms (a retrained BDT and a new neural network) and a new "multiple scattering goodness" (MSG) variable to suppress atmospheric NCQE backgrounds. The spectral fit now profiles all nuisance parameters. These upgrades, together with the higher Gd loading, raise SK-VII's final DSNB sensitivity to a level on par with the current best result [35].

In summary, SK has pursued DSNB searches for more than two decades, and loaded Gd to enhance neutron-tagging capability. SK has also established a robust data pipeline, with ongoing refinements to selection cuts and neutron-tagging algorithms. Together, these efforts deliver high IBD detection efficiency and stringent background suppression, both indispensable for the first DSNB discovery, for which only a few DSNB events per year are expected.

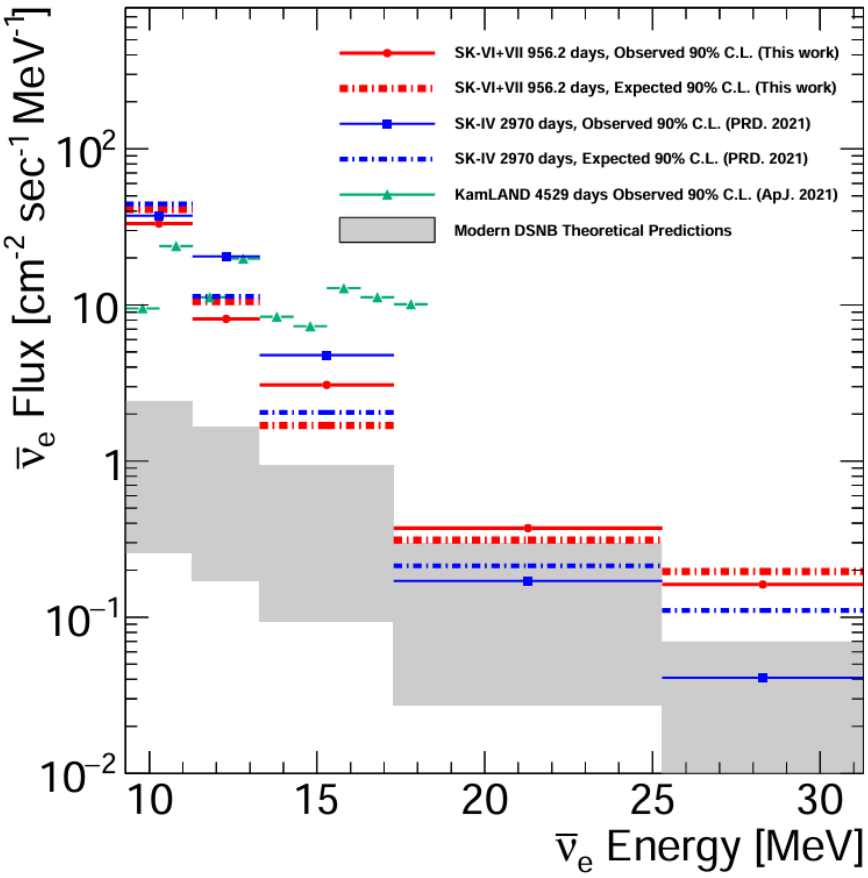

Figure 1.7: Per-bin 90% C.L. upper limits on the DSNB $\bar{\nu}_e$ flux. Red: SK-VI+VII observed (solid) and expected (dashed). Blue: SK-IV observed and expected [35]. Green: KamLAND observed limit [38]. Gray bands: range of DSNB flux predictions. Figure adapted from Ref. [36].

1.6 Previous NCQE Measurements

NCQE interactions have been measured with atmospheric neutrinos by SK [42, 43], KamLAND [44], with neutrino beams at US such as BNL E734 [45, 46] and MiniBooNE [47]. In Japan, the neutrino beam experiments K2K and T2K also have a long record of studying NCQE cross sections and observables with water-Cherenkov detectors, with published results from K2K (2006) [48], T2K (2014) [49], T2K (2019) [50], and several PhD theses [51, 52, 53].

A key motivation for studying NCQE with neutrino beams is to support SK's DSNB search. NCQE interactions produce a prompt–delayed γ signals that can mimic the inverse beta decay (IBD) event, making atmospheric NCQE a dominant background. T2K's neutrino flux peaks at energies comparable to the atmospheric neutrino flux, and T2K flux is well characterized. In addition, spill timing provides high-purity samples. Consequently, T2K measurements of NCQE cross sections and observables within SK provide representative data and tighten systematic uncertainties on the atmospheric NCQE background. Because both T2K- and atmospheric-induced NCQE events are recorded in SK, the T2K dataset is an almost ideal testbed for validating and tuning the NCQE-rejection selections used in the Super-K DSNB analysis. Below, we present the series of publications relevant to this objective.

(1) **K2K (0.097 x 10^{20} POT)** [48]: NC events from ν-beam in SK prototype (called 1 kton detector).
This study reports the first observation of nuclear deexcitation gamma rays near 6 MeV from oxygen produced by neutrino interactions in the 1 kt water Cherenkov near detector of K2K. This study build a few-MeV reconstruction using PMT hit timing and N_{eff}, and calibrate the energy scale with a ^{252}Cf + Ni source system. With tight fiducial cuts and careful rejection of beam-uncorrelated and sky-shine neutron backgrounds, they isolate a clean low-energy sample that shows a clear 6 MeV peak. This work establishes deexcitation gammas as a practical tag for neutral-current processes in water Cherenkov detectors.

(2) **T2K 2014 (3.1 x 10^{20} POT)** [49]: First T2K NCQE cross-section results.
This measurement delivers the first T2K flux-averaged NCQE cross-section measurement on oxygen, which measures $\langle\sigma_{\nu,\text{NCQE}}\rangle = 1.55 \times 10^{-38}$ cm^2 at a median neutrino energy of $\sim$ 630 MeV. It selects 43 events (51.0 expected) in the 4–30 MeV window after tight beam timing cuts, with a prominent 6 MeV deexcitation peak and backgrounds dominated by NC non-QE processes. Methodologically, it models both primary and secondary γ emission within an NCQE framework using a spectral-function description and NA61-tuned T2K flux, going well beyond K2K's measurement.

(3) **T2K 2019 (31.29 x 10^{20} POT)** [50]: First NCQE results in ν and $\bar{\nu}$
This study updates the T2K NCQE measurement at SK by substantially increasing the exposure to (14.94 and 16.35) $\times 10^{20}$ POT in ν and $\bar{\nu}$ mode, and by reporting flux-averaged NCQE-like cross sections on oxygen: $\langle\sigma_\nu\rangle = 1.70 \times 10^{-38}\,\mathrm{cm}^2$ at $\langle E_\nu\rangle = 0.82\,\mathrm{GeV}$ and $\langle\sigma_{\bar{\nu}}\rangle = 0.98 \times 10^{-38}\,\mathrm{cm}^2$ at $\langle E_{\bar{\nu}}\rangle = 0.68\,\mathrm{GeV}$, respectively. The analysis tightens event selections, introducing an energy-dependent Cherenkov cut, and finds secondary-γ modeling to be the dominant systematic. The update delivers the highest statistics to date for NCQE measurement in both beam polarities and enables calibration of atmospheric NCQE backgrounds for the DSNB search, reducing the associated uncertainty from $\sim 100\%$ to $\sim 60\%$.

The studies to date report only the γ_s results from NCQE interactions in T2K. Two PhD theses [52, 53] attempted to identify neutrons in the pure water SK and gd-loaded SK datasets, but neither was formally published or officially approved within T2K. Neutrons from NCQE interactions are crucial because neutron multiplicity is a primary selection variable in the DSNB search. Atmospheric NCQE interactions tend to produce multiple neutrons, while DSNB events are expected to yield single neutron. Using T2K's well-characterized neutrino beam, we can measure NCQE neutron multiplicity and constrain the systematic uncertainties in DSNB background estimates. Moreover, collaborators at SK have recently proposed several NCQE-suppression techniques, which will benefit strongly from T2K data.

1.7 Thesis Outline

This thesis advances NCQE measurements at T2K. It published the first neutron analysis of NCQE interactions using gd-loaded SK. Expanded model studies show hadron–nucleus interactions dominate the systematic error in mean neutron multiplicity. It also validates the new proposed Cherenkov-ring features for the first time. A review of nuclear de-excitation models finds that the Bertini dominates uncertainties in simulated γ rays and neutrons and overestimates these processes in simulation. Finally, this thesis updates the NCQE cross section and establishes state-of-the-art NCQE suppression using a neural-network algorithm, validated on T2K Runs 1–11 NCQE data set, improving background rejection and reducing systematics from $\sim 70\%$ to $\sim 43\%$. Together, these advances constitute the major contributions to the DSNB search at SK. The remainder of this thesis is organized as follows.

Part I. Part I reviews supernova neutrinos, the DSNB and its theoretical predictions, and the search methodology. To address the dominant background, we then discusses neutrino–nucleus interactions and the NCQE formalism. Finally, we briefly

summarizes the current status of DSNB searches and NCQE measurements.

Part II. Part II presents measurements of neutrons produced by NCQE–like interactions on oxygen in T2K. Chapter 2 presents an overview of the analysis. Chapters 3 and 4 describe the T2K and the Super–Kamiokande experiment, respectively, highlighting the calibration of Gd–captured neutrons for continuous water–transparency monitoring. Chapter 5 details the Monte Carlo simulation and event selection. Chapter 6 discusses systematic uncertainties. Chapter 7 presents the neutron–multiplicity results and discussion.

Part III. Part III presents an updated NCQE cross section, validates and refines the SK DSNB selection cuts with T2K NCQE Run 1–11 data, and derives an updated DSNB sensitivity. Chapter 8 outlines the overall analysis strategy. Chapter 9 describes the Monte Carlo updates incorporating the latest simulation improvements. Chapter 10 details the event selection, the NCQE cross-section systematics, and the resulting measurement. Chapter 11 introduces the DSNB selection at SK, highlighting the improvement of the third selection cut using a neural network based classifier. Chapter 12 summarizes calibrations that use the LINAC as a proxy source for DSNB, both for existing and newly developed cuts. Chapter 13 summarizes calibrations that use the T2K NCQE sample as a proxy for atmospheric NCQE, again for both existing and new cuts. Chapter 14 covers background estimates other than atmospheric NCQE in the DSNB search. Chapter 15 presents the expected DSNB sensitivity obtained with the improved selections and updated systematic uncertainties.

Conclusion. Chapter 16 concludes the thesis with a summary of the results from Parts II and III.

Part II

Neutron measurement of Neutrino-Oxygen Neutral-Current Quasielastic-like Interactions

Chapter 2

Measurement motivation

Only a handful of ν–^{16}O NCQE measurements exist, mostly from atmospheric neutrinos or accelerator beam experiments. Neutrino beam experiments typically have smaller systematics, while atmospheric data benefit from larger flux exposures. T2K has led the field since the KEK era. To date, measurements have focused on de-excitation γ rays from ν–^{16}O NCQE. Direct hadronic observables, such as neutron or proton, remain largely unexplored but are crucial for refining interaction models.

To address this gap, this analysis explicitly measures these hadronic final states to provide critical constraints for interaction models. We measure neutrons from T2K ν–^{16}O NCQE using capture 8 MeV γ rays from Gd(n,γ) or 2.2 MeV from H(n,γ) to determine the mean neutron multiplicity,

$$M = \frac{(N_{\text{delayed}} - \eta_{Noise} \times N_{\text{prompt}})}{\epsilon_n} \cdot \frac{1}{N_{\text{prompt}}}, \tag{2.1}$$

where N_{delayed} is the number of detected neutron capture signal, η_{Noise} the background rate, N_{prompt} the number of detected NCQE-like signal, and ϵ_n the overall neutron tagging efficiency.

Measuring the mean neutron multiplicity from NCQE is motivated by:

(1) Measuring NCQE neutron multiplicity precisely enables reliable identification of IBD events (one neutron) over NCQE backgrounds for DSNB search.

(2) Previous experiments at RCNP [54] measured hadron–nucleus interactions via de-excitation γ-rays from p–^{16}O and n–^{16}O. However, neutron remains unmeasured.

(3) A thorough systematic study is needed to determine whether hadron–nucleus interactions dominate the mean neutron multiplicity.

This work deepens that understanding by investigating the properties of neutrons produced in NCQE interactions, contributing to the broader effort to suppress DSNB backgrounds. In addition to neutron multiplicity, other characteristics such as neutron travel distance and direction offer a promising means to further distinguish IBD signals from NCQE backgrounds. This highlights the importance of measuring neutrons induced by NCQE events.

Recent preliminary measurements of NCQE-induced neutrons in pure water show a $\sim$40% discrepancy between Monte Carlo predictions and T2K data [52], highlighting the need for a systematic study. Neutron observables depend on the initial neutrino–nucleus interaction, the subsequent hadronic processes inside the nucleus, and the secondary interactions of particles in the detector medium.

Chapter 3

Experimental Setup

The T2K (Tokai to Kamoka) experiment [55] is a long-baseline experiment designed for precise neutrino oscillation and cross-section measurements. Neutrino and antineutrino beams from the J-PARC beamline are measured by near detectors (INGRID, ND280), located 280m downstream of the neutrino production target, before oscillation and observed at the far detector (Super-Kamiokande), located 295km downstream, after oscillation. Both the near and far detectors perform cross-section measurements independently. Figure 3.1 shows the schematic view of the T2K experiment.

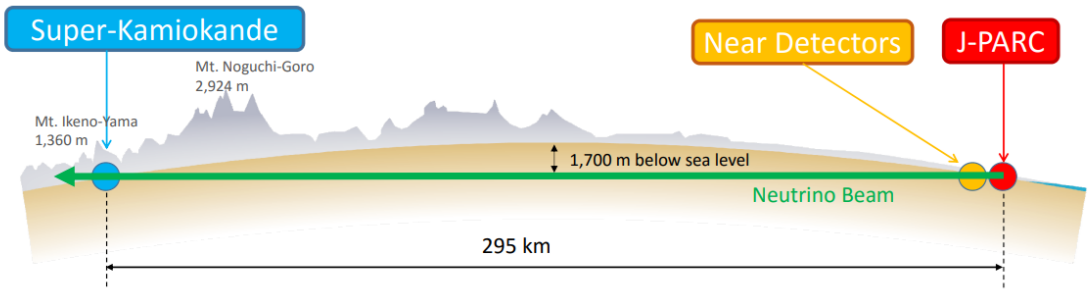

Figure 3.1: Schematic view of the T2K experiment [55].

3.1 J-PARC Accelerator and Neutrino Beamline

Neutrino beam production at J-PARC has two stages: the primary beamline accelerates protons, and the secondary beamline produces neutrinos and anti-neutrinos.

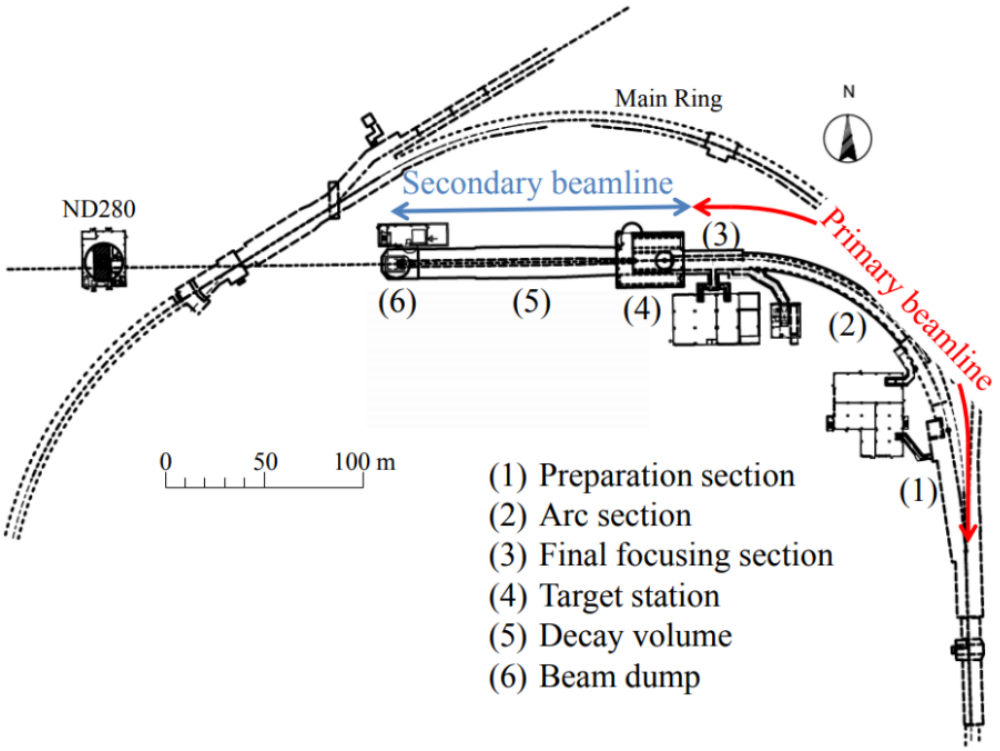

Figure 3.2: The structure of the neutrino beamline at J-PARC [55]

3.1.1 Primary neutrino beamline

In the primary beamline, protons are accelerated by a chain of three accelerators, a linear accelerator (LINAC), a rapid-cycling synchrotron (RCS), and the Main Ring (MR) synchrotron. A negative hydrogen ion (H^-) is injected into the LINAC and accelerated to 400 MeV, stripped to a proton (H^+) using charge-stripping foils, boosted to 3 GeV in the RCS, and finally to 30 GeV in the MR. The MR delivers the beam to the neutrino beamline in spills with a ∼2.48 s (in this study) repetition cycle, each spill comprising eight bunches and separations of ∼581 ns. This fine time structure enables timing cuts at the far detector to suppress backgrounds from cosmic rays and atmospheric neutrinos [55].

Upstream of the end of the primary beamline, the layout comprises a 54 m preparation section, a 147 m arc, and a 37 m final-focusing section. Downstream, the target station, decay volume, and beam dump form the secondary beamline. A schematic is shown in Figure 3.2.

At the final-focusing section, the proton beam is monitored by five current transformers (CTs) for intensity, 21 electrostatic monitors (ESMs) for position, 19 segmented secondary-emission monitors (SSEMs) for position and width, and 50 beam-loss monitors (BLMs), which are wire proportional counters filled with an Ar/CO_2 mixture. Only the most downstream SSEM is used during physics running to mini-

mize losses [55]. A schematic is shown in Figure 3.3.

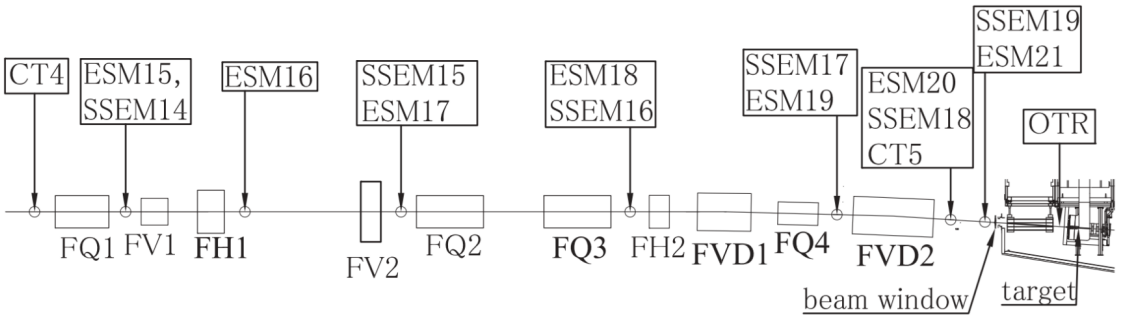

Figure 3.3: The arrangement of proton beam monitors at the final focusing section of the primary beamline upstream the target [55]

3.1.2 Secondary neutrino beamline

The secondary beamline produces neutrinos. After the final-focusing section, a baffle collimates the proton beam and an optical transition radiation monitor measures its position and width. The primary proton beam strike on a 91.4,cm long graphite target, producing charged hadrons, predominantly $\pi^{\pm}$ and $K^{\pm}$. The (anti)neutrino arises from $\pi^{\pm}$ and $K^{\pm}$ decays,

$$\pi^{(-)}_{(+)} \to \mu^{(-)}_{(+)} + \nu_\mu \ (\bar{\nu}_\mu), \tag{3.1}$$

$$K^{(-)}_{(+)} \to \mu^{(-)}_{(+)} + \nu_\mu \ (\bar{\nu}_\mu), \tag{3.2}$$

$$K^{(-)}_{(+)} \to \pi^0 + \mu^{(-)}_{(+)} + \nu_\mu \ (\bar{\nu}_\mu). \tag{3.3}$$

Secondary pions and kaons are focused by three aluminum magnetic horns pulsed at ±250 kA (in this study). The horn polarity selects the beam mode: +250 kA (forward current) focuses positive secondaries and yields a neutrino-dominated beam, while −250 kA (reverse current) focuses negative secondaries and yields an antineutrino-dominated beam. Secondaries traverse a 96 m decay volume, remaining hadrons are absorbed in a beam dump 109 m downstream, and penetrating muons are recorded by MUMON to infer bunch-by-bunch direction and intensity. Imperfect focusing introduces small wrong-sign and ν_e components, for example from hadrons produced outside the target or forward wrong-sign pions. A schematic for the secondary neutrino beam is shown in Figure 3.5. The neutrino beam is directed 2.5° off-axis relative to the Super-Kamiokande detector. As shown in Figure 3.4, this configuration yields a narrower energy spectrum compared to the on-axis flux, with a peak tuned to the oscillation maximum.

The neutrino beam flux is simulated with FLUKA [56] and GEANT3 [57], which model hadron production, transport, and decay in the beamline. Pion and kaon

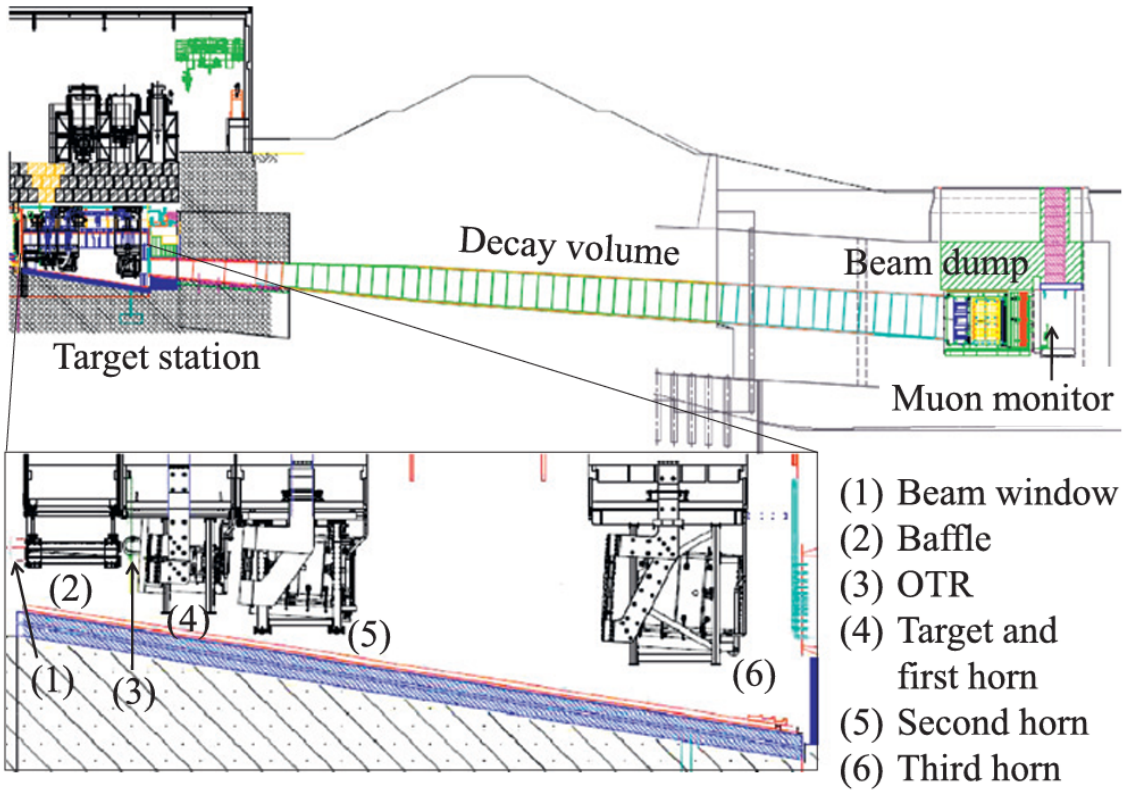

Figure 3.4: Schematic view of the J-PARC neutrino secondary beamline [55].

production cross sections are retuned to NA61/SHINE data from both replica [58] and thin targets [59, 60, 61]. Using the 2009 replica-target set, the latest flux tuning [62] reduces peak-region uncertainties from 9–12% [61] to 5–8% for the primary ν_μ flux. The wrong-sign $\bar{\nu}_\mu$ component remains limited by off-target interactions at 6–8%. The flux peaks near 0.6 GeV with a width of a few hundred MeV and is dominated by ν_μ (∼92.4%) with a small $\bar{\nu}_\mu$ fraction (∼6.4%). Figure 3.6 shows the predicted unoscillated flux at SK for the data set used in this analysis.

3.2 Near detectors

The near detector complex, consisting of the INGRID and ND280 detectors, is located 280 meters downstream of the graphite target. A schematic for the near detectors is shown in Figure 3.7.

INGRID (Interactive Neutrino GRID) is an on-axis neutrino detector centered on the primary proton beamline that monitors the beam direction and intensity. It samples a 10 m × 10 m area and covers ±18 mrad using 16 modules: 14 arranged in a cross and 2 placed off-axis to test the beam symmetry. Each module contains nine iron plates, each 124 × 124 × 6.5 cm^3, and 11 tracking scintillator planes. Adjacent modules share veto planes, three or four per module. Using module event rates, the

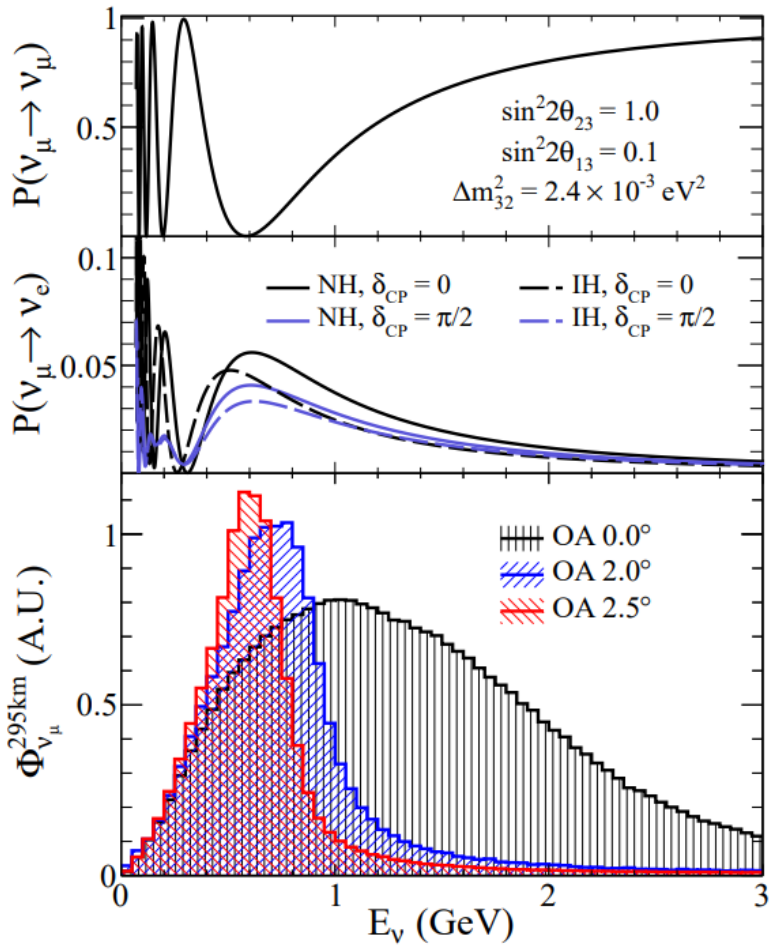

Figure 3.5: Oscillation probabilities for $\nu_\mu \to \nu_e$ (top) and $\nu_\mu \to \nu_\mu$ (middle), alongside T2K flux predictions at the far detector for various off-axis angles (bottom) [55].

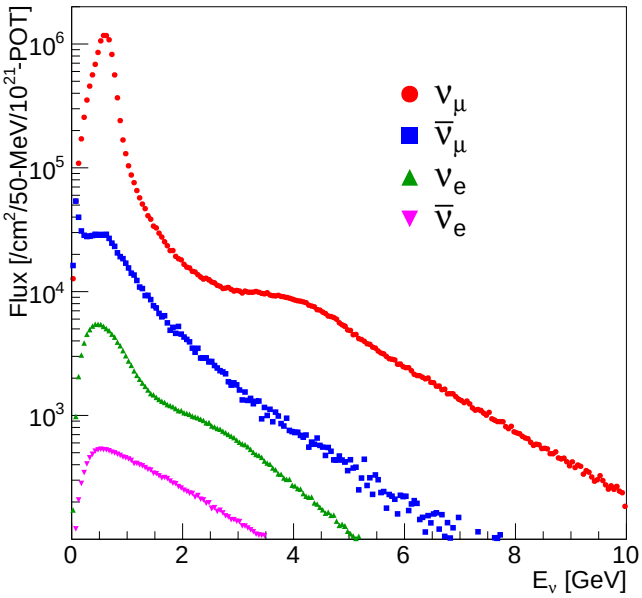

Figure 3.6: Predicted neutrino flux for T2K Run 11 at SK without oscillations.

beam center is measured with better than 10 cm precision, equivalent to 0.4 mrad at a baseline of 280 m.

ND280 is located 2.5° off axis from the graphite target, housed in a 0.2 T magnet, and comprises several subdetectors. **FGD:** Two fine-grained targets provide neutrino interaction vertices, FGD1 (plastic scintillator) and FGD2 (scintillator with water modules), enabling cross-section measurements on carbon and oxygen [63]. **TPC:** Three time projection chambers filled with Ar:CF_4:iC_4H_{10} at 95%:3%:2% track charged particles, measure momentum from curvature, and provide PID via dE/dx, μ/p separation is good, while π/μ separation is limited [64]. **ECal:** Lead–scintillator sampling calorimeters surround the tracker, adding PID and electromagnetic shower energy measurements [65]. **P0D:** An upstream π^0 detector targets NC π^0 production using alternating scintillator, water, and brass layers to increase mass and contain γ's [66]. **SMRD:** Scintillators embedded around the magnet tag high-energy muons that exit the tracker [67].

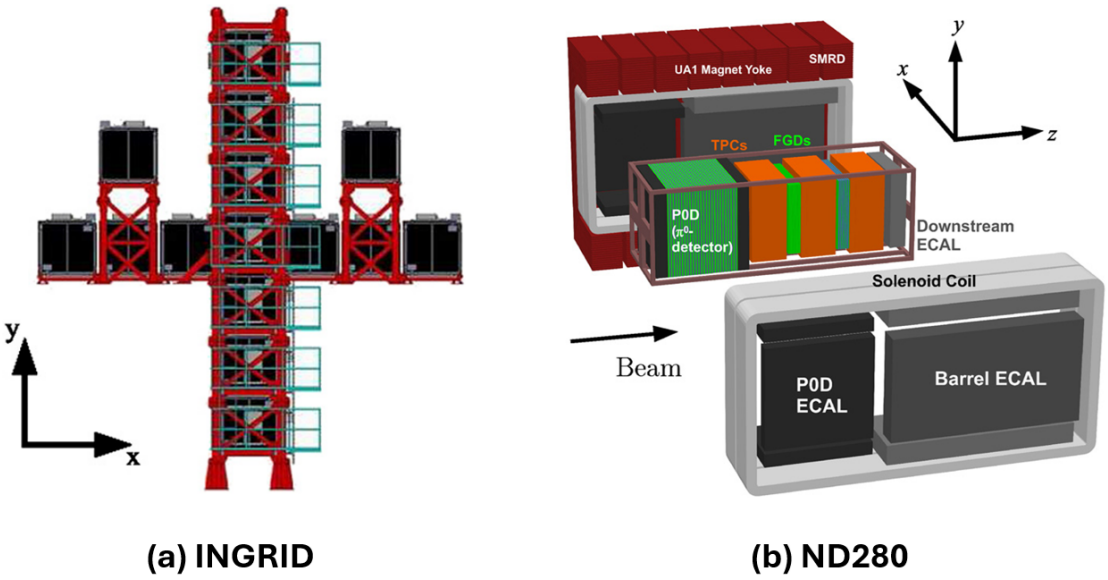

Figure 3.7: Schematic view of the Near Detectors [55].

3.3 Super-Kamiokande detector

The Super-Kamiokande (SK) detector [68] is T2K's far detector for studying neutrino oscillations and, in this analysis, neutrino neutral-current interactions. Located 295 km downstream of the beam source and 2.5° off-axis, SK sits 1 km underground at Mt. Ikenoyama within Kamioka mine. It is a cylindrical water-Cherenkov detector containing 50 kton of ultrapure water, with overall dimensions of 41.4 m (height) by 39.3 m (diameter). The detector is divided into an inner detector (ID) and an outer

detector (OD). The ID, 36.3 m high and 33.8 m in diameter, serves as the main analysis volume and is instrumented with 11129 inward-facing 20-inch photomultiplier tubes (PMTs). Surrounding it, the OD functions primarily as a veto and is separated from the ID by a 55 cm uninstrumented gap. Its thickness is 2.2 m on the barrel and 2.06 m on the top and bottom, and it is viewed by 1885 outward-facing 8-inch PMTs. A schematic view of the detector is shown in Figure 3.8.

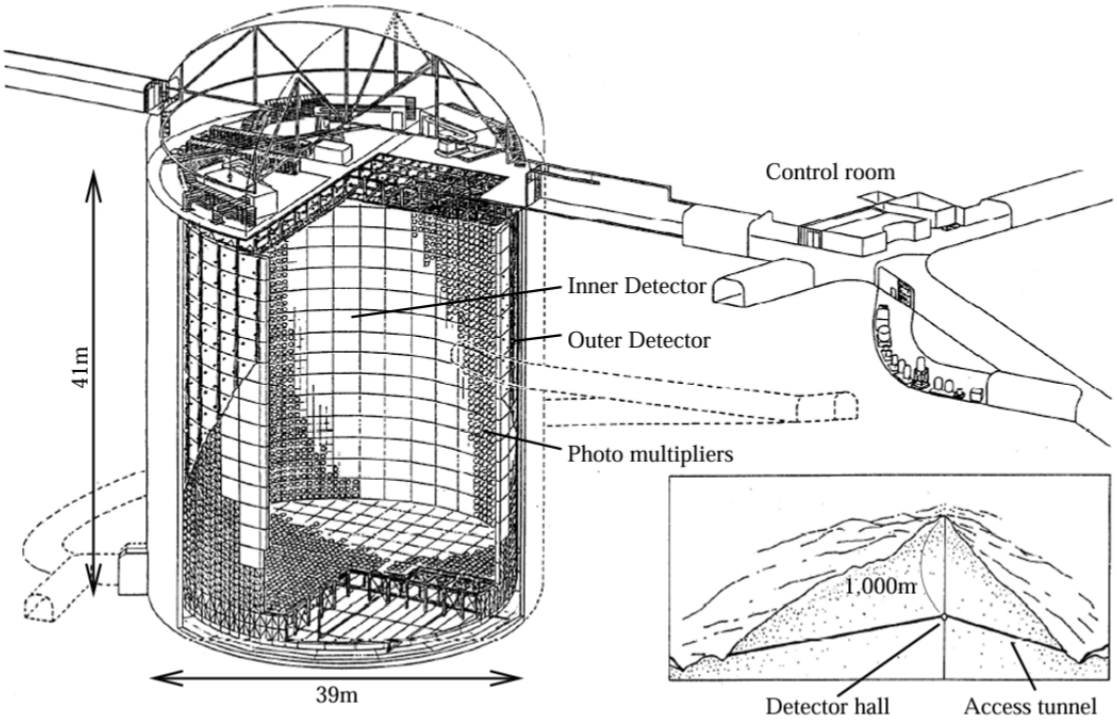

Figure 3.8: SK schematic [68].

3.3.1 SK Phases and the SK-Gd Experiment

The SK experiment began in April 1996 and has progressed through eight phases to date(SK-I to SK-VIII), each defined by changes in detector geometry, electronics, or gadolinium loading. A summary is given in Table 2.1.

SK with pure water (SK-I to SK-V) SK-I (1996–2001) used ATM(Analog & Timing Module) electronics and produced major results on solar [69] and atmospheric neutrinos, including the first evidence of neutrino oscillation [70]. This phase ended when a chain implosion in November 2001 destroyed about 7,900 PMTs.

SK-II (2002–2006) resumed operation with reinforced PMTs enclosed in acrylic and FRP covers and added OD PMTs, running with 5,182 ID PMTs (19% coverage).

SK-III (2006–2008) restored 40% photocathode coverage and stabilized at 11,129 ID and 1,885 OD PMTs. It delivered results including atmospheric-oscillation parame-

Phase	SK-I	SK-II	SK-III	SK-IV
Start	Apr. 1996	Oct. 2002	Jul. 2006	Sep. 2008
End	Jul. 2001	Oct. 2005	Aug. 2008	May. 2018
Live days	1496 days	791 days	548 days	3235 days
Num. of ID PMT (Coverage)	11146 (40%)	5182 (19%)	11129 (40%)	11129 (40%)
Electronics	ATM	ATM	ATM	QBEE
Gd concentration	None	None	None	None

Phase	SK-V	SK-VI	SK-VII	SK-VIII
Start	Feb. 2019	Jul. 2020	Jun. 2022	Aug. 2024
End	Jul. 2020	May. 2022	Aug. 2024	until now
Live days	530 days	623 days	806 days	until now
Num. of ID PMT (Coverage)	11129 (40%)	11129 (40%)	11129 (40%)	11129 (40%)
Electronics	QBEE	QBEE	QBEE	QBEE
Gd concentration	None	0.01%	0.03%	0.03%

Table 3.1: Summary of the Super-Kamiokande phases SK-I to SK-VII.

ters [71], a global oscillation fit to solar neutrino data [72], also the first atmospheric ν_τ appearance [73].

SK-IV (2008–2018) implemented a major electronics upgrade, replacing ATM with the QBEE-based DAQ, which enabled longer PMT readout windows and improved neutron tagging. This phase delivered key results: the first indication of the Earth (day–night) matter effect in solar neutrinos [74], three-flavor atmospheric-oscillation analyses [75], and then world-leading limits on proton decay [76] and the DSNB [35].

SK-V (2018–2019) was defined by a full tank refurbishment in preparation for gadolinium loading.

SK with Gd-loaded water (SK-VI and later) Gadolinium (Gd) was introduced to boost neutron tagging for DSNB and to assist other physics analyses. In pure water, neutrons capture on hydrogen and emit a 2.2 MeV γ, yielding only ∼20% tagging efficiency [35]. With its larger thermal capture cross section, Gd releases 7.9–8.5 MeV γ rays and becomes the dominant capture target, accounting for 50% (75%) of captures at a 0.01% [77] (0.03% [78]) loading concentration. Operationally, $Gd_2(SO_4)_3{\cdot}8H_2O$ was dissolved and injected from the tank bottom using water ∼0.3°C cooler to drive bottom–up replacement as shown in Figure 3.9. Note that the quoted gadolinium concentration refers to the mass fraction of gadolinium sulfate octahydrate, $Gd_2(SO_4)_3 \cdot 8H_2O$: a Gd concentration of 0.01% corresponds to 0.0263% of the hydrate. Technology readiness came from EGADS [79], following the original 2004 proposal [80].

SK-VI (2020–2022) loaded 13.2 t of $Gd_2(SO_4)_3{\cdot}8H_2O$, reaching 0.011% Gd. The Gd loaded in the tank was monitored via temperature, conductivity (pure water $\approx$ 55 nS/cm, 0.01% Gd $\approx$ 168 μS/cm), and by continuously tracking cosmogenic

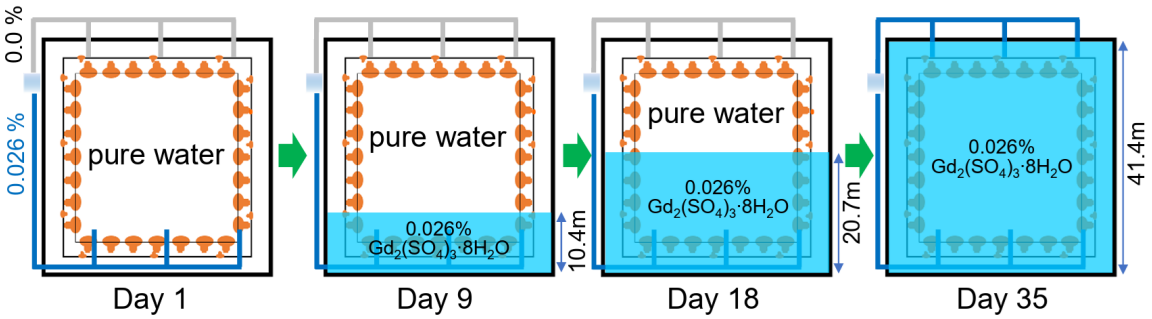

Figure 3.9: Gd loading scheme. Taken from [55]. Colder and higher Gd concentration water is heavier than tank water.

muon–induced neutrons.

SK-VII (2022–2023) added 27.3 t of $Gd_2(SO_4)_3{\cdot}8H_2O$, raising the concentration to 0.033% Gd. Monitoring followed SK-VI procedures (for 0.03% Gd, conductivity $\approx$ 383 μS/cm). After a failure of the geomagnetic compensation coil in November 2023, data taken until the coil repair in August 2024 are referred to as SK-VII.5.

SK-VIII (2024–present): This phase began with the installation of the new geomagnetic compensation coil in August 2024 and continues to date, with the Gd concentration remaining unchanged.

3.3.2 Detector Principle

Cherenkov radiation occurs when a charged particle moves through a medium faster than light's phase velocity in that medium, i.e., $v > c/n$ (still slower than c in vacuum). The condition can be written as $n\beta > 1$ with $\beta = v/c$. As the particle passes, it polarizes the medium and drives tiny electric dipoles. For $v < c/n$ their fields cancel by destructive interference, but for $v > c/n$ there is a cone of directions where the fields add coherently, producing a "light shockwave." In SK this conical light projects onto the detector walls as ring-shaped hit patterns. The Cherenkov cone opening angle θ_C satisfies

$$\cos\theta_C = \frac{c/n}{\beta c} = \frac{1}{n\beta}. \tag{3.4}$$

For pure water with $n \simeq 1.34$, a relativistic particle ($\beta \approx 1$) gives $\cos\theta_C \approx 1/1.34$, hence $\theta_C \approx 42°$. The corresponding momentum threshold depends on the particle mass m as

$$p_C = \frac{mc}{\sqrt{n^2 - 1}}. \tag{3.5}$$

Table 3.2: Cherenkov thresholds for charged particles of interest. The particle masses are taken from Ref. [81], and the threshold values are computed from Eq. 3.5.

Particle	Mass [MeV/c^2]	Momentum threshold [MeV/c]
$e^{\pm}$	0.511	0.573
$\mu^{\pm}$	105.7	118.4
$\pi^{\pm}$	139.6	156.5
p	938.3	1052

Threshold momenta for relevant particles are summarized in Table 3.2. Photons have no Cherenkov threshold. They are seen via Compton electrons (and high-energy e^+e^- pairs) that emit Cherenkov light.

3.3.3 Photo-Multiplier Tubes

Cherenkov light is detected by photomultiplier tubes (PMTs) mounted on the detector walls, as shown in Figure 3.10. In the inner detector (ID), 11,129 20-inch Hamamatsu R3600 PMTs cover about 40% of the surface [68].

Each PMT employs a bialkali (Sb–K–Cs) photocathode with a Venetian-blind dynode chain. At a high voltage of about 2000 V, the gain is $\sim 10^7$. The quantum efficiency, defined as the fraction of incident photons converted to photoelectrons, peaks near 22% around 400 nm and varies with wavelength (see Figure 3.10). A clear single-photoelectron response is observed, with a transit-time spread of about 2.2 ns. The average dark rate is roughly 3 kHz at a 0.25-photoelectron threshold [82].

Following the 2001 accident, each ID PMT was enclosed in a fiber-reinforced plastic cover. In the outer detector (OD), smaller 8-inch PMTs are used: 591 R1408 tubes from IMB [83] and 1,293 R5912 tubes installed after 2001 [68].

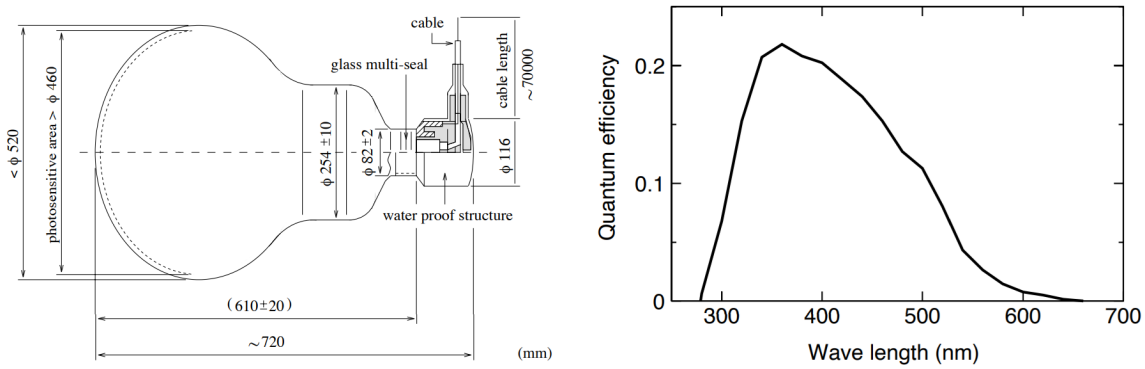

(a) Schematic view

(b) Quantum efficiency

Figure 3.10: Inner-detector PMT schematic and quantum efficiency versus wavelength [68].

3.3.4 Data Acquisition System

Front-End Electronics

Each PMT sends its analog signal over a roughly 70 m coaxial cable to electronics huts for digitization. The photon arrival time and integrated charge are then forwarded to the DAQ.

Since SK-IV, SK has used QTC-Based Electronics with Ethernet (QBEE) [84], which integrates an ASIC (the IWATSU CLC101 charge to time converter) and a time to digital converter (TDC). The ASIC offers three gain paths (dynamic ranges), and an on board FPGA selects the optimal one for each hit.

All hits are read out in periodic blocks (every 16.6,μs), time-ordered, and then processed by a software trigger to identify and record events. This hardware upgrade reduces the effective hit threshold and supports a long per event reasout window, enabling an additional delayed trigger, AFT trigger, that records data in $[35, 535]\,\mu$s after the primary trigger, which is well matched to neutron capture times ($\sim 200\,\mu$s in pure water [85], $\sim 115\,\mu$s at 0.01% Gd [77], $\sim 61\,\mu$s at 0.03% Gd [78]). All PMT signals, including dark noise, are streamed to a merger PC for software event building and delayed coincidence selection.

Triggers

SK employs several software trigger types defined by the number of PMT hits in a 200 ns window, N_{200}, and by specific operating conditions. The trigger set includes SLE, LE, HE, SHE, OD, AFT, and T2K. When N_{200} exceeds a preset threshold, the corresponding trigger fires and the readout window is chosen by trigger type. For example, SHE opens a $40\,\mu$s window ($5\,\mu$s before and $35\,\mu$s after the trigger). The OD trigger uses an N_{200} formed from OD PMTs and fires when it exceeds 22. AFT, designed for neutron tagging, is issued when a SHE trigger occurs without an OD trigger and extends the readout to $535\,\mu$s after the SHE time. During T2K running, J-PARC and SK are synchronized via Global Navigation Satellite System, and T2K trigger at beam arrival records all PMT charges and times over $\pm 500\,\mu$s (~ 1 ms). In this thesis, T2K trigger data are used for the NCQE-like measurement.

3.3.5 Water Purification System

The SK detector uses water purified from the Kamioka mine's groundwater. Impurities such as particles, metal ions, bacteria, and radionuclides scatter or absorb Cherenkov light. In addition, ^{214}Bi from ^{222}Rn emits electrons (β decay) below 3.26 MeV, which dominate backgrounds near the $\sim$3.5 MeV solar neutrino threshold. For these reasons, rigorous water purification is essential. Boardly speaking, the

Table 3.3: Summary of the SK triggers. The numbers in the second column are the number of hit PMTs within a 200 ns window (N_{200}).

Trigger Type	**Threshold**	**Time Window [μs]**
SLE	34 → 31 (after May of 2015)	[−1.5, +1.0]
LE	47	[−5, +35]
HE	50	[−5, +35]
SHE	70 → 58 (after September of 2011)	[−5, +35]
OD	22 (in OD)	[−5, +35]
AFT	SHE + no OD	[+35, +535]
T2K	Beam on	[−500, +535]

water circulation system could be divided into two, the pure water stage (until SK-V) and Gd-loaded water system stage (after SK-V).

Pure water circulation system (until SK-V) Water circulates at ∼60 tons per hour. It is withdrawn from the top, purified, and returned at the bottom, which lowers radon from 9.1 to ∼1.7 to 1.8 mBq/m^3 [86] and keeps the water attenuation length near 100 m. This vertical flow makes the bottom clearer than the top, so convection is suppressed by controlling temperature, flow rate, and the inlet and outlet geometry. The water temperature is held at approximately 13.3°C, which stabilizes PMT response, limits bacterial growth, and prevents convection. The transparency difference between top and bottom is ∼5% [68]. A schematic is shown in Figure 3.11.

The purification process operates in series. A 1 μm filter first removes fine particles. A heat exchanger then keeps the water at 14°C. Ion exchange removes dissolved metals and carbonates, and a cartridge stage further reduces ions to about 99% removal. Reverse osmosis strips large organic molecules. UV light kills bacteria, and an ultrafilter removes nanometer scale particles. Finally, a vacuum degassifier that uses radon free air removes dissolved gases, and a membrane degasser eliminates the remaining radon and oxygen. Together, these steps keep the water pure and clear for low background Cherenkov detection [68].

Gd loaded water circulation system (after SK-V) After SK-IV, a new system was installed for SK-Gd to keep the same level of bacteria and particle control as in SK IV while preserving dissolved Gd^{3+} and SO_4^{2-}. A selective ion-exchange design removes only other ions and is integrated into the new circulation layout [77], as shown in Figure 3.12.

During the initial loading phase, $Gd_2(SO_4)_3{\cdot}8H_2O$ is dispensed, weighed, dissolved in a buffer tank, and sent to a solution tank. The stream then passes through pretreatment where a cation resin that does not capture Gd^{3+} and an anion resin that does not capture SO_4^{2-} remove unwanted ions. TOC treatment with UV, direct

UV irradiation, and ultrafiltration remove organics, microbes, and fine particles. After blending with pure water, the Gd solution circulates through TOC lamps, heat exchangers, ion-exchange beds, UV sterilizers, and ultrafiltration in two identical branches (about 60 m^3 per hour each, 120 m^3 per hour in total). This layout allows either branch to operate while the other is under maintenance. During loading, pure water was withdrawn from the top to feed the dissolver, and Gd-loaded water was injected at the bottom. The tank water was kept about 0.3°C warmer than the incoming stream so the cooler Gd solution accumulated from below, producing a stable fill from the bottom upward. Upon completion of the loading, the system transitioned to full recirculation to maintain water transparency and ensure a uniform Gd concentration throughout the detector [77].

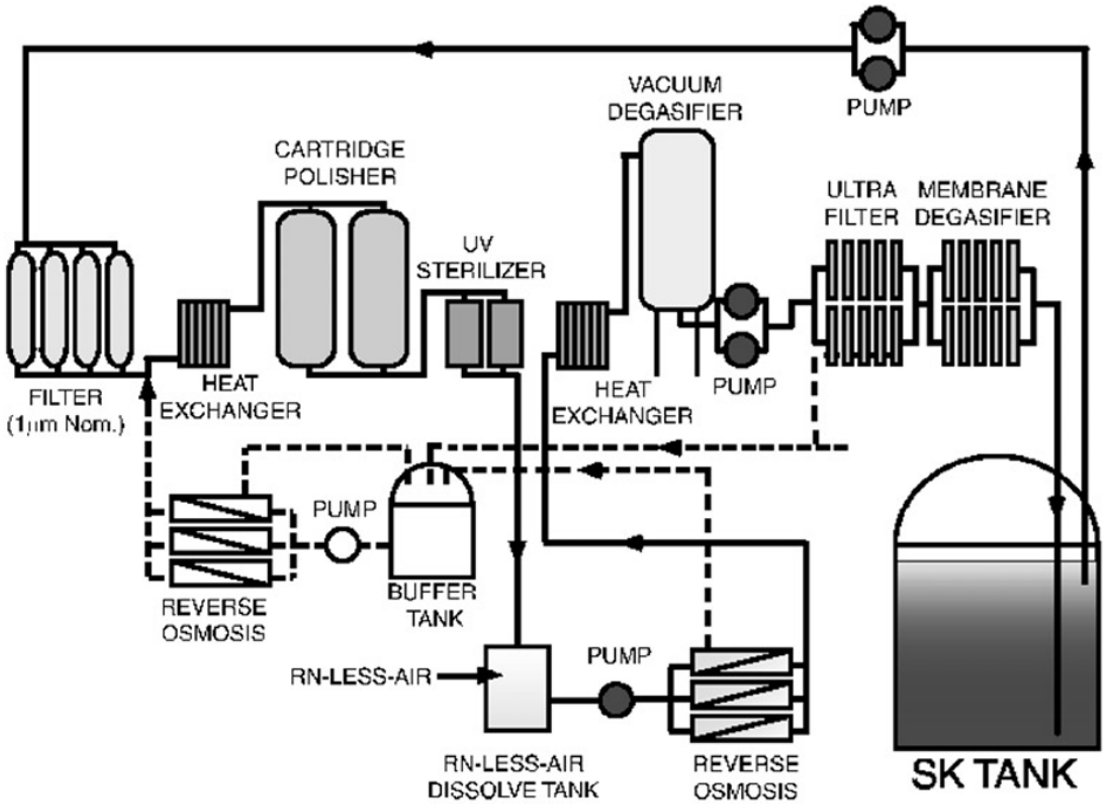

Figure 3.11: A schematic view of the water purification system [68].

3.3.6 PMT Calibration

Super-Kamiokande employs several procedures to calibrate PMT response. Here we highlight two that are critical to the low-energy analysis presented in this work:

1. **Relative Gain:** Determine per-PMT gain by illuminating a fixed isotropic source at two intensities and using the observed charge-hit ratio $Q_{\text{obs}}/N_{\text{obs}}$ to equalize tube response largely independent of geometry.

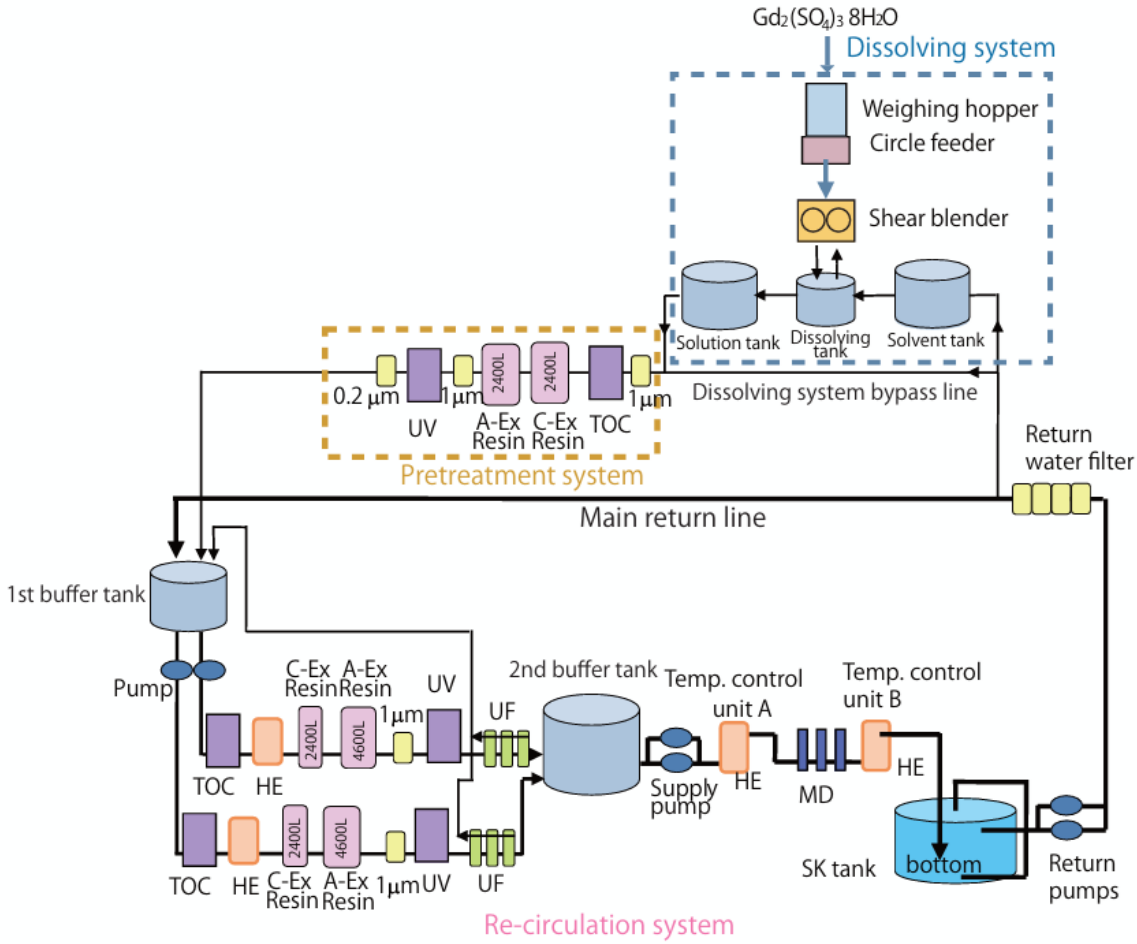

Figure 3.12: A schematic view of the Gd loaded water purification system [77].

2. **Relative Timing:** Align per-PMT hit times by pulsing light from a central diffuser to build time-charge (TQ) maps, then correct cable and electronics delays and time walk for precise reconstruction.

Relative Gain Calibration To remove batch-dependent gain drifts, all PMTs were calibrated and monitored in-situ. Practically, a Xe lamp (SK-I) or nitrogen–laser–driven dye laser (SK-IV) illuminates a diffuser ball via fiber as shown in the left panel of Figure 3.13. A UV filter wheel sets the flash intensity. We place a stable, isotropic light source at a fixed point in the tank and take two kinds of flashes: A bright flash so every PMT sees many photons, giving an average observed charge $Q_{\text{obs}}(i)$, and a dim flash so only a few tubes fire per event, letting us count threshold crossings $N_{\text{obs}}(i)$ that are effectively single–photoelectron hits. With the light source fixed, the two flash settings give

$$\begin{aligned} Q_{\text{obs}}(i) &\propto I_s \times a(i) \times \epsilon_{qe}(i) \times G(i), \\ N_{\text{obs}}(i) &\propto I_w \times a(i) \times \epsilon_{qe}(i), \end{aligned} \tag{3.6}$$

so the relative gain follows from their ratio:

$$G(i) \propto \frac{Q_{\text{obs}}(i)}{N_{\text{obs}}(i)}. \tag{3.7}$$

Because the source position is unchanged, geometric acceptance and QE enter both measurements in the same way and largely cancel out. The discriminator is set low so $N_{\text{obs}}(i)$ depends only weakly on gain (a 10% gain shift changes $N_{\text{obs}}(i)$ by $\sim$1.5%).

Across PMTs, the RMS of the normalized ratio is 5.9% (during SK-IV) [85] and 7.0% (During SK-I) [68].

Relative timing Calibration : Accurate relative PMT timing is essential for vertex and track reconstruction. Hit times vary with cable length, intrinsic PMT response, and pulse amplitude ("time walk"). We measure and correct these effects using a pulsed-light system. A nitrogen–laser–driven dye laser is wavelength-shifted into the Cherenkov-sensitive region, its intensity is set by a variable filter, and the light is transmitted via fiber to a central diffuser ball. A fast 2-inch PMT monitors the laser timing.

For each PMT we build a two-dimensional "TQ map" of timing versus charge, using

$$T \equiv T_{\text{obs}} - \text{TOF} - T_{\text{2-inch}}, \tag{3.8}$$

where T_{obs} is the PMT hit time, TOF is the photon time of flight from the source, and $T_{\text{2-inch}}$ is the monitor-PMT trigger time. Fitting the TQ map yields a per-PMT

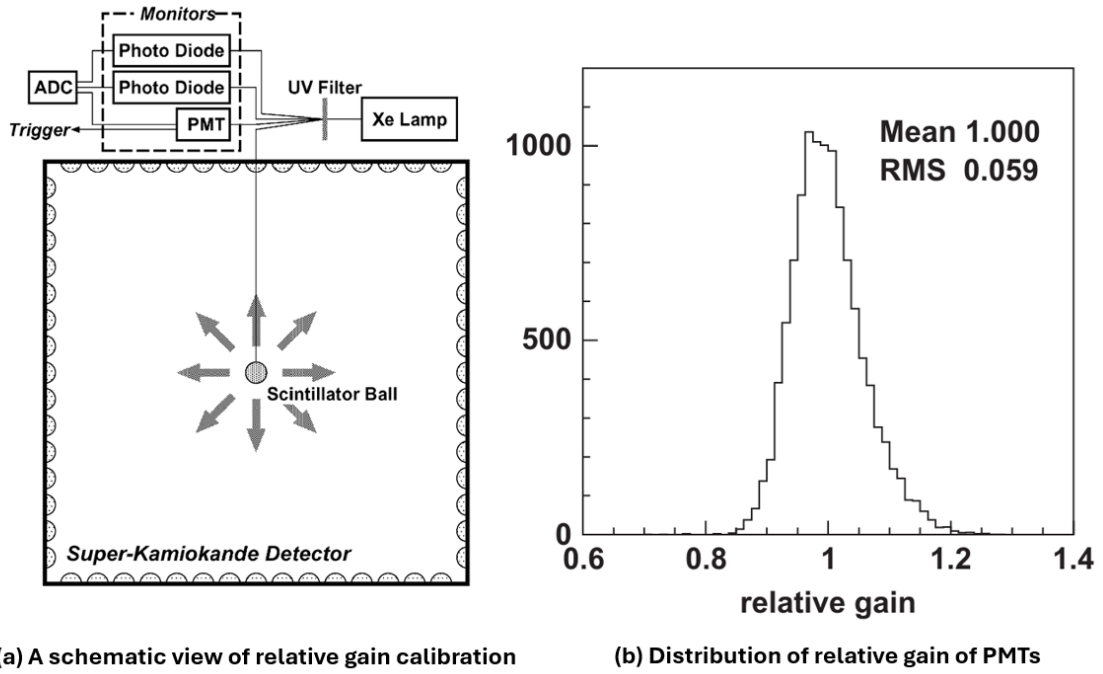

Figure 3.13: A schematic view of the relative PMT gain calibration (left) and the relative PMT gain distribution in SK-IV (right) [85].

time-walk correction applied in data reduction and reconstruction.

From the same dataset we also extract the charge-dependent timing resolution by fitting the corrected time distributions. The single-photoelectron resolution is typically better than 3 ns, and the full resolution curve is used in the detector simulation.

3.3.7 Water Calibration

Super-Kamiokande uses several methods to monitor water transparency. Here we highlight three that are highly related to the low-energy analysis presented in this work:

1. **Water-laser:** probes scattering and absorption (used in this analysis).
2. **Decay-electron:** extracts an effective total attenuation length (used in this analysis).
3. **Cosmogenic muon–induced neutron-capture:** extracts an effective total attenuation length (developed by the author to potentially improve total attenuation length calibration).

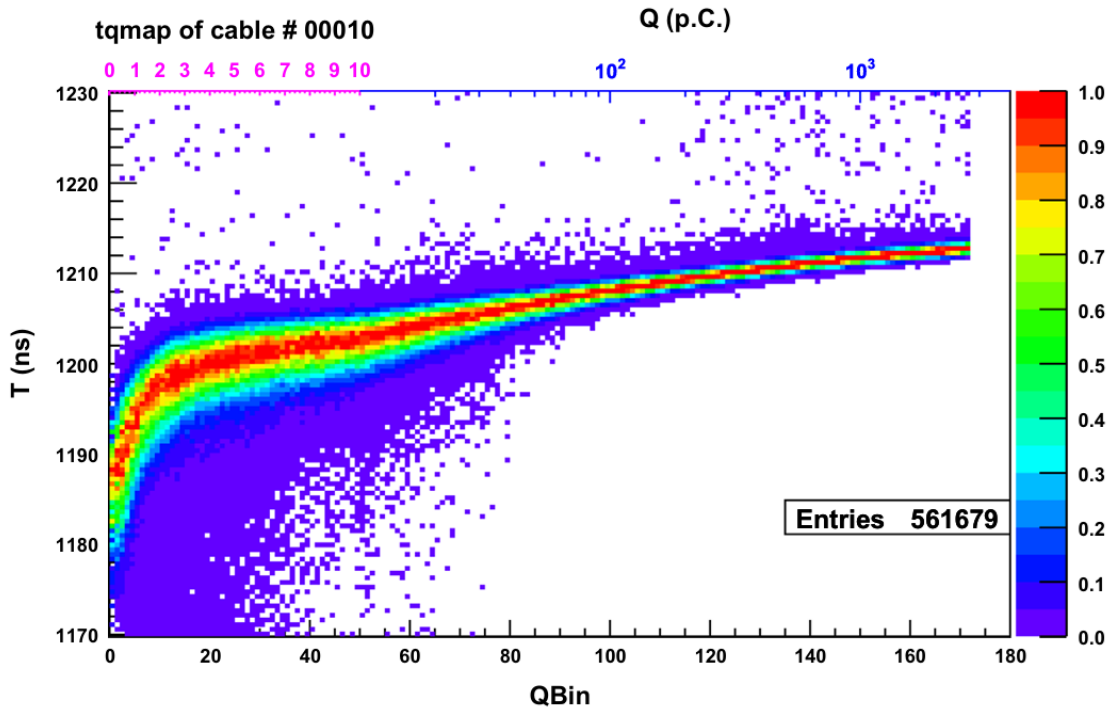

Figure 3.14: A typical TQ map for a readout channel in SK-IV [85].

Water–laser measurement

SK compares laser data with MC predictions and extracts both scattering and absorption as functions of wavelength. SK represents transparency with three wavelength-dependent terms: absorption $\alpha_{\text{abs}}(\lambda)$, symmetric scattering $\alpha_{\text{sym}}(\lambda)$, and asymmetric scattering $\alpha_{\text{asy}}(\lambda)$, where θ is the scattering angle. The transparency is

$$L(\lambda) = \frac{1}{\alpha_{\text{abs}}(\lambda) + \alpha_{\text{sym}}(\lambda) + \alpha_{\text{asy}}(\lambda)}. \tag{3.9}$$

These inputs are fitted with simple functions of λ^{-1}:

$$\begin{aligned}
\alpha_{\text{abs}}(\lambda) &= P_0 \frac{P_1}{\lambda^4} + C, \\
\alpha_{\text{sym}}(\lambda) &= \frac{P_1}{\lambda^4}\left(1 + \frac{P_5}{\lambda^2}\right), \\
\alpha_{\text{asy}}(\lambda) &= P_6\left(1 + \frac{P_7}{\lambda^4}(\lambda - P_8)^2\right), \\
C &= P_0 P_2 \left(\frac{\lambda}{500}\right)^{P_3}, \qquad \lambda \leq 464 \text{ nm}.
\end{aligned} \tag{3.10}$$

Here $P_0 \ldots P_8$ are fit parameters. These empirical forms, calibrated to the SK simulation in 2009, are not tied to a specific physical model [85].

Experimentally, a laser supplies monochromatic light at 337, 365, 400, and 445 nm. The beam is sent by optical fiber to six fixed injectors in the tank, namely five on the barrel and one on the bottom endcap, events are taken with a dedicated trigger. For each of the six detector regions (barrel 1 to 5, bottom endcap), PMT hits are corrected for time of flight and filled into charge-weighted hit-time histograms. Because the absolute laser intensity is hard to monitor, each regional histogram is normalized. This reduces sensitivity to absorption and makes the measurement primarily sensitive to scattering.

An MC grid is generated over absorption and scattering parameters. For each MC sample, a χ^2 is computed from the seven regional histograms, with the timing window tuned separately for each region. The parameters that minimize χ^2 are taken as the best-fit water scattering, with residual sensitivity to absorption. The left, center, and right panels of Figure 3.15 show the water-laser schematic, the timing distribution, and the fit results, respectively.

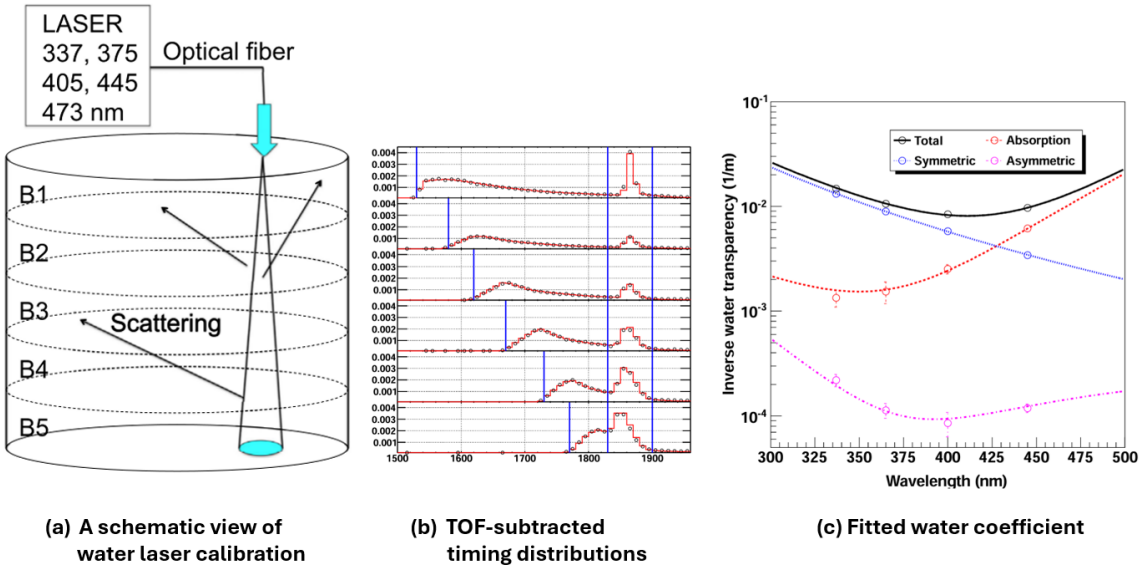

(a) A schematic view of water laser calibration

(b) TOF-subtracted timing distributions

(c) Fitted water coefficient

Figure 3.15: Water-laser schematic (left), representative timing distributions (center), and MC fit results (right) used by SK to determine wavelength-dependent absorption and scattering parameters in SK-IV. [85].

Decay electron measurement

Decay electron events allow for for a direct measurement of effective water transparency with Cherenkov photons. Transparency in SK changes from day to day because of water circulation, and the muon rate is about 2.2 Hz which is a suitable source for monitor it. Many of these muons decay in the tank and produce Michel electrons with a well-known momentum spectrum, providing a high-statistics daily sample for this calibration.

Unlike water-laser data selected by a dedicated trigger, decay–electron candidates are selected with cuts to suppress backgrounds, which are summarized in Table 3.4

Criterion	Condition
Time window	$2.0\ \mu\text{s} \leq \Delta t \leq 8.0\ \mu\text{s}$
ID wall distance	$L_{\text{wall}} > 2.5$ m
Muon–electron separation	$\lvert\vec{x}_\mu - \vec{x}_e\rvert < 250$ cm

Table 3.4: Selection summary, where Δt is the time between the parent muon and the decay–electron candidate.

For each selected event, let r be the distance between the ith PMT and the reconstructed electron vertex. ID PMTs are grouped into 60 bins in r. Define the effective hit per PMT,

$$N^i_{\text{eff}} = \left(X_i + \epsilon_{\text{tail}} - \epsilon_{\text{dark}}\right) \times \frac{N_{\text{all}}}{N_{\text{normal}}} \times \frac{R_{\text{cover}}}{S(\theta_i, \phi_i)} \times \frac{1}{QE_i}, \tag{3.11}$$

where X_i corrects for multi–photoelectron occupancy,

$$X_i = \frac{\ln\left(\frac{1}{1-x_i}\right)}{x_i},$$

and x_i is the fraction of hit PMTs in a 3×3 patch around PMT i. The terms ϵ_{tail} and ϵ_{dark} correct tail and dark–noise contributions. N_{normal} accounts for bad or dead channels. $R_{\text{cover}}/S(\theta_i, \phi_i)$ corrects the geometric acceptance of the candidate vertex to PMT i, and QE_i is the PMT quantum–efficiency table value.

For each distance bin r, we compute the mean N^i_{eff} and plot $\ln N^i_{\text{eff}}$ versus r as shown in the right plot of Figure 3.16. A linear fit is performed over 1200 to 3500 cm, and the inverse slope yields the attenuation length. To stabilize the fit, we impose two constraints. First, we fix the intercept of the $\ln N^i_{\text{eff}}$ fit by a value 1.499. Second, we apply a ± 7 day running average to the derived transparency.

Across SK-IV, the transparency remains stable within 10% as shown in Figure 3.20. The scalar sum $N\text{eff} = \sum_i N^i_{\text{eff}}$ tracks visible energy and is sensitive to transparency, and its stability confirms the transparency estimate.

Neutron capture for water calibration

Calibration with spallation-induced neutrons targets low-energy events relevant to solar neutrinos and the DSNB (3.5–30 MeV). Decay electrons peak near 30 MeV and extend to a few MeV, but their limited statistics and simulation accuracy introduce

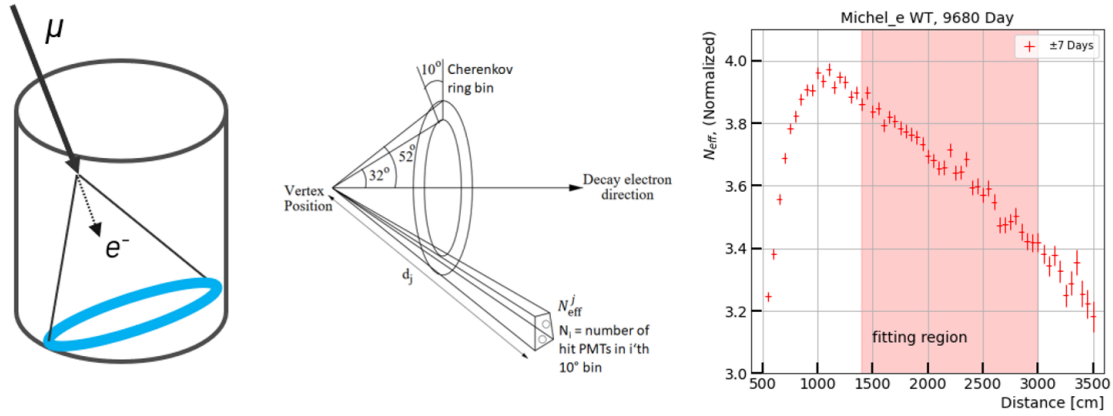

(a) A schematic view decay electron **(b) Analysis parameters** **(c) Histogram of N_{eff} versus r**

Figure 3.16: Decay-electron for water transparency monitoring in SK: schematic (left), analysis parameters (center), and N_{eff} versus PMT distance (right) used to extract the effective water attenuation length. [85].

large uncertainties at low energies. In contrast, neutron capture on Gd yields 8 MeV γ rays (the Gd(n,γ) process) with roughly an order of magnitude higher statistics than decay electrons. This makes it an ideal low-energy calibration source, capable of measuring position-dependent water parameters that decay-electron calibration cannot. Here we focus on using Gd(n,γ) source and compare it with decay electron source to calibrate water transparency.

Starting from the selection optimized for spallation muon–induced neutrons in Ref. [87], we develop the cuts for water-transparency calibration. The selection differences between the decay-electron and (n,γ)Gd used for water transparenct calibration are summarized in Table 3.5.

Cut Selection	Decay-e	(n,γ)Gd
Trigger	OD+SHE	OD+SHE+AFT
Q_μ	$Q_\mu > 1500$	$Q_\mu > 1500$
Cosmic muon type	Stopping muon	Every muon
Time window	$[2, 8]$ μs	$[20, 535]$ μs
# of PMT hits within 50ns	> 50	> 24

Table 3.5: Event selections for water-transparency calibration with decay electrons and (n, γ)Gd.

Most analysis settings match the decay electron based water transparency calibration(Table 3.6), but we adopt coarser binning for the (n,γ)Gd source. The bin for Cherenkov ring is defined as $\theta = 42° \pm 15°$ (decay electron: $42° \pm 10°$), and the distance histogram uses 150 cm bins (decay electron: 75 cm). This reflects the lower energy (n, γ)Gd cascade, which yields fewer PMT hits, especially at larger source-to-

PMT distance, so wider bins are required to improve statistics and reduce fluctuations. An illustration is shown in Figure 3.17.

Analysis settings	Decay-e	(n,γ)Gd
Distance	Crstnksk()	Crstnksk()
Hit select	$-10 < T - \text{TOF} < 40$	$-10 < T - \text{TOF} < 40$
Gain	Not corrected	Not corrected
Bin size	$\theta = 42° \pm 10°$, $\phi = 10° \times 36$	$\theta = 42° \pm 15°$, $\phi = 10° \times 36$
χ_i, occupancy	lfoccor_4.F	lfoccor_4.F
New Dark rate	Region&Deadtime	Region&Deadtime
Badrun	lfbadrun_local.F	lfbadrun_local.F
Coverage correction	skcoverage_sk4_final + barrel	skcoverage_sk4_final + barrel
QE table	qetable_DETSIM_5.dat	qetable_DETSIM_5.dat

Table 3.6: Comparison of analysis settings between Decay-e and (n,γ)Gd.

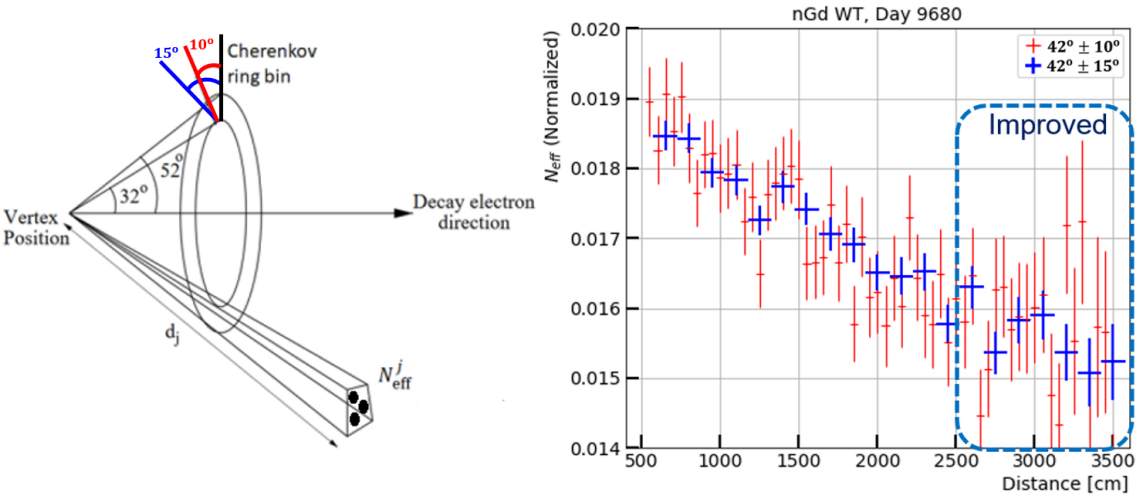

Figure 3.17: Left: schematic of the Cherenkov-ring selection at $\theta = 42° \pm 10°$ (red) and $\theta = 42° \pm 15°$ (blue). Right: N_{eff} as a function of distance for the (n, γ)Gd sample.

Figure 3.18 compares fits from decay electrons and (n,γ)Gd sources. The left panel shows a representative (n, γ)Gd fit with two linear–fit configurations: intercept fixed to the average threshold ("y-fixed," yellow) and intercept free ("y-free," purple). The right panel presents the SK-VI and early SK-VII transparency trends from both methods, with the y-fixed results overlaid as a y-free reference. Overall, (n, γ)Gd yields about 30m larger transparency than the decay electron. The histogram in the difference plot reports correlation coefficients of 0.66 (y-free) and 0.82 (y-fixed), indicating a positive correlation between the two calibration sources.

We next examine how bias in the water-transparency result arises from the chosen fit range. As shown in Figure 3.19, the fit windows in distance were selected independently for decay electrons and neutron capture, which introduces a methodological difference. For (n, γ)Gd, the distance range was set to include as many data

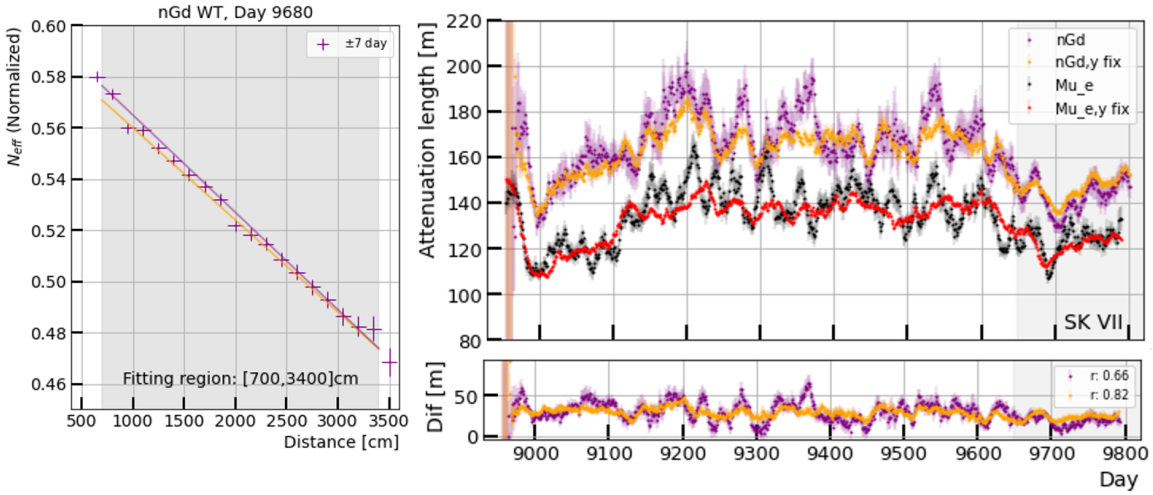

Figure 3.18: Comparison of water transparency from decay electrons and (n, γ)Gd. Left: example (n, γ)Gd fit with linear using a fixed intercept ("y-fixed, yellow) and a free intercept ("y-free, purple). Right: SK-VI to early SK-VII trends from both methods. (n, γ)Gd gives about 30m larger transparency, with attenuation-length differences < 50 m. Correlations between methods are 0.66 (y-free) and 0.82 (y-fixed).

points as possible, excluding only the first and last bins where fluctuations are large. Overlaying the two panels in Figure 3.19 yields the left panel of Figure 3.20, where the (n, γ)Gd distribution beyond 2200 cm closely follows the decay-electron effective-hit distribution. The right panel of Figure 3.20 confirms this in the fitted attenuation lengths: yellow points show (n, γ)Gd fits over 700–3400 cm, while purple points use 2200–3400 cm. The decay-electron result is shown in red, and the differences between each (n, γ)Gd setting are also plotted. In summary, the fit window has a large impact on the extracted attenuation length, even though the correlation coefficients between the two methods remain similar.

We summarize the fit-slope (water attenuation length) uncertainty as 0.7% for decay electrons. For (n, γ)Gd, the corresponding values are 2.1% in SK-VI and 1.1% in SK-VII when the fit range is from 700 to 3400 cm. We also examined angular dependence for both decay electrons and (n, γ)Gd. As shown in Figure 3.21, the uncertainty is about $\pm 1\%$ in θ and $\pm 0.75\%$ in ϕ. Uncertainties were summarized in Table 3.7. Further simulation studies would enable to find the physics reasons for the transparency bias between two sources, which further benefit solar, reactor, and isotope analyses in SK.

3.3.8 Energy Calibration

Super-Kamiokande uses serveral methods to calibrate energy scale, we mentioned two important calibrations that are critical to the low-energy analysis presented in this

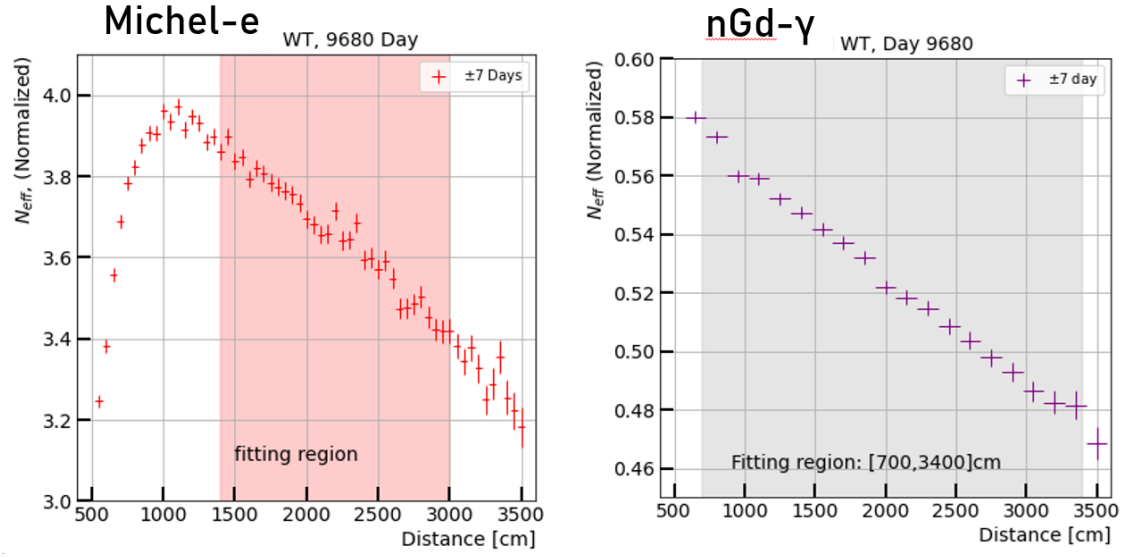

Figure 3.19: Fit-window comparison for water-transparency extraction. N_{eff} vs distance for decay electrons (Left) and (n,γ)Gd (Right) with their respective fit ranges. The (n,γ)Gd window is broad, excluding only edge bins.

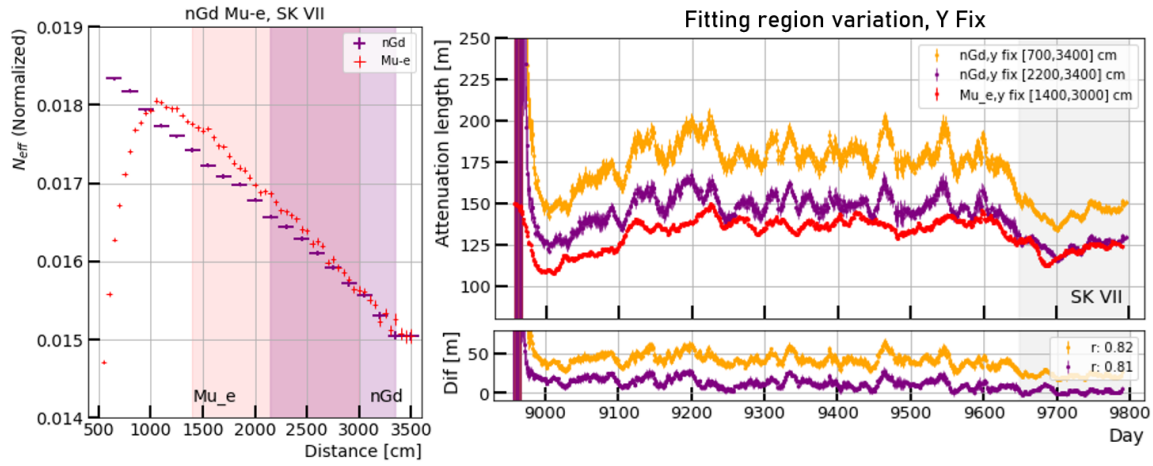

Figure 3.20: Impact of fit range on the inferred attenuation length. Left: overlay of decay-electron and (n,γ)Gd N_{eff} vs distance, showing agreement for $r \gtrsim 2200$ cm. Right: attenuation lengths from (n,γ)Gd using 700–3400 cm (yellow) and 2200–3400 cm (purple), compared with decay electrons (red). Differences relative to decay electrons are shown below, highlighting the fit-range dependence.

Table 3.7: Summary of water-transparency (attenuation-length) and directional uncertainties.

Source	**SK Phase**	**Fit Range (cm)**	**Attenuation Length Uncertainty**	**Directionality** θ / ϕ
Decay electron	SK-VI/VII	1200–3000	0.7%	$\pm 1.0\%$ / $\pm 0.75\%$
(n,γ)Gd	SK-VI	700–3400	2.1%	$\pm 1.0\%$ / $\pm 0.75\%$
(n,γ)Gd	SK-VII	700–3400	1.1%	

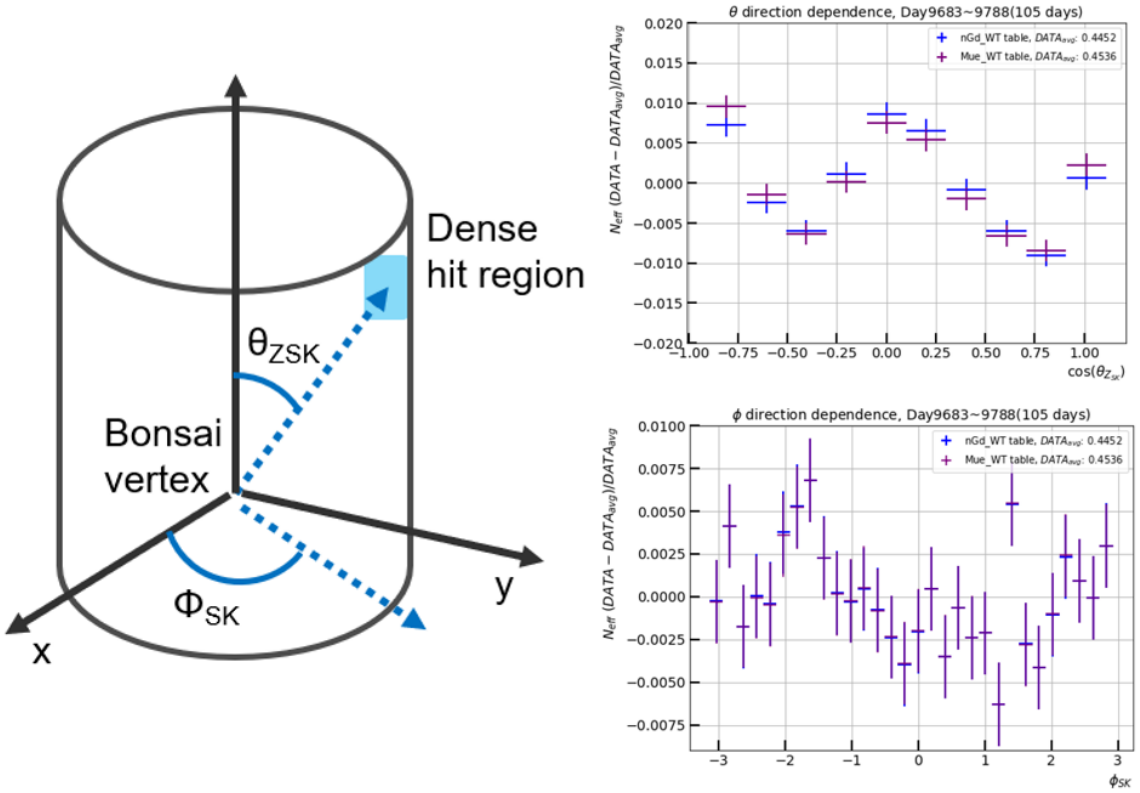

Figure 3.21: Angular dependence of the water-transparency calibration for decay electrons and (n, γ)Gd. Left: definitions of θ and ϕ. Upper right: variation in θ within $\pm 1.0\%$. Lower right: variation in ϕ within $\pm 0.75\%$.

work:

1. **LINAC:** A single-electron linear accelerator steers 4.4–18.0 MeV electrons to fixed points to set the absolute energy scale and calibrate low-energy performance.

2. **DT:** A deuterium–tritium source creates in-situ ^{16}N whose isotropic decays provide an independent cross-check of the absolute scale and map angular/positional dependences.

LINAC calibration

The absolute energy scale and low-energy performance (energy, angular, spatial resolutions. Detection efficiency) are calibrated with a single-electron LINAC. Installed above the tank and adapted for SK in 1996 as shown in left panel of Figure 3.22, it delivers a steered electron beam (through magnets D1–D4) to fixed fiducial points. A germanium detector measures energy, and a collimator and low beam intensity (10% trigger rate) keep multi-electron events at 1%.

Calibration uses positions fixed by the pipe and calibration-hole layout: three along x (-12, -6, -4 m) and three depths in z (-15, 0, 15 m), with 4.4–18.0 MeV electrons. The absolute energy scale is known to better than 1% for 5–16.3 MeV. Monte Carlo tuned with other inputs yields the global response factor COREPMT by matching N_{eff} peaks between data and simulation. In 2016, COREPMT was ≈ 0.87. Residual position dependence is treated as a systematic, keeping the energy-scale variation below 1% (right panels of Figure 3.22). More detailes could be found at Refs. [88].

DT calibration

The ^{16}N method provides an independent cross-check of the absolute energy scale set by the LINAC and, importantly, measures directional and positional dependences that the downward LINAC beam cannot cover. A deuterium–tritium generator produces 14.2 MeV neutrons,

$$^{3}\text{H} + {}^{2}\text{H} \rightarrow {}^{4}\text{He} + n,$$

which create ^{16}N in the detector water via

$$^{16}\text{O} + n \rightarrow {}^{16}\text{N} + p.$$

The ^{16}N then decays with a 7.13 s half-life,

$$^{16}\text{N} \rightarrow {}^{16}\text{O} + e^{-} + \bar{\nu}_e,$$

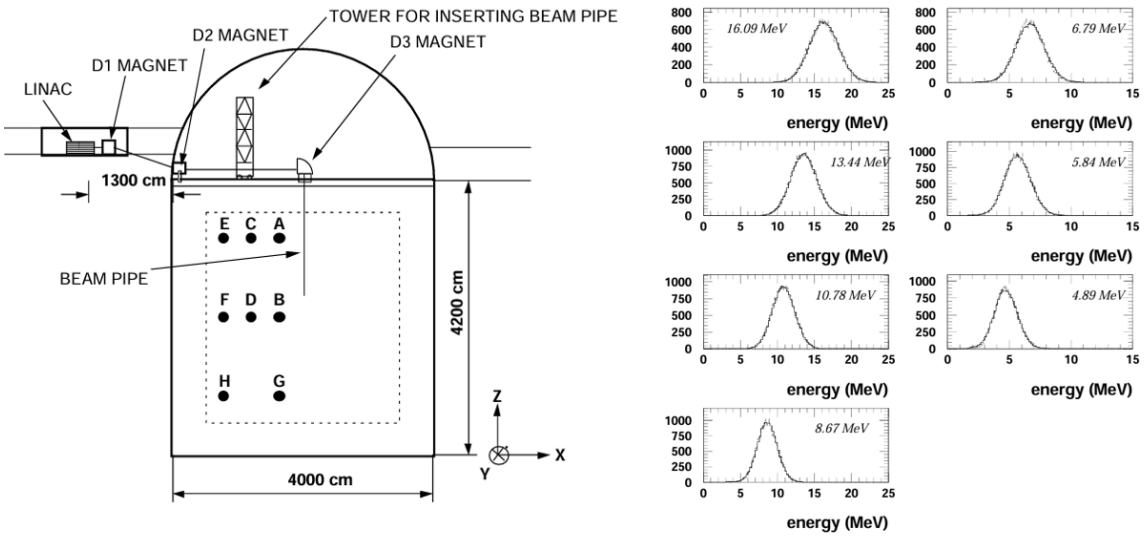

(a) A schematic view of LINAC calibration **(b) Energy distribution**

Figure 3.22: A schematic view of the LINAC calibration [88].

emitting either an electron with a 4.3 MeV endpoint accompanied by a 6.1 MeV γ-ray, or a 10.4 MeV electron, with branching ratios of 66% and 28%, respectively. Figure 3.23 (left panel) shows the experimental setup. Although the electron spectrum is not monochromatic, the isotropic, in situ decays enable precise studies of angular and spatial dependence of the energy scale with systematics distinct from the LINAC. Over extended periods the data agree with the LINAC-tuned Monte Carlo within $\pm 0.64\%$, quantified by

$$R = \frac{E_{\mathrm{MC}} - E_{\mathrm{Data}}}{E_{\mathrm{Data}}}.$$

The right panel of Figure 3.23 also shows the azimuthal and zenith angle distribution, which the uncertainty is within 0.3%. Further details of the DT system are given in Refs. [89].

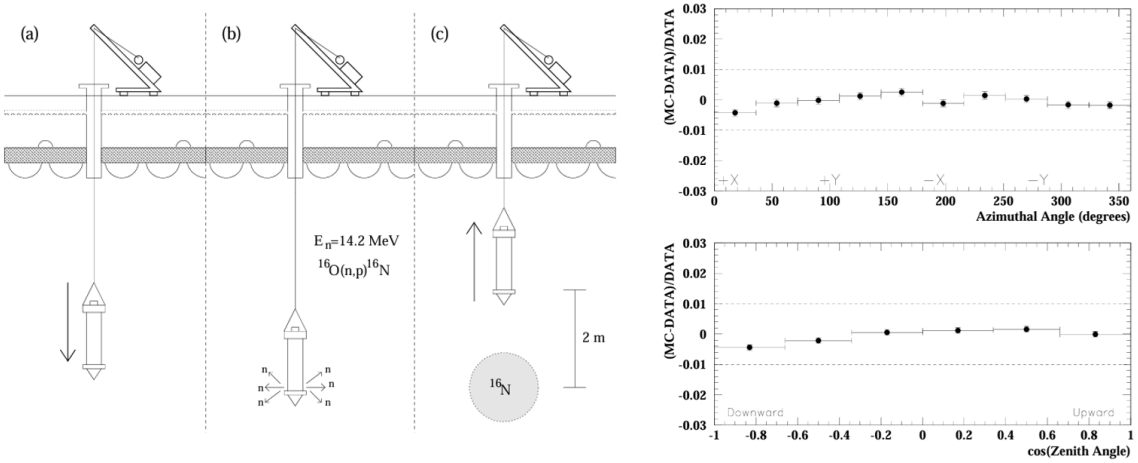

(a) A schematic view of DT calibration **(b) Azimuthal and Zenith angle distribution**

Figure 3.23: A schematic view of the DT calibration (left) and angle distribution results (right) [85].

Chapter 4

Event simulation and reconstruction

4.1 Event simulation

This chapter presents an overview of the T2K ν-^{16}O NCQE event Monte Carlo sample, focusing on the setting of NEUT, detector simulation, and reconstruction.

4.1.1 Neutrino interaction

NCQE interaction of a neutrino on ^{16}O, hereafter the *primary interaction*, can be written schematically as

$$\nu + {}^{16}\mathrm{O} \rightarrow \nu + {}^{A}_{Z}\mathrm{X} + m_p\, p + m_n\, n + \gamma, \tag{4.1}$$

where ${}^{A}_{Z}$X is the residual nucleus, and m_p and m_n are the primary proton and neutron multiplicities.

Neutrino experiments use Monte Carlo generators including NEUT [90], NuWro [91], and GENIE [92]. These generators share a common structure with components for the neutrino interaction and final state interactions (FSI). Their specific models and tunings differ across development teams, which leads to variations in predictions. In this work we use NEUT, the standard in the SK and T2K collaborations, and we include NuWro for supplementary comparison.

Neutrino interaction in NEUT (version 5.6.3) NEUT integrates multiple physics models to simulate neutrino interactions. For NCQE and CCQE it uses the Ankowski model [26] with the Benhar spectral function to describe the initial nucleon momentum distribution [93]. The axial vector mass in the dipole form factor is fixed

at $M_A = 1.21$ GeV/c^2 based on K2K fits [94]. Charged current two particle two hole (2p2h) interactions follow the model of Nieves et al. [25]. The corresponding neutral current 2p2h channel is not included because of limited experimental measurements. Vector and axial form factors use BBBA05 and a dipole parametrization, respectively [27]. Deep inelastic scattering is modeled with GRV98 parton distributions [95] together with the Bodek and Yang modification [96]. For coherent scattering in both CC and NC, NEUT applies the Berger and Sehgal model [97]. Final state interactions use cross section models by Bertini et al. for nucleons [98] and by Pinzon et al. for pions [99]. The default settings used in this work are summarized in Table 4.1, and NEUT is adopted as the nominal generator because it is naturally compatible with T2K and SK internal tools.

Table 4.1: Model configuration in NEUT.

Channel	Model	Parameter	
NCQE	Ankowski et al.[26]	M_A	1.21 GeV
		g_A^s	0.0
		VFF	BBBA05[27]
		strange VFF	Neglected
		Nuclear model	SF[93]
CCQE	Ankowski et al.[26]	M_A	1.21 GeV
		VFF	BBBA05[27]
		Nuclear model	SF[93]
CC 2p2h	Nieves et al.[25]		
CC and NC RES	Graczyk-Sobczyk[100]	FF	Dipole form
		M_A	0.95 GeV
		$C_4^A(0)$	1.01
		RES/DIS boundary	$W = 2.0$ GeV
CC and NC DIS	GRV98 PDF[95]	with modification by Bodek and Yang[96]	
CC and NC COH	Berger-Sehgal[97]		
FSI	NEUT cascade	Step length	0.2 fm
		Nucleon cross-section	Bertini et al.[98]
		Pion cross-section	Pinzon et al.[99]

Oxygen de-excitation in NEUT In NEUT, the de-excitation of the nuclei is simulated after the primary neutrino–nucleus interaction. A comparison of neutron-production modeling between the default NEUT de-excitation and NucDeEx is presented later in the systematic uncertainty section. Here we describe only the default NEUT settings.

The ground state of ^{16}O is dominated by three single-particle shells: $s_{1/2}$, $p_{3/2}$, and $p_{1/2}$. The proton separation energies are 42 MeV ($s_{1/2}$), 18.4 MeV ($p_{3/2}$), and 12.1 MeV ($p_{1/2}$). Neutrons are more tightly bound: removing a neutron from the same shells requires an additional 3.54 MeV relative to the corresponding proton thresholds.

A neutrino-induced single-nucleon knockout populates one of seven residual-nucleus categories: $(s_{1/2})^{-1}p$, $(p_{3/2})^{-1}p$, $(p_{1/2})^{-1}p$, $(s_{1/2})^{-1}n$, $(p_{3/2})^{-1}n$, $(p_{1/2})^{-1}_n$, or an *others* class. The first three are proton-hole configurations, the next three neutron-hole configurations, and *others* collects higher-excitation states beyond the simple single-hole picture, including configurations influenced by short-range correlations and related complex nuclear dynamics. The transition probabilities into each nucleon-hole state and the *others* class are listed in Table 4.2.

	$(p_{1/2})^{-1}$	$(p_{3/2})^{-1}$	$(s_{1/2})^{-1}$	*others*
Simple shell model	0.25	0.50	0.25	0
Ankowski et al. [26]	0.158	0.3515	0.1055	0.385
Standard NEUT 5.6.3	0.158	0.3515	0.4905	-

Table 4.2: Transition probabilities to nucleon-hole and others states for the considered models.

Table 4.3: Excited states and γ-ray emission modes of ^{16}O proton hole $(p_{3/2})^{-1}$ and neutron hole $(p_{1/2})^{-1}$.

Residual nucleus	E_{ex} [MeV]	J^π	E_γ [MeV]	R_γ [%]	Br$(X^* \to Y + \gamma)$ [%]
^{15}N	6.32	$(3/2)^-$	6.32	100	86.2
	9.93	$(1/2)^-$	-	15.3	1.1
		$(3/2)^-$	5.30	4.9	0.3
		$(1/2)^-$	6.32	2.1	0.1
		$(3/2)^-$	7.30	77.6	5.4
	10.70	$(3/2)^-$	-	-	6.9
^{15}O	6.18	$(3/2)^+$	6.18	100	100

The $(p_{1/2})^{-1}$ hole corresponds to the ground state of ^{15}O (or ^{15}N) after neutron (or proton) removal and produces γ-ray emission with hadron de-excitation. Table 4.3 summarizes the excited levels and γ-decay branches associated with the $(p_{3/2})^{-1}$ configuration. In this table, E_{ex} denotes the excitation energy, J^π the spin–parity of the residual nucleus, and E_γ the γ-ray energy. The parameter R_γ is the probability for γ-ray emission from a given excited state, and Br$(X^* \to Y + \gamma)$ is the branching ratio for the transition of the excited nucleus X (^{15}N or ^{15}O) to the ground state of Y, following Refs. [101, 102, 103]. The most prominent lines are a 6.32 MeV γ from ^{15}N and a 6.18 MeV γ from ^{15}O.

The $(s_{1/2})^{-1}$ state also accompanied by γ-ray emission with hadron de-excitation, especially with $E_\gamma \gtrsim 3$ MeV. Table 4.4 lists, for proton knockout, the relevant excited states and their γ-emission probabilities, either directly measured or inferred from Refs. [101, 102, 103]. By contrast, neutron-knockout cases are usually treated analogously to the proton case in standard Monte Carlo (MC) simulations.

States labeled *others* correspond either to configurations with excitation energies above the three principal shells or to components arising from short-range

nucleon–nucleon correlations. In principle, these *others* should be mapped onto a definite shell state. However, no experimental or theoretical constraints exist on their branching ratio or γ-ray emission yet. Assigning them to $p_{3/2}$ is disfavored because $(e, e'p)$ and $(p, 2p)$ measurements show no significant depletion of the $p_{3/2}$ strength [26, 102]. Conversely, mapping them to $(p_{1/2})^{-1}$ would be an extreme choice, as it would imply a large branching fraction into a narrow de-excitation γ-ray line around 6 MeV. Accordingly, in nominal NEUT MC production the *others* category is absorbed into the $(s_{1/2})^{-1}$ state. Figure 4.1 compares NEUT 5.6.3 predictions of neutron multiplicity using the default and NucDeEx [104] de-excitation models. The left panel shows that the two models yield different neutron multiplicities. The right panel shows that these de-excitation models predicts different kinetic energy for the outgoing hadrons, which changes the neutron multiplicity from hadron interactions on ^{16}O. The final observable is the total neutron count, given by the sum of ν-^{16}O–induced and hadron-^{16}O–induced contributions.

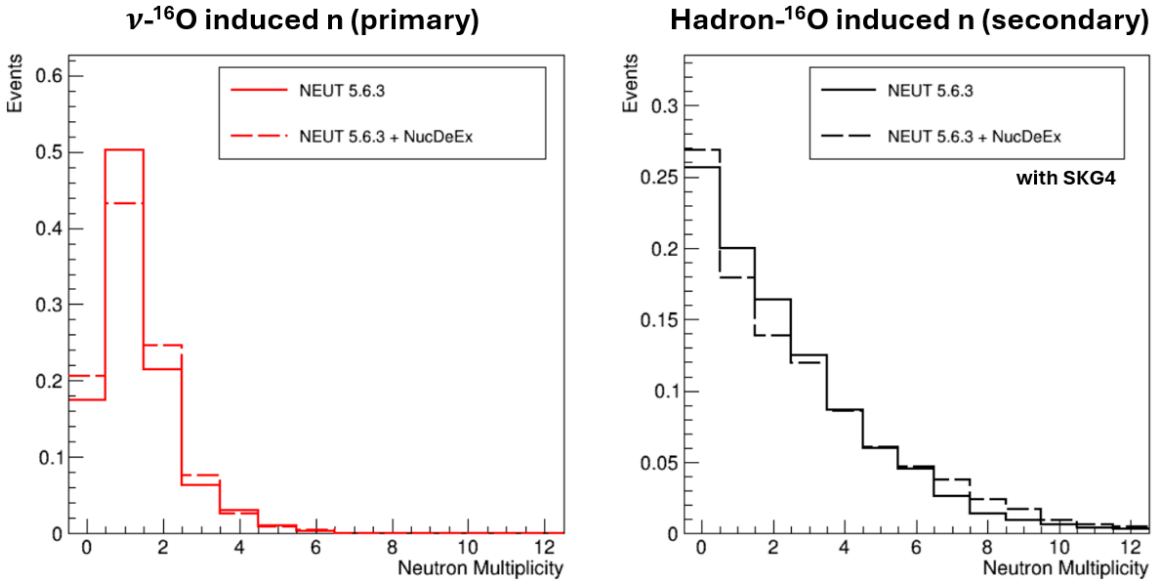

Figure 4.1: MC-truth neutron multiplicities for ν-^{16}O (left) and hadron-^{16}O (right) interactions predicted by NEUT using its de-excitation model options.

4.1.2 Detector simulation

Neutrino interactions products generated with NEUT are tracked through the detector, including secondary interactions in water, Cherenkov photon production/transport, and the PMTs response with run-dependent calibrations. Neutron capture on H and Gd is modeled, which Gd cascades use measured γ spectra. PMT dark noise and environmental radioactivity are overlaid using collected data. Details follow in the following subsections.

Residual nucleus	E_x [MeV]	J^π	E_γ [MeV]	R_y [%]	$Br(^{15}\mathrm{N} \rightarrow Y + \gamma)$ [%]
^{13}C	3.09	$(\frac{1}{2})^+$	3.09	100	3.0
	3.68	$(\frac{3}{2})^+$	3.68	99.3	4.2
	3.85	$(\frac{1}{2})^+$	3.09	1.20	< 0.1
^{12}C	4.44	2^+	4.44	100	5.8
^{14}N	g.s.	2^+	-	-	6.7
	4.92	0^-	4.92	97	5.0
	5.11	2^-	5.11	79.9	< 0.1
	5.69	1^-	3.38	63.9	2.9
			5.69	36.1	1.6
	5.83	3^-	5.11	62.9	0.3
			5.83	21.3	0.1
	6.20	1^+	3.89	76.9	< 0.1
			6.20	23.1	< 0.1
	6.45	3^+	5.11	8.1	0.2
			6.44	70.1	2.0
	7.03	2^+	7.03	98.6	(6.6)
^{14}C	g.s.	2^+			1.1
	6.09	1^-	6.09	100	< 0.1
	6.59	0^+	6.09	98.9	< 0.1
	6.73	3^-	6.09	3.6	< 0.1
			6.73	96.4	0.4
	6.90	0^-	6.09	100	< 0.1
	7.01	2^+	6.09	1.4	< 0.1
			7.01	98.6	(6.6)
	7.34	2^-	6.09	49.0	2.8
			6.73	34.3	2.0
			7.34	16.7	1.0

Table 4.4: Excitation energies and branching ratios for residual nuclei of ^{16}O proton hole $(\mathrm{s}_{1/2})^{-1}$. Table adapted from Ref. [105].

Hadron–nucleus interactions

After the primary particles are generated, their transport and interactions in the detector are simulated with SKDETSIM (GEANT3-based [57]) as the nominal configuration and SKG4 (GEANT4-based [106]) as a reference. As protons and neutrons traverse water, they undergo hadron–nucleus interactions (hereafter secondary interactions, SI). Hadron nucleus interaction and de-excitation of the struck nuclei produces additional γ rays and hadrons.

As in Eq. 4.1, the NCQE primary vertex is generated by NEUT. The hadron produced in Eq. 4.1 then undergoes SI in SKDETSIM or SKG4, which can be schematically written as

$$p + {}^{16}\mathrm{O} \to {}^{A}_{Z}X' + m'_p\, p + m'_n\, n + \gamma' + \text{Others}, \tag{4.2}$$
$$n + {}^{16}\mathrm{O} \to {}^{A}_{Z}X'' + m''_p\, p + m''_n\, n + \gamma'' + \text{Others}. \tag{4.3}$$

Combining the primary NCQE interaction with subsequent SI, the overall reaction observed in the detector can be summarized as

$$\nu + {}^{16}\mathrm{O} \to \nu + {}^{A}_{Z}X + M_p\, p + M_n\, n + \gamma_s + \text{Others}. \tag{4.4}$$

Here M_p and M_n denote the total multiplicities of protons and neutrons. The symbol γ_s collects de-excitation γ rays. Both the primary and secondary processes occur within $O(10)$ ns and therefore difficult to separate them with SK's timing resolution. However, the neutron capture typically occurs at $O(100)\,\mu$s, yielding a delayed signal, which allowing separation of γ rays and neutrons. Although protons are also produced in NCQE events, their momenta are below the Cherenkov threshold in water, and they are therefore invisible in this measurement.

Secondary-interaction modeling in SKDETSIM. Secondary interactions in SKDETSIM is simulated with GCALOR [107]. Neutron transport for $E_n < 20, \mathrm{MeV}$ uses the Monte Carlo Ionization Chamber Analysis Program (MICAP), which employs ENDF/B-V neutron–nucleus scattering cross sections [108]. For $E_n > 20, \mathrm{MeV}$, GCALOR calls the Nucleon Meson Transport Code (NMTC) for nucleons (up to $3.5, \mathrm{GeV}$) and charged pions (up to $2.5, \mathrm{GeV}$). Above these limits, HETC/SCALE is used. Both NMTC and HETC implement the Bertini intranuclear cascade. For $E_n > 10, \mathrm{GeV}$, interactions are handled by FLUKA. The SKDETSIM configuration employing GCALOR serves as the baseline in this study.

Secondary-interaction models within SKG4 Historically, SK and T2K simulations were performed with SKDETSIM, where GCALOR provided the only secondary-

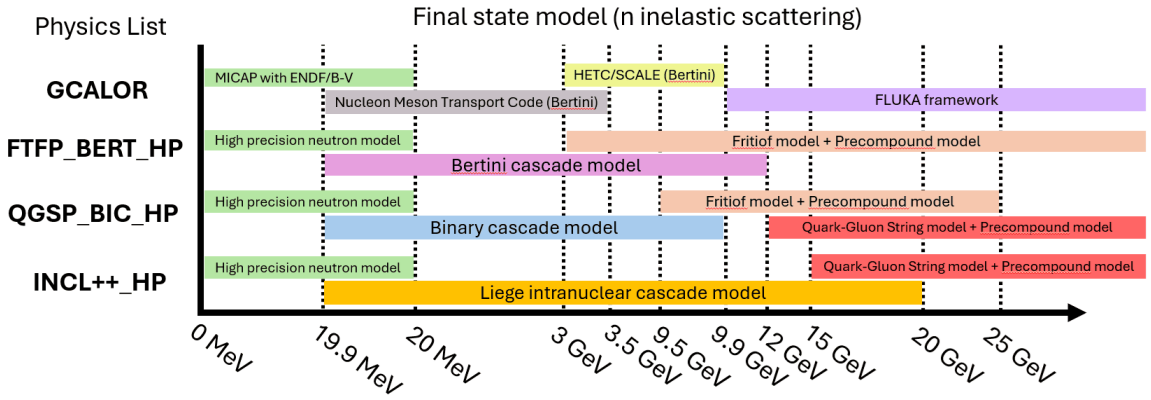

Figure 4.2: Illustration of various "physics lists" used for neutron inelastic scattering in SKDETSIM and SKG4. The horizontal axis indicates the kinetic energy of the incoming neutron. A physics list in GEANT4 defines which interaction models and cross sections are used over different energy ranges. In this study, SKDETSIM (based on GEANT3) employs GCALOR [107], while SKG4 (based on GEANT4) can choose from multiple physics lists [106]. Examples include FTFP_BERT_HP (Fritiof Parton & Precompound + Bertini Cascade + High Precision neutron model), QGSP_BIC_HP (Quark-Gluon String & Precompound + BInary Cascade + High Precision neutron model), and INCL++_HP (Liège INtranuclear Cascade + High Precision neutron model).

interaction model. The latest SKG4 introduces Geant4 physics-list control that permits switching among multiple SI models. In this work, we evaluate three Geant4 physics lists to study SI-model dependence:

- **BERT** (`FTFP_BERT_HP`): the Bertini cascade model [109], long used as a default in Geant4.
- **INCL** (`QGSP_INCLXX_HP`): the Liège intranuclear cascade model [110, 111].
- **BIC** (`QGSP_BIC_HP`): the Binary Cascade model [112], which implements a time-dependent intranuclear cascade.

At the energies relevant to this measurement (∼100 MeV), interactions are modeled with a specific cascade model, typically include an intranuclear cascade (INC) followed by nuclear de-excitation process. After thermalization of hadrons, all three physics lists use the high-precision (HP) neutron-transport treatment to simulate low-energy neutrons. The next section describes how these cascade models operate and compares BERT, INCL, and BIC.

Bertini cascade model The Bertini (BERT) intranuclear cascade treats a nucleus as a dilute gas of nucleons in which hadrons undergo successive two-body collisions. In this picture, particle transport approximates solutions of the Boltzmann equation.

The stochastic collision point x along a straight–line trajectory is sampled as [113]

$$x = -\lambda \ln \xi = -\frac{1}{\rho \sigma_{NN}} \ln \xi = -\frac{A}{\rho\,(Z, \sigma_{Np} + (A - Z), \sigma_{Nn})} \ln \xi, \tag{4.5}$$

where λ is the mean free path, ξ is a uniformly distributed random variable between 0 and 1, ρ is the nucleon density, A and Z are the mass and atomic numbers, and σ_{Np} (σ_{Nn}) denotes the nucleon–proton (nucleon–neutron) cross section.

To specify the nuclear geometry used in BERT, a convenient parameterization [114] for the oxygen nucleus radii is

$$r_i(\alpha_i) = C_2, \log\left(\frac{1 + e^{-C_1/C_2}}{\alpha_i} - 1\right) + C_1, \qquad (A > 11), \tag{4.6}$$

with $C_1 = 3.3836, A^{1/3}$, $C_2 = 1.7234$, and $\alpha_i \in 0.01, , 0.3, , 0.7$.

To date, BERT is most reliable for incident kinetic energies from ~ 200 MeV up to a few GeV. Near 200 MeV, the projectile's de Broglie wavelength is comparable to the inter-nucleon spacing, justifying a cascade description of a discrete nucleon gas. Below this regime, collective nuclear structure effects dominate. The cascade stage ends once secondaries leave the nucleus or are trapped by the mean field, after which de-excitation proceeds without a sharp energy threshold but typically around primary energies of order 200 MeV. Secondaries with energies below the nuclear potential remain confined and populate a pre-equilibrium ensemble described by the Griffin exciton model [115]. The subsequent decay of these exciton states is governed by level-density parameterizations that depend on Z and A, and particle emissions are taken to be isotropic in the exciton rest frame.

Liège intranuclear cascade model The Liège Intranuclear Cascade (INCL) model [110, 111] describes the time-dependent cascade of binary collisions and decays, followed by statistical evaporation, G4PreCompound. Particles propagate on straight-line trajectories in the average nuclear potential until they either collide or leave the potential well. A collision with target nucleon i is scheduled at the point of closest approach d_i if [114]

$$d_i < \sqrt{\frac{\sigma_i}{\pi}}, \tag{4.7}$$

where σ_i is the total two-body cross section at the relevant energy.

The nuclear density is modeled by a Woods–Saxon (Fermi) profile [111]:

$$\rho(r) = \begin{cases} \dfrac{\rho_0}{1 + \exp\left(\dfrac{r - R_0}{a}\right)} & \text{for } r < R_{\max}, \\ 0 & \text{for } r > R_{\max}, \end{cases} \tag{4.8}$$

with

$$R_0 = \left(2.745 \times 10^{-4}\, A + 1.063\right) A^{1/3} \text{ fm}, \tag{4.9}$$

$$a = 0.510 + 1.63 \times 10^{-4}\, A \text{ fm}, \tag{4.10}$$

$$R_{\max} = R_0 + 8a, \tag{4.11}$$

and ρ_0 chosen to normalize the distribution to A. A distinctive aspect of INCL is that the end of the cascade is determined dynamically in time, enabling a smooth handover to the de-excitation stage. The stopping time [114] is parameterized as

$$t = t_0 \left(\frac{A}{208}\right)^{0.16}, \tag{4.12}$$

where t_0 is a model scaling constant and A is the nuclear mass number.

Binary cascade model The Binary Cascade (BIC) model [112] follows the standard intranuclear cascade plus de-excitation scheme, augmented by a realistic nuclear density profile and an explicitly time-dependent cascade. Additionally, it resolves reactions as sequences of binary (two-body) collisions between the projectile (and produced secondaries) and bound nucleons. By combining traditional cascade algorithms with concepts from quantum molecular dynamics (QMD) [116], BIC forms a hybrid semi-classical approach. In the Binary Cascade (BIC) model, participating nucleons are treated as Gaussian wave packets. These packets propagate through space and time, governed by an average nuclear field and subject to stochastic binary collisions. The wave function for a single nucleon is defined as:

$$\phi(x, q_i, p_i, t) = \frac{2}{(L\pi)^{3/4}} \exp\left(-\frac{2}{L}(x - q(t))^2 + i p_i(t) x\right), \tag{4.13}$$

where x and t represent spatial and temporal coordinates, and q_i and p_i denote the centroid position and momentum of the i-th nucleon, respectively. The total many-body state is formed by the product of the single-particle wave packets for all active nucleons and hadrons. This state subsequently serves as the input for the statistical evaporation stage.

Differences of secondary interaction models We compare BERT and INCL across two distinct stages: the intranuclear cascade and the de-excitation process.

- **Intranuclear cascade process**
  In the context of n-^{16}O interactions during the cascade process, INCL and BERT exhibit a distinct and systematic divergence regarding neutron multiplicity, with INCL consistently predicting fewer free neutrons than Bertini. This discrepancy is primarily driven by the "surface coalescence" mechanism in INCL++. This feature was first introduced in INCL version 4.5 to correct the underestimation of light charged particle yields observed in the Bertini model [117]. The mechanism was later refined in INCL version 4.6 [111] (using in this study) to formally describe how an escaping leading nucleon captures neighbors that are close in both spatial and momentum phase space. This allows the formation of composite clusters (such as deuterons, tritons, or α particles) directly during the cascade phase. Consequently, neutrons bound within these clusters are excluded from the free neutron count. Conversely, Bertini focuses on independent nucleon-nucleon collisions that tend to emit individual nucleons. Therefore, a reaction that INCL might model as the emission of a neutron and a deuteron $(n+d)$ is simulated by Bertini as separate free neutrons and protons $(n+p+n)$, resulting in a higher overall free neutron multiplicity for the latter. A comparison of the truth-level neutron multiplicity predictions between the BERT and INCL models, using an identical de-excitation process, is presented in the lower left panel of Figure 4.3.

- **De-excitation process**
  BERT manages the de-excitation process by treating the nucleus as a thermodynamic system. Instead of relying on pre-defined branching ratios, it determines decay pathways through dynamic probability calculations based on entropy maximization. Furthermore, BERT utilizes the Weisskopf-Ewing [118] theory to model the competition between particle emissions, accounting for key physical parameters such as Q-values, Coulomb barriers, and level densities. Kinetic energies within BERT are sampled from a continuous Maxwell spectrum, defined by the relationship $P(E) \sim E \cdot e^{-E/T}$ based on the Dostrovsky approximation [119], which results in smooth distributions that lack fine quantum structures. The mechanism functions as an iterative evaporation loop where the nucleus gradually cools as binding and kinetic energies are subtracted. This cycle repeats until the residual excitation energy is insufficient for further emission, at which point the remaining energy is released as continuum gamma rays. In contrast, G4PreCompound using in INCL, is an experimentally data-driven model that relies on established databases such as ENSDF [120] and G4LEVELGAMMADATA [121] to simulate discrete transitions. By utilizing

table lookups and fixed branching ratios, this model accurately determines neutron multiplicity and reproduces precise energy level structures, providing a high degree of detail that differs from the statistical smoothing seen in the BERT approach. A comparison of the truth-level neutron multiplicity predictions between the de-excitation model, G4Cascade and G4PreCompound, using an identical cascade process, INCL, is presented in the lower right panel of Figure 4.3.

- **Existence neutron measurements on SI models**
  In the quasi-elastic regime, BERT is known to overpredict the products. This leads to observable differences in neutron multiplicities compared to INCL, such as those seen in the proton bombardment of lead isotopes [110]. Supporting this trend, the SK-Gd atmospheric NCQE analysis [43] shows that aligning BERT's modeling with INCL and BIC produces gammas and neutron multiplicities that more closely match those models, identifying SI modeling as a primary source of BERT's discrepancy. Furthermore, atmospheric CCQE studies [122] examining the interface between neutrino generators and detector simulations have reinforced these findings. This study confirms the trend and demonstrates that both the intranuclear cascade and de-excitation processes significantly affect neutron predictions, warranting more detailed investigation.

Neutron capture simulation

The SK–Gd upgrade significantly increases the neutron-capture efficiency by exploiting gadolinium's exceptionally large thermal absorption cross section. The natural isotopic composition and thermal capture cross sections are summarized in Table 4.5. In particular, ^{155}Gd and ^{157}Gd dominate the capture probability. The corresponding capture reactions produce $\sim$8 MeV γ-ray cascades, as illustrated in Eqs. (4.14)–(4.15).

Isotope	Abundance [%]	Cross section [b]
^{152}Gd	0.200	735
^{154}Gd	2.18	85
^{155}Gd	**14.80**	**60900**
^{156}Gd	20.47	1.8
^{157}Gd	**15.65**	**254000**
^{158}Gd	24.84	2.2
^{160}Gd	21.86	1.4

Table 4.5: Natural abundances and thermal neutron-capture cross sections of gadolinium isotopes.

$$n + {}^{155}\mathrm{Gd} \;\rightarrow\; {}^{156}\mathrm{Gd}^{*} \;\rightarrow\; {}^{156}\mathrm{Gd} + \gamma\ (8.536\ \mathrm{MeV}), \tag{4.14}$$

$$n + {}^{157}\mathrm{Gd} \;\rightarrow\; {}^{158}\mathrm{Gd}^{*} \;\rightarrow\; {}^{158}\mathrm{Gd} + \gamma\ (7.937\ \mathrm{MeV}). \tag{4.15}$$

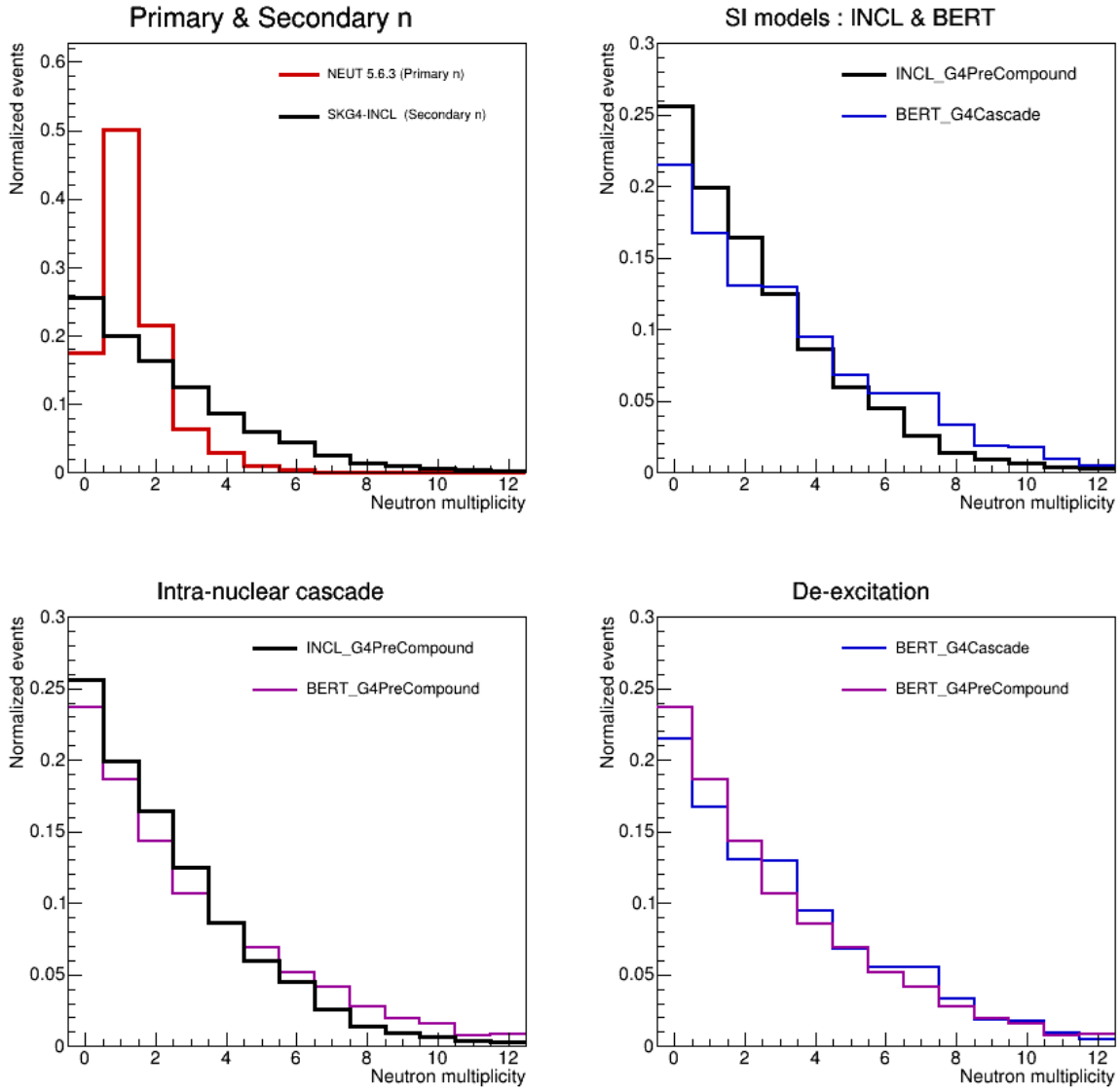

Figure 4.3: MC-truth neutron multiplicity across SI models. Upper Left: NEUT 5.6.3 primary vs. SKG4–INCL secondary. Upper Right: BERT vs. INCL. Lower Left: INCL and BERT with a common de-excitation (G4PreCompound). Lower Right: BERT with G4Cascade (default) vs. G4PreCompound. Consistent with the SK-Gd atmospheric NCQE study [105], using G4PreCompound for BERT brings the multiplicity closer to INCL/BIC, indicating de-excitation modeling drives the original BERT discrepancy.

The γ-ray cascades from ^{155}Gd and ^{157}Gd have been measured with the Accurate Neutron Nucleus Reaction Measurement Instrument (ANNRI) using the pulsed neutron beam from JSNS at the MLF of J–PARC. The resulting high-resolution spectra, recorded with a Ge spectrometer, are encoded in the ANNRI-Gd model [123].

The default GEANT4 treatment of thermal neutron capture on Gd (GLG4sim) uses a photon-evaporation scheme that enforces event-by-event energy conservation but does not reproduce the detailed line structure of individual cascades. In contrast, the ANNRI-Gd model explicitly separates discrete lines from the continuum, yielding more accurate event-level γ-energy distributions.

In this work, ANNRI-Gd is used as the nominal Gd capture model in both SKDETSIM and SKG4. Note that the quoted gadolinium concentration refers to the mass fraction of gadolinium sulfate octahydrate, $Gd_2(SO_4)_3 \cdot 8H_2O$: a Gd concentration of 0.01% corresponds to 0.0263% of the hydrate. SKDETSIM adopts 0.0263%, while SKG4 uses 0.0247%, tuned to match the gadolinium capture fraction measured with an AmBe calibration source.

Table 4.6: Summary of the configuration parameters used in the SKDETSIM and SKG4 simulations.

SKDETSIM Parameter	**Description**	**Value**
SKCNTL-SKGEOMETRY	SK detector geometry	6 (SK-VI)
SKCNTL-GDCONC	The concentration of $Gd_2(SO_4)_3 \cdot 8H_2O$	0.0263 [%]
SKCNTL-GDMODEL	The (Gd(n, γ) cascade gamma-ray model	3 (ANNRI-Gd model)
DS-DARK	The dark rate constant	8.0844 [kHz]
SKG4 Parameter		
Geometry	SK detector geometry	6 (SK-VI)
GdConcentration	The concentration of $Gd_2(SO_4)_3 \cdot 8H_2O$	0.0247 [%]
DarkNoise/Run	The reference run of dark rate	85555
SetPhysicsHadronInelastic	PhysicsList for Secondary interaction	FTFP_BERT_HP QGSP_INCLXX_HP QGSP_BIC_HP

Background noise

Two background components are overlaid in the simulation output with distinct generation schemes and time ranges: (i) PMT dark noise and (ii) environmental radioactivity. PMT dark noise is generated as uncorrelated single–photoelectron hits uniformly in space and time within the prompt PMT window $[-5, +2]$ μs around the trigger. Environmental radioactivity is injected by overlaying randomly selected *off-beam* (beam-off) data in the delayed neutron-tagging window $[2, 500]$ μs. The detailed procedures are as follows.

PMT dark noise All the ID PMTs ($N_{\mathrm{ID}} = 11146$) can each produce accidental hits that may mimic H(n, γ) or Gd(n, γ) signals. Because dark counts are uncorrelated

across tubes, their spatial distribution is uniform, and the multiplicity in a fixed gate follows Poisson statistics. For the neutron capture search timing width, $T = 14$ ns, the expected mean number of dark hits across the ID is

$$\mu_{\text{dark}} \;=\; \langle \text{dark} \rangle \times T \times N_{\text{ID}} \;=\; \frac{8.08 \text{ kHz}}{\text{PMT}} \times 14 \text{ ns} \times 11146 \;\approx\; 1.26, \tag{4.16}$$

where $\langle \text{dark} \rangle \approx 8.08$ kHz/PMT is the average dark rate per ID PMT. Thus, on average, about 1.26 accidental dark hits are expected per 14 ns gate over the full ID.

Environmental radioactivity Natural radioactivity from detector materials (PMTs, PMT covers, black Tyvek) and the surrounding rock can generate clusters of hits that often point to vertices near the ID wall and can occasionally resemble neutron-capture signals. Because first-principles modeling of these backgrounds is difficult and condition dependent, we adopt a data-overlay approach: data recorded during T2K beam-off periods are merged into the neutron-tagging window, $t \in [2, 500]$ μs after the trigger. During T2K Run 11, PMT gain, and water transparency were stable. Accordingly, SK Run #85555 is used as the nominal reference for both SKG4 and SKDETSIM.

Monte Carlo sample normalization

Monte Carlo (MC) events are generated with NEUT and NuWro and then propagated through the detector with SKDETSIM and SKG4. Each run simulates a single neutrino flavor with 100 events. Repeating this procedure 1000 times per flavor for ν_e, $\bar{\nu}_e$, ν_μ, and $\bar{\nu}_\mu$ yields a total of 4×10^5 events (i.e., 10^5 per flavor).

Event-by-event normalization is applied so that the MC corresponds to the T2K Run 11 exposure in protons on target (POT). The weight assigned to an event of neutrino energy E_ν is

$$w(E_\nu) \;=\; \frac{N_T \;\cdot N_{\text{POT}}}{N_{\text{MC}}} \int \phi(E_\nu)\, \sigma(E_\nu)\, \mathrm{d}E_\nu \;\times\; \phi_{\text{tune}}(E_\nu), \tag{4.17}$$

where $N_T = 35.38 \times 10^{32}$ is the number of target nucleons in SK, $N_{\text{POT}} = 1.76 \times 10^{20}$ is the total POT in T2K Run 11, $\phi(E_\nu)$ is the neutrino flux, $\sigma(E_\nu)$ is the $\nu -^{16} O$ interaction cross section, and N_{MC} is the number of generated events for a given flavor (here $N_{\text{MC}} = 10^5$). The factor $\phi_{\text{tune}}(E_\nu)$ applies the T2K flux-tuning correction (release 21bv2), implemented using the `enu_sk_tuned21b_(flavor)` histogram in `sk_tuned21bv2_13anom_run11_numode_fine.root` (used throughout the following analyses).

Accounting for oscillations is necessary when evaluating the flux in this study. The ν–^{16}O NCQE signal is flavor–independent and thus unaffected by oscillations, but

a small charged–current (CC) contamination exists in the MC sample. We therefore apply oscillation weights to CC events as

$$\begin{aligned} w_{cc}(E_\nu) &= P_{\nu_\mu\to\nu_\mu}(E_\nu) + P_{\nu_\mu\to\nu_e}(E_\nu)\,\frac{\sigma_{\nu_e\mathrm{CC}}(E_\nu)}{\sigma_{\nu_\mu\mathrm{CC}}(E_\nu)} \\ &\approx P_{\nu_\mu\to\nu_\mu}(E_\nu) + P_{\nu_\mu\to\nu_e}(E_\nu) \\ &= 1 - \cos^4\theta_{13}\,\sin^2 2\theta_{23}\,\sin^2\left(1.267\,\frac{\Delta m^2_{32}[\mathrm{eV}^2]\cdot L[\mathrm{km}]}{E_\nu[\mathrm{GeV}]}\right), \end{aligned} \tag{4.18}$$

Oscillation parameter	**Value**
$\sin^2\theta_{13}$	0.0211 ± 0.0008
$\sin^2\theta_{23}$	$0.541^{+0.027}_{-0.037}$
$\lvert\Delta m^2_{32}\rvert$	$(2.469^{+0.073}_{-0.071}) \times 10^{-3}$ eV^2

Table 4.7: Oscillation parameters used in Eq. 4.18, with the reactor constraint [124].

In the weights we set $\sigma_{\nu_e\mathrm{CC}}/\sigma_{\nu_\mu\mathrm{CC}} = 1$ (and likewise for antineutrinos), neglecting small $e^\pm$–$\mu^\pm$ kinematic differences.

4.2 Event reconstruction

In the data, only PMT hit charge and timing are recorded. We therefore reconstruct derived observables such as the event vertex, direction, energy, and Cherenkov ring features, and use them to suppress backgrounds.

4.2.1 BONSAI fitter

Neutrino events in both data and MC are reconstructed with BONSAI(Branch Optimization Navigating Successive Annealing Iterations) [125]. Using PMT hit times and charges within a 1.3 μs window, BONSAI estimates the event vertex and direction.

Vertex reconstruction We estimate the interaction vertex with a maximum likelihood fit to PMT hit times. At energies around 10 MeV, electrons and positrons travel approximately 10 cm in water. As this distance is small relative to the detector scale, the source is treated as a point.

For each hit PMT i, the time residual associated with a trial vertex x in the BONSAI grid is

$$\Delta t_i = t_i - t_{\mathrm{tof}}(x) - t_0, \tag{4.19}$$

where t_i is the PMT hit time, $t_{\text{tof}}(x)$ is the photon time of flight from the trial vertex x to PMT i, and t_0 is the fitted interaction time. The likelihood is

$$\mathcal{L}(x, t_0) = \sum_{i=1}^{N_{\text{hit}}} \ln P(\Delta t_i), \tag{4.20}$$

where P is the probability density of the time residuals, and PMT dark noise is modeled as uniform in time. The BONSAI fit maximizes $\mathcal{L}$ over x and t_0 to obtain the best fit vertex and interaction time.

The vertex quality metric $g_V(t, x)$ is defined as

$$g_V(t,x) = \frac{\sum_{i\in\text{PMT hits}} w_i \exp\left[-\left(\frac{t-t_0}{5}\right)^2\right]}{\sum_{i\in\text{PMT hits}} w_i}, \qquad w_i \equiv \exp\left[-\left(\frac{t-t_0}{60}\right)^2\right]. \tag{4.21}$$

Here t and x are the fit time and position, and in this expression t_0 denotes the light propagation time from the trial vertex x to PMT i. The weights w_i use a time resolution of 60 ns. The metric ranges from 0 to 1, and values close to 1 indicate better vertices.

Direction reconstruction After fixing the vertex, we determine the track direction $\hat{d}$ with a maximum likelihood fit that uses PMT hit angles inside a ± 20 ns time window:

$$\mathcal{L}(\hat{d}) = \sum_{i=1}^{N_{20}} \ln\left[f(\cos\theta_{\text{dir},i};\, E)\,\frac{\cos\theta_i}{a(\theta_i)}\right]. \tag{4.22}$$

Here N_{20} is the number of hits in the window. The angle $\theta_{\text{dir},i}$ is between the trial direction $\hat{d}$ and the line from the reconstructed vertex to PMT i. The angle θ_i is the PMT viewing angle relative to the vertex, and $a(\theta_i)$ corrects for PMT angular acceptance. The function $f(\cos\theta_{\text{dir},i};\, E)$ refers to the expected distribution of $\theta_{\text{dir},i}$ dependent on the particle energy E due to multi-scattering. The best direction is the $\hat{d}$ that maximizes $\mathcal{L}(\hat{d})$.

The directional quality is defined as

$$g_A = \frac{\max_i\left[\angle_{\text{uniform}}(i) - \angle_{\text{data}}(i)\right] - \min_i\left[\angle_{\text{uniform}}(i) - \angle_{\text{data}}(i)\right]}{2\pi}. \tag{4.23}$$

Here $\angle_{\text{uniform}}(i)$ is the azimuth of the ith hit PMT around the particle direction assuming hits lie uniformly on a Cherenkov cone, and $\angle_{\text{data}}(i)$ is the measured azimuth. Good directions have g_A near 0, indicating that the reconstructed result is almost identical to the LINAC calibration data.

Common parameters in SK Besides the vertex (x, y, z) and the event timing, geometric observables defined after vertex and direction reconstruction, are

- *dwall*: the closest distance from the vertex to the ID wall,
- *effwall*: the distance from the vertex to the ID wall along the reconstructed track,
- *OvaQ*: the difference of squared quality metrics, $g_V^2 - g_A^2$.

4.2.2 Energy Reconstruction

The visible energy (E_{vis}) is obtained from the effective number of PMT hits (N_{eff}), which is built from the hits within a 50 ns window after time-of-flight correction (N_{50}). The conversion between N_{eff} and N_{50} is defined as follows:

$$N_{eff} = \sum_{i=1}^{N_{50}} (X_i + \epsilon_{tail} - \epsilon_{dark}^i) \times \frac{N_{all}}{N_{normal}} \times \frac{R_{cover}}{S(\theta_i, \phi_i)} \times \exp\left(\frac{r_i}{\lambda_{run}}\right) \times \frac{1}{QE_i}. \quad (4.24)$$

We note that the only difference between N_{eff} using in Eq. 3.11, the water transparency measurement, and here is the inclusion of the water transparency term, "r_i/λ_{run}" or not. We explained these parameters more detailed here as follows:

- X_i : The corrected gain occupancy for a PMT, which adjusts for multiple photoelectron impacts. Here, X_i stands for the proportion of hit PMTs to the total in a 3x3 grid surrounding the i-th PMT, which is established as follows:

$$X_i = \begin{cases} \log\left(\frac{1}{1-f_i}\right) & (f_i < 1) \\ 3.0 & (f_i = 1) \end{cases} \quad (4.25)$$

- ϵ_{tail} : The late hits correction. Cherenkov photons that undergo scattering and reflection may reach the PMTs too late, missing the 50 ns detection window.
- ϵ_{dark} : The dark noise correction. The dark noise is determined from off-time window hits, applying a per-run and per-PMT correction.
- $N_{\text{all}}/N_{\text{normal}}$: The dead PMTs correction. The status of PMTs may fluctuate over time, leading to instances where some PMTs may not function as intended. This correction is addressed using a ratio, with N_{all} denoting the total number of PMTs and N_{normal} indicating the number of PMTs that are functioning properly.

- $R_{\text{cover}}/S(\theta_i, \phi_i)$: The correction for the PMT coverage. The effective area of the photocathode is denoted as $R_{\text{cover}}/S(\theta_i, \phi_i)$, where θ_i is the incident angle and ϕ_i is the azimuth angle. The acceptance of the PMT is adjusted by the factor R_{cover}.

- r_i/λ_{run}: The correction for water transparency. The decrease in photon intensity due to their passage through water accounts for events occurring at a distance r_i from the vertex to the r_i-th PMT.

- $1/QE_i$: The correction for the PMT quantum efficiency. A quantum efficiency table is measured by the Ni-Cf used in the absolute gain calibration.

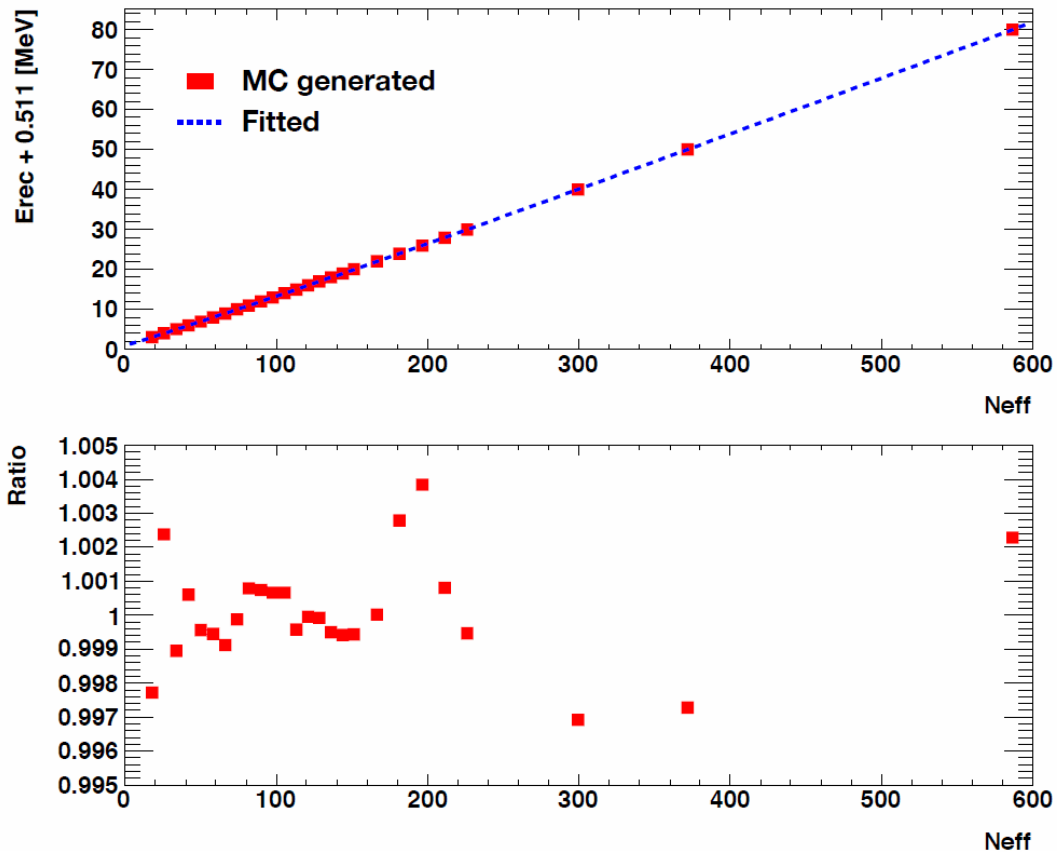

Figure 4.4: The relationship between the effective hits N_{eff} and the reconstructed visible energy for electrons simulated in Monte Carlo analysis, along with the result of a linear fitting (top), and the ratio of the MC to the fitted values (bottom). This Figure is taken Ref. [4].

The effective PMT hits could be almost linearly transformed to the reconstructed visible energy as shown in Figure 4.4.

4.2.3 Cherenkov angle reconstruction

For each event, we estimate the Cherenkov angle θ_C, which is a topology sensitive variable used to distinguish cherenkov rings from electrons, muons, pions, and multiple γ rays (see Figure 4.5 for examples). The estimate uses the geometry of PMT hits recorded within 15 ns of the reconstructed vertex time. Because three points determine a circle, we consider all triplets of in-time PMT hits and, for each triplet, compute the opening angle θ on the Cherenkov cone using only the pairwise lengths a, b, and c between the three PMTs. By the law of sines and the cosine theorem, the circumradius R satisfy

$$\frac{a}{\sin A} = 2R, \qquad R = \frac{a}{2\sqrt{1 - \left(\dfrac{b^2 + c^2 - a^2}{2bc}\right)^2}}, \tag{4.26}$$

and the angle can be expressed purely in terms of side lengths as

$$\sin\theta = \frac{abc}{\sqrt{2(a^2b^2 + b^2c^2 + c^2a^2) - (a^4 + b^4 + c^4)}}. \tag{4.27}$$

Allθ values are histogrammed with 0.9° bin width. We slide a 7-bin window over the histogram, find the window with the largest total counts, and define θ_C as the center of that window. (See the blue lines in Figure 4.5) Electrons and single γ ray typically yield $\theta_C \sim 42°$. Multiple γ rays tend to give larger angles, enabling effective particle identification.

4.2.4 Multiple Scattering Goodness

The multiple scattering goodness (MSG) measures how close the Cherenkov light pattern is to a single ring, helping to separate signal events from NCQE and multi-γ backgrounds beyond Cherenkov angle cut. From PMT hits within a 20 ns window and the reconstructed vertex, we build candidate 42° Cherenkov cones consistent with the hit geometry. Operationally, we pair PMTs, draw 42° cones around each, and use cone–cone intersections to define directions. Each candidate cone yields a unit axis vector $\vec{u}_i$. We then cluster these directions by grouping vectors within 50° of a seed direction. Let $C_{\max}$ be the cluster whose vector sum has the largest magnitude, and let N_{cones} be the total number of candidate cones. The MSG is

$$\text{MSG} = \frac{1}{N_{\text{cones}}} \left| \sum_{i \in C_{\max}} \vec{u}_i \right|. \tag{4.28}$$

Large MSG values (empirically near 0.5 for well-aligned light) indicate a co-

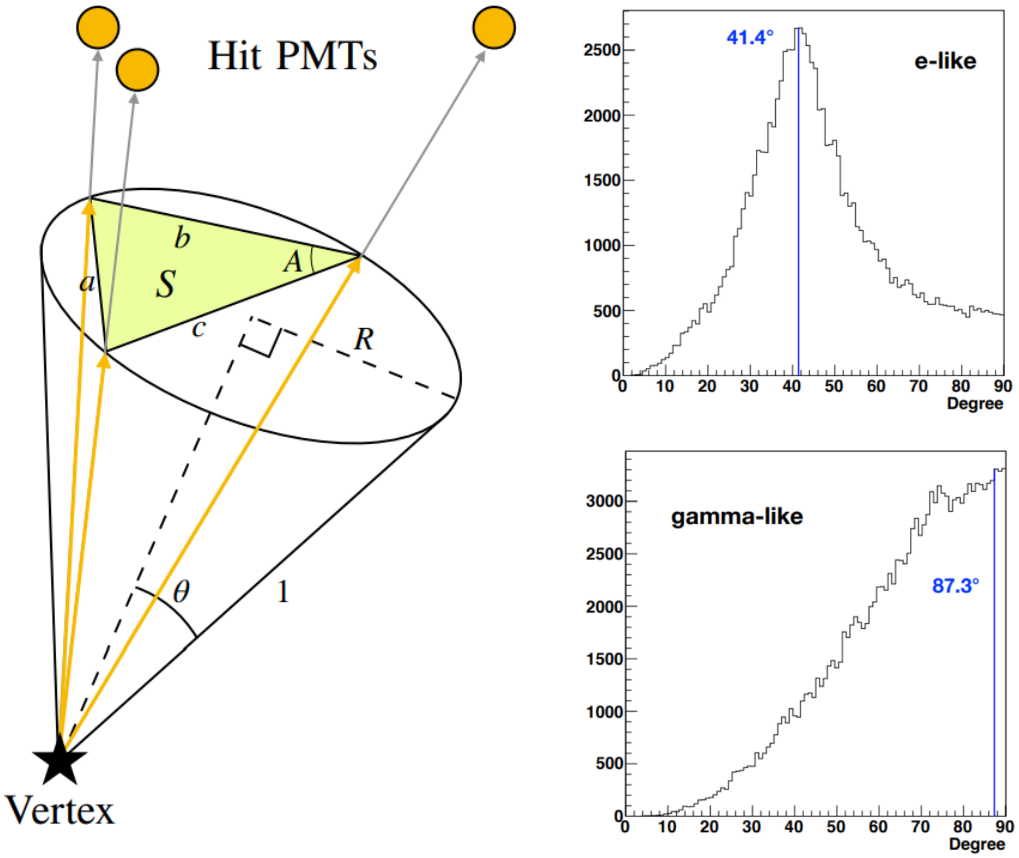

Figure 4.5: Schematic view of Cherenkov angle definitation (Left). Distributions of opening angles from all PMT triplets for electron events (upper right), and events with multiple γ rays (lower right). Blue lines mark the reconstructed Cherenkov angles. Figure adapted from Ref. [4].

herent, single preferred direction as expected for single $e^{\pm}$ or single-γ events. Smaller values point to multiple preferred directions from multiple Coulomb scattering or multi-γ topologies.

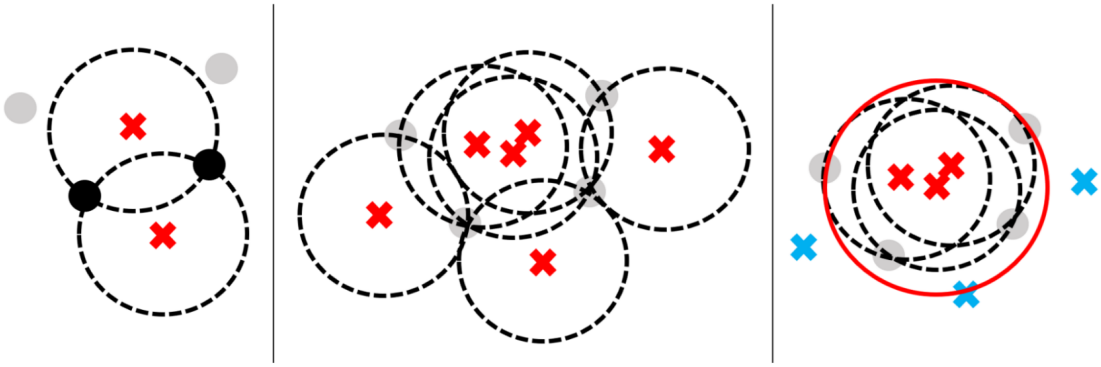

Figure 4.6: Steps to compute MSG value. **Left:** Start with one pair of PMT hits (black dots). From the reconstructed prompt vertex, draw any 42° cones whose edges (black, dashed) pass through both hits. The cone axis is marked by the red cross. **Middle:** Repeat for every PMT pair. Each pair yields zero, one, or two candidate cones. **Right:** Identify the largest cluster of candidate cones whose axes fall within 50° of a single direction (red, solid). Clustering is iterated to maximize the magnitude of the summed axis vectors in the largest cluster. Figure taken from Ref. [36]

4.2.5 Neutron tagging algorithm

This study uses the `NTag` algorithm, developed in SK [122], to identify neutron-capture signals. `NTag` operates in two stages: (i) a pre-selection that finds clusters of PMT hits consistent in time with a neutron capture, and (ii) a neural-network classifier that separates neutron signals from background noise. The configuration used for neutron tagging is described below.

Pre-selection

The pre-selection stage finds delayed, time-clustered PMT hits that are consistent with neutron capture. We scan from 3 to 535 μs after the prompt signal using a sliding 14 ns window over the TOF-corrected time ($t - t_{\mathrm{TOF}}$). For each window, we count the hits and select local maxima as cluster candidates (Figure 4.7).

The 14 ns window is chosen from the capture-time resolution and the signal-to-noise metric $S/\sqrt{S+B}$. A window is accepted as a hit cluster when its hit count satisfies

$$\texttt{NHITSTH} \leq N_{\mathrm{hits}} < \texttt{NHITSMX}. \tag{4.29}$$

To avoid double counting, a subsequent peak is counted as an additional

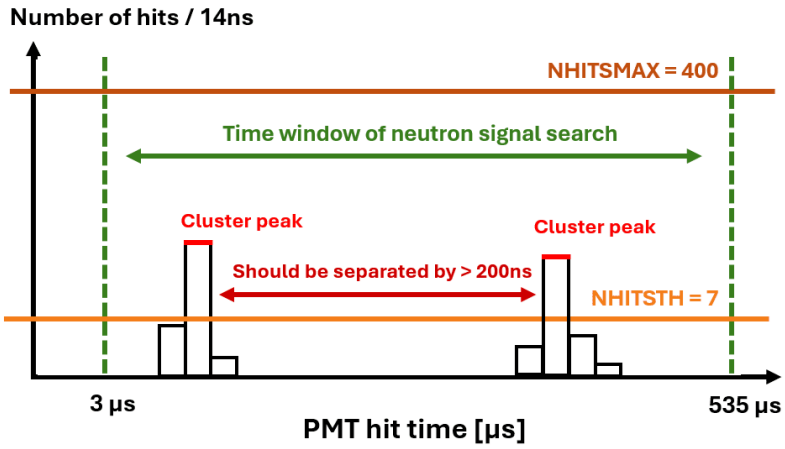

Figure 4.7: Concept of the pre-selection.

neutron candidate only if it occurs at least 200 ns after the previous peak and its N_{200} (hits within 200 ns of the peak) also lies in [NHITSTH, N200MX]. Windows with excessive hits ($N_{\text{hits}} \geq$ NHITSTMX) are rejected as likely high-energy, non-neutron event. The threshold NHITSTH is set to 7 to maximize tagging efficiency after the neural-network stage. Table 4.8 summarizes the parameter values used in this study. The signal passed pre-selection is termed as neutron candidates.

Table 4.8: Summary of parameter values for pre-selection.

Parameter Name	Description	Value
TWIDTH	Search window width	14 ns
T0TH	Lower threshold for the timing range of neutron search	3 μs
T0MX	Upper threshold for the timing range of neutron search	535 μs
NHITSTH	Lower threshold of the number of hits within the time window	7
NHITSMX	Upper threshold of the number of hits within the time window	400
N200MX	Upper threshold of N200	200
TMINPEAKSEP	Minimum time difference of neutron candidates	200 ns

Neural Network Classification

After pre-selection, the features of each neutron candidate cluster are fed into a neural network (NN) that outputs an *n-likelihood* in $[0, 1]$. Candidates with n-likelihood above a chosen threshold are tagged as neutron capture signals. The NN uses the following feature set.

- `NHits`
  Number of PMT hits within a 14 ns window centered on the candidate time. Because Gd(n,γ) releases higher γ-ray energy than H(n,γ), Gd captures tend to yield larger `NHits` than H captures or noise.

- `NResHits`
  Residual hits in a wider window, defined as `N200` − `NHits`, where `N200` counts

hits in $[-100, +100]$ ns around the candidate. This complements `NHits` by capturing late and early light.

- `TRMS`
  Root-mean-square of hit times within the 14 ns window. True neutron capture signals produce a compact time profile, while random noise is more spread out, giving a larger `TRMS`.

- `DWall`
  Shortest distance from the reconstructed vertex to the SK ID wall. Noise from dark counts and radon often reconstructs near PMTs, so `DWall` tends to be smaller for noise and larger for neutron capture signal, which is more uniformly distributed.

- `DWallMeanDir`
  Shortest distance from the vertex to the wall along the average Cherenkov-ring direction. Neutron-capture light exhibits directional coherence, whereas noise lacks a preferred direction and typically yields larger `DWallMeanDir`.

- `OpeningAngleStdev`
  Standard deviation of the reconstructed Cherenkov opening-angle distribution (see Figure 4.5). Noise appears at arbitrary positions and produces a broader spread than neutron signals.

- `Beta1-5` (β_l)
  Sphericity-like moments built from pairwise PMT-hit angles,

$$\beta_l \equiv \frac{2}{\texttt{NHits}\,(\texttt{NHits}-1)} \sum_{i \neq j} P_l(\cos\theta_{ij})\,, \quad l = 1, 2, 3, 4, 5, \tag{4.30}$$

  where P_l is the Legendre polynomial of degree l, and θ_{ij} is the angle between hits i and j as viewed from the reconstructed capture vertex. Isotropic patterns give $\beta_l \approx 0$. Neutron patterns are closer to isotropic than structured noise, so $|\beta_l|$ tends to be smaller for neutron capture signal.

- `BurstRatio`
  Fraction of hits that occur in short bursts characteristic of PMT-glass scintillation with a ~ 10 μs time constant:

$$r_{\text{burst}} = \frac{\#\{\text{PMT hit pairs with } \Delta t < 10\ \mu\text{s}\}}{\#\{\text{all candidate hits}\}}. \tag{4.31}$$

  Large `BurstRatio` indicates a higher probability of noise.

- `FitGoodness`

Vertex-fit quality,

$$G(t,x) = \frac{\sum_i w_i \exp\left[-\left(\frac{t_i - t_0}{5}\right)^2\right]}{\sum_i w_i}, \quad w_i = \exp\left[-\left(\frac{t_i - t_0}{60}\right)^2\right], \tag{4.32}$$

where t_i is the hit time, x is the fitted position, and t_0 is the expected photon time of flight from x to PMT i. Values near 1 indicate a well-reconstructed vertex. This is the same goodness used in the BONSAI fitter.

- `DarkLikelihood`
  Likelihood that the cluster arises from PMT dark noise,

$$L_{\text{dark}} = \prod_i \frac{r_i^{\text{dark}}}{\bar{r}_{\text{dark}}}, \tag{4.33}$$

with r_i^{dark} the dark rate of PMT i and $\bar{r}_{\text{dark}}$ the detector-average dark rate. Values near 1 suggest dark-noise–like activity.

Feature distributions before and after NN classification are shown in Figs. 4.8 and 4.9. In this work, candidates with n-likelihood > 0.7 are defined as neutron capture signal.

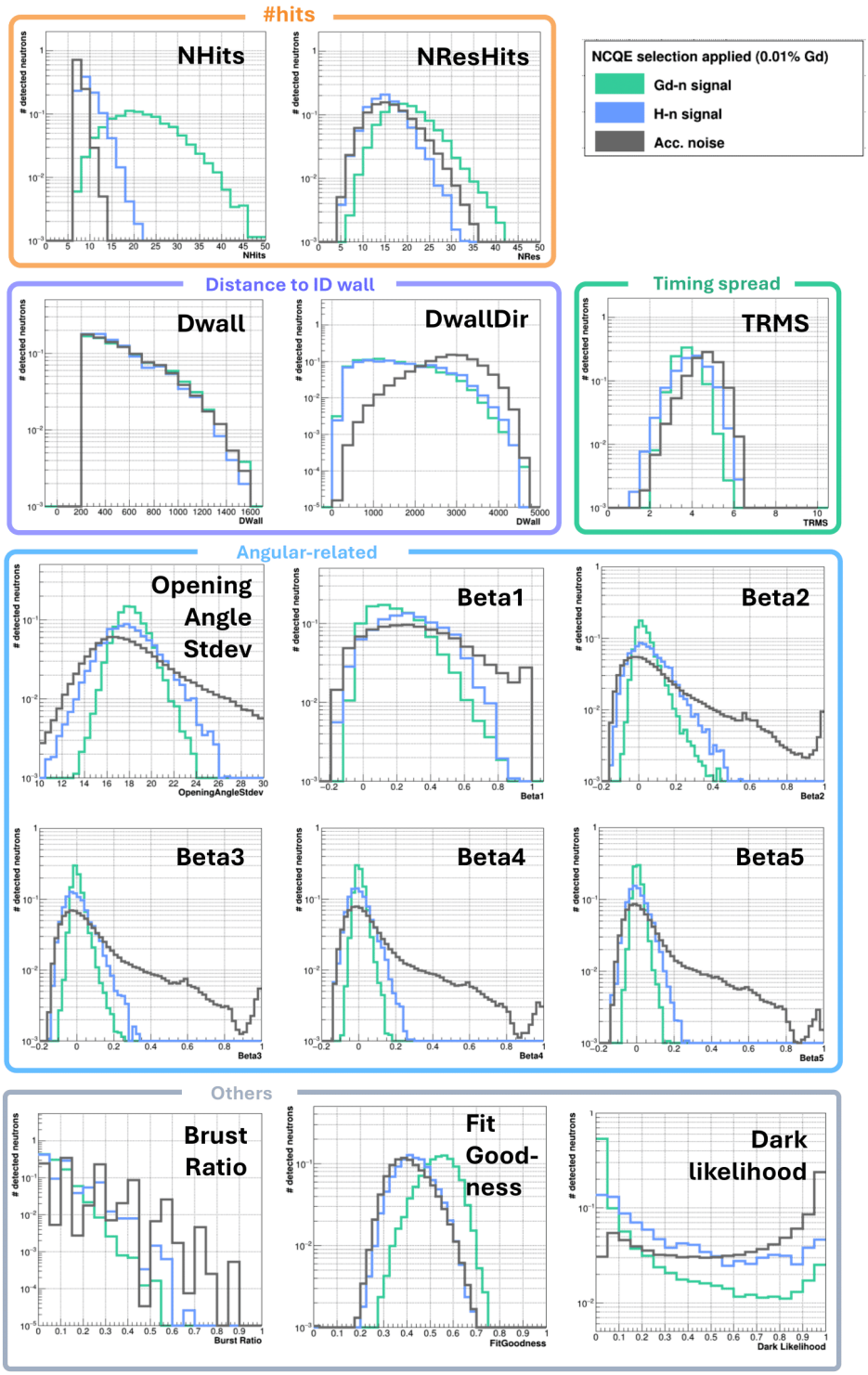

Figure 4.8: Normalized 14 feature variables before neural network classification. Green and blue lines are Gd(n,γ) and H(n,γ) signal, respectively. The gray line is the mis-tagged neutrons from the background noise.

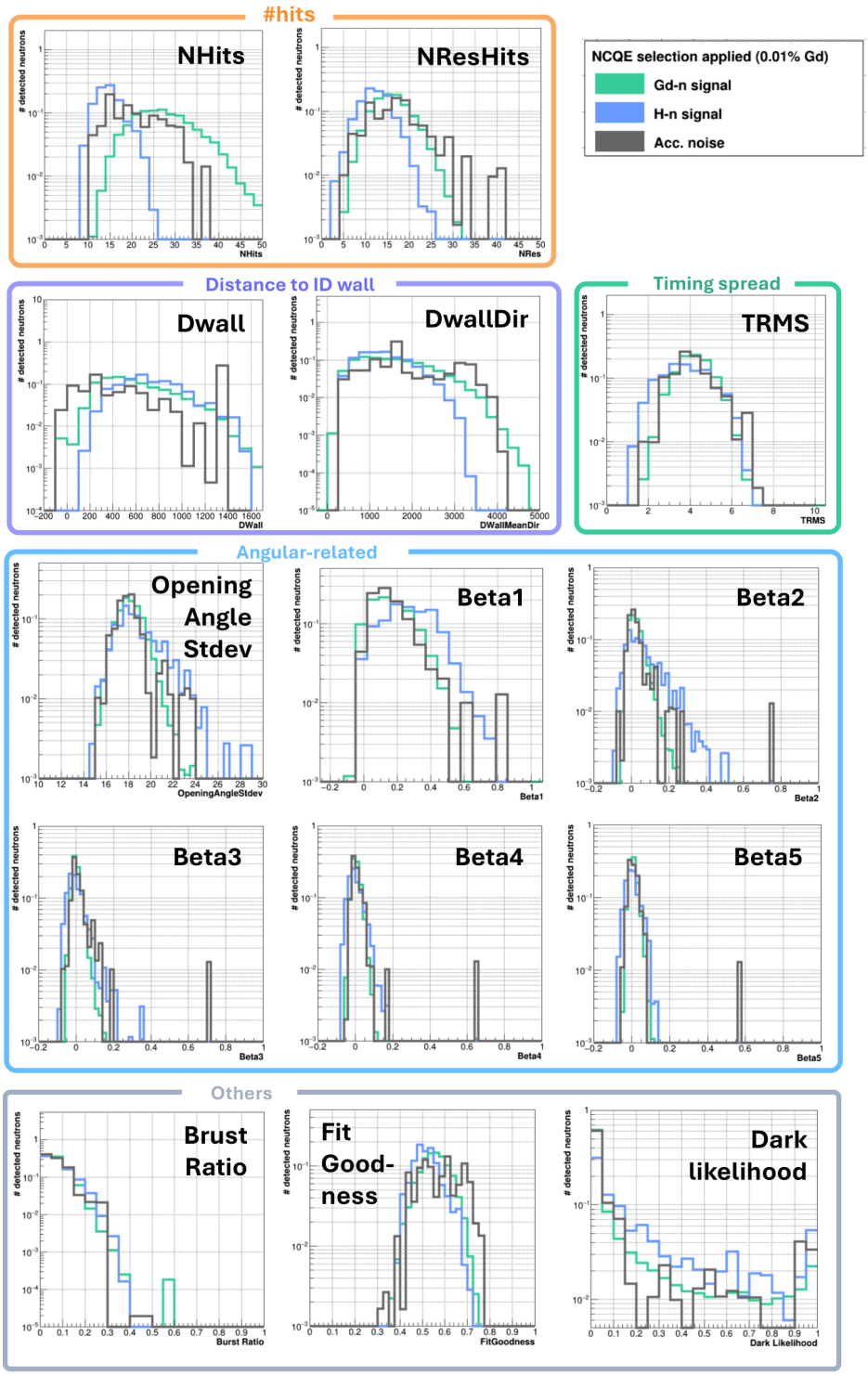

Figure 4.9: Normalized 14 feature variables after neural network classification. Green and blue lines are Gd(n,γ) and H(n,γ) signal, respectively. The gray line is the mis-tagged neutrons from the background noise.

Chapter 5

Event Analysis

NCQE events in SK have two observable components: a prompt signal from oxygen de-excitation γ rays and a delayed signal from neutron capture. The prompt selection uses observables from the BONSAI reconstruction, and the delayed selection employs `NTag`. This chapter first details the selection methods for the prompt and delayed signals, then presents results for the T2K Run 11 data alongside the corresponding MC samples.

5.1 prompt signal selection

The prompt-signal selection suppresses backgrounds and non-NCQE interactions. In SK, T2K-beam neutrinos can produce several ^{16}O interaction channels beyond NCQE, and accidental noise near the detector wall introduces additional noise that must be removed. We follow the T2K 2019 NCQE analysis [50], which defines seven selection cuts to isolate ν–^{16}O NCQE events. The Good-Spill, Timing, and decay-e cuts are applied only to T2K data, whereas the Visible-Energy, Fiducial-Volume, Ambient low-energy background, and CC-interaction cuts are applied to both the T2K data set and the MC sample.

1. **Good–spill selection**
   Beam spills are recorded only when the T2K and SK GNSS clocks are synchronized and the SK detector is fully operational, with continuous quality monitoring of the PMTs and the data-acquisition (DAQ) system. This analysis uses the 1st round good-spill selection from T2K Run 11.

2. **Timing cut**
   Each event's relative time Δt_0 with respect to the leading edge of the beam spill is defined after correcting for the neutrino time of flight (TOF) with reconstructed vertex and hardware offsets. For prompt signal selection, the trigger

time must fall within ±100 ns of the nominal center of a beam bunch,

$$t_i = \Delta t_0 + i \times 581.0 \text{ ns} \quad (i = 1, 2, \ldots, 8), \tag{5.1}$$

which defines the on-timing window in T2K data. Beam-unrelated (off-timing) events are selected when trigger time falls within [-500, -5] μs

Ideally, $\Delta t_0 = 0$ for every run. In practice, GNSS conditions introduce run-dependent time shifts, so each T2K run is assigned a specific $\Delta t_0 = 0$ relative to Runs 1–3. Table 5.1 summarizes these offsets.

	Time Shift w.r.t. Runs 1∼3 (ns)	**Time w.r.t previous Run (ns)**
Runs 1∼3	0.0	-
Run 4	-32.3	-32.3
Run 5	-253.0	-220.7
Run 6	-166.8	+86.2
Run 7	-212.8	-46.0
Run 8	-180.7	+32.1
Run 9	-179.4	+1.3
Run 10	-138.6	+40.8
Run 11	-3.9	+134.6

Table 5.1: Run-by-run timing shifts relative to Runs 1–3 and to the preceding run.

We scanned Δt_0 and found that $\Delta t_0 = -190.0$ ns produces a residual-time distribution well described by a Gaussian centered at 0 ns with exact 30 NCQE events. Figure 5.1 shows residual-time distributions for several Δt_0 settings, and Figure 5.2 presents the Gaussian-fit results from the scan, indicating an optimal range of 189.5–190.5 ns. We thus adopt $\Delta t_0 = -190.0$ ns for this study.

A plausible explanation for this shift is an additional beam-synchronization correction. For example, the RF-synchronized correction is 4177 ns in Run 10 and 4368 ns in Run 11, a difference of about 190 ns, consistent with the scan. Further checks are needed to identify the exact source of the offset.

3. **Decay-e cut**
   To reject electrons from cosmic-muon decay, we search for pre-activity before the triggered candidate. A 30 ns window is slid across the interval 0.2–20 μs prior to the candidate time. For each window we count the number of hit PMTs, N_{30}. Any event with a window satisfying $N_{30} > 22$ is rejected. This pre-activity veto is applied only to the T2K data. A post-trigger veto was also checked and found to have negligible effect, so it is not used in this study [50].

4. **Visible-energy cut**
   We require the reconstructed visible energy to satisfy $E_{\text{rec}} \in [3.49, 29.49]$ MeV. The lower edge (3.49 MeV) reflects the detector's effective threshold for low-

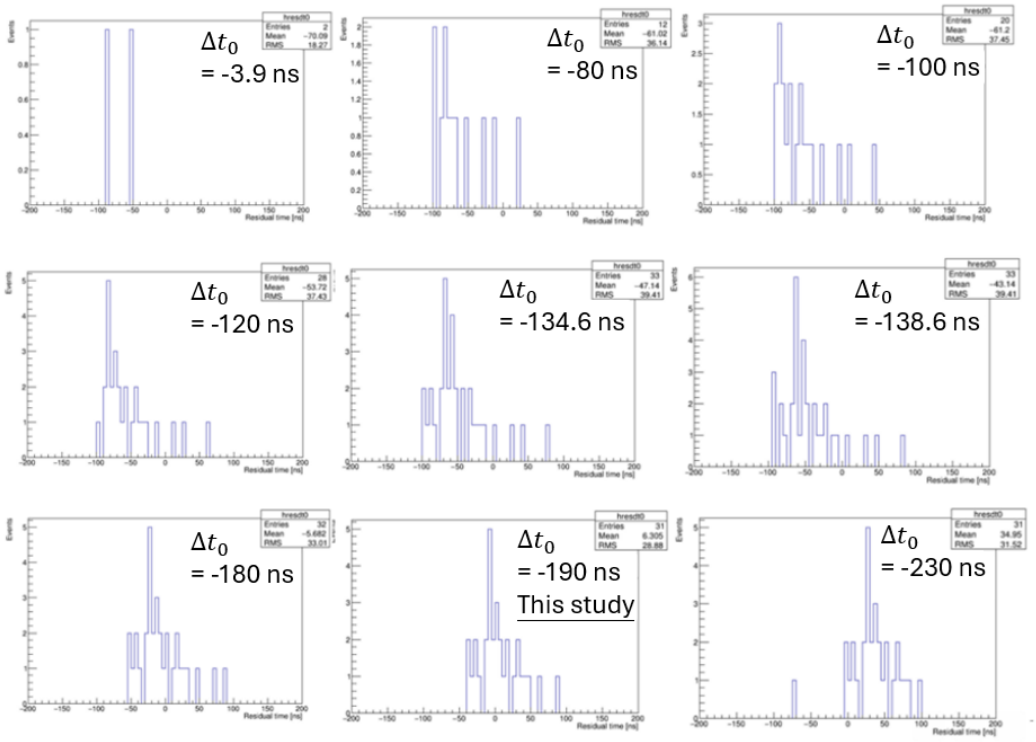

Figure 5.1: Residual-time distributions for various Δt_0 settings in the Run 11 NCQE study.

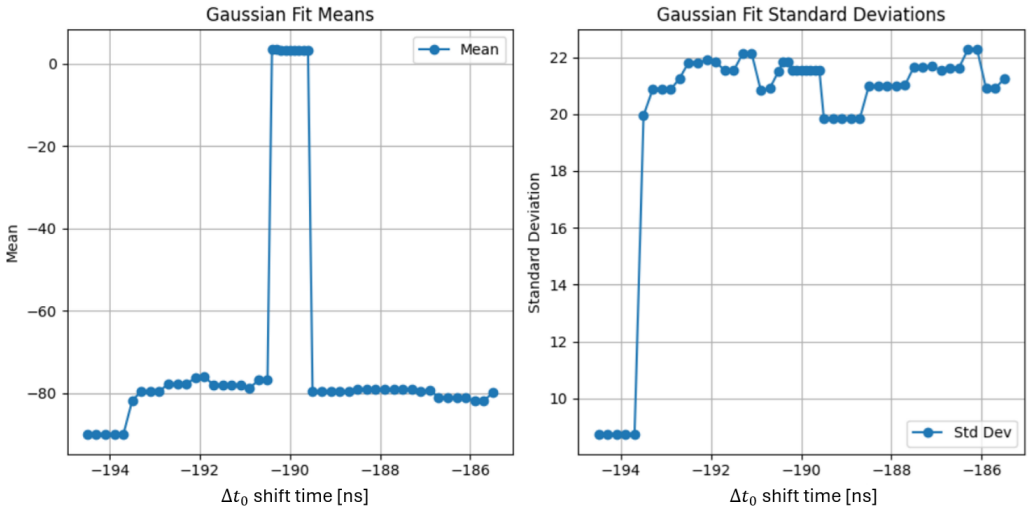

Figure 5.2: Gaussian-fit results from scanning Δt_0 in the Run 11 NCQE study, showing an optimal range near 190 ns.

energy neutrino events. The upper edge (29.49 MeV) suppresses decay-electron backgrounds from ν_μ CC interactions, which increasingly dominate above this range and would overshadow NCQE events.

5. **Fiducial-volume cut**
   To suppress radioactivity near the detector walls, we define the fiducial volume by requiring the reconstructed vertex to lie at least 200 cm from the wall: $d_{\text{wall}} > 200$ cm. Events outside this region are rejected.

6. **Ambient low-energy background cut**
   The fiducial-volume requirement is a coarse selection, especially for the lowest energy bins, which need finer tuning. To further suppress residual backgrounds below $E_{\text{rec}} = 5.99$ MeV, we optimize additional thresholds on the BONSAI variables `dwall`, `effwall`, and `OvaQ`. The visible-energy range from 3.49 to 5.99 MeV is divided into five bins: $[3.49, 3.99]$, $[3.99, 4.49]$, $[4.49, 4.99]$, $[4.99, 5.49]$, and $[5.49, 5.99]$ MeV. For each bin, the thresholds are chosen to maximize

$$\text{FOM} = \frac{N_{\text{sig}}}{\sqrt{N_{\text{sig}} + N_{\text{bkg}}}}, \tag{5.2}$$

   where N_{sig} is the number of NCQE events in MC and N_{bkg} is the sum of the beam-off data and the non-NCQE MC. The resulting thresholds are modeled as linear functions of E_{rec}:

$$\begin{aligned} \texttt{dwall}^{\text{CUT}} &= p_{\text{dwall}}[0] + p_{\text{dwall}}[1]\, E_{\text{rec}}, \\ \texttt{effwall}^{\text{CUT}} &= p_{\text{effwall}}[0] + p_{\text{effwall}}[1]\, E_{\text{rec}}, \\ \texttt{OvaQ}^{\text{CUT}} &= p_{\text{OvaQ}}[0] + p_{\text{OvaQ}}[1]\, E_{\text{rec}}. \end{aligned} \tag{5.3}$$

   Because the optimal `dwall` saturates at 200 cm above ~ 4 MeV, its fit uses only the first two bins. The fitted dependences are shown in Figure 5.3, and the Run 11 parameters are summarized in Table 5.2.

Table 5.2: Parameters for `dwall`, `effwall`, and `OvaQ` in T2K Run 11.

Run#	$p_{\text{dwall}}[0]$	$p_{\text{dwall}}[1]$	$p_{\text{effwall}}[0]$	$p_{\text{effwall}}[1]$	$p_{\text{OvaQ}}[0]$	$p_{\text{OvaQ}}[1]$
11	580.0	-80.0	1941.5	-314.0	0.4125	-0.042

7. **CC-interaction cut**
   The Cherenkov angle depends on the particle type and energy. Single $e^{\pm}$ or γ events typically give $\theta_C \approx 42°$, while multiple γs can produce larger angles due to overlapping rings. We exploit this by applying a linear boundary in the

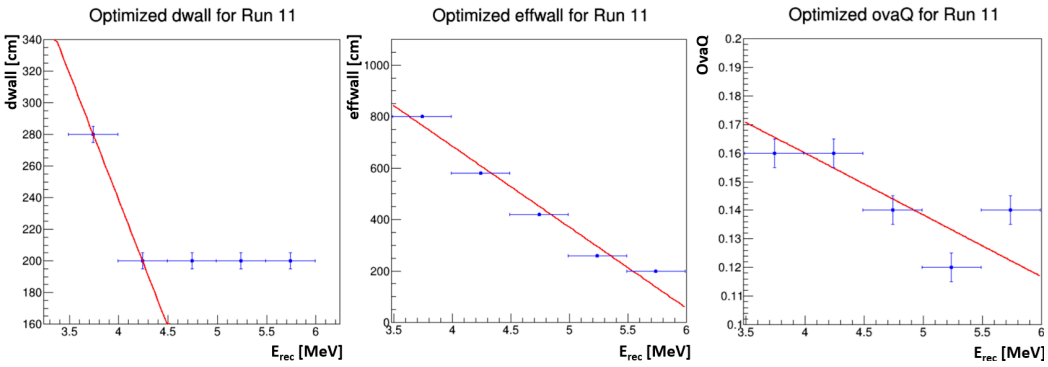

Figure 5.3: Linear fits for the ambient low-energy background cuts. The events above the red lines were kept.

$(E_{\mathrm{rec}}, \theta_C)$ plane to reject CCQE and retain NCQE:

$$\theta_C^{\mathrm{CUT}} = a_{\mathrm{opt}}\, E_{\mathrm{rec}} + b_{\mathrm{opt}}. \tag{5.4}$$

The coefficients are chosen to maximize the Figure of merit (FOM), taking NCQE MC as signal and combining non-NCQE MC with off-beam data as background. The optimized values are $a_{\mathrm{opt}} = 1.67$ and $b_{\mathrm{opt}} = 15.0$. Figure 5.4 shows the resulting separation: events above the line are selected (NCQE-like) and those below are rejected (CCQE-dominated).

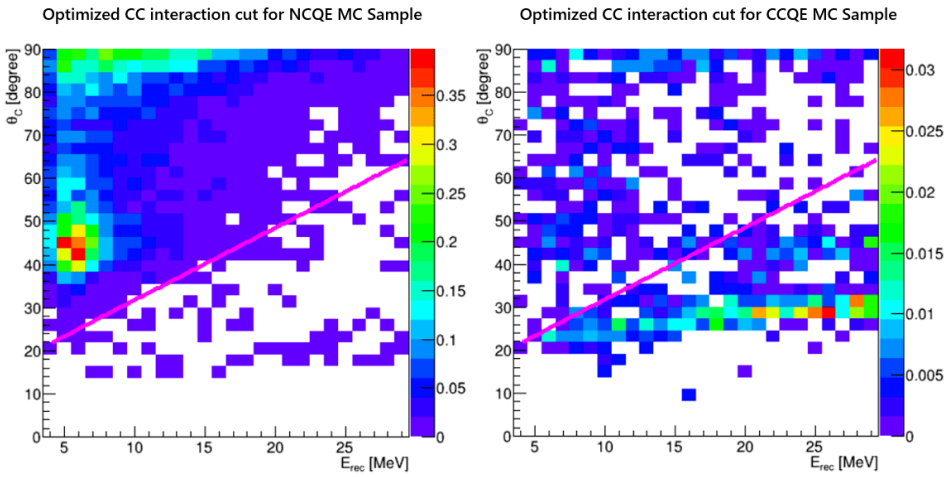

Figure 5.4: Two-dimensional E_{rec}–θ_C distributions of NCQE and CCQE MC with the optimized cut. The region above the line is NCQE-enriched and selected. The lower region is CCQE-dominated and rejected.

5.2 prompt signal selection results

This section summarizes observables for prompt signals that pass the selection in both MC samples and T2K Run 11 data. Table 5.3 lists the expected Run 11 neutrino yields and the selection fractions at each reduction stage. Table 5.4 reports the channel

fractions for different secondary-interaction(SI) models. To compare SI modeling, we include SKG4 predictions with BERT, INCL, and BIC alongside SKDETSIM. Finally, Table 5.5 gives the on-beam and off-beam event counts. Because on-beam data include signal plus accidental radioactivity that is difficult to simulate reliably, the accidental rate is estimated from selected off-beam data. Overall, the MC predictions and the T2K data after this subtraction agree within statistical uncertainties at all selection stages.

Table 5.3: Expected number of neutrino events for Run 11 (MC) that passing each NCQE selection criteria for each interaction mode.

SKDETSIM					
Cuts	ν-NCQE	$\bar{\nu}$-NCQE	NC-other	CC	Total
E_{rec}	32.46	1.01	9.99	4.45	47.91 (100%)
FV	25.25	0.79	7.31	2.60	35.94 (75.0%)
$dwall$	25.08	0.78	7.29	2.60	35.75 (74.6%)
$effwall$	24.70	0.76	7.28	2.60	35.34 (73.8%)
$ovaQ$	23.69	0.74	7.08	2.56	34.06 (73.7%)
CC interaction cut	23.46	0.73	6.26	1.09	31.54 (65.8%)

Table 5.4: Expected number of neutrino events for Run 11 (MC) that pass all NCQE selections using SKSETSIM and SKG4, with the choice of secondary model indicated in parentheses.

MC Sample	SKDETSIM(BERT)	SKG4(BERT)	SKG4(INCL)	SKG4(BIC)
$\nu - NCQE$	23.5 (74.3%)	22.4 (66.8%)	20.8 (66.9%)	20.8 (67.2%)
$\bar{\nu} - NCQE$	0.7 (2.4%)	0.6 (2.1%)	0.6 (2.0%)	0.6 (2.0%)
$NC - other$	6.3 (19.7%)	6.0 (18.1%)	5.6 (18.1%)	5.5 (17.8%)
CC	1.1 (3.6%)	4.4 (12.9%)	4.0 (13.0%)	4.0 (13.0%)
Total	31.5 (100%)	33.5(100%)	31.0 (100%)	30.9(100%)

Table 5.5: Number of events passing each NCQE selection criteria for data and MC. For MC, the nominal SKDETSIM and prediction from three SI models with SKG4 are provided, where the selection efficiency is also shown in the parentheses.

	Data set		MC Sample			
Cuts	On-Beam	Off-Beam	SKDETSIM(BERT)	SKG4(BERT)	SKG4(INCL)	SKG4(BIC)
Timing	358	331.2	-	-	-	-
Decay-e	356	330.9	-	-	-	-
FV	92	67.4	35.9 (75.0%)	41.7(72.5%)	40.0(71.4%)	40.3(71.8%)
$dwall$	82	58.5	35.7 (74.6%)	41.5(72.1%)	39.8(70.9%)	40.0(71.4%)
$effwall$	60	34.7	35.3 (73.8%)	41.1(71.5%)	39.3(70.1%)	39.5(70.5%)
$ovaQ$	31	0.4	34.6 (73.7%)	39.5(68.7%)	37.5(66.9%)	37.8(67.4%)
CC interaction cut	30	0.4	31.5 (65.8%)	33.5(58.2%)	31.0(55.3%)	30.9(55.1%)

Figure 5.5 shows the BONSAI variables E_{rec}, θ_C, `dwall`, `effwall`, `OvaQ`, and $\cos\theta_{\mathrm{beam}}$. Here, $\cos\theta_{\mathrm{beam}}$ is the cosine of the angle between the reconstructed event and the T2K beam direction.

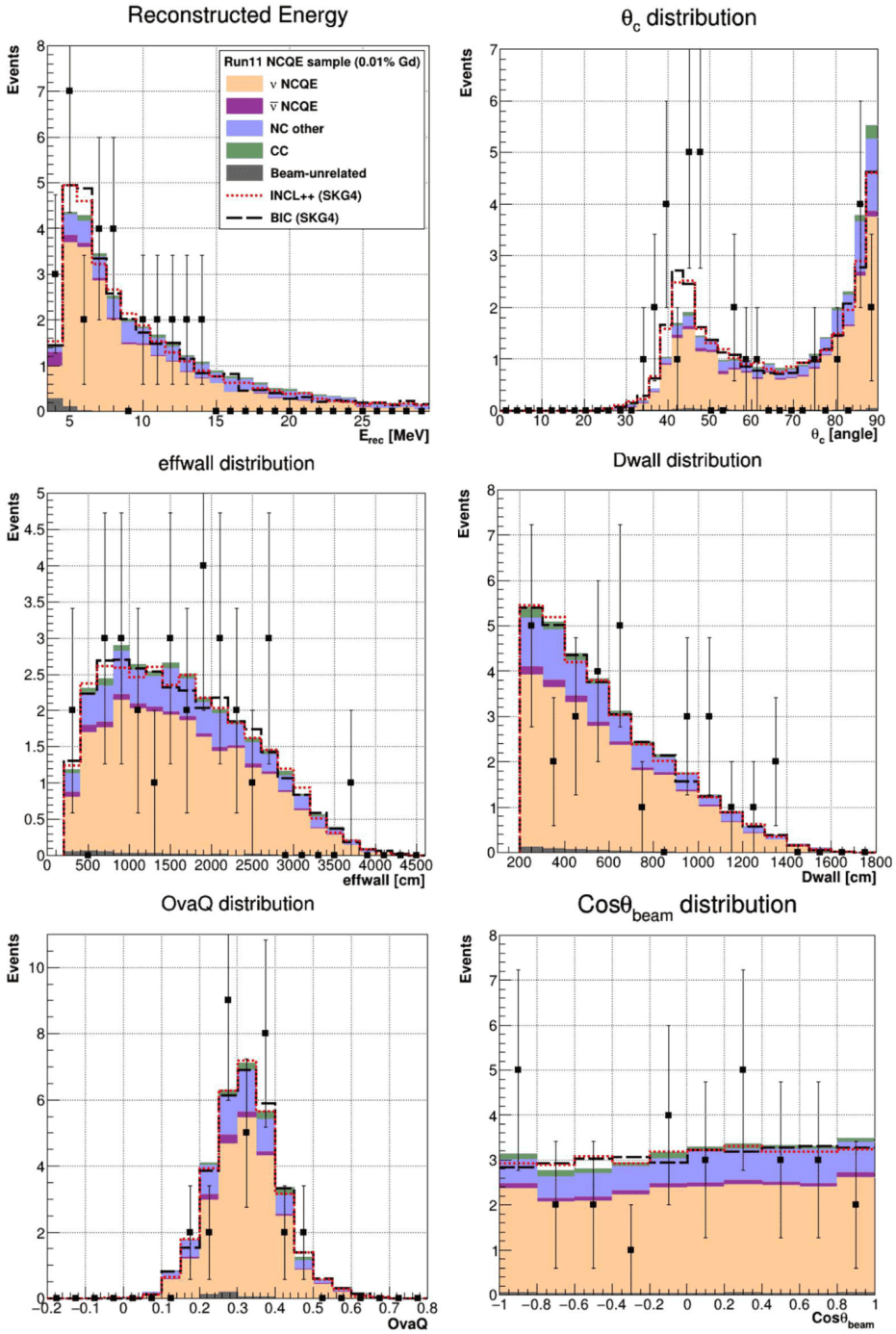

Figure 5.5: Distributions of E_{rec}, θ_C, `dwall`, `effwall`, `OvaQ`, and $\cos\theta_{\mathrm{beam}}$. The SKDETSIM MC is shown as stacked histograms by interaction channel. SKG4 predictions with INCL and BIC are overlaid as red and black lines. The T2K Run 11 data are consistent with the MC within statistical uncertainties.

Figure 5.6 presents the vertex coordinates X_v, Y_v, Z_v, and the radius square R_v^2 for MC and Run 11 data.

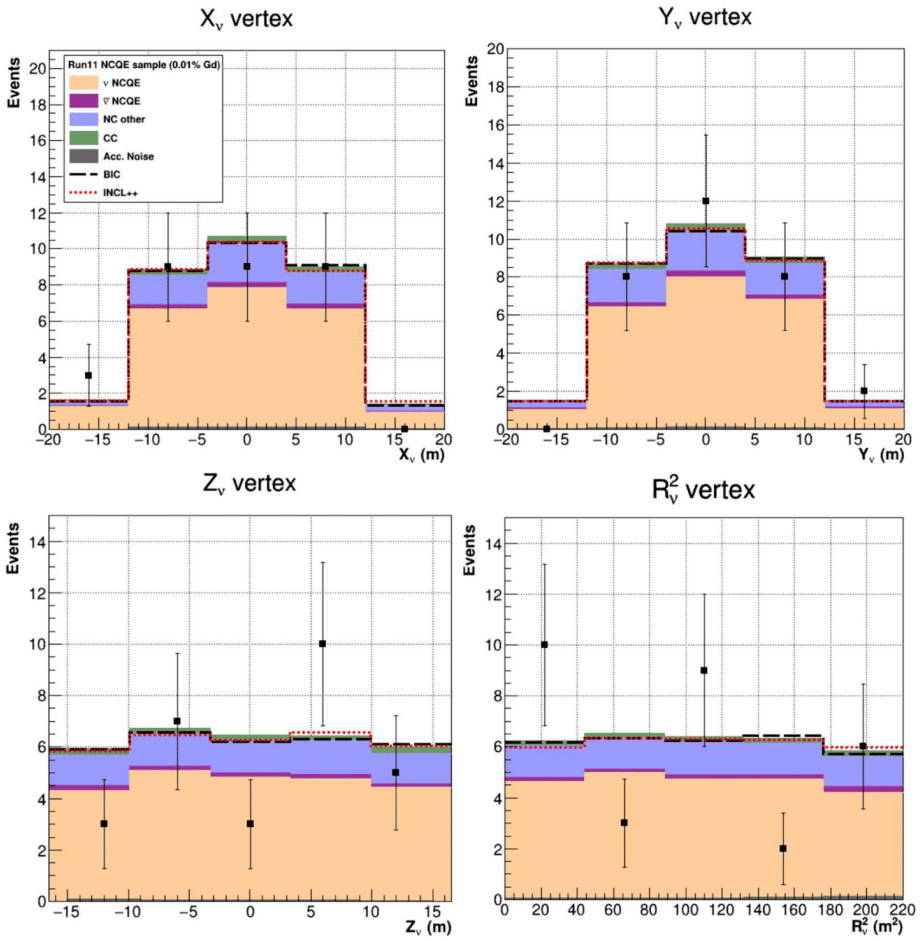

Figure 5.6: Vertex distributions X_v, Y_v, Z_v, and R_v^2 for MC and T2K Run 11 data.

Figure 5.7 shows the corresponding 2 dimentaional vertex distributions: the top-down view X_v–Y_v and the side view R_v^2–Z_v. Both MC and data indicate that prompt signal vertices are uniformly distributed within SK.

5.3 The delayed signal selection

This section describes the delayed signal selection, the configuration of `NTag` used in this study. We first define the neutron related parameters then review the legacy implementation, `prompt_keras` [52], then the nominal configuration, `bonsai_keras` [122], and the setting used in the SK-VI, VII DSNB search, `lowe_tmva` [36]. We then compare delayed signal results between `bonsai_keras` and `lowe_tmva`, followed by neutron observables using both settings.

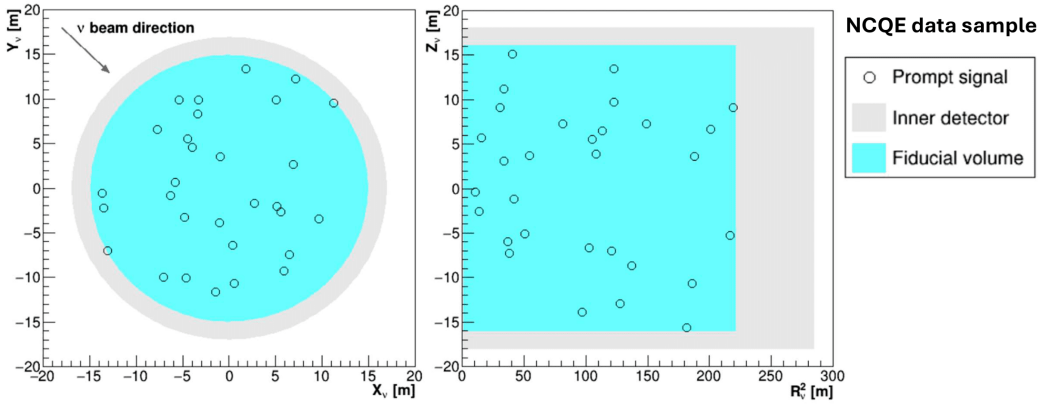

Figure 5.7: Two-dimensional vertex distributions for MC and T2K Run 11 data: X_v–Y_v (top-down) and R_v^2–Z_v (side view).

5.3.1 Definition of neutron tagging efficiency

Since `NTag` runs in two stage, pre-selection and neural-network (NN) classification (Section 4.2.5), we define three efficiencies:

- **Pre-selection efficiency** $\varepsilon_{\mathrm{Pre}}$: the fraction of true neutrons that are selected as neutron candidates after pre-selection.
- **NN classification efficiency** $\varepsilon_{\mathrm{NN}}$: the fraction of pre-selected candidates that the NN correctly classifies as neutrons.
- **Overall tagging efficiency** $\varepsilon_{\mathrm{Overall}}$: the fraction of true neutrons that are ultimately selected after both stages.

Formally,

$$\varepsilon_{\mathrm{Pre}} = \frac{\#\,\text{neutron candidates after pre-selection}}{\#\,\text{true neutrons}}\,, \tag{5.5}$$

$$\varepsilon_{\mathrm{NN}} = \frac{\#\,\text{true neutrons correctly tagged by the NN}}{\#\,\text{pre-selected neutron candidates}}\,, \tag{5.6}$$

$$\varepsilon_{\texttt{NTag}} \equiv \varepsilon_{\mathrm{Overall}} = \varepsilon_{\mathrm{Pre}} \times \varepsilon_{\mathrm{NN}} = \frac{\#\,\text{selected delayed signals}}{\#\,\text{true neutrons}}\,. \tag{5.7}$$

Besides neutron signals, accidental noise also requires careful consideration. The noise rate, often called the mis-tagged rate, is defined as the number of mis-tagged neutrons per NCQE event. Furthermore, purity, which utilizes MC truth information, is defined as the fraction of true neutrons among all tagged neutrons.

The equations for the noise rate and purity are given as follows:

$$\textbf{Noise rate: } \eta_{\text{Noise}} = \frac{\#\text{ of mis-tagged neutron (acc. noise)}}{\#\text{ of prompt signals}} \tag{5.8}$$

$$\textbf{Purity: } P_{\text{NTag}} = \frac{\#\text{ of truth neutrons within delayed signals}}{\#\text{ of neutron candidates}} \tag{5.9}$$

5.3.2 `NTag` configuration

In SK-IV, the delayed signal tagging efficiency depended strongly on the neutron's travel distance. The main reason was the limited vertex resolution for $H(n,\gamma)$ captures. We therefore set the delayed vertex equal to the prompt vertex, since neutrons typically capture near the prompt signal vertex. However, as the neutron traveled farther, the separation between the true capture point and the assumed vertex grew, reducing the tagging efficiency. Because the prompt event is typically brighter than the 2.2 MeV $H(n,\gamma)$ capture, this approximation was the most practical choice at the time. We refer to this configuration as `prompt_keras`.

In this study, BONSAI is used to reconstruct delayed vertices for both $H(n,\gamma)$ and $Gd(n,\gamma)$ captures. The $\sim$ 8 MeV γ-ray cascade from Gd(n,γ) yields a vertex resolution of approximately 50 cm, a improvement over the 100 cm resolution associated with the 2.2 MeV γ from H(n,γ). This improvement leads to an overall tagging efficiency that is effectively independent of neutron displacement. We refer to this configuration as `bonsai_keras`.

For rare signals such as DSNB, the SK group continues to assign the delayed vertex to the prompt vertex in SK VI and SK VII. This choice retains events with few PMT hits (e.g., from $H(n,\gamma)$), increasing the number of delayed tags at the cost of larger systematics related to neutron travel distance. We refer to this configuration as `lowe_tmva`.

Details of the three settings are summarized below.

1. **`prompt_keras`**
   Following Ref. [52], the delayed vertex is set equal to the prompt event vertex. Pre-selection uses PMT hit times corrected by photon time-of-flight from this prompt vertex to identify neutron candidates. A Keras [126] NN then classifies candidates as noise or true neutron captures.

2. **`bonsai_keras`**
   Building on the Ref. [122], this option assigns the delayed vertex from BONSAI rather than reusing the prompt vertex. Using the reconstructed delayed vertex

improves the neutron displacement estimate and yields a distance-independent tagging efficiency. The `bonsai_keras` configuration is adopted as the nominal setting in this study.

3. **`lowe_tmva`**
   This option matches the DSNB search at SK-VI&VII : the delayed signal vertex is set to be the prompt signal vertex. The NN is implemented with TMVA, using a weight file retrained with SK-VI calibration data. We also apply this setting here to enable a direct comparison and to support the DSNB search at SK.

All three delayed signal selection options are available in `NTag`. The parameter settings are described in Table 5.6 and summarized in Table 5.7. All neural networks are trained on SKDETSIM-based thermal–neutron particle-gun MC. Training and model details for `prompt_keras` and `bonsai_keras` follow Ref. [122], while the `lowe_tmva` model follows Ref. [36].

Figure 5.8 shows the overall tagging efficiency versus neutron travel distance for the three options. The `prompt_keras` (blue) and the `bonsai_keras` (brown) take the delayed vertex as the prompt vertex and therefore exhibit similar distance dependence. In contrast, the `lowe_tmva` (green) is approximately flat with distance, indicating that the overall tagging efficiency is independent of neutron travel distance.

Table 5.6: Summary of NTag settings used in this analysis.

Parameter Name	**Description**
NHITSTH	Hit trigger for candidate selection
TMINPEAKSEP	Minimum time separation between two signal triggers (ns)
PMTDEADTIME	Artificial PMT deadtime (ns)
E_CUTS	Cuts for decay-e selection
prompt_vertex	Whether to use prompt vertex in pre-selection
NN_type	Options for NN structure keras or tmva
mode	NN library and the type of delayed vertex used for feature variables

Table 5.7: Summary of NTag parameters adopted in this analysis.

Parameter Name	`bonsai_keras`	`lowe_tmva`	`prompt_keras`
NHITSTH	7	7	5
TMINPEAKSEP	200	50	50
PMTDEADTIME	1000	900	1000
E_CUTS	NHits<50 && FitT<20	TagOut>0.7 && NHits<50 && FitT<20	NHits<50 && FitT<20
prompt_vertex	bonsai	lowfit	prompt
NN_type	keras	tmva	keras
mode	bonsai_keras	lowe_tmva_2023dec	prompt_keras

The travel distance-independent overall tagging efficiency is crucial, particularly as it improves systematic errors associated with the secondary interaction. This represents one of the major systematic uncertainties on mean neutron multiplicity, primarily due to the uncertainties in the SI cross-sections, which affect the neutron

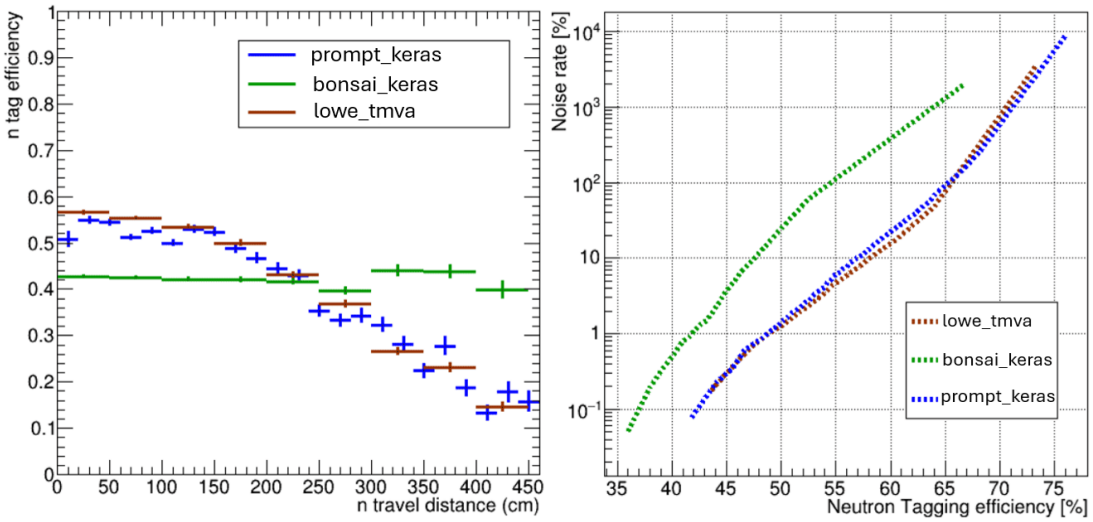

Figure 5.8: The left plot illustrates how the delayed neutron tagging efficiency varies with distance in `prompt_keras` (blue), `bonsai_keras` (green), and `lowe_tmva` (brown) settings. The right plot demonstrates the delayed neutron tagging efficiency varies with noise rate.

travel distance, as highlighted in Ref. [52]. A detailed discussion can be found in Chapter 6.6.

A neutron likelihood threshold of 0.7 was applied to both `bonsai_keras` and `lowe_tmva`, targeting a purity of about 99% with a noise rate near 1%, which is optimal for studies that focus on neutron signals. The right plot of Figure 5.8 shows the relationship between noise rate and overall tagging efficiency, where `prompt_keras` and `lowe_tmva` outperform `bonsai_keras`. To explain why, Figure 5.9 presents the neutron likelihood distributions: the $H(n,\gamma)$ signal with `lowe_tmva` exceeds that with `bonsai_keras`, indicating that `lowe_tmva` retains more low hit neutron capture signals by H.

The NN classification efficiencies for `bonsai_keras` and `lowe_tmva` are calculated based on a threshold of 0.7. The pre-selection efficiency, NN efficiency, overall tagging efficiencies, noise rate, and purity for both the `bonsai_keras` and `lowe_tmva` are summarized in Table 5.8.

Table 5.8: Summary of neutron tagging efficiencies for `bonsai_keras` and `lowe_tmva` settings.

	`bonsai_keras`	`lowe_tmva`
Pre-selection efficiency	68.3%	73.3%
NN classification efficiency	63.1%	69.5%
Overall tagging efficiency	43.1%	50.9%
Purity	98.7%	98.3%
Noise rate	1.28%	1.47%

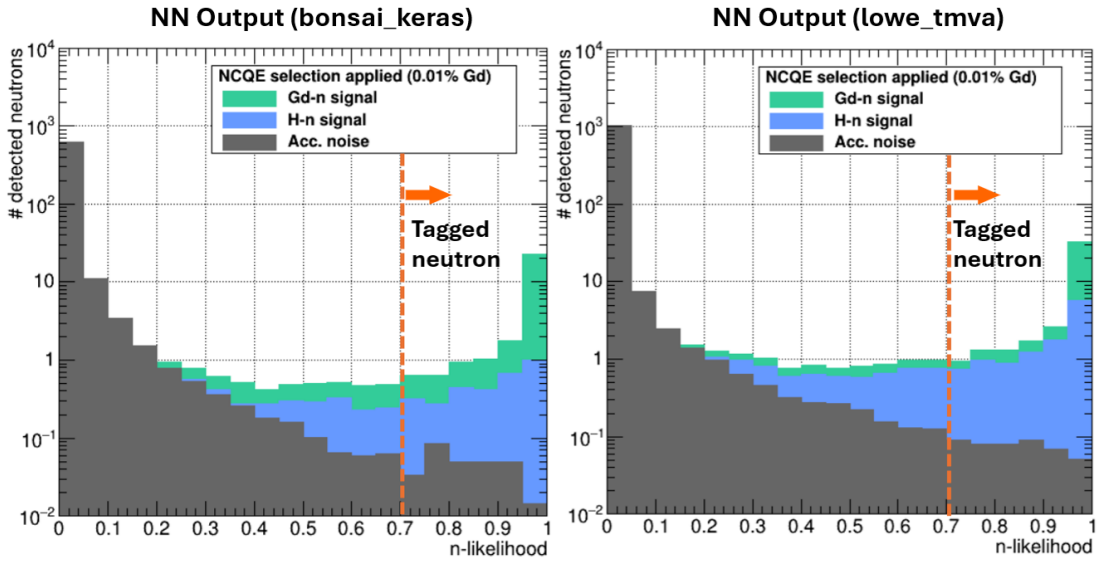

Figure 5.9: The NN output values for `bonsai_keras` (left plot) and `lowe_tmva` (right plot). The `lowe_tmva` performs better in tagging $H(n,\gamma)$ events, as shown in a more prominent blue region in the right plot compared to the left plot.

5.4 Observable difference between `bonsai_keras` and `lowe_tmva`

This section compares differences in delayed signal features between `bonsai_keras` and `lowe_tmva`. Monte Carlo predictions are normalized to the T2K flux at the SK site and include all interaction channels that pass the prompt signal selection. We present pure MC comparisons of neutron capture signals, including PMT hits (NHits), multiplicity, capture time, and travel distance.

Figure 5.10 shows the NHits distribution for delayed signals. The `lowe_tmva` setting selects more $H(n,\gamma)$ captures than `bonsai_keras`, especially apparent in the low–hit region. This shifts the feature distributions, so separate neural network models were trained for `bonsai_keras` and `lowe_tmva`.

Figure 5.11 compares expected neutron multiplicity, capture time, and travel distance for `bonsai_keras` (black) and `lowe_tmva` (red). Because `lowe_tmva` has higher overall neutron–tagging efficiency, it yields fewer zero–tag events and more events with multiple tagged neutrons. The higher efficiency also raises the number of neutrons observed at a given capture time. Differences with travel distance are more selective: the advantage of `lowe_tmva` appears only for distances below 300 cm, consistent with their distinct distance–dependent efficiencies. This trend is hard to resolve in Run 11 due to limited delayed signal statistics, but it should become clearer with additional T2K beam data in the near future.

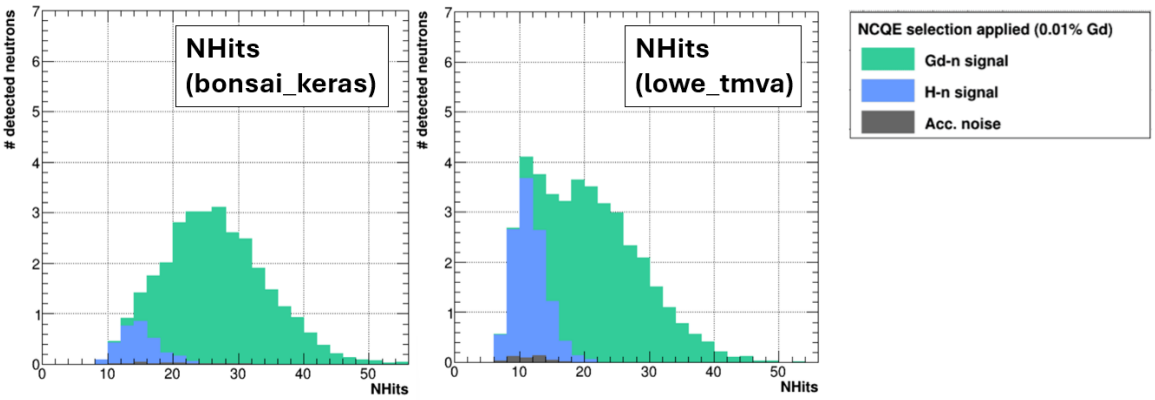

Figure 5.10: NHits comparison for delayed signals between `bonsai_keras` and `lowe_tmva`.

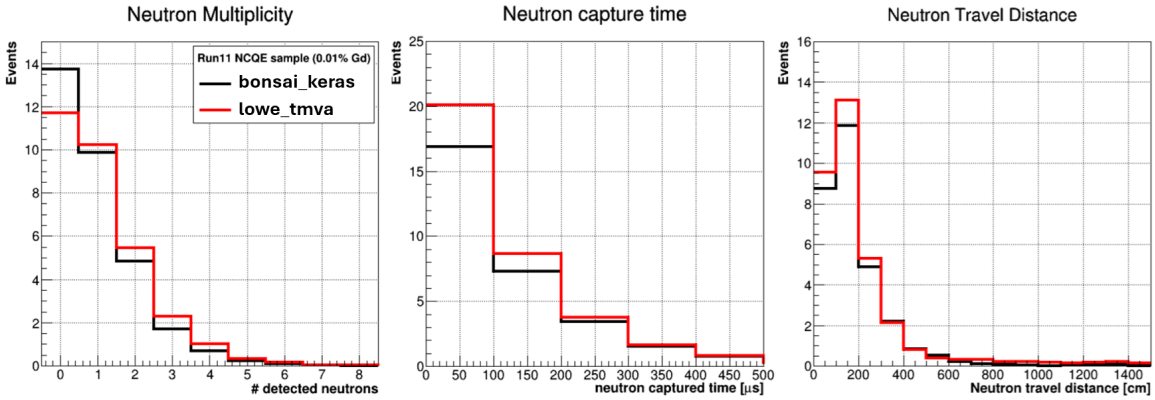

Figure 5.11: Comparison between `bonsai_keras` and `lowe_tmva`: neutron multiplicity, capture time, and travel distance.

5.5 Delayed signal results with `bonsai_keras`

This section reports the application of `bonsai_keras` to MC samples and the T2K Run 11 dataset. Figure 5.12 shows neutron candidate features after preselection stage. In these distributions, the true $H(n,\gamma)$ and $Gd(n,\gamma)$ signals (blue/green) are largely submerged under accidental noise (grey), motivating a subsequent NN selection to suppress noise. The agreement between MC and Run 11 data in Figure 5.12 indicates that accidental noise behaves as expected and supports using off-beam data as the noise sample for NN training.

Events passing both the preselection and the NN classification stage are labeled as delayed signals. Figure 5.13 shows the NN feature distributions of these delayed signals for both MC and data after the NN selection. The NN output (likelihood) distribution is shown in Figure 5.14. A likelihood threshold of 0.7 is applied for the NN classification, align with the AmBe calibration in Ref. [122].

Table 5.9 summarizes the observed delayed signals in on-beam and off-beam data and in MC, broken down by interaction channel and SI models. The INCL and BIC models predict fewer neutrons than the nominal Bertini-style model used in SKDETSIM.

Table 5.9: Neutron event numbers from the MC sample and dataset with `bonsai_keras` are presented. SKDETSIM and SKG4 are provided, and ratios of each interaction channel to total events are shown in parentheses. Datasets are categorized into On-Beam and Off-Beam, where Off-Beam assesses beam-unrelated noise. There is slight overprediction with the BERT model, while the dataset is more consistent with the INCL model.

`bonsai_keras`	MC sample				Data set	
Channel	SKDETSIM(BERT)	SKG4(BERT)	SKG4(INCL)	SKG4(BIC)	On-Beam	Off-Beam
$\nu - NCQE$	19.3 (62.6%)	17.9 (53.8%)	12.9(51.8%)	13.0(51.6%)	-	-
$\bar{\nu} - NCQE$	0.5 (1.6%)	0.5 (1.5%)	0.4(1.5%)	0.4(1.5%)	-	-
$NC - other$	9.5 (30.9%)	9.4 (28.2%)	7.0(28.2%)	7.1(28.2%)	-	-
CC	1.1 (3.7%)	4.6 (13.9%)	3.9(15.5%)	4.0(15.8%)	-	-
$Noise$	0.4 (1.2%)	0.9 (2.6%)	0.8(3.0%)	0.8(2.9%)	-	-
$N_{delayed}$	30.8 (100%)	33.3 (100%)	25.0 (100%)	25.3(100%)	18 (100%)	0.32 (1.7%)

Figure 5.15 shows delayed–signal features, including neutron multiplicity, capture time, and travel distance. The nominal MC (SKDETSIM) appears as colored histograms. Alternative secondary–interaction (SI) models, INCL and BIC, are overlaid as red and black dashed lines. While INCL, BIC, and SKDETSIM yield similar overall neutron–tagging efficiencies, they predict different neutron yields (a modeling, not detector–response effect). Consequently, the multiplicity panel (left) shows more zero–tag events for INCL and BIC than for SKDETSIM. Despite overall MC–data agreement, two events with unusually long travel distances are observed (right panel). One is compatible with an accidental noise (expected ~ 0.4 events in this study).

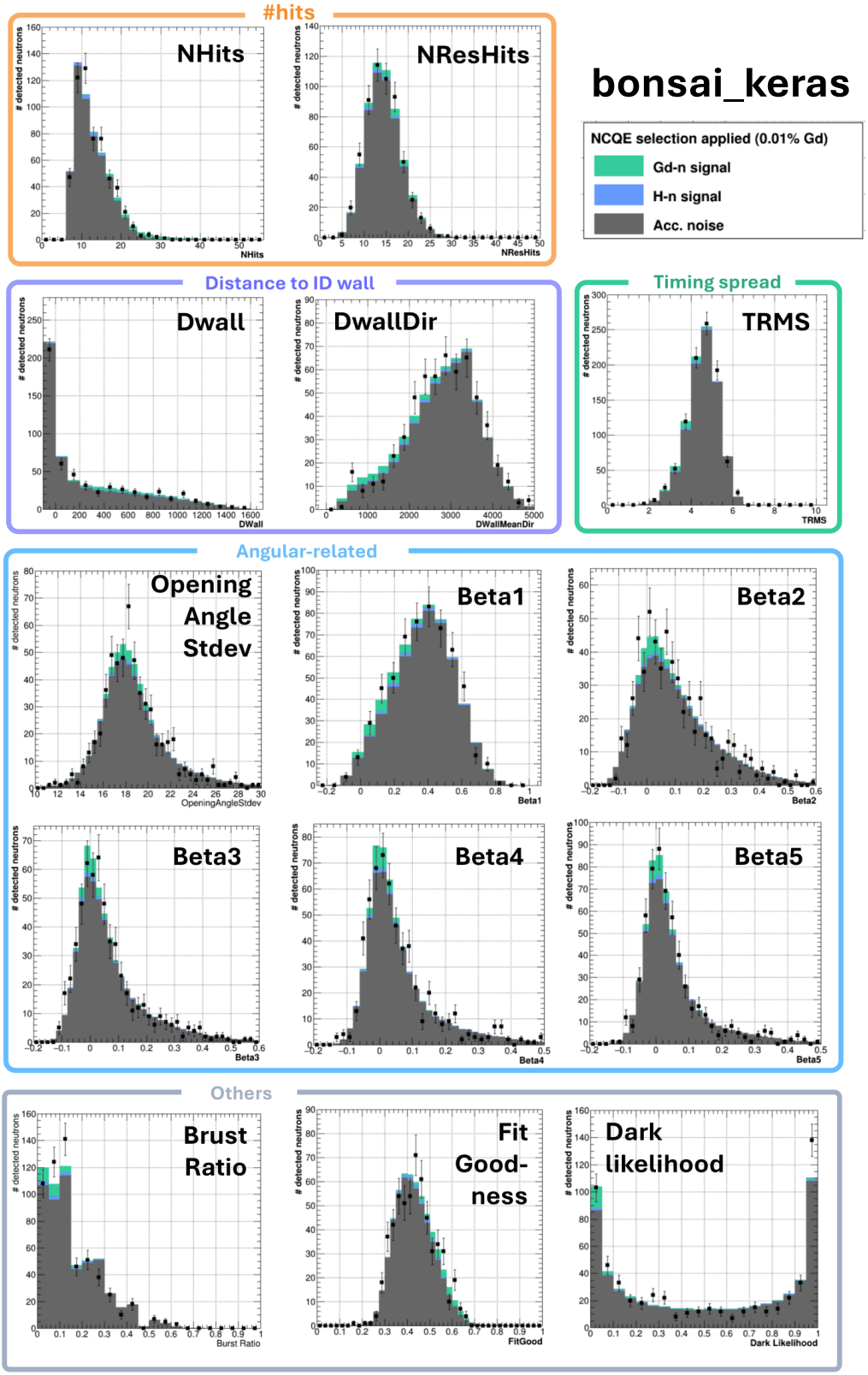

Figure 5.12: Neutron candidate features before NN classification. Stacked components: accidental noise (grey), $H(n,\gamma)$ (blue), and $Gd(n,\gamma)$ (green).

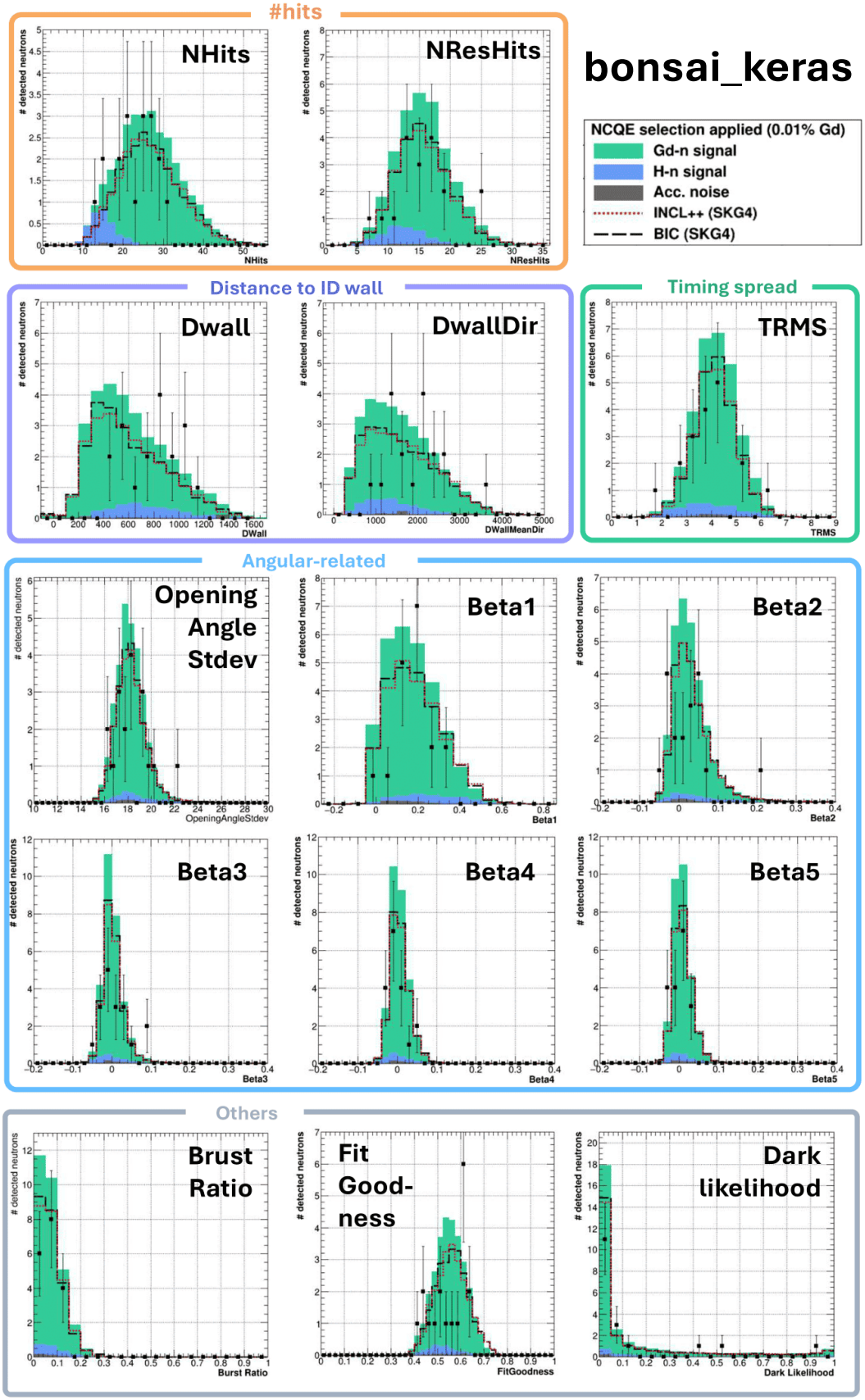

Figure 5.13: Neutron candidate features after NN classification. Stacked components: accidental noise (grey), $H(n,\gamma)$ (blue), and $Gd(n,\gamma)$ (green).

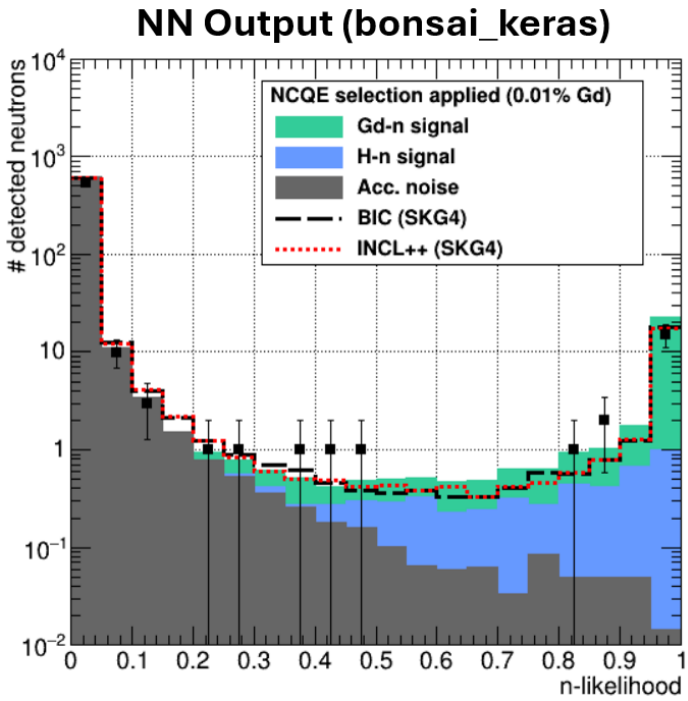

Figure 5.14: NN output values for $Gd(n,\gamma)$ (green), $H(n,\gamma)$ (blue), and accidental noise (grey). Run 11 data are consistent with the MC prediction, indicating stable NN performance.

Another candidate is consistent with a long-range neutron (> 700 cm), a category with an expectation of only ~ 0.5 events. Since two independent neutron tagging algorithms (`bonsai_keras` and `prompt_tmva`) identified this event, it is considered a high-confidence neutron capture.

The data also appear shifted to longer travel distances distribution relative to MC, hint by a deficit in the 0–100 cm bin.

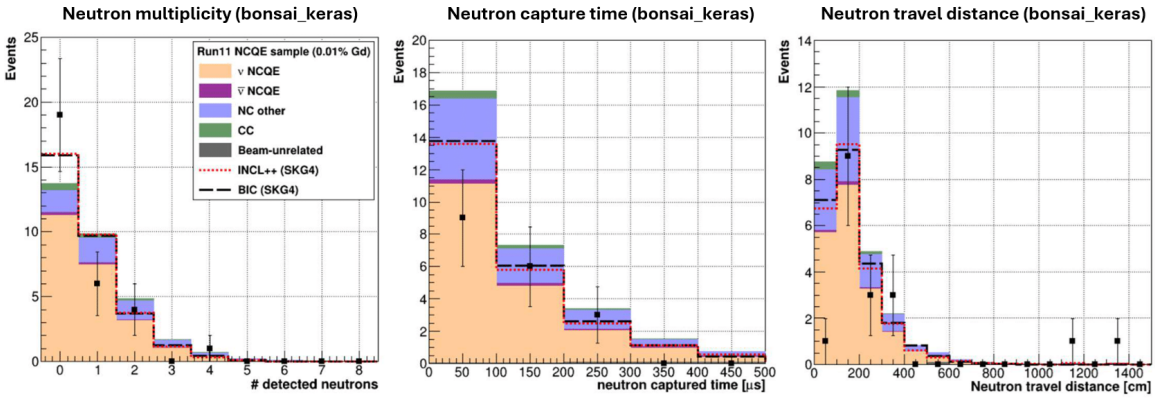

Figure 5.15: Delayed–signal features: neutron multiplicity (left), capture time (middle), and travel distance (right). SKDETSIM is shown as colored histograms by interaction channel. INCL and BIC SI variants are dashed overlays.

Because the T2K beam provides an incoming–neutrino direction, four neutron–

kinematic variables are shown in Figure 5.16: $\cos\theta_{\mathrm{nb}}$, $\cos\theta_{\mathrm{n}\gamma}$, and the longitudinal/transverse distances. Here, $\cos\theta_{\mathrm{nb}}$ is the cosine of the angle between the neutron–vertex direction and the T2K beam, and $\cos\theta_{\mathrm{n}\gamma}$ is the cosine of the angle between the neutron–vertex direction and the NCQE event direction. Longitudinal/Transverse distances are defined by projecting along/orthogonal to the beam axis. In this analysis, the neutron direction is taken as the vector from the delayed–signal vertex to the prompt vertex, rather than using a direction reconstructed from $Gd(n,\gamma)$ or $H(n,\gamma)$ captures. Although MC predicts directionality in θ_{nb}, no clear trend is seen in Run 11, consistent with SK pure–water measurements in Ref. [127].

Figure 5.17 presents the delayed vertex coordinates X_n, Y_n, Z_n, and R_n^2, together with 2D views. The bottom panels show the top–down view (X_n–Y_n) and side view (R_n^2–Z_n) of SK. The grey region denotes the inner detector. The blue region indicates the fiducial volume region.

5.6 Delayed signal results with `lowe_tmva`

This section presents delayed–signal results obtained with `lowe_tmva` for both the MC samples and the T2K Run 11 data. We use `lowe_tmva` to match the DSNB selection in SK6 and SK7 [36], which is tuned for SK analyses. Figure 5.18 shows the NN input features of neutron candidates after pre-selection. Small differences from `bonsai_keras` arise from the different preselection settings. The good agreement of the accidental–noise between MC and Run 11 in Figure 5.18 indicates that the noise distributions used for NN training on MC and for classification on data are modeled appropriately. Figure 5.19 displays the features of events that pass the NN selection, referred to as the delayed signal. The consistency between MC predictions and data after the NN selection shows that the network performs reliably in both cases. Figure 5.20 shows the NN score distributions for Gd(n,γ), H(n,γ), and accidental noise. A threshold of 0.7 is applied.

Table 5.10 summarizes the delayed signals for on-beam, off-beam data, and MC. The MC sample is organized by interaction channel and by SI models. Compared with the nominal Bertini-style model in SKDETSIM, the INCL and BIC models predict fewer delayed signals. The overall tagging efficiency agrees with the expectations of MC. Thus, the observed data–MC differences in the delayed signal are attributable to the modeling of hadron–nucleus interactions and are less dependent of the specific delayed signal selection settings.

Figure 5.21 shows the delayed signal features: neutron multiplicity, capture time, and travel distance. The nominal MC (SKDETSIM) appears as colored histograms, while the SI-model variations (INCL, BIC) are drawn with red and black

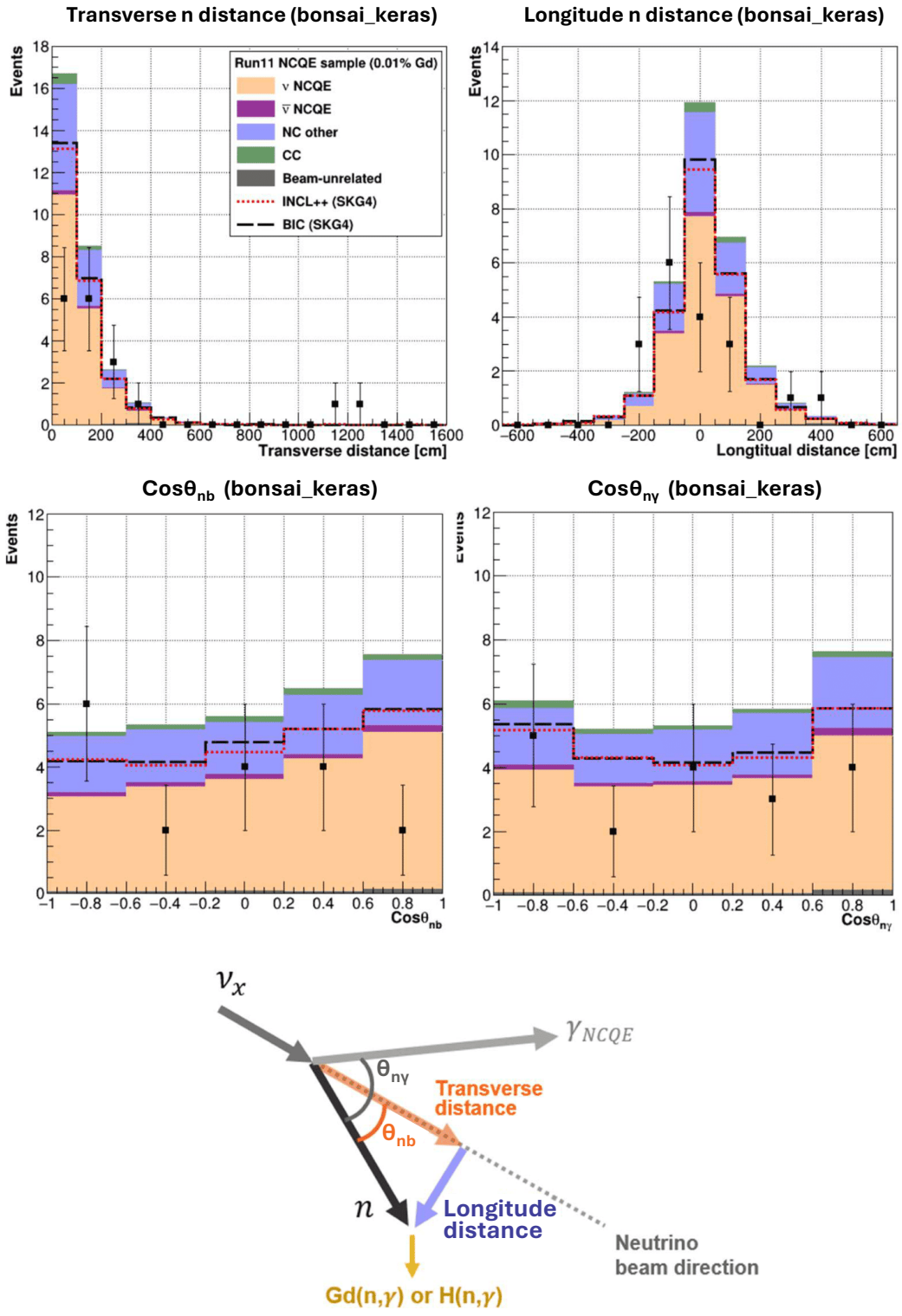

Figure 5.16: Neutron–kinematic distributions: $\cos\theta_{\mathrm{nb}}$, $\cos\theta_{\mathrm{n}\gamma}$, longitudinal distance, and transverse distance.

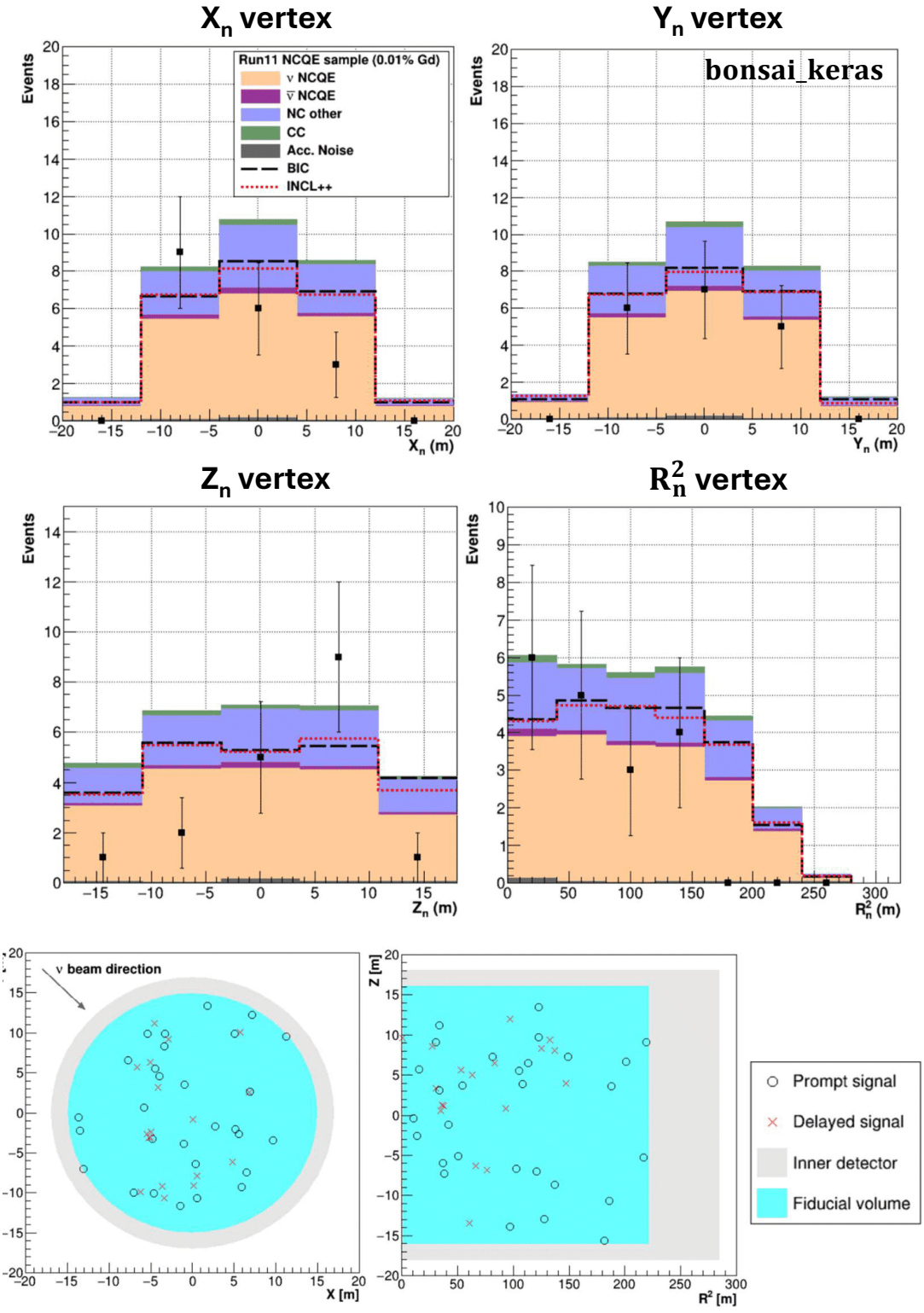

Figure 5.17: Delayed signal vertex geometry: X_n, Y_n, Z_n, R_n^2, and the 2D projections Y_n–X_n and Z_n–R_n^2.

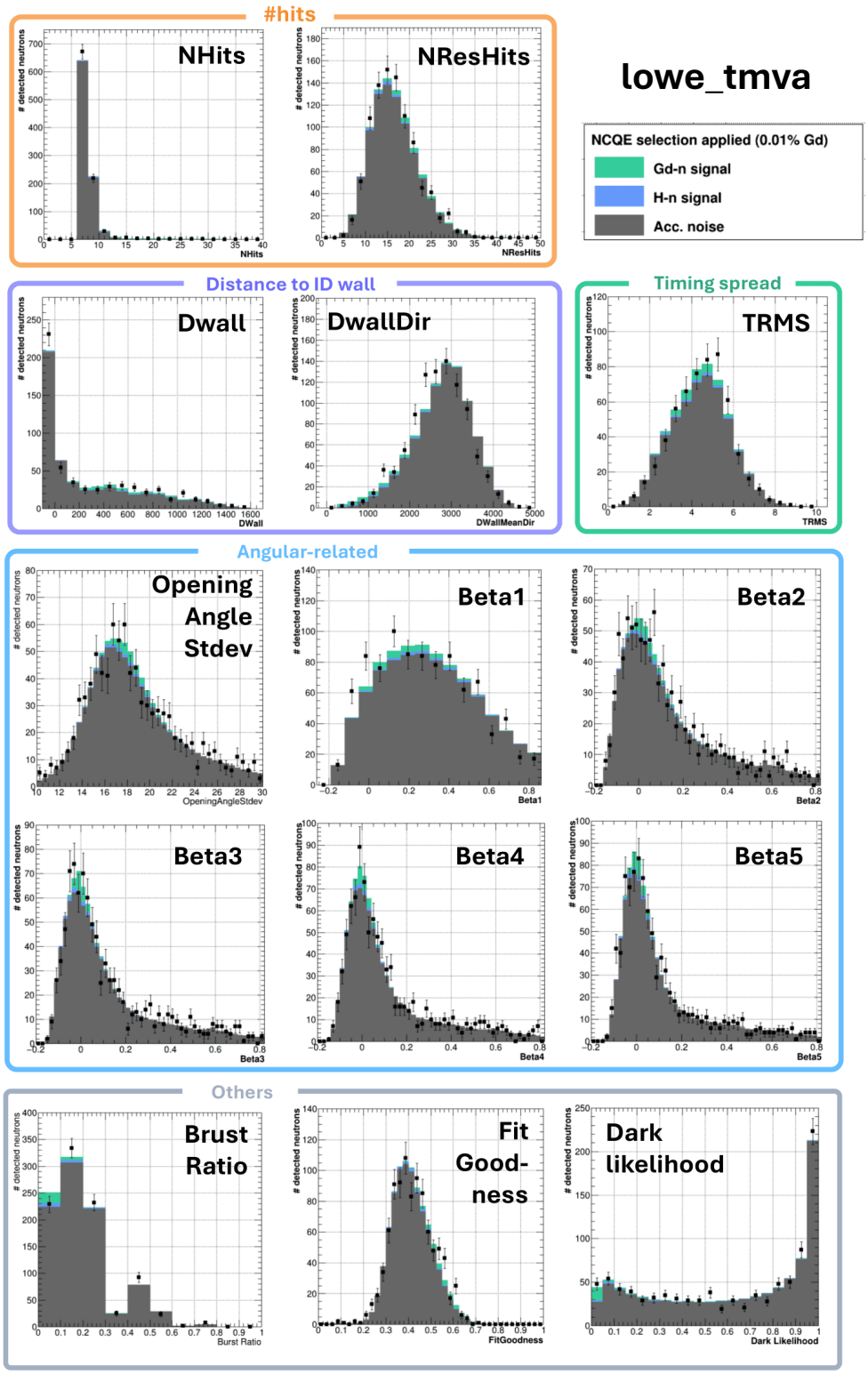

Figure 5.18: NN input–feature distributions of neutron candidates before the NN selection (pre-selection only).

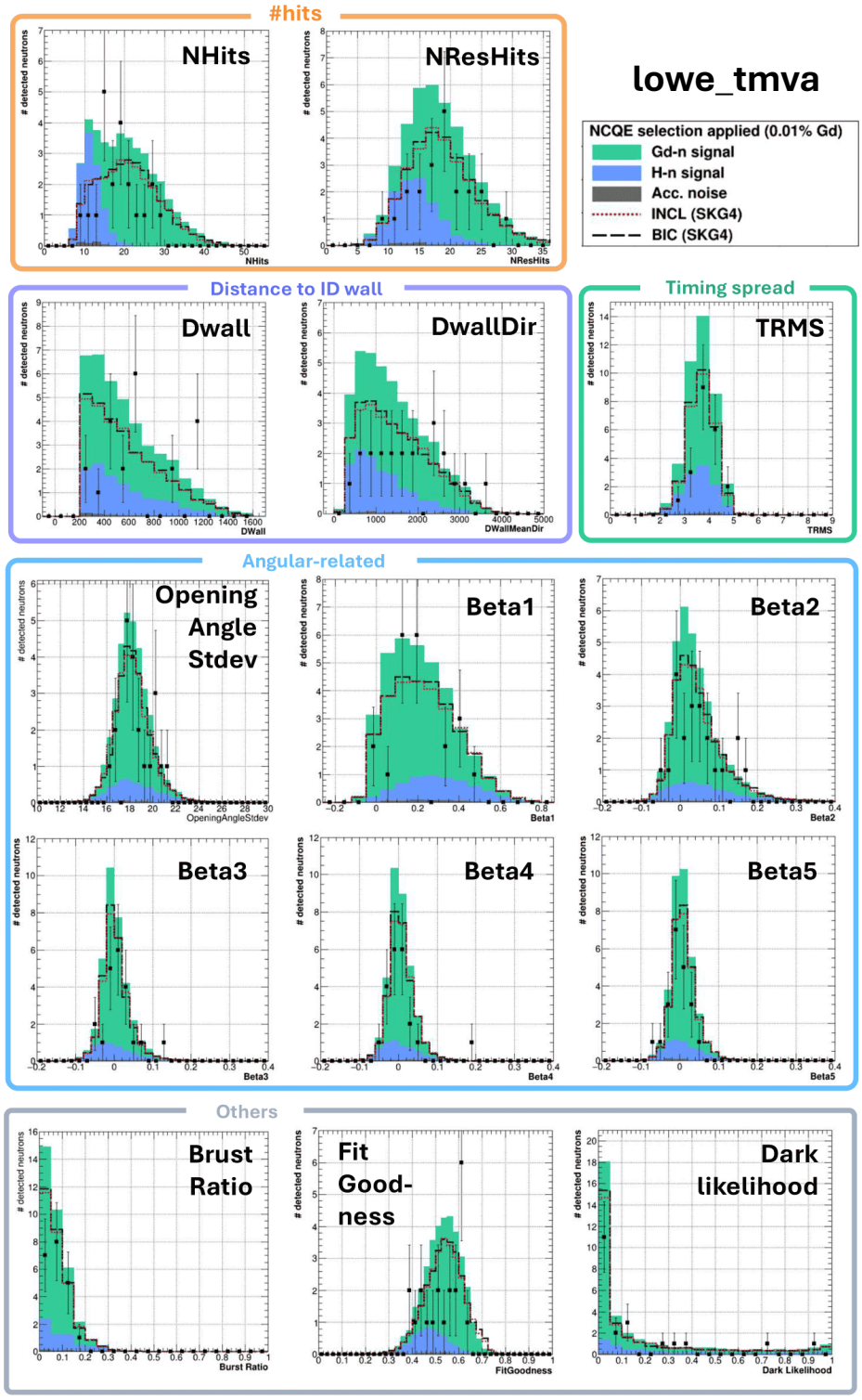

Figure 5.19: Features of candidates that pass the NN selection, defining the delayed–signal sample (pre-selection plus NN classification).

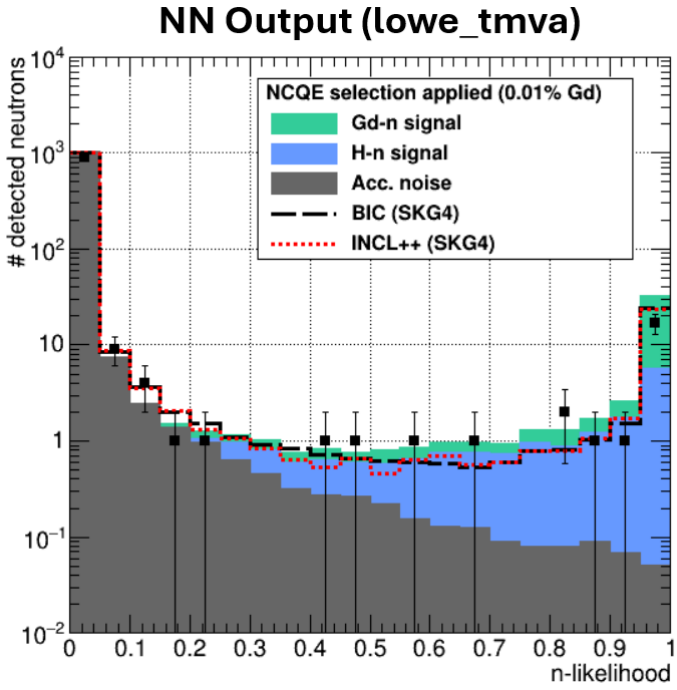

Figure 5.20: NN output score distributions for Gd(n,γ), H(n,γ), and accidental noise in MC and T2K Run 11. Data agree with MC, indicating stable NN performance with `lowe_tmva`, the DSNB selection using in SK6&7 [36].

Table 5.10: Neutron event numbers from the MC sample and dataset with LOWE ntag setting are presented. SKDETSIM and SKG4 are provided, and ratios of each interaction channel to total events are shown in parentheses. Datasets are categorized into On-Beam and Off-Beam, where Off-Beam assesses beam-unrelated noise. There is slight overprediction with the BERT model, while the dataset is more consistent with the INCL model.

`lowe_tmva`	MC sample				Data set	
Channel	SKDETSIM(BERT)	SKG4(BERT)	SKG4(INCL)	SKG4(BIC)	On-Beam	Off-Beam
$\nu - NCQE$	22.8 (63.3%)	20.8 (55.6%)	15.3 (53.7%)	15.4 (53.4%)	-	-
$\bar{\nu} - NCQE$	0.6 (1.7%)	0.6 (1.6%)	0.5(1.7%)	0.5(1.7%)	-	-
$NC - other$	11.1 (30.6%)	10.6 (27.7%)	8.0(27.5%)	8.5(28.7%)	-	-
CC	1.4 (3.8%)	5.4 (14.0%)	4.6(15.8%)	4.5(15.2%)	-	-
$Noise$	0.5 (1.4%)	1.0 (2.6%)	0.8(2.6%)	0.8(2.5%)	-	-
$N_{delayed}$	36.4 (100%)	38.4 (100%)	29.2(100%)	29.7(100%)	21(100%)	0.37 (1.8%)

dashed lines. With the `lowe_tmva` selection, two candidates exhibit unusually long travel distances, consistent with what is seen using `bonsai_keras`. One of the events has the same SK run and trigger ID in both selections, highly suggesting that it is a true long-travel neutron.

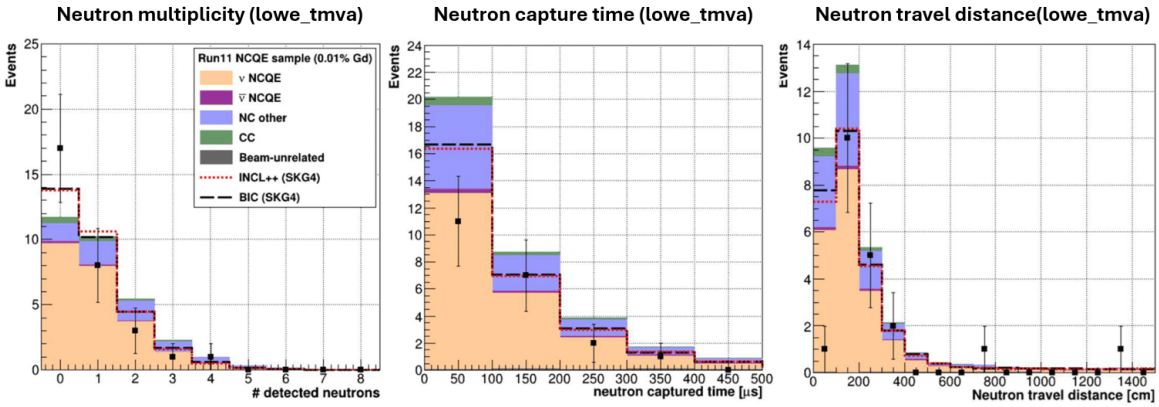

Figure 5.21: Neutron multiplicity, capture time, and travel-distance distributions with `lowe_tmva` setting.

Four neutron kinematic variables are shown in Figure 5.22. The lower schematic defines each parameter. Although MC predicts directionality in θ_{nb}, the Run 11 data show no clear directionality with the `lowe_tmva` selection.

Finally, Figure 5.23 presents the delayed-signal vertex distributions in X_n, Y_n, Z_n, and R_n^2. The lower panels show 2D projections of the detector: a top view (X_n, Y_n) and a side view (R_n^2, Z_n). The blue area marks the fiducial volume, and the gray area indicates the inner detector.

Table 5.11 lists the event IDs (SK run, sub-run, and event number) for the 30 selected NCQE events, together with key quantities: Cherenkov angle, reconstructed energy, multiple scattering goodness (MSG), and the number of tagged neutrons under the `bonsai_keras` and `lowe_tmva` selections.

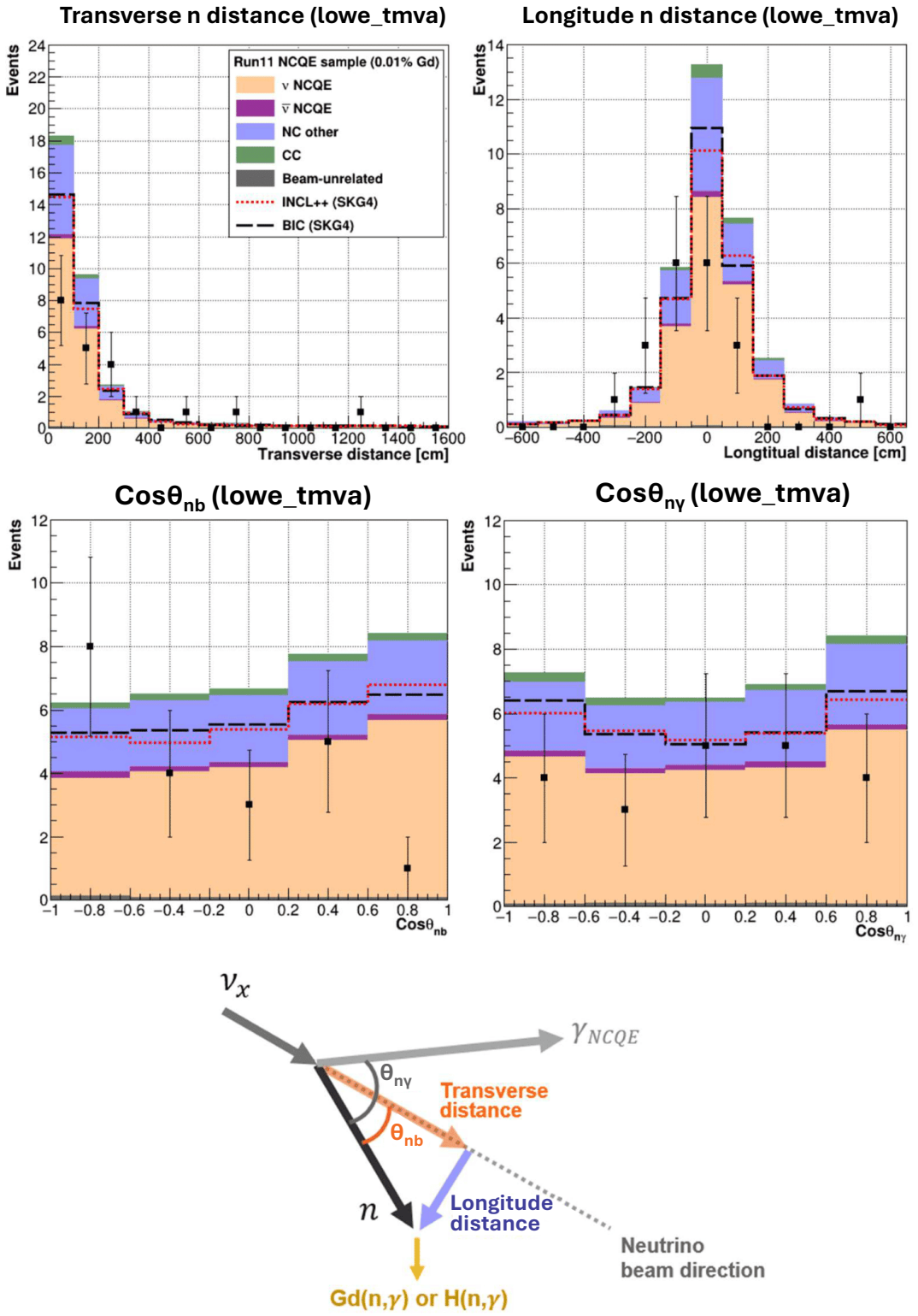

Figure 5.22: Neutron kinematics features distribution with `lowe_tmva` setting.

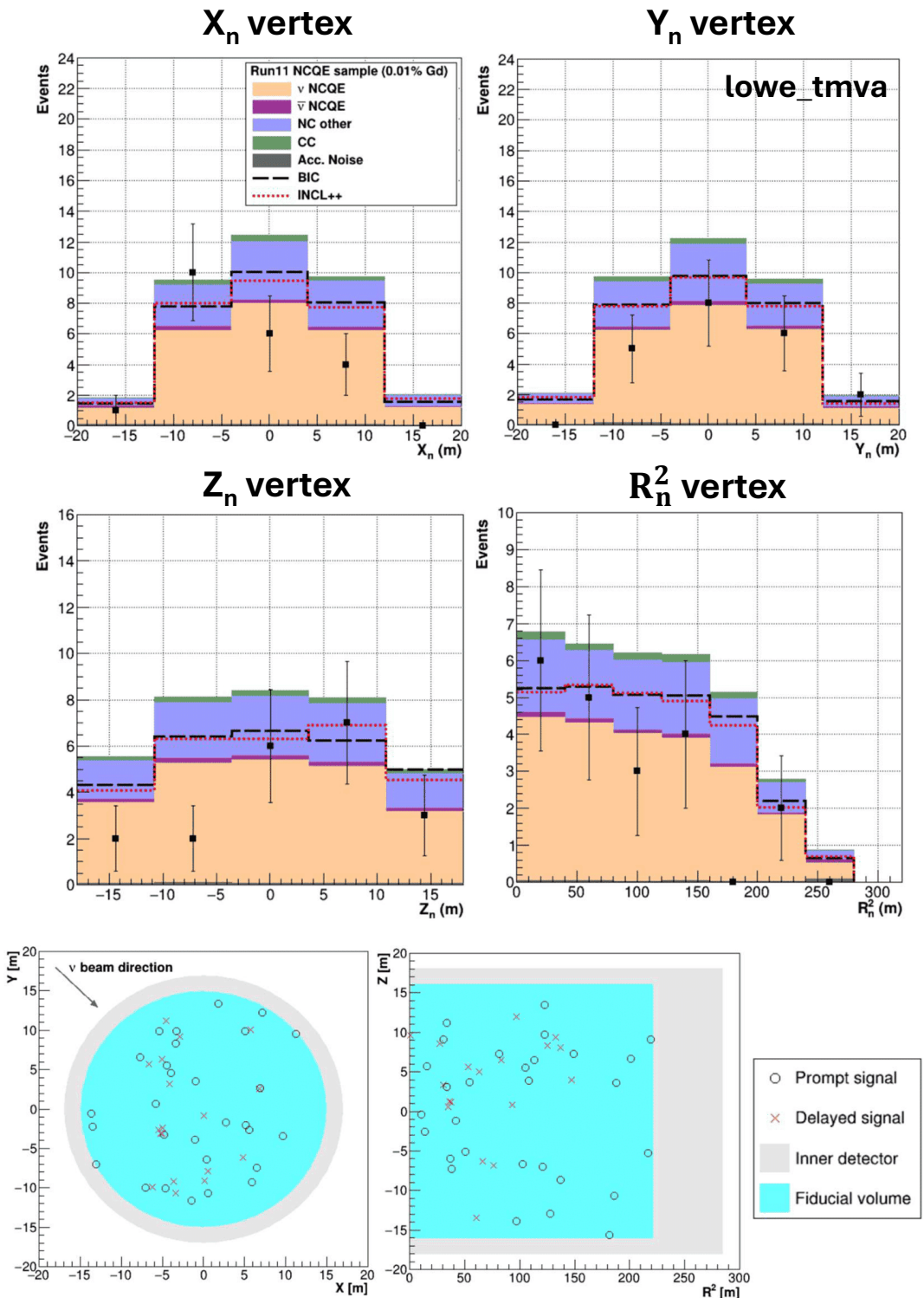

Figure 5.23: Delayed signal vertex distributions in X_n, Y_n, Z_n, and R_n^2. Lower panels: top view (X_n, Y_n) and side view (R_n^2, Z_n). The blue region shows the fiducial volume. The gray region indicates the inner detector region.

Table 5.11: EventID Summary

SK Run	Subrun #	Event #	E_{vis} (MeV)	θ_C (degree)	MSG (a.r.b)	#Signal$_{Delayed}$ `bonsai_keras`	#Signal$_{Delayed}$ `lowe_tmva`
85783	775	710048906	7.11	46.8	0.34	0	0
85783	1279	1174769051	6.59	47.70	0.36	1	0
85788	886	813176401	5.15	43.20	0.40	1	2
85788	664	608989645	10.12	40.50	0.49	0	0
85790	331	301351383	12.12	56.70	0.21	1	1
85814	463	418332351	5.12	45.90	0.55	2	2
85815	150	136881621	13.69	85.50	0.17	1	1
85816	562	514297914	8.47	57.60	0.34	0	0
85816	1137	1043895593	4.84	62.10	0.33	0	0
85818	1340	1231332949	3.81	45.00	0.31	0	0
85818	1205	1107352912	6.40	44.10	0.48	0	0
85819	1034	951607029	13.10	47.70	0.26	2	2
85819	453	416523477	4.68	40.50	0.48	1	1
85819	247	226952470	9.71	87.30	0.17	0	0
85819	459	422765851	13.31	85.50	0.18	0	0
85819	672	617741200	4.94	40.50	0.38	0	1
85835	77	69610411	3.59	37.80	0.26	0	0
85835	921	847430803	4.85	79.20	0.21	0	0
85837	1338	1231140300	10.97	85.50	0.16	2	1
85838	786	723133309	7.77	35.10	0.58	0	0
85838	21	18567860	8.22	44.10	0.31	0	1
85838	1058	974295614	6.17	47.70	0.32	2	3
85839	84	76634601	6.63	74.70	0.26	0	0
85841	644	592187091	14.42	85.50	0.12	0	0
85841	1183	1088194136	4.11	39.60	0.48	0	0
85847	42	37862849	7.34	36.00	0.59	0	0
85849	1182	1088399253	8.11	47.70	0.43	1	1
85850	312	286805917	12.05	87.30	0.15	0	1
85851	246	218657573	5.22	45.90	0.42	0	0
85851	755	687219878	10.82	54.90	0.25	4	4

Chapter 6

Systematic

This section quantifies the uncertainties on the mean neutron multiplicity M (Eq. 2.1). The computation proceeds as follows:

1. Start from the observed number of delayed candidates, N_{delayed}.
2. Subtract mis-tagged neutrons from accidental noise.
   For MC, we compute this with $\eta_{\text{Noise}} \times N_{\text{prompt}}$.
   For data, we estimate this from the Off-Beam window.
3. Correct for the overall tagging efficiency, ϵ_n.
4. Divide by the total number of prompt events, N_{prompt}, to obtain M, the mean neutron multiplicity per NCQE interaction.

Equivalently,

$$M = \frac{(N_{\text{delayed}} - \eta_{Noise} \times N_{\text{prompt}})}{\epsilon_n} \cdot \frac{1}{N_{\text{prompt}}}. \tag{6.1}$$

Statistical uncertainties on N_{delayed}, N_{prompt}, η_{Noise}, and ϵ_n are taken from the data directly or the size of MC samples and propagated to M using standard error propagation.

The overall tagging efficiency ϵ_n depends on modeling choices. To evaluate its systematic uncertainty, we vary: (i) the Gd concentration, (ii) the SI models, and (iii) the detector response to neutron capture signals, (iv) other relevant components from the previous NCQE induced neutron study [52], with updates were also adapted. Systematics on ϵ_n are estimated via MC regeneration: vary the parameters, regenerate the full MC, recompute ϵ_n, and take the spread between the minimum and maximum discrepancies, $\delta_{\max} - \delta_{\min}$, as the systematic uncertainty.

6.1 Statistical uncertainty

The overall tagging efficiency ϵ_n is subject to statistical fluctuations due to the finite size of the MC sample. Defining ϵ_n as the fraction of true neutrons that are tagged, its statistical uncertainty follows binomial errors:

$$\sigma_{\epsilon_n} = \sqrt{\frac{\epsilon_n\,(1-\epsilon_n)}{N_n^{\text{true}}}}\,, \tag{6.2}$$

where N_n^{true} is the total number of true neutrons in the MC. We compute this using raw event counts in MC (without POT normalization). For the MC sample in this study, the statistical contribution to $\epsilon_n^{\texttt{bonsai_keras}}$ is 0.3%.

The accidental-noise rate η_{Noise} is derived from dummy-spill data and therefore carries no model-dependent systematic. Under a Poisson approximation, this is defined as

$$\sigma_{\eta_{Noise}} = \sqrt{\frac{\#False\ positive}{\#\nu\ event}}, \tag{6.3}$$

yielding a total uncertainty of 5.7%.

For N_{prompt} and N_{delayed}, the MC samples in this study contain $\mathcal{O}(10^5)$ events, so the corresponding statistical uncertainties are below 1%. In data, however, we have $N_{\text{prompt}} = 30$ and $N_{\text{delayed}} = 18$ (`bonsai_keras`) or 21 (`lowe_tmva`); treating these as Poisson-distributed gives relative uncertainties of around 20%, each:

$$\sigma(N) = \sqrt{N}, \qquad \text{and} \qquad \frac{\sigma(N)}{N} = \frac{1}{\sqrt{N}}. \tag{6.4}$$

6.2 Gd concentration

SK-VI was loaded with a $Gd_2(SO_4)_3 \cdot 8H_2O$ concentration of 0.0263%. An Am/Be calibration based on neutron-capture time indicated a slightly lower effective concentrations: 0.0251 ± 0.0005% with SKDETSIM and 0.0247 ± 0.0005% with SKG4 [77]. This discrepancy is likely related to neutron-tracking physics in the simulation used for the Am/Be study and is under investigation. Because the Gd concentration affects the Gd-capture fraction and will propogate to the overall tagging efficiency, we evaluate its impact on systematic uncertainty.

We assess the systematic uncertainty from the Gd concentration by regenerating MC with the SKDETSIM setting, changing the $Gd_2(SO_4)_3 \cdot 8H_2O$ concentration from the nominal 0.0263% to 0.0251%, and comparing to the nominal sample. As shown in Table 6.1, the changes in the numbers of prompt and delayed signals are

small. We also observe the expected difference in overall tagging efficiency between the `bonsai_keras` and `lowe_tmva` selections. The fractional change in overall tagging efficiency between the two Gd concentrations (within the same delayed-signal selection) is used as the systematic:

$$\Delta\epsilon_{\mathrm{Gd}} = \frac{\epsilon_{\mathrm{n}}^{(0.0251\%\ \mathrm{MC})} - \epsilon_{\mathrm{n}}^{(0.0263\%\ \mathrm{MC})}}{\epsilon_{\mathrm{n}}^{(0.0263\%\ \mathrm{MC})}}. \tag{6.5}$$

We find that the resulting systematic uncertainty exceeds the MC statistical uncertainty (0.3%) yet remains within 1.6%. Numerically, the systematic uncertainties are ±1.2% for `bonsai_keras` and ±1.6% for `lowe_tmva`. The POT-normalized yields are summarized in Table 6.1.

Figure 6.1 compares neutron multiplicity, capture time, and travel distance at 0.0263% and 0.0251% Gd. No significant shape differences are observed in these distributions.

Table 6.1: Summary of Gd concentration settings used in this uncertainty evaluation.

SKDETSIM	`bonsai_keras`		`lowe_tmva`	
Gd Concentration	0.0251%	0.0263%	0.0251%	0.0263%
Prompt signal	31.5	31.5	31.5	31.5
Truth neutron	69.3	70.8	70.2	70.8
Delayed signal	30.2	30.5	36.3	36.1
Overall tagging efficiency	43.6%	43.1%	51.7%	50.9%

6.3 Nucleon SI

SI models are a major source of systematic uncertainty. Following Ref. [52], we assign a ±30% uncertainty to the nucleon–oxygen scattering cross section predicted by NEUT. This range was chosen to cover nucleon–carbon data and the predictions of GENIE, GEANT4, NUWRO, and FLUKA, since measurements on nucleon–oxygen are scarce. Our reproduction of that procedure agrees with the published result (see Table 6.2).

Beyond the ±30% cross section variation, we evaluate the systematic uncertainty by interchanging the SI models used in the detector simulation. Because SKDETSIM uses the Bertini cascade, we take physics list BERT as the reference in the SKG4 framework and compare it with INCL and BIC.

We quantify the relative change in overall tagging efficiency as

$$\Delta\varepsilon_{\mathrm{SI}} = \frac{\varepsilon_n^{\mathrm{regen.}} - \varepsilon_n^{\mathrm{nominal}}}{\varepsilon_n^{\mathrm{nominal}}}, \tag{6.6}$$

where $\varepsilon_n^{\mathrm{nominal}}$ is the efficiency from the nominal MC and $\varepsilon_n^{\mathrm{regen.}}$ is the efficiency from

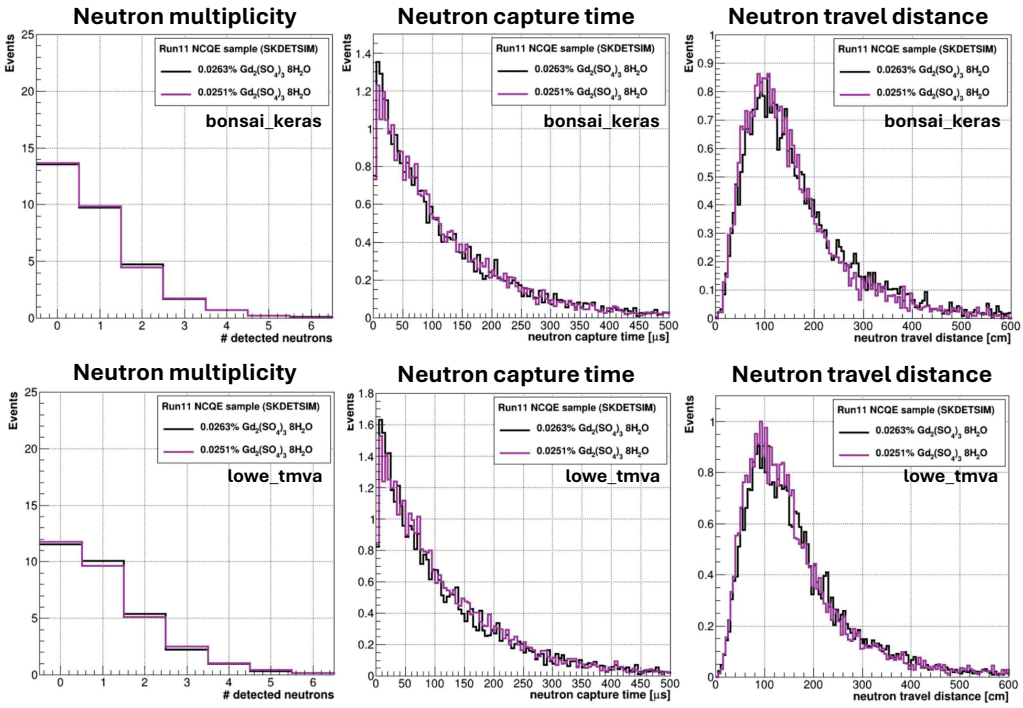

Figure 6.1: Neutron multiplicity (left), neutron-capture time (center), and neutron travel distance (right) for $Gd_2(SO_4)_3 \cdot 8H_2O$ concentrations of 0.0263% (black) and 0.0251% (purple). Upper row: `bonsai_keras`. Lower row: `lowe_tmva`.

regenerated MC using an alternative SI treatment (the ±30% cross section variation or the BERT/INCL/BIC options).

The `bonsai_keras` configuration yields an overall neutron tagging efficiency that is effectively independent of the neutron travel distance. This distance independence reduces the SI–model systematic uncertainty, as seen from the change in $\Delta\varepsilon_{\mathrm{SI}}$ between `bonsai_keras` and `lowe_tmva` in SKDETSIM (Table 6.2). Switching from `lowe_tmva` to `bonsai_keras` shrinks $\Delta\varepsilon_{\mathrm{SI}}$ from $^{+3.3\%}_{-6.7\%}$ to $^{+0.0\%}_{-1.7\%}$.

Figure 6.2 compares delayed–signal observables across secondary–interaction (SI) models. The three columns show, from left to right, the neutron–capture time, the neutron travel distance, and the overall tagging efficiency as a function of travel distance. The top two rows correspond to the `bonsai_keras` tagger: the first row contrasts SKDETSIM and SKG4 using INCL and BIC, and the second row repeats the comparison both using the Bertini (BERT) model within SKDETSIM and SKG4. The third and fourth rows present the same SKDETSIM and SKG4 comparison for the `lowe_tmva` settings.

Comparing regenerated and nominal MC under ±30% cross-section variations, we assign asymmetric systematic uncertainties on the overall tagging efficiency. For the `bonsai_keras` setting, relative changes of −0.9% and −1.7% yield an uncertainty of $^{+0.0\%}_{-1.7\%}$, while for `lowe_tmva`, changes of +3.3% and −6.7% result in an uncertainty

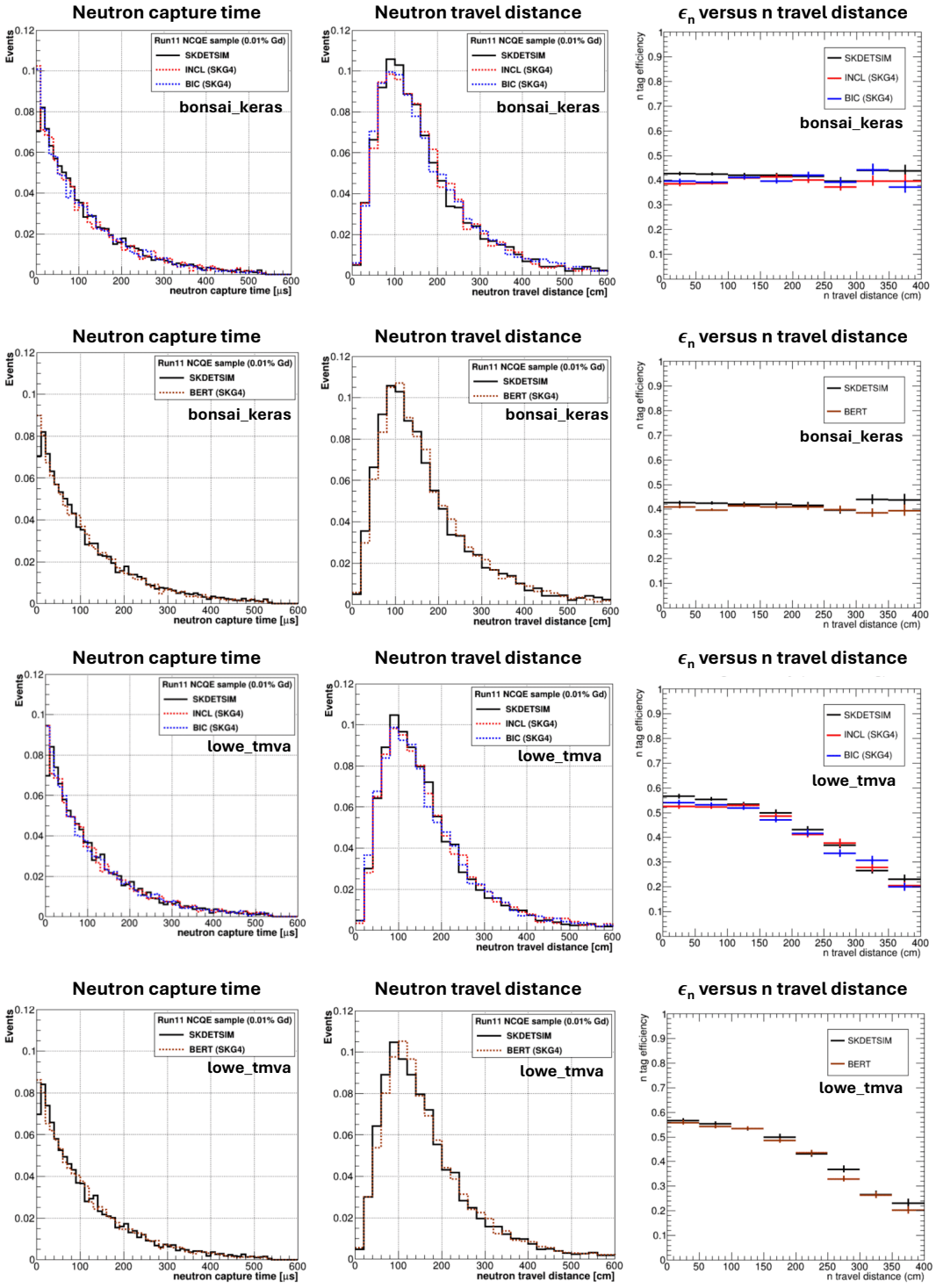

Figure 6.2: Delayed–signal observables for SKDETSIM and SKG4 under several SI models. Columns show capture time, travel distance, and tagging efficiency versus travel distance. Rows are, in order: `bonsai_keras` with SKDETSIM/INCL/BIC, `bonsai_keras` with SKDETSIM/BERT, and `lowe_tmva` with the same framework comparisons.

Table 6.2: Variations of delayed signal selection performance by nucleon SI. These numbers are normalized by Run 11, 1.76×10^{20} POT.

	bonsai_keras					
	SKDETSIM			SKG4		
	-30%	Nominal	+30%	INCL	BIC	BERT
# Truth neutrons	66.5	70.8	73.3	57.0	57.8	76.2
# n candidates (Pre-selec.)	44.0	48.3	49.9	37.3	38.0	50.4
# Delayed signals (Pre-selec. + NN)	28.1	30.5	31.3	23.5	23.9	31.6
Noise rate	1.1%	1.3%	1.1%	3.7%	3.7%	3.3%
Overall tagging efficiency	42.3%	43.1%	42.7%	41.2%	41.3%	41.5%
$\Delta\epsilon_{SI}$	-1.7%	-	-0.9%	-0.7%	-0.5%	-
	lowe_tmva					
	SKDETSIM			SKG4		
	-30%	Nominal	+30%	INCL	BIC	BERT
# Truth neutrons	66.5	70.8	73.3	57.0	57.8	76.2
# n candidates (Pre-selec.)	47.8	51.9	53.4	40.3	41.3	54.9
# Delayed signals (Pre-selec. + NN)	31.5	36.0	38.5	27.6	28.3	37.6
Noise rate	1.3%	1.5%	1.3%	4.4%	4.5%	3.9%
Overall tagging efficiency	47.4%	50.9%	52.5%	48.5%	48.8%	49.5%
$\Delta\epsilon_{SI}$	-6.7%	-	+3.3%	-2.0%	-1.3%	-

of $^{+3.3\%}_{-6.7\%}$.

6.4 Detector Response for Neutron Signal

The detector–response systematic associated with the neutron capture signal was evaluated using an Americium–Beryllium (AmBe) neutron source [122]. The source reactions are

$$\alpha + {}^{9}\mathrm{Be} \rightarrow {}^{12}\mathrm{C}^{*} + n, \tag{6.7}$$

$$ {}^{12}\mathrm{C}^{*} \rightarrow {}^{12}\mathrm{C} + \gamma\ (4.4\ \mathrm{MeV}). \tag{6.8}$$

Approximately half [128] of the emitted neutrons coincide with a 4.438 MeV γ-ray from the de-excitation of the $^{12}\mathrm{C}^{*}$ first excited state, providing a distinct signature for identification. The remaining neutrons, associated with the ground or higher excited states, typically lack detectable γ-rays and therefore contribute to an unwanted continuous pile-up background. Because the source position is known and the statistics are high, this serves as a robust calibration source for neutron capture signal. We compare the AmBe calibration data with MC generated using SKG4, which includes the detailed AmBe source geometry and the relevant detector–response physics process.

A dedicated AmBe simulation exists only in SKG4. To apply the calibration to SKDETSIM, which uses a different neutron–tracking treatment and lacks the

AmBe geometry, Ref. [129] generates neutron particle–gun MC samples in both SKG4 and SKDETSIM and transfers the result via a ratio:

$$\varepsilon_{\mathrm{AmBe}}^{\mathrm{SKDETSIM}} = \frac{\varepsilon_{\text{p-gun}}^{\mathrm{SKDETSIM}}}{\varepsilon_{\text{p-gun}}^{\mathrm{SKG4}}} \cdot \varepsilon_{\mathrm{AmBe}}^{\mathrm{SKG4}}, \tag{6.9}$$

where $\varepsilon_{\mathrm{AmBe}}^{\mathrm{SKG4}}$ is the neutron tagging efficiency from the AmBe in SKG4, and the $\varepsilon_{\text{p-gun}}$ terms represent neutron tagging efficiencies from particle-gun simulations in the respective frameworks. This procedure accounts for differences between SKG4 and SKDETSIM.

Table 6.3 summarizes the fractional uncertainties affecting the overall tagging efficiency. The uncertainty is seperated with source type as AmBe neutron modeling, detector modeling, and Gd modeling.

AmBe neutron modeling The Am/Be source emits fast neutrons ($\mathcal{O}(1)$ MeV) in a range where invisible $^{16}\mathrm{O}(n,\alpha)^{13}\mathrm{C}$ reactions compete with elastic thermalization. Based on discrepancies between the standard ISO spectrum [135] and recent measurements [137], we assign a ± 0.5 MeV uncertainty to the neutron kinetic energy. This variation alters the expected fraction of alpha emissions and propagates a 0.6% fractional uncertainty to the neutron tagging efficiency.

Detector modeling To evaluate the impact of time-varying detector conditions, we performed run-by-run MC simulations incorporating continuously monitored parameters such as PMT gain, dark rates, water transparency, and top-bottom asymmetry. Restricted to periods with available background data, the resulting efficiency distributions yield relative standard deviations of 1.3%, which we adopt as the systematic uncertainty for the time evolution of detector characteristics.

The overall PMT response scaling factor is calibrated for each SK phase using cosmic ray muons to minimize data-MC charge discrepancies. Adopting a 1% for the systematic uncertainty from the PMT quantum efficiency.

Gd modeling The dominant contributions arise from the capture fractions on hydrogen and gadolinium, r_H and r_{Gd}.

As figure 6.3 shows, the ^{241}AmBe MC simulation underestimates the r_H compared with the AmBe calibration result. By examining the PMT-hit distribution, we obtain a χ^2-fitted r_H of $56\pm3\%$, which is consistent with the analytically predicted value of $56.2\pm1.5\%$ from ENDF/B-VII.1. In contrast, the ^{241}AmBe MC simulation in SKG4 predicts a lower value, 48% for r_H [129].

The underestimation of r_H occurs because the GEANT4 Neutron High-Precision model

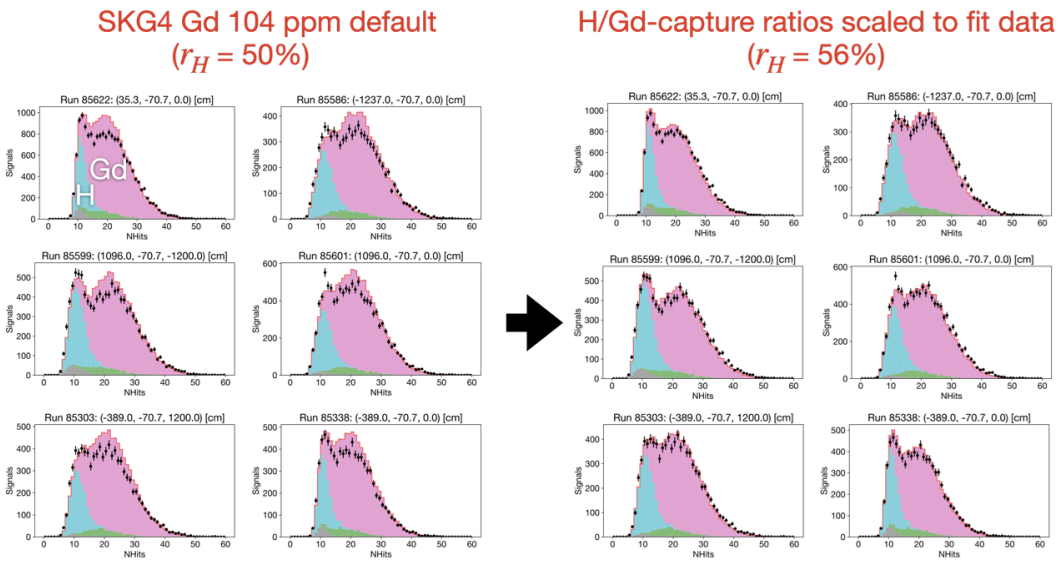

Figure 6.3: Comparison of NHits distributions for Am/Be data (black) and MC simulations (red) across different source positions, with r_H set to 50% (left) and 56% (right). The simulation components are color-coded: true Gd(n,γ) (pink), H(n,γ) (cyan), 4.438 MeV γ-rays (green), and background PMT hits (gray). All histograms are normalized by the number of events. Figure adapted from Ref. [129]

currently treats hydrogen as a free nucleus rather than accounting for water's molecular mass. As a result, hydrogen is simulated to move 18 times faster than it should, reducing the probability of neutron capture on hydrogen and thus lowering the r_H [130]. After combining all the detector response uncertainties, we obtain r_H with a central value of $48^{+8.2}_{-1.5}$%, and this uncertainty carries over to the r_{Gd} because $r_{Gd} \approx 1 - r_H$. The ϵ_n is obtained by adding the hydrogen contribution, given by the product of r_H and detection efficiency on hydrogen, to the gadolinium contribution, defined analogously.

The total detector–response systematic for neutron capture is $\Delta\varepsilon_{\text{Detector}} = {}^{+12.3\%}_{-18.9\%}$ for both `bonsai_keras` and `lowe_tmva`, as summarized in Table 6.3.

Table 6.3: Detector response uncertainties on tagging efficiency.

Source type	Source name	How to compare with nominal MC	Fractional uncertainty
AmBe neutron modeling	1. neutron kinetic energy	-0.5 MeV shifted MC	0.6%
Detector modeling	2. Time evolution of detector characteristics	run-by-run MC	1.3%
	3. PMT quantum efficiency	$\pm1\sigma$ shifted MC	1.0%
Gd modeling	4. Gd/H-capture ratio	Analytical prediction	+3.1% / -14.1%
	5. Gd-capture γ model	Alternative model MC	11.8%
	Total		+12.3% -18.9%

6.5 Discussions about Other Systematic Uncertainties

Beyond the dominant systematic uncertainties discussed above, we also evaluate additional sources relevant to this analysis: the neutrino beam flux, neutrino oscillation, nucleon FSI, π FSI/SI, μ and π capture on ^{16}O, prompt-signal selection, PMT gain, and water conditions. Our treatment largely follows the existing study [52], with modifications designed for this study.

6.5.1 ν beam flux

Uncertainties in the T2K beam flux for the four neutrino flavors (ν_e, $\bar{\nu}_e$, ν_μ, $\bar{\nu}_\mu$) over 0.1–10 GeV are propagated to the MC to quantify their impact on the overall tagging efficiency. The resulting fractional uncertainty from flux parameters is 0.38%.

6.5.2 ν oscillation

Oscillation parameter uncertainties, taken from [124], are propagated by reweighting the nominal MC and evaluating the change in overall tagging efficiency. The resulting fractional uncertainty is 0.02%, which is small because oscillation-parameter errors alter oscillation probabilities and impact only CC interactions in the MC.

6.5.3 Nucleon FSI

Uncertainty in nucleon final–state interactions can change both the yield and the kinetic energy of neutrons from ν–^{16}O NCQE interaction, which in turn affects the overall tagging efficiency. We vary the scattering and particle–production probabilities as in Ref. [52] and obtain a 0.9% fractional uncertainty on the overall tagging efficiency. This value is small compared with other sources. It is also conservative, since the `bonsai_keras` settings is effectively distance independent, which reduces sensitivity to neutron travel distance effects in a manner similar to the SI model case. We therefore adopt 0.9% for the nucleon FSI contribution to the total systematic uncertainty.

6.5.4 π FSI/SI

Uncertainties in π FSI and SI, as modeled in NEUT, modify the mixture of interaction topologies and can change the overall tagging efficiency. We evaluates this by varying the parameter vectors as shown in Table 6.4 that control π FSI and SI in NEUT. The resulting fractional uncertainty to total tagging uncertainty is $\pm$0.42%. Given its small size, we adopt $\pm$0.42% for the total systematic uncertainty calculation.

Parameter	Interaction	Type	Value
p_F^O	CCQE	^{16}O Fermi momentum	225 ± 31 MeV/c
E_B^O	CCQE	^{16}O binding energy	27 ± 9 MeV
M_A^{CCQE}	CCQE	Axial mass	1.2 ± 0.41 GeV/c^2
2p2h	2p2h	Normalization par.	1.0 ± 1.0
C_{A5}^{RES}	CC and NC1π	Axial form factor	1.01 ± 0.12
M_A^{RES}	CC and NC1π	Axial mass	0.95 ± 0.15 GeV/c^2
BG_A^{RES}	CC and NC1π	I=1/2 continuum background	1.3 ± 0.2
CC other	CC other	E-dependent par.	0.0 ± 0.4
CC coherent	CC coherent	Normalization par.	1.0 ± 0.3
NC other	NC other	E-dependent par.	1.0 ± 0.3
NC coherent	NC coherent	Normalization par.	1.0 ± 0.3
FS e^- Bremsstrahlung	CC ν_e	Normalization par.	1.00 ± 0.03

Table 6.4: ν cross-section parameters. Figure taken from Ref. [52].

6.5.5 μ and π capture on ^{16}O

A small fraction of CC events in the MC sample produce μ^- that can be captured on ^{16}O, yielding additional neutrons. Likewise, a small fraction of NC events produce π^- that may be captured and also generate neutrons. For example,

$$\mu^- + {}^{16}O \rightarrow \nu_\mu + n + {}^{15}N. \tag{6.10}$$

We estimate the uncertainty of these interactions by switching the cascade models between the intra–nuclear cascade model (Bertini) and the Chiral Invariant Phase Space (CHIPS) [131] model within SKDETSIM. The resulting fractional uncertainties on the total tagging efficiency are $^{+0.00\%}_{-3.47\%}$ for π^- capture on ^{16}O and $^{+0.00\%}_{-1.10\%}$ for μ^- capture on ^{16}O. These values are used in the total systematic uncertainty.

6.5.6 Prompt signal selection

Variations in the prompt selection variables ($E_{\rm rec}$, θ_C, `ovaQ`, `dwall`, `effwall`) can change the MC sample composition and thus the overall tagging efficiency.

We propagate the calibration uncertainties for $E_{\rm rec}$, θ_C, `ovaQ`, and vertex from Ref. [85], summarized in Table 6.5. For `dwall` and `effwall`, we derive position-related uncertainties from the NiCf vertex calibration using the worst case.

Using these values, we smear the reconstructed vertex, recompute the overall tagging

efficiency, and take the induced variation as the systematic uncertainty. The systematic uncertainty from prompt signal selection is ±1.16%, which we adopt in the total systematic uncertainty.

Table 6.5: Uncertainties for non-positional selection parameters.

Reduction parameter	Description	Uncertainty
E_{rec}	Reconstructed energy	±5%
θ_C	Cherenkov angle	±2°
ovaQ	Vertex and direction goodness	±1.5%
R_ν	Radial resolution	±10 cm
Z_ν	Vertical resolution	±5 cm

6.5.7 PMT gain

Ref. [52] reported a +1.6% shift in overall tagging efficiency from long-term increases in ID-PMT gain. Our dataset (Run 11) spans only ∼ 50 days, during which the gain remained relatively stable (Figure 6.4). Consequently, time-dependent PMT-gain effects are negligible for this analysis, and we assign no additional uncertainty from PMT-gain variation.

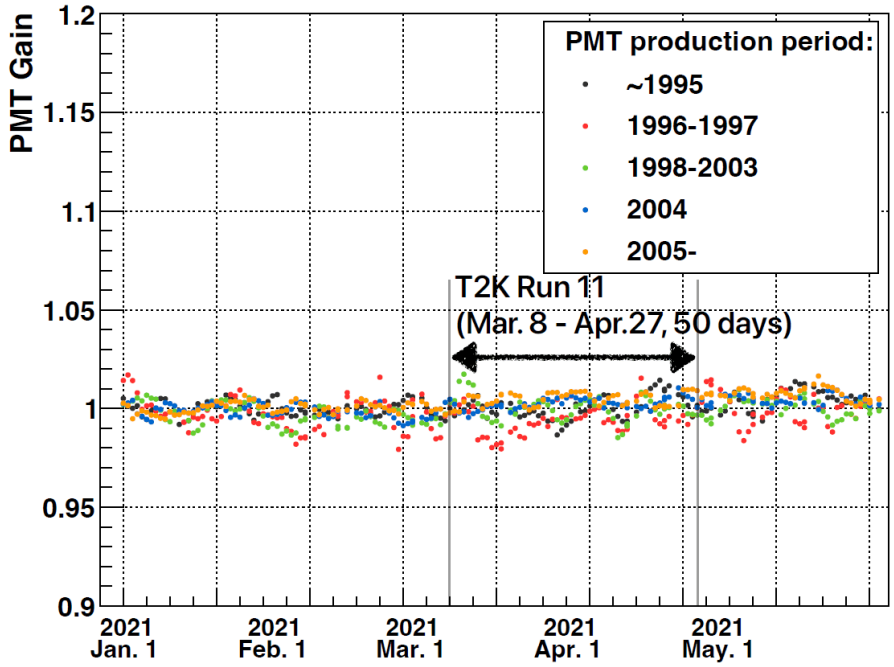

Figure 6.4: PMT gain variation within the T2K Run 11 period.

6.5.8 Water status

Water-related systematics are driven by two effects: water transparency and PMT dark noise. Changes in either quantity can alter the number and timing of PMT hits, thereby affecting the overall tagging efficiency. Water transparency is continuously

monitored with cosmic muon data, providing a monitor of the detector's water status. The trends for transparency and PMT dark rates during Run 11 are shown in Figure 6.5 and are stable over the $\sim$ 50-day period. We therefore treat time variation in water status as negligible and assign no additional uncertainty from this source.

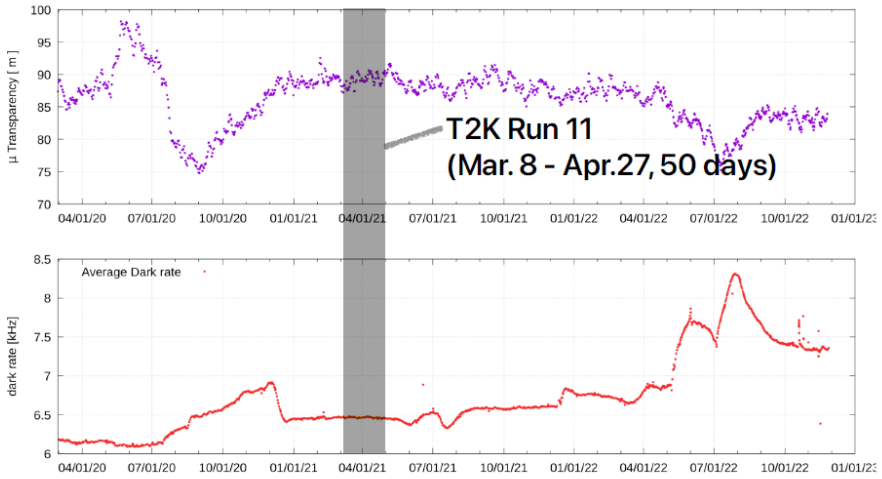

Figure 6.5: Water transparency and PMT dark-rate trends during the T2K Run 11 period.

6.6 Total Systematic Uncertainties

Table 6.6 compiles all contributions to the total uncertainty on the overall tagging efficiency. In this work, we re-evaluate the statistical and systematic uncertainties on the mean neutron multiplicity arising from Gd concentration, SI models, prompt-signal selection, PMT gain, and water status, with treatments specific to Run 11. Detector response systematics related to the neutron signal, namely the Gd/H capture ratio and the Gd-capture γ model, follow Ref. [122]. The ν beam flux, nucleon FSI, π FSI/SI, π capture on ^{16}O, and μ capture on ^{16}O are taken from Ref. [52] and adapted to this analysis where needed.

We summarize results for two delayed-signal selection settings, `bonsai_keras` and `lowe_tmva`. The main difference between these settings is the nucleon SI contribution: `bonsai_keras` yields a smaller Nucleon SI uncertainty because it uses the delayed signal vertex directly in the selection setting, which reduces sensitivity to neutron travel distance effects. At the same time, SK-Gd introduces additional detector-response systematics from the mixture of H and Gd neutron captures: the Gd/H capture ratio and the Gd-capture γ model are among the dominant contributors. The resulting overall fractional uncertainties on the neutron-tagging efficiency are $^{+12.5\%}_{-19.9\%}$ for `bonsai_keras` and $^{+12.9\%}_{-20.5\%}$ for `lowe_tmva`.

Table 6.6: Summary of systematic uncertainties on the overall neutron tagging efficiency. Sources between the dashed lines are those that were taken from AmBe calibration results [129].

Source	Fractional uncertainty	
	`bonsai_keras`	`lowe_tmva`
MC statistics	$\pm 0.3\%$	$\pm 0.3\%$
Gd concentration	$\pm 1.2\%$	$\pm 1.6\%$
Nucleon SI	$+0.0\%/-1.7\%$	$+3.3\%/-6.7\%$
AmBe n modeling	$\pm 0.6\%$	$\pm 0.6\%$
Detector modeling	$\pm 1.6\%$	$\pm 1.6\%$
Gd modeling	$+12.2\%/-18.4\%$	$+12.2\%/-18.4\%$
ν beam flux	$\pm 1.0\%$	$\pm 1.0\%$
ν oscillation	$\pm 0.02\%$	$\pm 0.02\%$
Nucleon FSI	$\pm 0.9\%$	$\pm 0.9\%$
π FSI/SI	$\pm 0.4\%$	$\pm 0.4\%$
π capture on ^{16}O	$+0.0\%/-3.5\%$	$+0.0\%/-3.5\%$
μ capture on ^{16}O	$+0.0\%/-1.1\%$	$+0.0\%/-1.1\%$
Prompt signal selection	$\pm 1.2\%$	$\pm 1.2\%$
PMT gain	negligible	negligible
Water status	negligible	negligible
Total	$+12.5\%/-19.9\%$	$+12.9\%/-20.5\%$

Finally, we report the key parameters that drive the mean neutron multiplicity: the overall tagging efficiency (ϵ_{n}) and the noise rate (η_{Noise}).

Table 6.7: Total uncertainties on overall neutron tagging efficiency and background rate for Run 11.

Run 11	ϵ_{n}	η_{Noise}
`bonsai_keras`	$43.1\%^{+5.4\%}_{-8.4\%}$	$1.3\% \pm 0.1$
`lowe_tmva`	$50.8\%^{+6.5\%}_{-9.9\%}$	$1.5\% \pm 0.1$

Chapter 7

Mean neutron multiplicity result

The mean neutron multiplicity is computed by inserting N_{prompt} from Tables 5.5, N_{delayed} from Tables 5.9 (`bonsai_keras`) and 5.10 (`lowe_tmva`), and ϵ_n and η_{Noise} from Table 6.7 into Eq. 6.1. The uncertainties on all inputs are summarized in Tables 6.6 and 6.7. For the T2K Run 11 data we obtain

$$M_{\text{data}}(\texttt{bonsai_keras}) = 1.37 \pm 0.33\ (\text{stat.})^{+0.17}_{-0.27}\ (\text{syst.}), \tag{7.1}$$

$$M_{\text{data}}(\texttt{lowe_tmva}) = 1.35 \pm 0.30\ (\text{stat.})^{+0.17}_{-0.28}\ (\text{syst.}). \tag{7.2}$$

For comparison, MC predictions using NEUT 5.6.3 and NuWro 21.09 with the `bonsai_keras` selection are

$$M_{\text{MC}}(\text{NEUT 5.6.3}) = 2.24 \pm 0.01\ (\text{stat.}), \tag{7.3}$$

$$M_{\text{MC}}(\text{NuWro 21.09}) = 2.22 \pm 0.01\ (\text{stat.}). \tag{7.4}$$

Figure 7.1 compares the measured values with these predictions and with the T2K Run 1–9 result from Ref. [52], alongside expectations from NEUT 5.3.3, NuWro 18.02, and GENIE. This measurement indicates that mean neutron multiplicity from the Run 11 data is overpredicted in MC, a trend consistent with Ref. [52].

As discussed in Sec. 6.6, the choice of SI model may contribute to this discrepancy. Using SKG4 with different SI models and the `bonsai_keras` selection, the MC expectations are

$$M_{\text{MC}}(\text{SKG4-BERT}) = 2.28 \pm 0.01\ (\text{stat.}), \tag{7.5}$$

$$M_{\text{MC}}(\text{SKG4-BIC}) = 1.87 \pm 0.01\ (\text{stat.}), \tag{7.6}$$

$$M_{\text{MC}}(\text{SKG4-INCL}) = 1.84 \pm 0.01\ (\text{stat.}). \tag{7.7}$$

Figure 7.2 compares the data with SI-model variants from SKDETSIM and SKG4, showing more consistent agreement between data and MC across mean neutron multiplicity with alternative SI models.

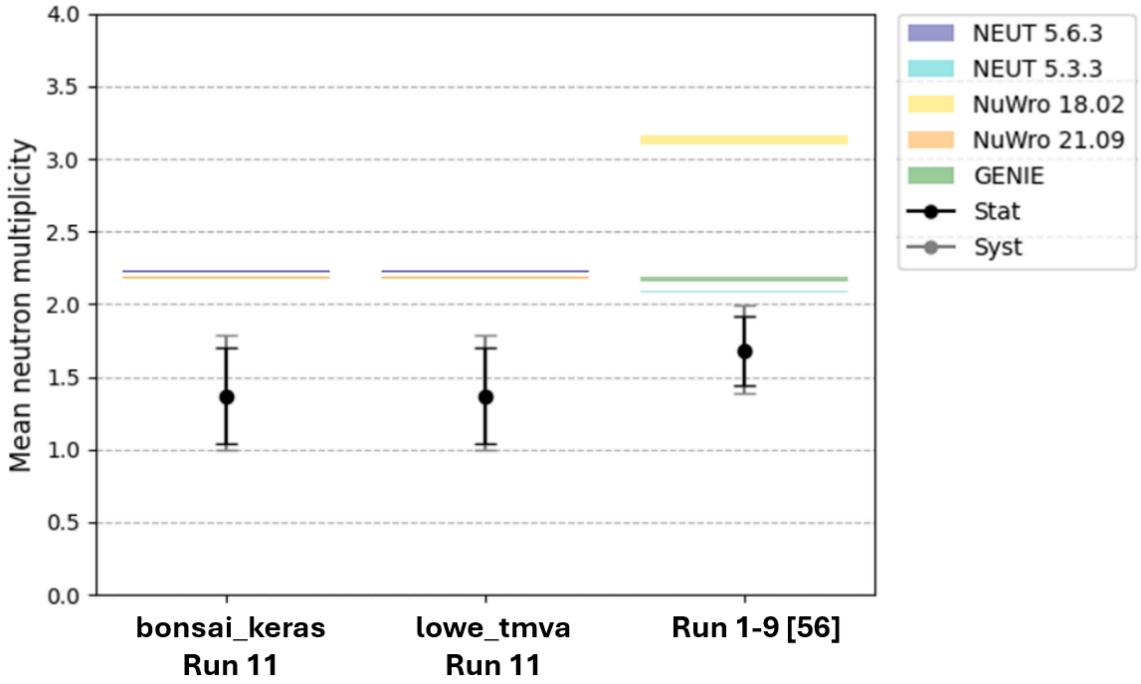

Figure 7.1: Mean neutron multiplicity for different neutrino generators. MC predictions use SKDETSIM with the Bertini-style SI model.

7.1 Discussion

This section examines factors beyond SI models that can influence neutron predictions: neutral-current two-particle–two-hole (NC 2p2h) interactions, the strange axial coupling g_A^s, hadrons produced during nuclear de-excitation (NucDeEx), and the spectral-function framework, including short-range correlations (SRC), Pauli blocking, and the random-phase approximation (RPA).

Although direct measurements are limited, NC 2p2h processes [25] may change the expected neutron yield and needs to be assessed. Uncertainties in g_A^s, which differs between electron-scattering and ν-NCQE determinations, can also shift the prediction. De-excitation of ^{16}O, as modeled in NucDeEx, can emit neutrons and alter the total multiplicity. Finally, SRC, Pauli blocking, and RPA within the SF description can modify neutron production and should be quantified. Table 7.1 quantified each factor's impact on the delayed signals, where the following sections detail each one.

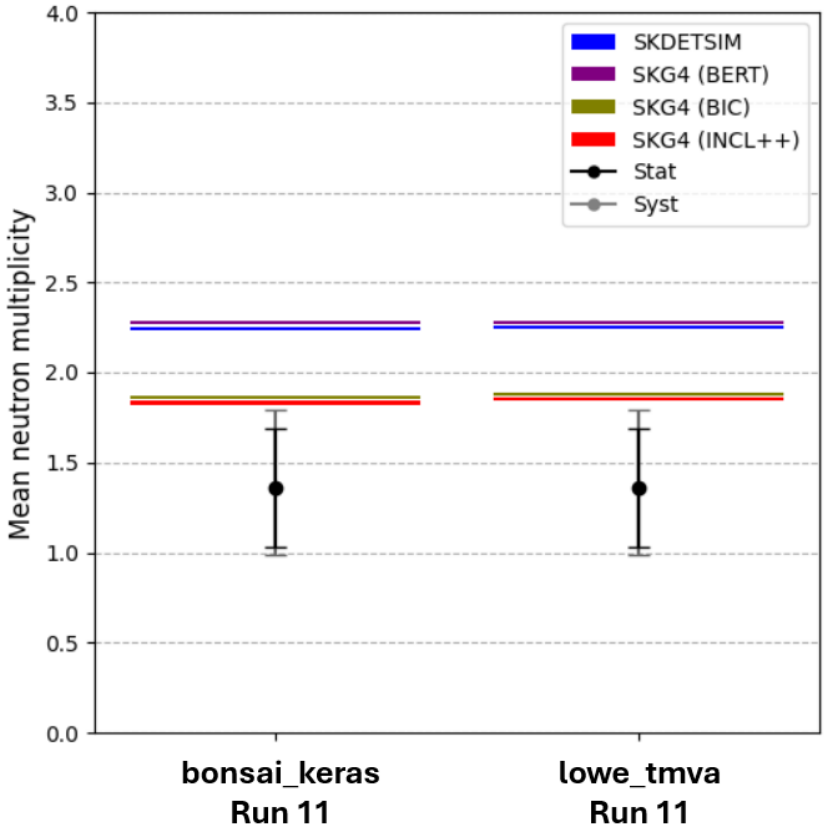

Figure 7.2: Mean neutron multiplicity for different SI models. MC predictions use NEUT 5.6.3.

Table 7.1: Summary of the delayed signal variations under different conditions beyond the SI models.

Factors	$\Delta N_{delayed}$	Reference setting
Nominal setting	-	NEUT w/ GEANT3 GCALOR
Short-Range Correlations	+9.4%	NuWro [132]
NC 2p2h	+12.0%	NuWro w/ TEM model [133]
g_A^s	−9.0%	NuWro w/ $g_A^s = -0.3$
Deexcitaion in ν-^{16}O NCQE	+0.9%	NEUT w/ NucDeEx [104]
Pauli Blocking	−0.5%	NEUT w/ PB
Randon Phase Approximation	−13.0%	NEUT w/ MDLQE = 1002
GEANT3 SI model	−7.9%/+2.5%	NEUT w/ GEANT3 GCALOR ±30% Xsec
GEANT4 SI models	−25.6%	NEUT w/ GEANT4 INCL++

7.1.1 NC 2p2h interaction

The two-body current, or meson-exchange current (MEC), is an interaction of a correlated nucleon pair inside the nucleus. Although the neutrino NC 2p2h interaction has never been measured, electron-scattering results establish the existence of 2p2h processes. It is therefore appropriate to examine how NC 2p2h could change the predicted neutron yield in this study.

For modeling, the Valencia model [25] provides CC 2p2h but not NC 2p2h. Because NEUT relies on the Valencia model for 2p2h, NC 2p2h cannot be generated in NEUT. In contrast, the Transverse Enhancement Model (TEM) [133] in NuWro modifies the vector magnetic form factors and supports both CC and NC 2p2h, which enables NC 2p2h simulations in NuWro. In addition to the cross section of NC 2p2h, the composition of interacting nucleon pairs (pp, pn, nn) can vary. This study adopts the default value for np pairs in NuWro, which is $85^{+15}_{-20}\%$.

Figure 7.3 illustrates the neutron multiplicity prediction, including NC 2p2h interaction with NuWro. The left plot shows the nominal simulation from NEUT depicted with a solid black line, while NuWro's simulations with and without NC 2p2h interaction are presented with dashed red and dashed blue lines, respectively. The center plot compares NEUT and NuWro with NC 2p2h interaction. Here, different colors separate each interaction channel in NEUT. The right plot displays the interaction channels from NuWro, highlighting the NC 2p2h interaction with a light blue histogram. Notably, neutrons resulting from NC 2p2h interactions constitute approximately a 12% increase of the delayed signals, following the model switch from Nieves to TEM for both CC and NC 2p2h interactions in NuWro. In predicting the total neutron number, SI models introduced a 26% decrease, making the 12% increase from NC 2p2h interactions relatively minor.

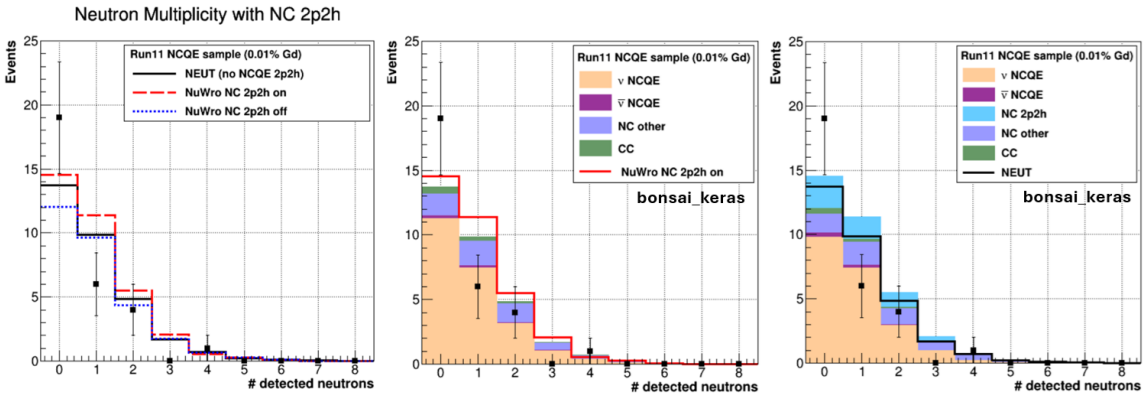

Figure 7.3: The neutron multiplicity with NC 2p2h simulation with TEM. The left plot compares the 2p2h simulation in NEUT (black), NuWro with Nieves (blue), and NuWro with TEM (red). The center plot presents interaction channels for NEUT. The right plot highlights the NC 2p2h interactions in NuWro with a light blue histogram.

7.1.2 Strange axial coupling constant

The strange axial coupling g_A^s characterizes the strange quark–antiquark contribution to the nucleon spin, conventionally written as δs. Polarized lepton deep inelastic scattering has provided several measurements, including $\delta s = -0.18 \pm 0.05$ (EMC) [134, 135], $\delta s = -0.085 \pm 0.018$ (HERMES) [136], and $\delta s = -0.08 \pm 0.02$ (COMPASS) [137].

Neutrino NCQE measurements also constrain g_A^s. Results from BNL E734 [46] and MiniBooNE [138] exhibit correlations with the axial mass M_A, largely because they rely on proton targets. The strongest constraint to date comes from KamLAND, which uses neutron multiplicity in ν–NCQE interactions [44]. A summary of these results is shown in Figure 7.4 (adapted from Ref. [44]).

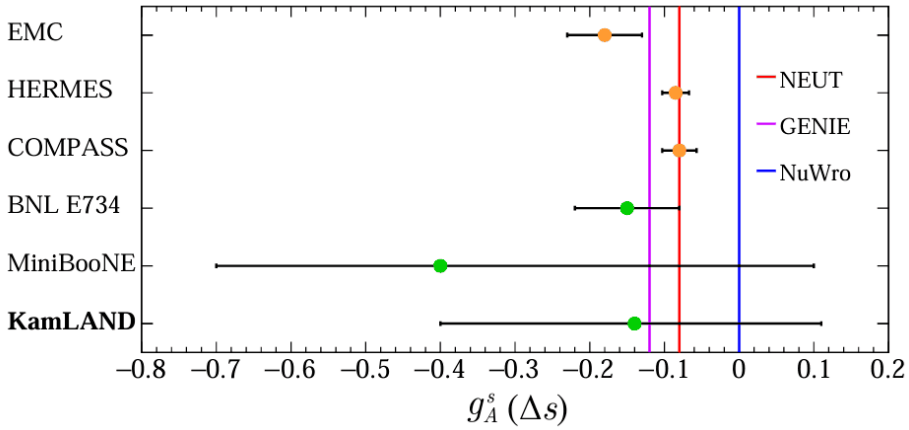

Figure 7.4: Summary of experimental constraints on the strange axial coupling g_A^s. Orange points: δs from polarized lepton deep inelastic scattering (EMC [134, 135], HERMES [136], COMPASS [137]). Green points: ν–NCQE measurements (BNL E734 [46], MiniBooNE [138], KamLAND [44]). Adapted from Ref. [44].

Neutron multiplicity depends on the strange axial coupling g_A^s. A negative g_A^s increases the NCQE cross section on protons and decreases it on neutrons. Because NCQE interactions on free protons do not emit neutrons, making g_A^s more negative lowers the expected neutron count.

NEUT simulates NCQE with the spectral–function model of Ankowski [26] and fixes $g_A^s = -0.08$. Total cross sections are precomputed and stored in `crsdata/qelSF*`, and there is no available tool to regenerate these tables for other g_A^s values. Adjusting g_A^s in NEUT is therefore nontrivial. In contrast, NuWro allows g_A^s to be set as an input, so we vary g_A^s using NuWro 21.09 and compare neutron multiplicities (Figure 7.5). In the left panel of Figure 7.5, the black curve corresponds to $g_A^s = -0.08$ (NEUT default), the dashed blue to $g_A^s = 0.0$ (NuWro default), and the dashed red to $g_A^s = -0.3$ (KamLAND–motivated). Moving to $g_A^s = -0.3$ lowers the predicted neutron count by about 9% relative to the NuWro default. For comparison, switching the SI model from BERT to INCL reduces the MC neutron prediction by about 26%.

Thus, the g_A^s dependence is present in this analysis but subdominant to the SI–model choice.

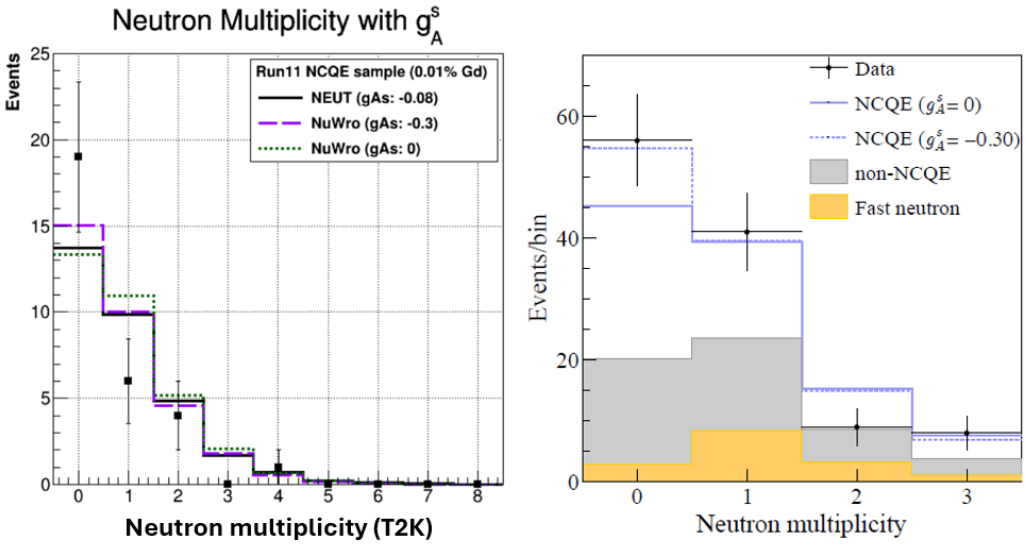

Figure 7.5: Left: MC predictions of neutron multiplicity for several g_A^s choices. The solid black curve uses the NEUT default $g_A^s = -0.08$. The dashed blue curve shows the NuWro default $g_A^s = 0.0$. The dashed red curve uses $g_A^s = -0.3$, following the KamLAND analysis, which is the neutron multiplicity result from KamLAND is shown in the right panel [44]. Lower g_A^s reduces the predicted neutron yield in both cases. Although g_A^s shifts the prediction, changes of the SI model produce a larger reduction, indicating a smaller relative impact from g_A^s.

7.1.3 De-excitation models in NEUT

This subsection evaluates how hadrons from the de-excitation model of ^{16}O in NEUT affect neutron multiplicity.

In ν–^{16}O NCQE interactions, the residual nucleus is frequently left in an excited state. It then de-excites and can emit protons, alpha particles, gamma rays, and neutrons. The predicted neutron yield therefore depends on the chosen de-excitation models in NEUT and can vary the neutron multiplicity. Quantifying this effect is important for accurate predictions.

Besides of the default de-excitation model, we use the NucDeEx package [104] as alternative, which calls TALYS [139] to model de-excitation of ^{16}O, with emphasis on nucleon emission and subsequent decays. TALYS applies the Hauser–Feshbach statistical model [140] to compute branching ratios and separation energies that govern emission of neutrons, protons, alpha particles, and gamma rays after the primary interaction and FSI. These outputs are then passed to NEUT to propagate the emitted particles on an event basis with realistic kinematics.

We regenerated the MC sample by interfacing NEUT with NucDeEx in SKDET-

SIM. Because the early NucDeEx release supported only pure NCQE, the simulation was restricted to NCQE pure events without other interaction channels. Compared with NEUT alone, NEUT+NucDeEx produces about a 5% increase in the total number of generated neutrons after all simulation stages. The excess depends on the prompt signal reconstructed energy (Figure 7.6) and is concentrated below 5 MeV. The prompt selection requires $E_{\mathrm{rec}} > 3.5$ MeV, which removes more than half of these additional neutrons. After applying this selection, the predicted increase in neutron yield is 2.3%.

In the delayed signal selection stage, interfacing NEUT with NucDeEx yields about 1% lower pre-selection efficiency than NEUT alone, while the NN classification efficiency remains comparable. The net effect is a 0.9% increase in the number of delayed signals.

Figure 7.7 shows the neutron multiplicity with and without NucDeEx. The distribution shifts to higher values when NucDeEx is enabled, and the number of delayed signals with more than two neutrons is larger for NEUT+NucDeEx (red) than for NEUT (black) in MC. The stage-by-stage neutron counts are summarized in Table 7.2. Overall, the de-excitation effect is small compared with the changes induced by switching SI models between SKDETSIM and SKG4.

Table 7.2: Stage-by-stage delayed signals for NEUT and NEUT+NucDeEx after NCQE cuts. NucDeEx increases delayed singal by 0.9% while slightly reducing overall tagging efficiency (-0.5%). The overall effect is small.

	NEUT	NEUT+NucDeEx	Diff.
N_{True} (no NCQE cuts)	540678	567897	+5.1%
N_{True}	256325 (100%)	262167 (100%)	+2.3%
Pre-selection	170215 (66.4%)	171950 (65.5%)	+1.3%
Pre-selection + NN	104129 (61.2%)	105092 (61.1%)	+0.9%
Overall tagging efficiency	40.6%	40.1%	-0.5%

7.1.4 Short Range Correlation

In NEUT, the spectral function is taken from the Ref. [93], which include both Mean-Field (MF) and Short-Range Correlation (SRC) components. The SRC term corresponds to CCQE events that can eject two nucleons from the primary interaction. NEUT attributes about 5% of the total CCQE cross section to SRC, whereas NuWro estimates about 15%. Because NCQE is also modeled with the spectral function, SRC can influence the final-state hadrons and thus the neutron multiplicity, so its impact is evaluated here.

We use two approaches. First, we compare neutron-multiplicity predictions from NEUT and NuWro to evaluate the impact of SRC. NuWro predicts 9.4% more

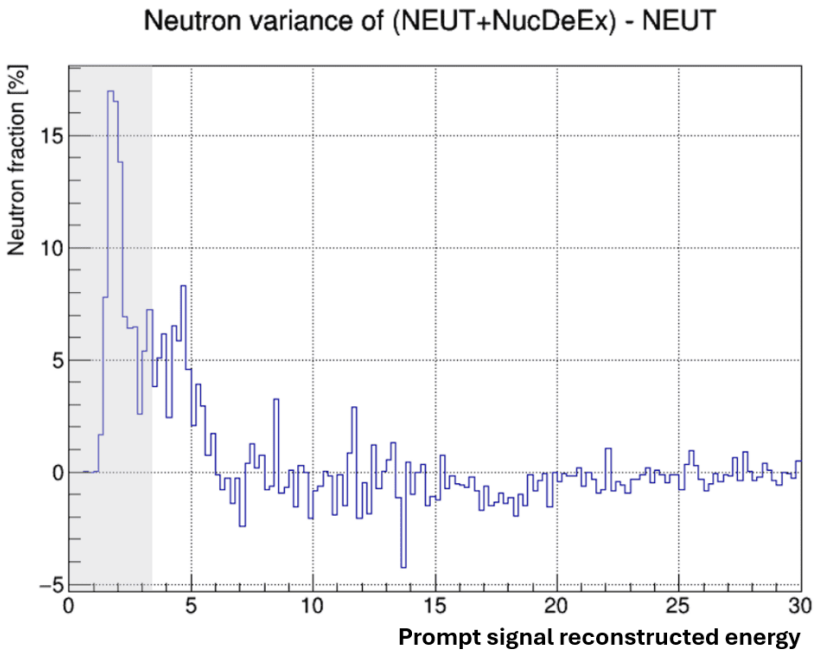

Figure 7.6: Fractional difference in NEUT+NucDeEx relative to NEUT only. The gray region marks the reconstructed energy region below 3.5 MeV, which will be filtered out in the prompt NCQE event selection.

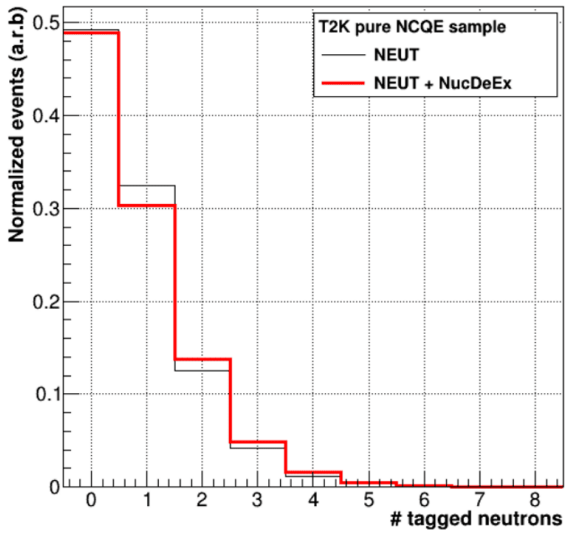

Figure 7.7: Neutron multiplicity with NucDeEx (red) and without (black) for pure NCQE interaction events. NEUT+NucDeEx yields slight more neutrons, shifting the distribution to higher multiplicities as expected.

neutrons than NEUT. Second, we vary the NEUT parameter `SFCORRNNFRAC`, which controls the correlated-pair component in the SF, from its default 0.3 to 0.6 and examine the change in neutron yield. Figure 7.8 shows the neutron multiplicity for the NEUT default (black) and the SRC-modified setting (red).

Increasing `SFCORRNNFRAC` to 0.6 yields about 11% fewer neutrons than the NEUT default. These shifts are modest compared with those from changing SI models, so the SRC contribution is subdominant in this analysis.

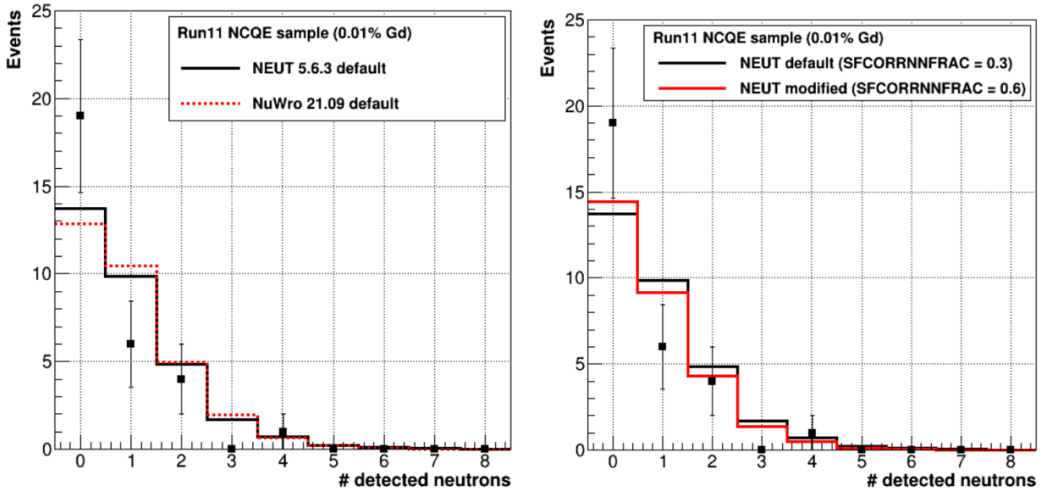

Figure 7.8: Neutron multiplicity for the NEUT default (black) and an SRC-modified configuration (red). Left: NEUT vs. NuWro. Right: NEUT with `SFCORRNNFRAC` varied from 0.3 to 0.6.

7.1.5 Pauli Blocking and Random Phase Approximation

In the NEUT spectral–function model, Pauli blocking is implemented assuming a simple Fermi–gas [141]: the cross section is set to zero when the momentum of the pre–FSI outgoing primary nucleon lies below the Fermi momentum. This suppresses the cross section and alters the shape of kinematic distributions at low momentum transfer.

The SF model is based on the plane–wave impulse approximation and does not include random–phase–approximation (RPA) effects. RPA modifies the outgoing nucleon wave function and redistributes strength at low Q^2. Omitting Pauli blocking and RPA can therefore lead to an overestimate of the SF prediction at low Q^2, with possible consequences for neutron production.

To quantify these effects, we use the following NEUT settings. For Pauli blocking, the dial `NEUT-PAUL` is set to 1 by default (turns off the Pauli Blocking). We compare to `NEUT-PAUL` = 0 (turns on the Pauli Blocking). For RPA, the dial `NEUT-MDLQE` offers configurations that include RPA but are not compatible with the

SF model. We therefore compare an RPA–enabled configuration, `NEUT-MDLQE` = 1002, with the SF default, `NEUT-MDLQE` = 422.

The upper panels of Figure 7.9 show the NCQE Q^2 distributions from NEUT. Enabling Pauli blocking produces almost no visible change, whereas including RPA yields a clear modification at low Q^2. The lower panels display the corresponding neutron multiplicities. With Pauli blocking, the predicted neutron yield is lower by about 0.5%, and the zero–neutron bin decreases slightly (consistent with a modest increase in proton emission). Including RPA reduces the neutron yield by about 13%. Both effects are smaller than the shifts induced by changing the SI model, so their overall impact on neutron multiplicity is subdominant in this study.

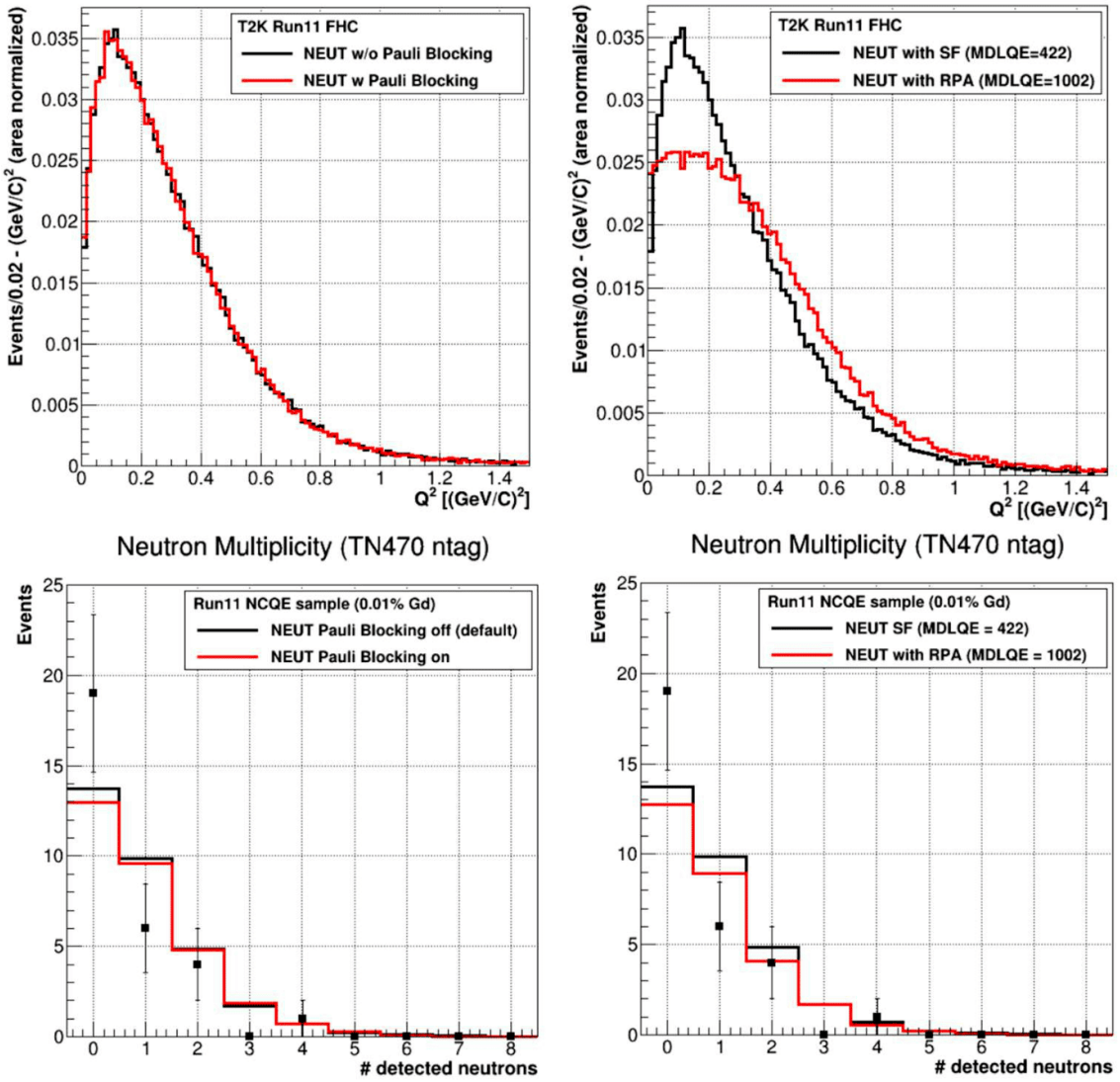

Figure 7.9: Impact of Pauli blocking (left) and RPA (right) on the Q^2 distribution (top) and neutron multiplicity (bottom). Pauli blocking causes a $\sim 0.5\%$ reduction in neutrons with minimal shape change, while RPA produces a noticeable low-Q^2 suppression and a $\sim 13\%$ reduction in neutrons.

7.2 Conclusion

In this study we presented the first measurement of neutron capture multiplicity resulting from ν-^{16}O NCQE-like interactions, based on a data set corresponding to 1.76×10^{20} POT using the T2K neutrino beam. The observed mean neutron capture multiplicity was 1.37 ± 0.33 (stat.)$^{+0.17}_{-0.27}$ (syst.). The measurement deviates from the prediction made by NEUT combined with the Bertini-based SI model (2.24 ± 0.01 (stat.)). However, the predictions using other SI models, INCL++ (1.84 ± 0.01 (stat.)) and BIC (1.87 ± 0.01 (stat.)), are in closer agreement with the data. We found that SI modeling dominates the uncertainty in the predicted numbers of neutrons, compared to modeling of processes, such as short-range correlations, NC 2p2h interactions, the strange axial coupling constant, Pauli blocking, and nuclear de-excitation following the neutrino interaction. Similar neutron overprediction has been observed in experiments using BERT-based SI models in both the CCQE [127, 142, 143, 144] and NCQE [43] channels, that is not observed in measurements using BIC model [44].

This work and these measurements highlight the need for a more precise understanding of SI processes and show that more data are needed to assess discrepancies and their origin. Despite the current uncertainties, the neutron detection efficiency of NCQE-like events estimated in this study can be utilized in atmospheric neutrino studies, for example, by accounting for the flux differences between T2K and atmospheric neutrinos. Further, the results of this study will serve as an essential validation tool for DSNB studies at water Cherenkov detectors, which aim to reduce atmospheric NCQE backgrounds using neutron information in Part III.

7.3 Future prospect

7.3.1 Insights from Other Neutrino-induced Neutron Measurements

So far, only a few measurements of neutrons associated with neutrino interactions have been conducted. The T2K [127], ANNIE [142], MINERνA [143] and SNO [144] collaborations have all observed an overprediction of the neutron (capture) multiplicity with either beam or atmospheric neutrinos. These results collectively indicate that simulation settings with BERT-based models, which are used in these experiments, tend to overpredict the neutron (capture) multiplicity, while KamLAND [44], whose simulation is based on the BIC model, does not see such an overprediction. Given the wide range of energies spanned by these experiments, from MeV to GeV, neutron overprediction observed in both the CCQE and NCQE channels may hint at a connection to FSI modeling. However, as demonstrated above, the effect of SI

modeling appears to dominate. SK [43] similarly tested several SI models, including BERT, INCL++, and BIC, using atmospheric neutrino NCQE events and reached a similar conclusion: BERT tends to overpredict, whereas INCL++ and BIC provide more accurate predictions for neutron capture multiplicity. One of the main reasons is that BERT used the de-excitation model native to the Bertini code, while others use the G4PreCompound model [105]. As described in Ref. [145], the G4PreCompound model relies on an exciton-based pre-equilibrium approach followed by semi-classical de-excitation mechanisms (e.g., Weisskopf-Ewing [118] or GEM [146]) once the nucleus reaches equilibrium, which provides higher accuracy for lower-energy processes but requires more computational time.

7.3.2 Insights from Other NCQE Related Measurements

A precise understanding of NCQE interactions and their final state particles is essential for DSNB searches at SK, Hyper-Kamiokande [147] and JUNO [148], as these detectors rely on neutron information to effectively reduce atmospheric NCQE backgrounds. In addition, improving our understanding of NCQE events is essential for dark matter [149, 150] and sterile neutrino search [151, 152, 153] in accelerator neutrino experiments, which further motivates improvements to measurements such as this work.

The statistical uncertainty on this measurement is expected to improve in the foreseeable future, as the anticipated POT proposed by T2K [154] has not yet been reached. Furthermore, T2K data collected during the pure water and 0.03% gadolinium phases of SK could enhance the available statistics, providing roughly 10 times the neutron statistics used in this study. Understanding secondary interactions then becomes essential to reduce uncertainties in this measurement. Indeed, despite better data-MC compatibility in the current measurement when switching to the INCL++ and BIC models, there is still room for improvement.

While RCNP [155, 156, 54] and the ChipIr beamline at the Rutherford Appleton Laboratory [157] provide γ measurements from SI, there remains a lack of neutron measurements from SI. An inverse-kinematics experiment using an oxygen beam at RIKEN-RIBF and the SAMURAI spectrometer [158] can address this gap. We anticipate that SI models will be better constrained in the near future by such measurements.

Dedicated upgrades to the GEANT4-based simulation may help reduce uncertainties on the neutron multiplicity and detection efficiency. The flexibility of GEANT4 allows users to customize the physics list based on the SI measurement mentioned above, offering the potential to enhance neutron kinematics predictions. A further dedicated calibration on the neutron capture, including the modification of

GEANT4 secondary interaction model, could further minimize uncertainties. While experiments like NINJA [159] can help confirm CC 2p2h, direct measurements of NC 2p2h are an important missing piece. Electron scattering experiments, such as those at Jefferson Lab [160], provide precise data on nucleon momentum distributions and could potentially improve short-range correlation modeling. These efforts will assist precise measurements of the strange axial coupling constant with neutrino sources, ultimately enhancing the accuracy of NCQE interactions.

7.3.3 Application to DSNB search at SK

The multiple scattering goodness (*MSG*) is a reconstructed parameter (detailed in Chapter 4.2.4) recently introduced in the DSNB analysis flow at SK [36], though it was originally developed for the solar neutrino analysis. This parameter is designed to assess the extent to which a particle has scattered during propagation in the detector by analyzing the pattern of PMT hits to determine their anisotropy. At energies relevant to this analysis and the DSNB study at SK, lower energy electrons are more likely to undergo multiple Coulomb scattering than those at higher energies. As a result, the lower energy particles typically produce a more isotropic pattern of hits after multiple scatterings. Since events with one or multiple γ's have an even more isotropic pattern, *MSG* is useful for separating the single-positron prompt event characteristic of the DSNB signal from NCQE backgrounds. An *MSG* value around 0.5 indicates consistency with a single particle direction, suggesting a more coherent Cherenkov pattern. Lower values indicate more isotropy.

The *MSG* distribution of T2K NCQE-like events in Run 11, as shown in the left plot of Figure 7.10. The histogram is generated using SKG4 with the BERT SI model, while the red dotted and black dashed lines correspond to the SI models INCL++ and BIC, respectively. The right plot of Figure 7.10 displays the θ_C versus *MSG* distribution, where delayed signal multiplicities are labeled as follows: zero neutrons are marked with blue squares, one neutron with red circles, and more than one neutron with orange triangles. We note that the NCQE-like events tend to populate lower *MSG* values as expected. The distribution itself is a valuable tool for estimating uncertainties in the DSNB analysis stemming from this paramater.

The *MSG* distribution varies with energy as is shown in Figure 7.11 (3.49 to 7.49 MeV) and Figure 7.12 (7.49 to 29.49 MeV). The agreement between the data and MC in both figures supports the use of *MSG* information to exclude NCQE events in the DSNB study. Figure 7.12 is particularly significant as it focuses on the reconstructed energy range that overlaps with the DSNB search. The efficiency of a $MSG > 0.38$ cut, shown in the left plot of Figure 7.12, is $21.4\% \pm 17.1\%$ (stat.). In the right plot, the gray region highlights the naive cut settings for the DSNB search

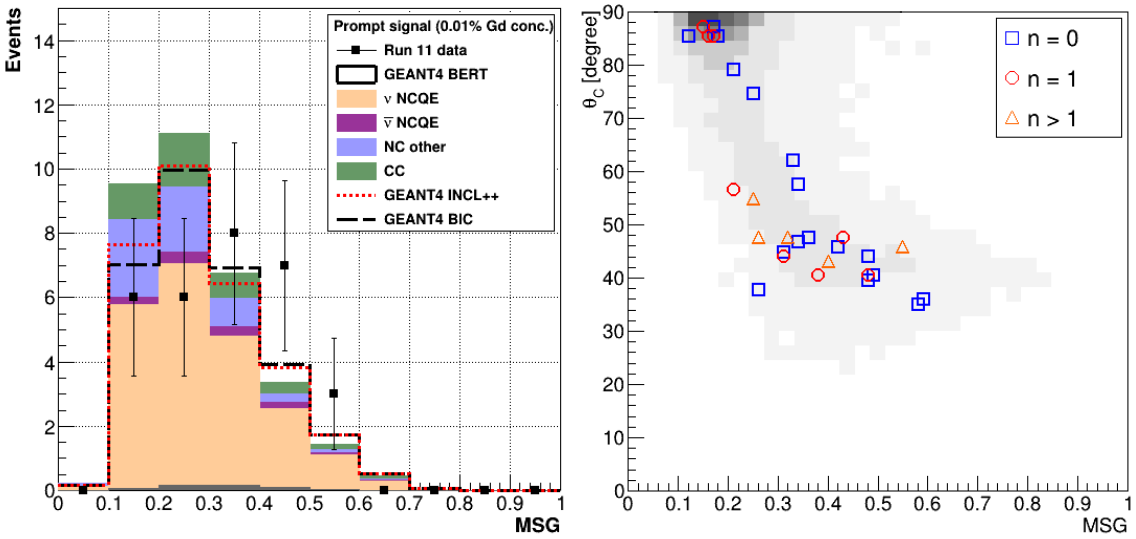

Figure 7.10: For both panels, events in the full energy range [3.49, 29.49] MeV are shown. Left panel: *MSG* distributions for prompt events, comparing data set with MC using the BERT SI model (histogram), INCL++ (dotted red), and BIC (dashed black). Right panel: Correlation between Cherenkov angle and *MSG*, with *MSG* $\sim$ 0.5 indicating coherent patterns. Delayed signal multiplicity for each prompt event is categorized as zero (blue squares), one (red circles), or more than one (orange triangles).

region at SK, defined as $38° < \theta_C < 53°$ with $MSG > 0.37$. However, we note that the cuts used in the SK DSNB search [36] will be determined on an energy bin-by-bin basis. The information presented here will be useful for a more detailed assessment of the systematic uncertainties associated with the *MSG* selection applied between atmospheric NCQE and DSNB events.

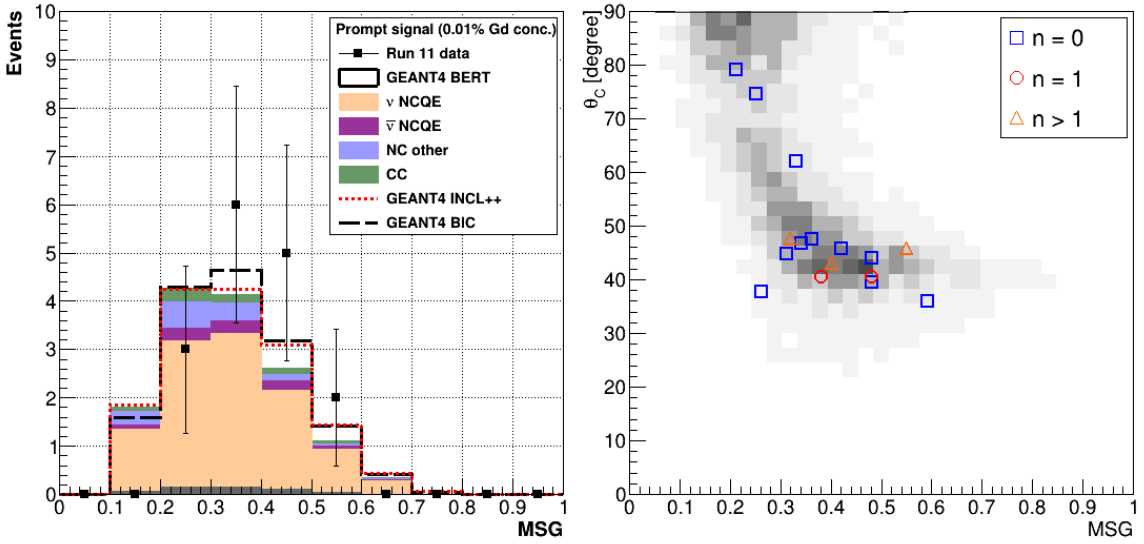

Figure 7.11: Comparisons of data and MC predictions for NCQE-like events within the reconstructed energy range of [3.49, 7.49] MeV, showing *MSG* distributions alongside θ_C.

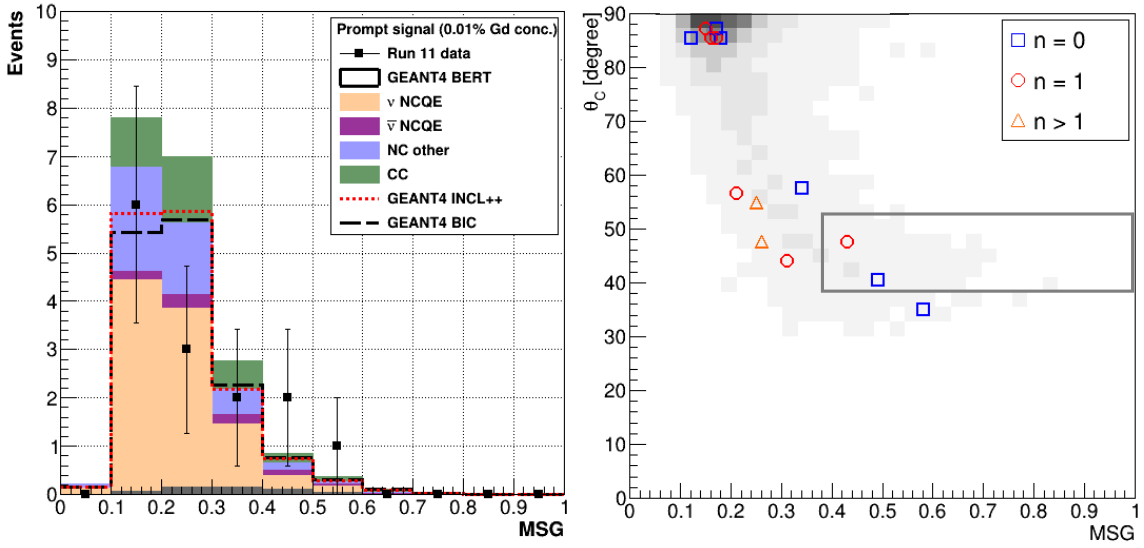

Figure 7.12: Same as Figure 7.11, but for the higher-energy range of [7.49, 29.49] MeV, which overlaps with the DSNB search window. In the left plot, an $MSG > 0.38$ selection yields an efficiency of 21.4% ± 17.1 (stat.), while the right plot highlights (in gray) the naive DSNB cut region ($38° < \theta_C < 53°$, $MSG > 0.37$).

Part III

Validation of DSNB Feature Classifiers Against atmospheric NCQE Using the T2K NCQE sample

Chapter 8

Measurement motivation

In SK searches for the DSNB, atmospheric NCQE is the dominant background, so suppression methods must be developed and the uncertainty quantified. The analysis of T2K Runs 1–9 (2019) [50] constrains the uncertainty of event features, specifically the Cherenkov angle (θ_C), using T2K data. This result reduced the total uncertainty for atmospheric NCQE cuts from about 100% to about 60%.

The event features of NCQE samples in T2K have been extensively studied across Runs 1–3 (2014) [49], Runs 1–9 (2019) [50], and Run 11 (2025) [161]. These measurements are especially useful because both T2K and atmospheric NCQE events have similar neutrino flux energy and are recorded with the SK. In this context, T2K NCQE events can serve as a proxy for atmospheric NCQE when evaluating uncertainties in event features.

More recently, another event features, Multiple Scattering Goodness (MSG), has been proposed to further suppress atmospheric NCQE events [36]. Although MSG is used in SK solar neutrino analyses, it has not yet been tested with NCQE events. Using the T2K NCQE sample, we will provide the data-driven uncertainty for MSG, study its correlations with the Cherenkov angle and visible energy (or the number of PMT hits), and refine classification strategies to better separate DSNB from atmospheric NCQE. With improved detector simulations that provide more reliable predictions of few MeV γ spectra, this is an ideal moment to test whether tighter selection cuts work as expected using T2K NCQE Run 1-11 data.

8.1 Measurement goal

Our goal is to determine the selection efficiencies and associated uncertainties for both DSNB and atmospheric NCQE events, and to estimate the resulting improvement in DSNB sensitivity. Current DSNB searches are limited by the large uncertainty in

atmospheric NCQE, as summarized in Table 8.1. To address this, we present a detailed investigation into the nucleon-nucleus interaction simulation. We demonstrate that the modeling of the dominant uncertainty sources, specifically the T2K cross-section, neutron multiplicity, and spectral shape, can be improved, resulting in an updated total uncertainty with T2K data. For Runs 1–9, the data is adopted from Ref. [50] with newly estimated MC, whereas Run 10 introduces both new data and MC. Finally, Run 11 data is sourced from PART-II with updated MC.

Table 8.1: The total uncertainty of the atmospheric NCQE spectrum used in the SK-VI DSNB study [23].

Source of Uncertainty	Value
T2K cross-section	44% (To be improved)
Atmospheric neutrino flux	15%
Flux difference	7%
Reductions	2%
Neutron tagging efficiency	9%
Neutron multiplicity	30% (To be improved)
Spectral shape	37% (To be improved)
Total	68% (To be improved)

First, we updated the T2K NCQE MC to match the latest simulation setup planned for the upcomming DSNB search. The update includes both the neutrino generator: NEUT, and detector simulations: the legacy SKDETSIM and the latest SKG4. Our top priority is the evaluation of the nuclear deexcitation model, the largest known systematic uncertainty for the NCQE sample. We studied MC truth γ multiplicities and energy spectra while switching the deexcitation models in NEUT and in SKG4. We then revised the uncertainties for the T2K NCQE event prediction and updated the NCQE cross section.

Next, we presented improvements to the DSNB selection that suppress the atmospheric NCQE background and describe how we constrained them. We evaluated the new selection separately for DSNB and atmospheric NCQE, each with its own uncertainty. The DSNB selection uncertainty is estimated using the LINAC calibration source, and the atmospheric NCQE selection uncertainty is estimated using T2K NCQE data.

Chapter 9

T2K NCQE Run 1-11 MC production and Data sample

This chapter presents an overview of the T2K ν-^{16}O NCQE MC simulation updates. We focus on the NEUT version 5.9.0 and the de-excitation models at both neutrino interaction and detector simulations. We update both the uncertainty and the measured value of the T2K NCQE cross section. We also summarize the Run 1–11 data set, which will be used later to validate the DSNB selection cuts.

9.1 T2K NCQE MC production

9.1.1 Neutrino flux (`21bv2` relative to `13av4`)

We update the T2K NCQE MC with the latest flux release `21bv2` (covering through Run 1–11). Key updates include the incorporation of the latest NA61 / SHINE 2010 measurements and a new horn cooling-water layer model [162].

- **NA61/SHINE 2010 replica–target tuning**
  The hadron–production weights in `21bv2` are now derived from the high-statistics NA61/SHINE 2010 run ($\pi^{\pm}, K^{\pm}, p$, $\sim 10\times$ the 2009 data set, used for `13av4`). This extends the data-driven coverage into the kaon and proton phase space and shrinks the hadron-interaction envelope to roughly 4% over 0.2–30 GeV. A side effect is a $\sim$ 5–10 % hardening of the flux above 5 GeV where kaons dominate.

- **Horn cooling water layer model**
  A 3 ± 2 mm water film is now modelled on the horn-1 inner conductor, together with aluminium striplines on horns 2–3. We suspect that the low-momentum pions that formerly survived now interact in water. The 'unconstrained interactions' in water are now dominant above the flux peak.

9.1.2 Neutrino interaction (NEUT 5.9.0 relative to 5.6.3)

NEUT simulates the initial ν–nucleus interaction, the subsequent intranuclear reactions (final-state interactions, FSI), and the de-excitation of the residual nucleus. We prepared two NEUT versions for this study: 5.6.4 (to match the existing atmospheric NCQE MC) and 5.9.0 (to match the upcoming atmospheric NCQE MC).

NEUT 5.6.3 and NEUT 5.6.4 differ only by a bug fix to the 2p2h cross-section normalization, which should have a negligible impact here. Accordingly, we use the same NEUT configuration as in Part II, updated to version 5.6.4. The configuration for NEUT 5.9.0 is listed in Table 9.1. Version 5.9.0 includes several updates to the quasi-elastic and neutral-current quasi-elastic treatments. This update is absent from Part I, as NEUT 5.9.0 was released (in Jan. 2025) only after Part I had been officialized. Below, we summarise how these changes differ from the simulation used in Part II.

Table 9.1: Model configuration of NEUT 5.9.0 in this study.

Channel	Model	Parameter	
NCQE	Ankowski et al.[26]	M_A	1.21 GeV
		g_A^s	0.0
		VFF	BBBA05[27]
		strange VFF	Neglected
		Nuclear model	SF[93]
		de-excitation model	NucDeEx[104]
CCQE	Ankowski et al.[26]	M_A	1.21 GeV
		VFF	BBBA05[27]
		de-excitation model	NucDeEx[104]
CC 2p2h	Nieves et al.[25]		
CC and NC RES	Graczyk-Sobczyk[100]	FF	Dipole form
		M_A	0.95 GeV
		$C_4^A(0)$	1.01
		RES/DIS boundary	$W = 2.0$ GeV
CC and NC DIS	GRV98 PDF[95]	with modification by Bodek and Yang[96]	
CC and NC COH	Berger-Sehgal[97]		
FSI	NEUT cascade	Step length	0.2 fm
		Nucleon cross-section	Bertini et al.[98]
		Pion cross-section	Pinzon et al.[99]

- **Furmanski–Abe NCQE model (replacing Ueno–Mori)**:
  The legacy Ueno–Mori implementation (`-MDLQE 2022`) in NEUT 5.6.3 and 5.6.4 for NCQE scattering lacked reproducible source code and relied on hard-coded cross-section tables. It has been replaced by the "Furmanski–Abe [163]" model in NEUT 5.9.0, which uses the Benhar spectral function and the formalism of Furmanski and Sobczyk.

  With the source code available, the strange axial coupling g_A^s is now a parameter

in NEUT input: it defaults to 0.0, offers a preset of -0.08, and can be computed for other values as needed. The neutral-current pseudoscalar form factor F_P, previously fixed to zero, is now tied to the axial form factor F_A following Ref. [26]. When these tables are used, the axial mass is set to $M_A^{QE} = 1.21\,\mathrm{GeV}$ and Pauli blocking is enabled (`NEUT-PAUL`=0).

With these settings, the total NCQE cross sections predicted by the Furmanski–Abe and Ueno–Mori models agree within a few percent.

- **NucDeEx – TALYS based de-excitation model**
  NEUT's original de-excitation model could emit only a single γ or neutron from s- and p-hole states in ^{16}O and ran before the intranuclear cascade, which is adopted in NEUT 5.6.3, 5.6.4 and 5.9.0. NEUT version 5.9.0 provides NucDeEx [104], a Hauser–Feshbach with Fermi-break-up framework. NucDeEx is enabled by setting `-NEUT-NUCDEXITE 2`, which activates it for QE interactions on ^{12}C and ^{16}O while other channels default to the original treatment. It takes as inputs the excitation energy inferred from the spectral-function missing energy and the (Z, N) of the post-cascade residual nucleus, then returns continuous kinetic-energy spectra for n, p, d, t, α, and γ that follow the expected Coulomb barriers.

To quantify the differences between NEUT 5.6.4 and 5.9.0, we compare their MC-truth outputs. We define "primary γ" as the gamma produced by NEUT, which is differentiated from "secondary γ_s" generated by SI during the detector simulation, SKDETSIM or SKG4. We then ask how the primary γ yield changes due to (i) the NCQE model update or (ii) enabling `NucDeEx`.

NCQE model updates We assess the impact of the NCQE model updates by comparing MC-truth γ distributions from NEUT 5.6.4 and NEUT 5.9.0, using the original de-excitation model in both versions. Figure 9.1 compares the primary γ multiplicity and energy spectra. The two versions are nearly identical, and the error bars show the statistical uncertainty of the MC sample.

NucDeEx The `NucDeEx` model can alter both the multiplicity of particles produced during deexcitation and their kinetic energies. For primary γ, Figure 9.2 shows clear differences between the default one and the `NucDeEx` option for ^{16}O de-excitation γ emission. Because `NucDeEx` implements a more realistic simulation than the previous default, we adopt `NucDeEx` as the default in this study.

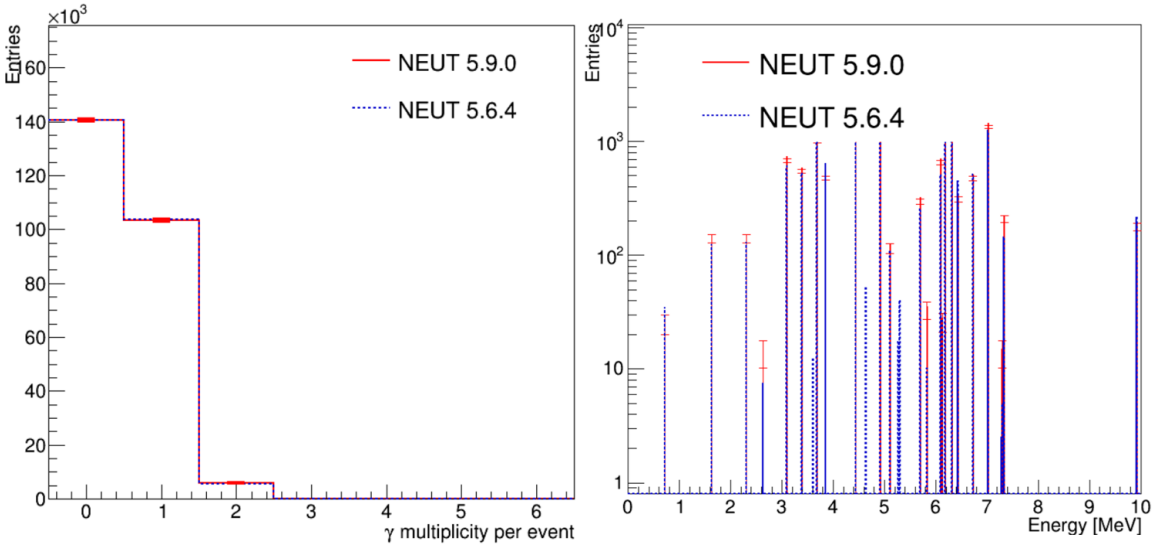

Figure 9.1: The primary γ multiplicity (left) and total energy (right) between NEUT 5.9.0 and 5.6.4 of all interactions. The error bars indicate the statistical uncertainty of the MC sample.

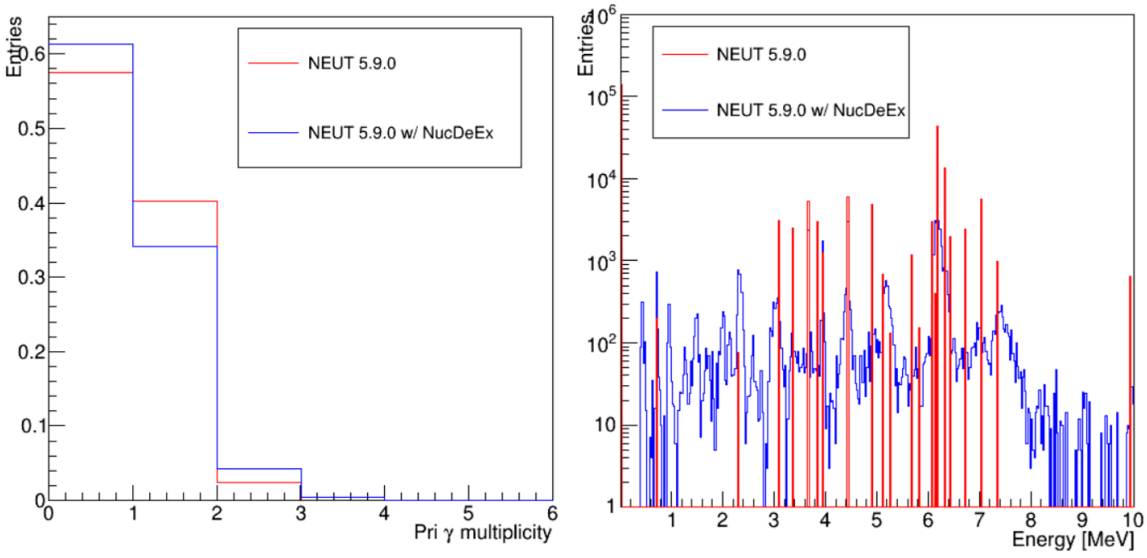

Figure 9.2: The primary γ multiplicity (left) and total energy (right) for NEUT 5.9.0 with default de-excitation model and NucDeEx.

9.1.3 Detector simulation

The NEUT-predicted outgoing hadrons propagate through the SK water, and their hadron–nucleus interactions generate additional γ-rays. These are termed as secondary γ and are discussed in this section.

- **SKDETSIM and SKG4**
  Two detector simulation packages are employed in this study: SKDETSIM, which is based on GEANT3 (GEANT3.2.1), and SKG4, which is built on GEANT4 (GEANT4.10.5p01). SKDETSIM was adopted as the nominal MC setting in this study, due to its long-standing use within SK and T2K, while SKG4 is additionally utilised to access alternative hadron–nucleus (secondary) interaction models available in GEANT4. Both SKDETSIM and SKG4 are independently calibrated.

- **The physics list and hadron–nucleus interaction models**
  The physics lists employed in the two SK detector simulations are summarised in Figure 9.3: SKDETSIM, which relies on GCALOR, and SKG4, configured with `FTFP_BERT_HP`, and `INCL++_HP`. Because NEUT predicts that T2K NCQE-produced hadrons have kinetic energies around $\mathcal{O}(100)$, MeV, intra-nuclear cascade models largely govern their interactions.

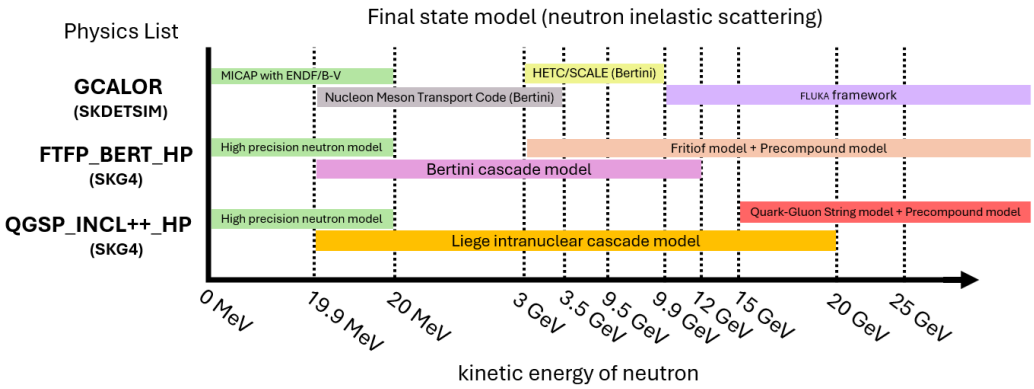

Figure 9.3: The physics list used in SKDETSIM and SKG4

Ref. [50] has revealed the hadron–nucleus interaction model as a dominant source of systematic uncertainty. Therefore, the SKG4 framework is adopted here for a more detailed examination of secondary γ production by checking MC truth information from switching physics lists. Conceptually, hadron–nucleus interaction couples an intranuclear cascade to a nuclear de-excitation model. In this work we test two cascade models: (1) the `Bertini` cascade (`BERT`) [109] and (2) the Liège intranuclear cascade (`INCL`) [110, 111], in combination with three de-excitation models: (I) `G4Cascade` (native to `BERT`), (II) `G4PreCompound`, and (III) `NucDeEx`.

- **Comparison between hadron–nucleus interaction models**
  To assess whether the intranuclear cascade or the de-excitation place an stronger influence on the secondary-γ prediction, we inspect MC truth of secondary-γ multiplicity and energy for the `BERT` cascade model paired with `G4Cascade` and `G4PreCompound`. As shown in Figure 9.4, the two configurations yield different multiplicity and energy spectra.

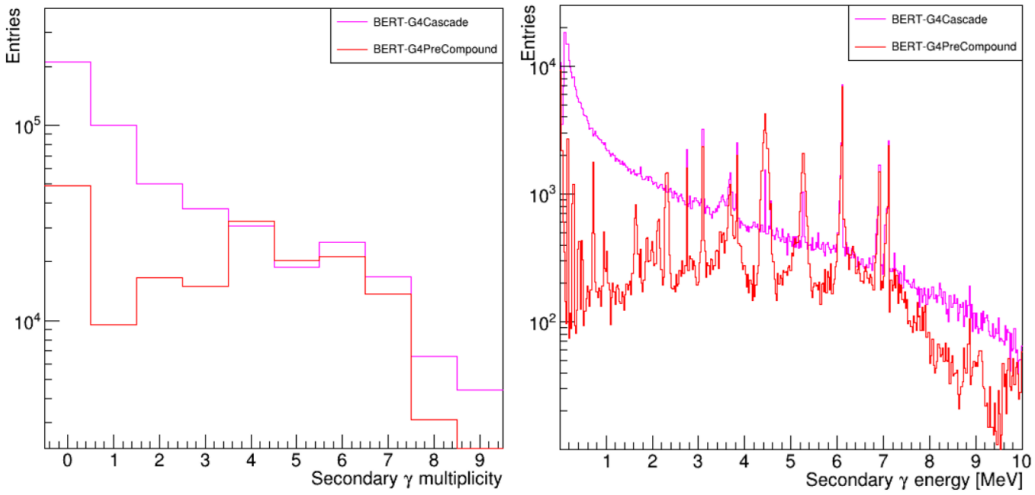

Figure 9.4: Secondary gamma difference between `G4Cascade` and `G4PreCompound` with `BERT` with T2K flux of all interactions.

We found that G4Cascade neglects discrete nuclear levels, so only the peaks already handled by `ParticleHPInelastic()` are reproduced. G4Cascade emits gammas until the excitation energy E^* is virtually exhausted, increasing the predicted γ multiplicity and yielding a spectrum that contains neither explicit level structure nor transition modelling.

We next compared the secondary-γ produced by `BERT` with `G4PreCompound` and `INCL` with `G4PreCompound`. As Figure 9.5 illustrates, these two configurations yield nearly identical secondary γ multiplicity and energy distributions, implying that the de-excitation model, rather than the intranuclear cascade, is the principal cause of the prediction difference of γ.

Figure 9.5 also presents the spectrum for `INCL` paired with `NucDeEx`. Although the latter differs from `G4PreCompound` by a 6.13 MeV γ spectrum peak from $^{15}N^*$ de-excitation, such a minor discrepancy would be difficult to observe in SK.

MC samples are generated with NEUT v5.9.0 (nominal) and NEUT v5.6.4, then processed by either SKDETSIM (nominal) or SKG4. In total, seven distinct generator–detector configurations are prepared, and the corresponding abbreviations are summaried in Table 9.2. MC configurations are chosen to isolate one specific

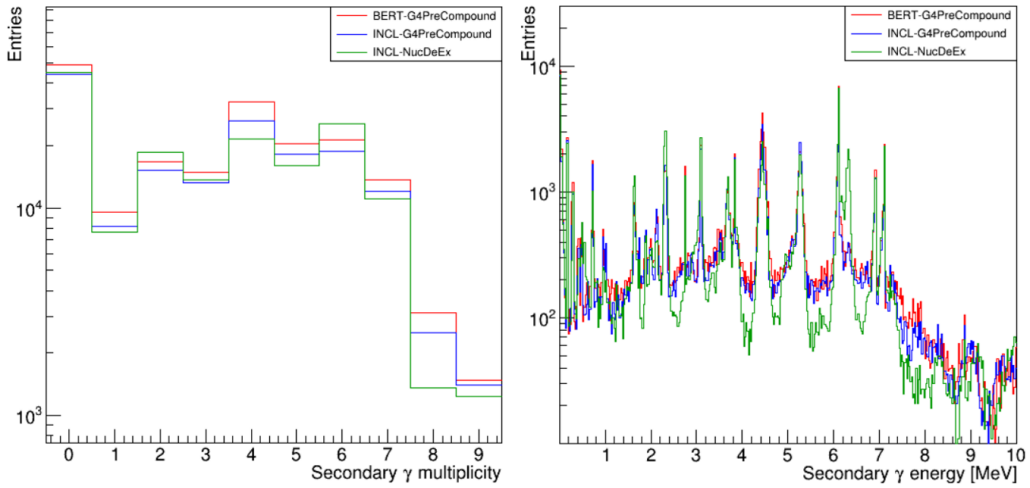

Figure 9.5: Secondary γ difference between `G4PreCompound` and `NucDeEx`. Also shown the secondary γ difference between `BERT` and `INCL` with same de-excitation model (`G4PreCompound`)

Table 9.2: MC generator–detector configurations and their abbreviations.

Configuration	**Abbreviation**
$\text{NEUT}^{5.9.0}_{w/o\,\text{NucDeEx}}$ + SKG4 (BERT-G4Cascade)	NEUT-BERT-G4Cas
$\text{NEUT}^{5.9.0}_{w/o\,\text{NucDeEx}}$ + SKG4 (BERT-G4PreCompound)	NEUT-BERT-G4Pre
$\text{NEUT}^{5.9.0}_{w/o\,\text{NucDeEx}}$ + SKG4 (INCL-G4PreCompound)	NEUT-INCL-G4Pre
$\text{NEUT}^{5.6.4}_{w/o\,\text{NucDeEx}}$ + SKG4 (INCL-G4PreCompound)	NEUT564-INCL-G4Pre
$\text{NEUT}^{5.9.0}_{w/o\,\text{NucDeEx}}$ + SKG4 (INCL-NucDeEx)	NEUT-INCL-NucDeEx
$\text{NEUT}^{5.9.0}_{w/\,\text{NucDeEx}}$ + SKG4 (INCL-NucDeEx)	NEUTNuc-INCL-NucDeEx
$\text{NEUT}^{5.9.0}_{w/\,\text{NucDeEx}}$ + SKDETSIM (GCALOR)	NEUTNuc-GCALOR (nominal)

modelling difference as summarized in Table 9.3.

First, **NEUT-BERT-G4Cas** and **NEUT-BERT-G4Pre** differ only in the GEANT4 de-excitation model, G4Cascade versus G4PreCompound, thereby revealing the impact of this choice (see Figure 9.4). Second, the comparison between **NEUT-INCL-G4Pre** and **NEUT564-INCL-G4Pre** isolates the version change from NEUT 5.6.4 to NEUT 5.9.0, whose primary-γ differences are illustrated in Figure 9.1. Third, contrasting **NEUT-INCL-G4Pre** with **NEUT-INCL-NucDeEx** tests the alternative de-excitation model NucDeEx in place of G4PreCompound (Figure 9.5). Fourth, the pair **NEUT-INCL-NucDeEx** and **NEUTNuc-INCL-NucDeEx** quantifies the effect of the NucDeEx implementation inside NEUT 5.9.0 (Figure 9.2). Finally, **NEUTNuc-INCL-NucDeEx** is compared with the nominal **NEUTNuc-GCALOR** configuration to highlight differences between the SKG4 and SKDETSIM predictions.

For each trial we generate 250 events for each of Run1-9 and Run10, while 100 events are generated for Run11. The simulation is repeated 1000 runs with independent random seeds for each of the four flavors ν_e, $\bar{\nu}_e$, ν_μ, and $\bar{\nu}_\mu$. In total, the

Table 9.3: Summary of MC-setting comparisons

Setting #	MC-setting name	Compared with (# / name)
1	NEUT-BERT-G4Cas	De-excitation model: **G4Cascade** vs. **G4PreCompound** (Fig. 9.4)
2	NEUT-BERT-G4Pre	
3	NEUT-INCL-G4Pre	NEUT version: **590** vs. **564** (Fig. 9.1)
4	NEUT564-INCL-G4Pre	
3	NEUT-INCL-G4Pre	De-excitation model: **G4PreCompound** vs. **NucDeEx** (Fig. 9.5)
5	NEUT-INCL-NucDeEx	
5	NEUT-INCL-NucDeEx	NEUT option: **w/o NucDeEx** vs. **w/ NucDeEx** (Fig. 9.2)
6	NEUTNuc-INCL-NucDeEx	
6	NEUTNuc-INCL-NucDeEx	hadron model: **INCL** vs. **GCALOR**
7	NEUTNuc-GCALOR, nominal	

simulations produce 1 M events for Runs 1–9, Run 10 and 0.4 M events for Run 11, which match the statistics used in Ref [50](Runs 1–9) and the study done in Part II (Run 11).

Each MC event is normalized individually by applying a weight that aligns the simulation with the Protons-on-Target (POT) accumulated during T2K Runs 1–11. All subsequent analyses use this normalized MC sample to accurately reflect the experimental conditions.

Chapter 10

Event Analysis

This analysis uses T2K data from Runs 1–11. Table 10.1 summarizes, for each period, the beam mode (FHC or RHC), MR Run number, SK DAQ number, and the protons-on-target (POT) for SK good spills. Run 1 used six beam bunches. All later runs used eight. The total exposures are 21.42×10^{20} POT for FHC, and 16.34×10^{20} POT for RHC. SK operated with pure water in Runs 1–10 and with 0.01% Gd in Run 11.

We focus on γ rays from T2K ν–^{16}O NCQE-like interactions. The left panel of Figure 10.1 illustrates the event topology, highlighting both primary and secondary γ rays. In such interactions, one or more γ rays are emitted during deexcitation of the residual nucleus. Additional secondary γ rays (and other particles) appear within tens of nanoseconds as hadrons undergo hadron–nucleus interactions. This timming delay is too short for SK to resolve. The right panel of Figure 10.1 shows the MC truth energy spectrum in detector simulation, where γ rays dominate in the region of interest, $[3.5, 29.5]$ MeV.

The NCQE-like event, as in previous NCQE studies, is composed of five channel categories: (1) neutrino NCQE interactions (ν-NCQE), (2) antineutrino NCQE interactions ($\bar{\nu}$-NCQE), (3) other NC interactions (NC-other), (4) CC interactions (CC), and (5) beam-unrelated backgrounds (Accidental). ν-NCQE, $\bar{\nu}$-NCQE, NC-other, and CC channels were simulated by NEUT. Beam-unrelated backgrounds are evaluated using data recorded from -500 to -5 μs in the T2K trigger, where the beam reaches SK at 0 μs. This interval is termed the Off-Beam time window. Conversely, the On-Beam window spans from the beam spill arrival (0 ns) to 500 μs in the T2K trigger.

The selection described below was optimized to identify NCQE-like events from both ν-NCQE and $\bar{\nu}$-NCQE interactions while minimizing backgrounds from other processes. Finally, we present results based on the T2K Run 1–11 dataset and

Table 10.1: Summary on T2K Run 1–11 with the operation mode, MR Run, SK DAQ Run, and POT for the SK good spills used in this analysis.

T2K Run#	Operation Mode	MR Run	SK DAQ Run#	POT [$\times 10^{19}$]	
1	FHC	29–34	66251–66945	3.26	SK4
2	FHC	36–38	67877–68208	11.22	SK4
3b	FHC	41	69552–69586	2.17	SK4
3c	FHC	42–43	69626–69753	13.82	SK4
4	FHC	44–49	70524–71245	35.97	SK4
5a	FHC	55	72674–72726	0.66	SK4
5b	FHC	55–56	72726–72767	1.78	SK4
5c	RHC	56	72735–72764	5.12	SK4
6a	FHC	58	73133–73160	1.03	SK4
		60	73331–73342		SK4
		61	73443–73449		SK4
6b	RHC	58	73161–73225	13.04	SK4
		59	73238–73305		SK4
6c	RHC	61	73463–73485	5.25	SK4
6d	RHC	61	73485–73520	7.89	SK4
6e	RHC	62–63	73596–73651	9.29	SK4
6f	FHC	63	73653–73654	0.89	SK4
7a	FHC	66	74363–74366	0.89	SK4
7b	RHC	66–68	74369–74610	34.99	SK4
7c	FHC	68	74628–74637	3.96	SK4
8	FHC	70–74	75363–75777	71.70	SK4
9a	FHC	76	77033–77044	2.04	SK4
9b	RHC	76–77	77044–77222	26.53	
9c	RHC	77	77222–77298	10.25	
9d	RHC	78–79	77783–77958	51.10	
10a	FHC	83	82143–82375	26.24	SK5
10b	FHC	84	82420–82498	21.02	SK5
11	FHC	86	85780–85852	17.6	SK6 (Gd)
Total	FHC	–	–	214.24	
Total	RHC	–	–	163.46	

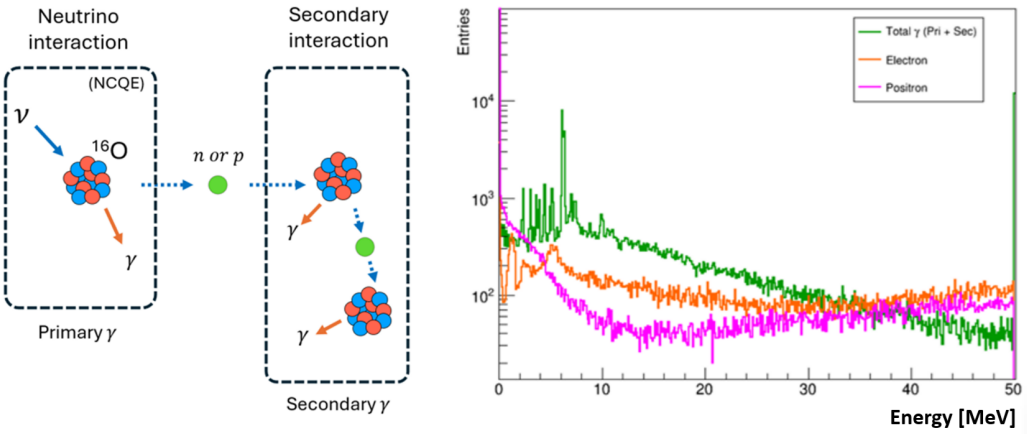

Figure 10.1: NCQE event overview and MC comparisons. **Left:** schematic of an NCQE interaction on ^{16}O showing a primary and secondary γ production. **Right:** total (primary + secondary) energy distributions for γ's, electrons, and positrons. γ's dominate in the analysis range of $[3.5, 29.5]$ MeV.

the corresponding MC sample, including the total uncertainty and measurement result of the NCQE cross section.

10.1 prompt signal selection

We take the same selection parameters from Part II, and following the optimization procedure for the new added Run 10 sample introduced here. The same seven criteria are applied to achieve high-purity ν–^{16}O NCQE events from the T2K beam: (1) Good spill selection, (2) Timing cut, (3) Decay-e cut, (4) Visible Energy, (5) Fiducial Volume, (6) Ambient Low-Energy Background, and (7) CC Interaction Cut. Because the cuts were introduced in Part II, we focus here only on those newly evaluated for Run 10: (2) Timing cut, (6) Ambient low energy background, and (7) CC interaction cut.

6. **Ambient low energy background cut**
   As introduced in Part. I, chapter 5.1, we evaluated the new opened Run 10 data set for ambient low energy cut here. Consistent with the methodology of the NCQE Run 1–9 study, we evaluate Runs 10a and 10b (as defined by the T2K flux group) separately. Figures 10.2 and 10.3 show the optimal cut values versus energy, and Table 10.2 lists the fitted parameters. Because `dwall` is fixed at 200 cm for $E_{\text{vis}} > 4$ MeV, only the first three energy bins are used to determine its linear fit.

7. **CC interaction cut**
   Cherenkov angles vary with particle type and energy, single electrons or γ give $\sim 42°$, while overlapping rings from multiple γ can lead to a rather higher value.

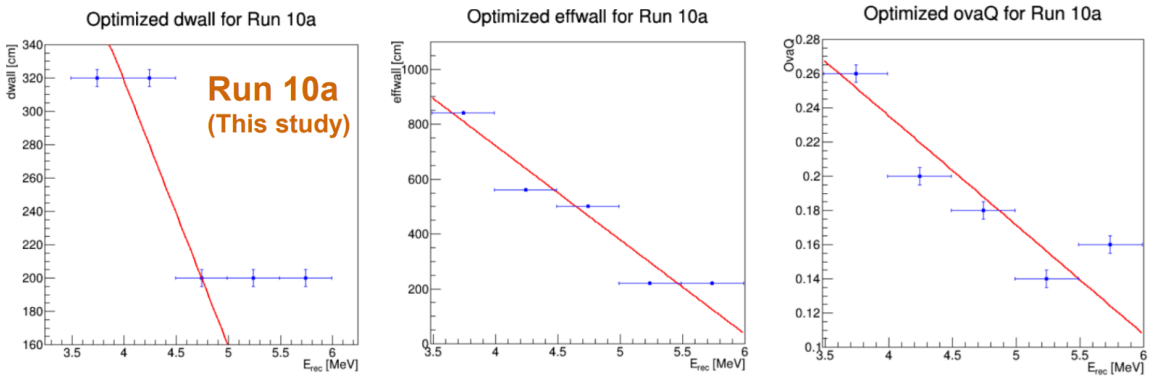

Figure 10.2: The Run 10a linear fitting result of ambient low energy background cuts.

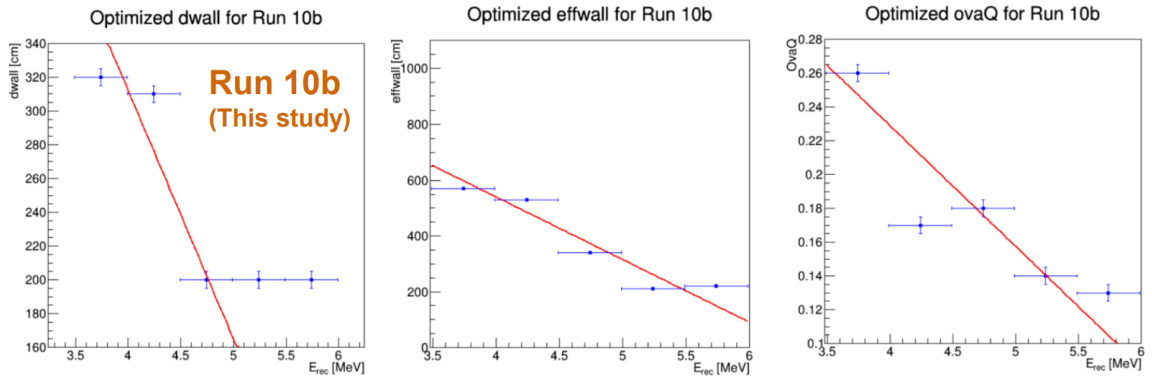

Figure 10.3: The Run 10b linear fitting result of ambient low energy background cuts.

We therefore apply a linear cut in the $(E_{\text{vis}}, \theta_C)$ plane,

$$\theta_C^{\text{CUT}} = a_{\text{opt}}\, E_{\text{vis}} + b_{\text{opt}}, \tag{10.1}$$

optimized via the FOM by treating NCQE as signal and CCQE plus off-beam events as background. This study also evulated the paraters for Run 10, which is $a_{\text{opt}} = 1.67832$ and $b_{\text{opt}} = 15.0$. When comparing with the Run 1-9 [50] and Run 11 [161] parameters are $a_{\text{opt}} = 1.67832$ and $b_{\text{opt}} = 17.7273$ (FHC) and $a_{\text{opt}} = 1.57343$ and $b_{\text{opt}} = 17.7273$ (RHC), where $a_{\text{opt}} = 1.67832$ and $b_{\text{opt}} = 17.7273$ for Run 11. They shown a similiar results.

10.2 prompt signal selection results

10.2.1 Features among runs and MC settings

- **Run 1–9 (FHC):** The Runs 1–9 (FHC) data set is directly taken from Ref. [50]. This study updates the corresponding MC predictions. The selected NCQE events for the seven MC configurations are listed in Table 10.4, and the reconstructed feature distributions (N_{50}, E_{vis}, θ_C, MSG, *effwall*, and *dwall*) are shown in Figure 10.4.

Table 10.2: Summary on parameters for `dwall`, `effwall`, and `OvaQ` in each T2K run.

Run#	$p_{\mathrm{dwall}}[0]$	$p_{\mathrm{dwall}}[1]$	$p_{\mathrm{effwall}}[0]$	$p_{\mathrm{effwall}}[1]$	$p_{\mathrm{OvaQ}}[0]$	$p_{\mathrm{OvaQ}}[1]$
1	523.5	–70.0	2087.7	–332.0	0.3831	–0.042
2	477.7	–60.0	1934.0	–300.0	0.4095	–0.048
3b	389.6	–40.0	2154.5	–352.0	0.3641	–0.038
3c	386.3	–40.0	2154.5	–352.0	0.3811	–0.042
4	539.2	–80.0	2035.7	–332.0	0.3506	–0.036
5a	539.2	–80.0	2131.0	–350.0	0.3866	–0.044
5b	539.2	–80.0	2131.0	–350.0	0.3866	–0.044
5c	539.2	–80.0	1939.0	–296.0	0.3906	–0.044
6a	539.2	–80.0	2100.6	–344.0	0.3277	–0.032
6b	624.0	–100.0	2579.5	–452.0	0.3726	–0.036
6c	624.0	–100.0	2579.5	–452.0	0.3726	–0.036
6d	624.0	–100.0	2579.5	–452.0	0.3726	–0.036
6e	624.0	–100.0	2579.5	–452.0	0.3726	–0.036
6f	539.2	–80.0	2134.5	–352.0	0.3277	–0.032
7a	539.2	–80.0	1972.3	–322.0	0.3401	–0.038
7b	539.2	–80.0	1840.2	–290.0	0.3457	–0.032
7c	539.2	–80.0	1972.3	–322.0	0.3401	–0.038
8	539.2	–80.0	1668.8	–266.0	0.3771	–0.042
9a	539.2	–80.0	1793.1	–288.0	0.3895	–0.048
9b	539.2	–80.0	1837.6	–294.0	0.3911	–0.042
9c	539.2	–80.0	1837.6	–294.0	0.3911	–0.042
9d	539.2	–80.0	1837.6	–294.0	0.3911	–0.042
10a	900.6	–147.2	1437.5	–224.3	0.5138	–0.071
10b	954.9	–159.2	2092.8	–342.7	0.4905	–0.064
11	580.0	-80.0	1941.5	-314.0	0.4125	-0.042

- **Run 10 (FHC):** The Run 10 (FHC) data set and MC prediction are presented here for the first time. The selected NCQE event prediction is summarized in Table 10.4, and the associated distributions of N_{50}, E_{vis}, θ_C, MSG, *effwall*, and *dwall* are shown in Figure 10.5.

- **Run 11 (FHC):** The Run 11 (FHC) data set is directly taken from Part II, and its MC predictions are likewise updated. The corresponding NCQE event prediction appear in Table 10.4. The feature distributions are displayed in Figure 10.6.

Figure 10.7 compares the normalized feature distributions for Runs 1–9, 10, and 11. The largest discrepancies appear in the lowest four bins of visible energy, N_{50}, and *effwall*. The modest variation observed between Run 1–9 (SK4), Run 10 (SK5), and Run 11 (SK6) conclude that detector response-related systematic uncertainties on the NCQE γ_s signal are minor and consistent across runs.

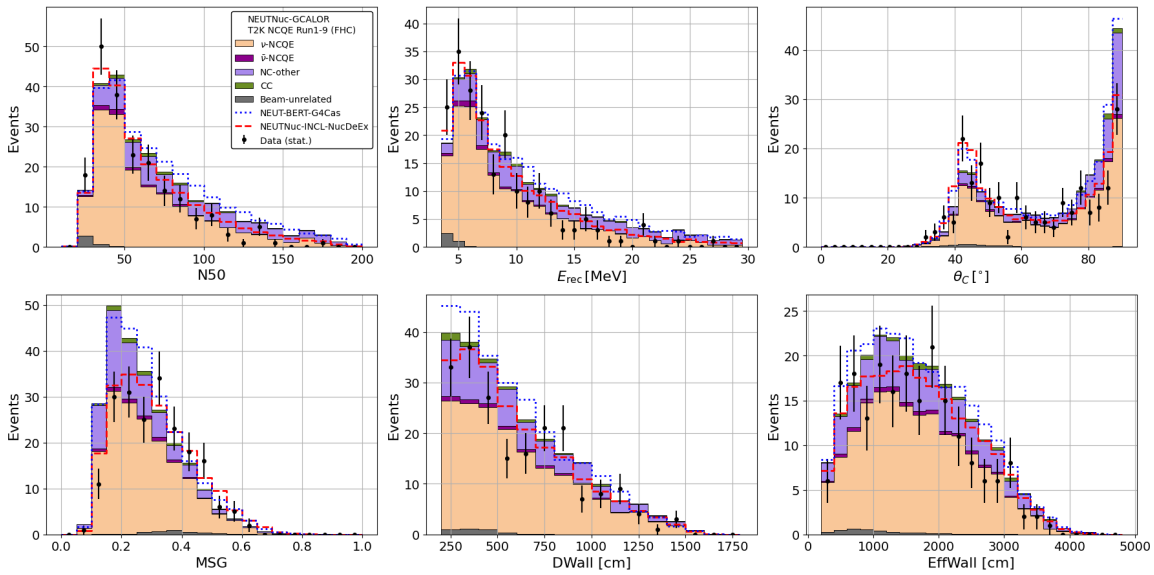

Figure 10.4: The features of T2K NCQE events (FHC) for Run 1-9.

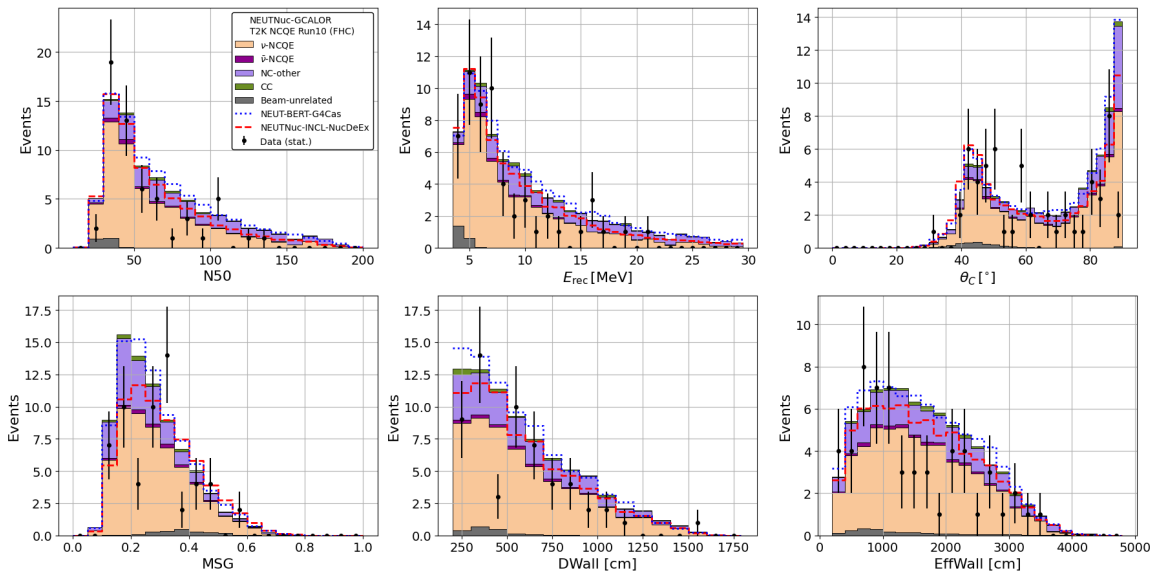

Figure 10.5: The features of T2K NCQE events (FHC) for Run 10.

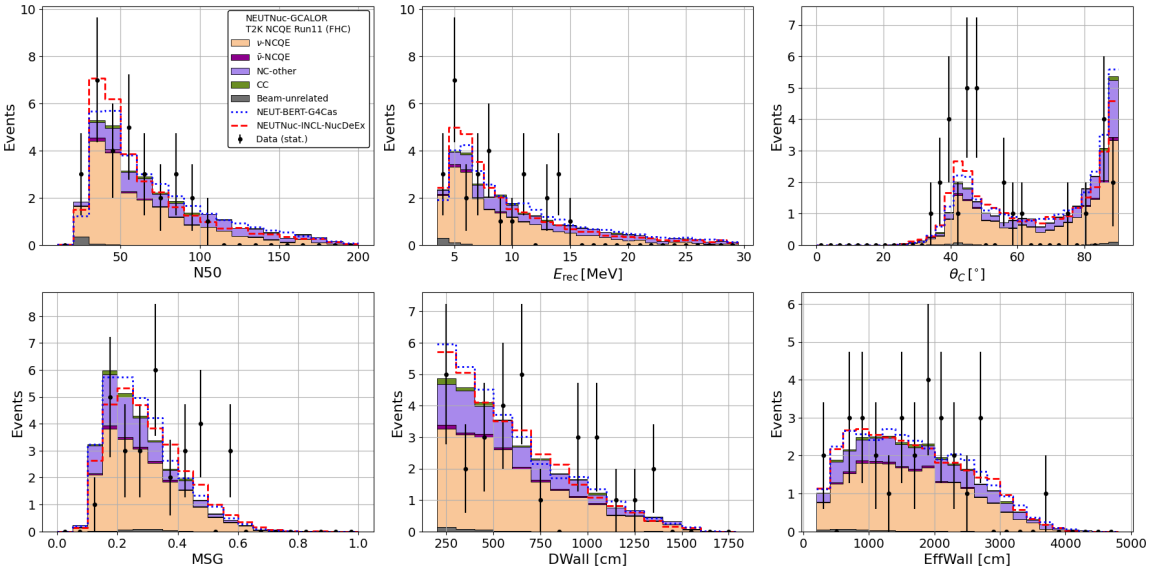

Figure 10.6: The features of T2K NCQE events (FHC) for Run 11.

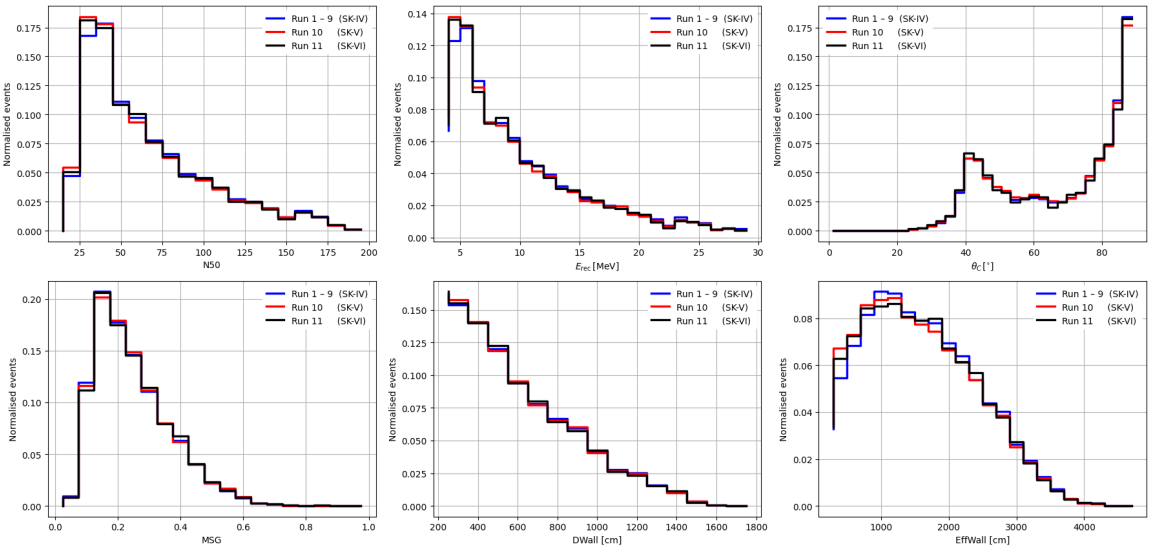

Figure 10.7: The features of T2K NCQE events (FHC) among Runs 1-9, 10, and 11.

Table 10.3: Summary on parameters for a_{opt} and b_{opt} in each T2K run.

Run#	a_{opt}	b_{opt}
Run 1-9 (FHC)	1.67832	17.7273
Run 1-9 (RHC)	1.57343	17.7273
Run 10 (FHC)	1.67832	15.0
Run 11 (FHC)	1.67832	17.7273

Table 10.4: Summary on Run 1-9, 10, and 11 NCQE event

NCQE Run 1-9	$\nu - NCQE$	$\bar{\nu} - NCQE$	$NC - other$	CC	Total$_{MC}$	Acc.	Total$_{Data}$
NEUT-BERT-G4Cas	172.2 (66.9%)	5.4 (2.1%)	63.1 (24.5%)	16.6 (6.4%)	257.3 (100%)		
NEUT-BERT-G4Pre	163.0 (67.4%)	5.1 (2.1%)	58.9 (24.3%)	14.9 (6.2%)	241.9 (100%)		
NEUT-INCL-G4Pre	159.6 (67.2%)	5.0 (2.1%)	57.4 (24.2%)	15.4 (6.5%)	237.3 (100%)		
NEUT564-INCL-G4Pre	164.1 (67.5%)	5.3 (2.2%)	57.1 (23.5%)	16.8 (6.9%)	243.2 (100%)	3.6	202
NEUT-INCL-NucDeEx	160.9 (67.5%)	5.1 (2.1%)	57.5 (24.1%)	14.9 (6.2%)	238.4 (100%)		
NEUTNuc-INCL-NucDeEx	143.6 (66.4%)	4.8 (2.2%)	54.8 (25.3%)	13.1 (6.1%)	216.4 (100%)		
NEUTNuc-GCALOR	167.4 (69.6%)	5.4 (2.3%)	62.2 (25.9%)	5.3 (2.2%)	240.4 (100%)		
NCQE Run 10	$\nu - NCQE$	$\bar{\nu} - NCQE$	$NC - other$	CC	Total$_{MC}$	Acc.	Total$_{Data}$
NEUT-BERT-G4Cas	55.3 (67.9%)	1.7 (2.1%)	20.1 (24.7%)	4.3 (5.3%)	81.4 (100%)		
NEUT-BERT-G4Pre	52.2 (67.9%)	1.6 (2.1%)	18.9 (24.5%)	4.2 (5.5%)	77.0 (100%)		
NEUT-INCL-G4Pre	51.5 (67.8%)	1.6 (2.1%)	19.0 (25.0%)	3.9 (5.1%)	76.0 (100%)		
NEUT564-INCL-G4Pre	53.7 (68.4%)	1.7 (2.2%)	18.5 (23.6%)	4.5 (5.8%)	78.5 (100%)	1.5	57
NEUT-INCL-NucDeEx	51.6 (67.6%)	1.6 (2.1%)	19.1 (25.0%)	4.0 (5.3%)	76.4 (100%)		
NEUTNuc-INCL-NucDeEx	45.8 (66.7%)	1.5 (2.3%)	17.8 (25.9%)	3.5 (5.1%)	68.7 (100%)		
NEUTNuc-GCALOR	54.1 (70.0%)	1.8 (2.3%)	19.7 (25.5%)	1.7 (2.2%)	77.2 (100%)		
NCQE Run 11	$\nu - NCQE$	$\bar{\nu} - NCQE$	$NC - other$	CC	Total$_{MC}$	Acc.	Total$_{Data}$
NEUT-BERT-G4Cas	20.9 (66.1%)	0.6 (2.0%)	8.2 (25.9%)	1.9 (5.9%)	31.6 (100%)		
NEUT-BERT-G4Pre	19.7 (66.1%)	0.6 (2.0%)	7.7 (25.8%)	1.8 (6.0%)	29.7 (100%)		
NEUT-INCL-G4Pre	19.6 (65.6%)	0.6 (2.0%)	7.8 (26.0%)	1.9 (6.3%)	29.9 (100%)		
NEUT564-INCL-G4Pre	20.3 (66.9%)	0.7 (2.2%)	7.5 (24.7%)	1.9 (6.2%)	30.3 (100%)	0.4	30
NEUT-INCL-NucDeEx	20.2 (66.3%)	0.6 (2.0%)	7.8 (25.7%)	1.8 (5.9%)	30.4 (100%)		
NEUTNuc-INCL-NucDeEx	20.9 (68.6%)	0.6 (2.0%)	7.4 (24.4%)	1.5 (5.1%)	30.5 (100%)		
NEUTNuc-GCALOR	20.1 (69.5%)	0.7 (2.3%)	7.5 (25.9%)	0.7 (2.3%)	28.9 (100%)		

Run 1-11 (FHC and RHC), hadron-nucleus model examination: Table 10.5 presents the MC updated predictions across the seven MC configurations: FHC for Runs 1–11 and RHC for Runs 1–9.

To evaluate NEUT's de-excitation models, we compared its default implementation with the NuDeEx option. Activating `NucDeEx` in NEUT 5.9.0 lowers the predicted event rate by roughly 8%, as summarized in Table 10.5. This reduction arises because, as shown in Figure 9.2, parts of NuDeEx-generated de-excitation γ rays were below 3 MeV, which the default de-excitation model in NEUT does not. These low-energy photons fail the "visible-energy cut," leading to the MC predicted drop in NCQE event predictions.

We note that NucDeEx employs the Hauser-Feshbach [140] model, which considers angular momentum conservation and is regarded as more accurate [104] than the de-excitation model used in NEUT for predicting particle emission spectra and branching ratios. We also note that NucDeEx evaluates the excitation energy as the difference between the removal energy and the separation energy, where the

Table 10.5: Summary on FHC and RHC NCQE event (Run 1-11)

NCQE Run 1-11 FHC	$\nu - NCQE$	$\bar{\nu} - NCQE$	$NC - other$	CC	Total$_{MC}$	Acc.	Total$_{Data}$
NEUT-BERT-G4Cas	248.4 (67.1%)	7.8 (2.1%)	91.4 (24.7%)	22.8 (6.2%)	370.3 (100%)		
NEUT-BERT-G4Pre	234.9 (67.4%)	7.3 (2.1%)	85.4 (24.5%)	20.9 (6.0%)	348.6 (100%)		
NEUT-INCL-G4Pre	230.7 (67.2%)	7.2 (2.1%)	84.2 (24.5%)	21.1 (6.2%)	343.3 (100%)		
NEUT564-INCL-G4Pre	238.1 (67.6%)	7.6 (2.2%)	83.1 (23.6%)	23.2 (6.6%)	352.1 (100%)	5.5	289
NEUT-INCL-NucDeEx	232.7 (67.4%)	7.3 (2.1%)	84.4 (24.5%)	20.7 (6.0%)	345.1 (100%)		
NEUTNuc-INCL-NucDeEx	210.3 (66.7%)	7.0 (2.2%)	80.1 (25.4%)	18.2 (5.8%)	315.5 (100%)		
NEUTNuc-GCALOR	241.5 (69.7%)	7.9 (2.3%)	89.4 (25.8%)	7.7 (2.2%)	346.5 (100%)		
NCQE Run 1-9 RHC	$\nu - NCQE$	$\bar{\nu} - NCQE$	$NC - other$	CC	Total$_{MC}$	Acc.	Total$_{Data}$
NEUT-BERT-G4Cas	29.6 (29.3%)	43.3 (42.9%)	23.7 (23.5%)	4.3 (4.3%)	101.0 (100%)		
NEUT-BERT-G4Pre	28.1 (29.5%)	40.5 (42.6%)	22.5 (23.6%)	4.1 (4.3%)	95.1 (100%)		
NEUT-INCL-G4Pre	27.5 (29.4%)	40.0 (42.8%)	21.9 (23.4%)	4.1 (4.4%)	93.4 (100%)		
NEUT564-INCL-G4Pre	28.2 (29.3%)	42.1 (43.7%)	21.7 (22.5%)	4.4 (4.6%)	96.4 (100%)	2.1	96
NEUT-INCL-NucDeEx	27.7 (29.4%)	40.5 (43.0%)	22.0 (23.4%)	4.0 (4.2%)	94.2 (100%)		
NEUTNuc-INCL-NucDeEx	24.8 (27.8%)	38.5 (43.2%)	21.9 (24.6%)	3.9 (4.4%)	89.0 (100%)		
NEUTNuc-GCALOR	29.3 (29.2%)	43.7 (43.6%)	25.3 (25.3%)	1.9 (1.9%)	100.2 (100%)		

separation energy values are taken from the spectral function. Since the spectral function reference by NEUT [26] and NucDeEx [93] are different, which yields different probablity for the primary shell hole states, $s_{1/2}$, $p_{3/2}$, and $p_{1/2}$, as summarised in Table 10.6. This difference could be an explanation of the observed 6.32 MeV γ peak in Figure 9.5 for which NucDeEx predicts a larger $p_{3/2}$ contribution, even though the overall branching ratios are comparable to G4PreCompound.

Nucleus	Hole	Prob. (%)		E_x (MeV)
		NEUT	NucDeEx	
^{16}O	$s_{1/2}$	49.05	35.8	$E_x \geq 16$
	$p_{3/2}$	35.15	44.8	$4 \leq E_x < 16$
	$p_{1/2}$	15.8	19.4	$E_x < 4$

Table 10.6: Probabilities for nucleon–hole configurations in ^{16}O.

We also assessed the updated NCQE model in NEUT 5.9.0 (Furmanski–Abe) against the earlier implementation in NEUT 5.6.4 (Ueno–Mor) labeled as MC configurations "NEUT564-INCL-G4Pre" and "NEUT-INCL-G4Pre." The effect was minimal: event-rate predictions differed by only about 1%, and the feature distributions were almost identical. Event totals are listed in Table 10.5, with the corresponding feature comparisons shown in Figure 10.10.

Next, we assess the influence of the de-excitation model by comparing the BERT + G4Cascade and BERT + G4PreCompound setups (denoted NEUT-BERT-G4Cas and NEUT-BERT-G4Pre), which display pronounced feature differences (see Figure 10.9). We then contrast BERT + G4PreCompound with INCL + G4PreCompound (NEUT-BERT-G4Pre vs.NEUT-INCL-G4Pre). Their predictions are nearly identical, indicating that the intra-nuclear cascade choice affects the results far less than the de-excitation model (also Figure 10.9). This observation agrees with the MC-truth information shown in Figure 9.4. Under the BERT cascade, the G4PreCompound

configuration predicts fewer events than G4Cascade because G4PreCompound models the ^{16}O de-excitation spectrum. The resulting change in γ-ray multiplicity alters both the Cherenkov-angle and MSG distributions.

Because de-excitation models have the largest influence on both the NCQE event rate and feature shapes, we next evaluated the INCL cascade paired with either G4PreCompound or NucDeEx, labeled as NEUT-INCL-G4Pre and NEUT-INCL-NucDeEx (see Figure 10.10). The two setups differ only slightly in their predicted event counts and observable distributions. This small divergence is expected, since NucDeEx produces a ^{16}O de-excitation spectrum that closely mirrors that of G4PreCompound (Figure 9.5).

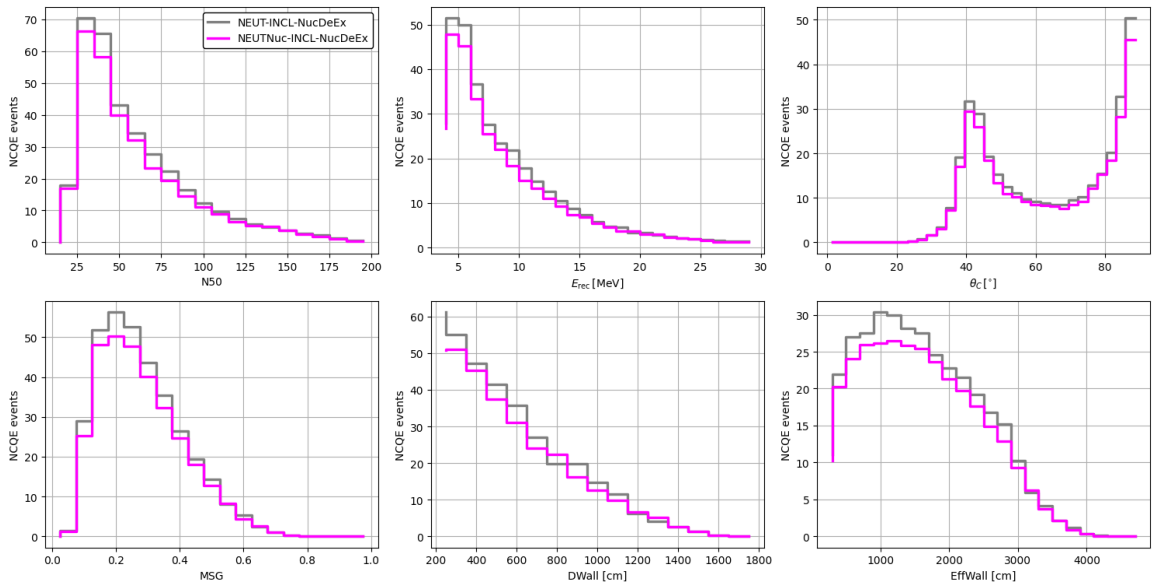

Figure 10.8: The features of T2K NCQE events (FHC, Run1-11) among NEUT 5.9.0 with default de-excitation model (gray) and NucDeEx (magenta).

In the present analysis, SKDETSIM is referred to as NEUTNuc-GCALOR. As illustrated in Figure 10.11, its predicted features show strong agreement with those of NEUT-BERT-G4Cas. For comparison, the SK DSNB baseline MC, NEUTNuc-INCL-NucDeEx, is also plotted in the same figure. Feature distributions for Runs 1–11 in FHC mode appear in Figure 10.11, while the corresponding RHC results are shown in Figure 10.12.

Across all configurations, the choice of de-excitation model has the largest impact on both event rates and feature shapes, and is therefore the dominant systematic uncertainty in prior studies [50, 161]. Combining the FHC and RHC event counts predicted by NEUT-BERT-G4Cas (NEUTNuc-GCALOR) yields a deviation from the data of 4.4σ (3.1σ) when considering statistical uncertainties only, whereas NEUTNuc-INCL-NucDeEx differs by just 1.0σ under the same assumption.

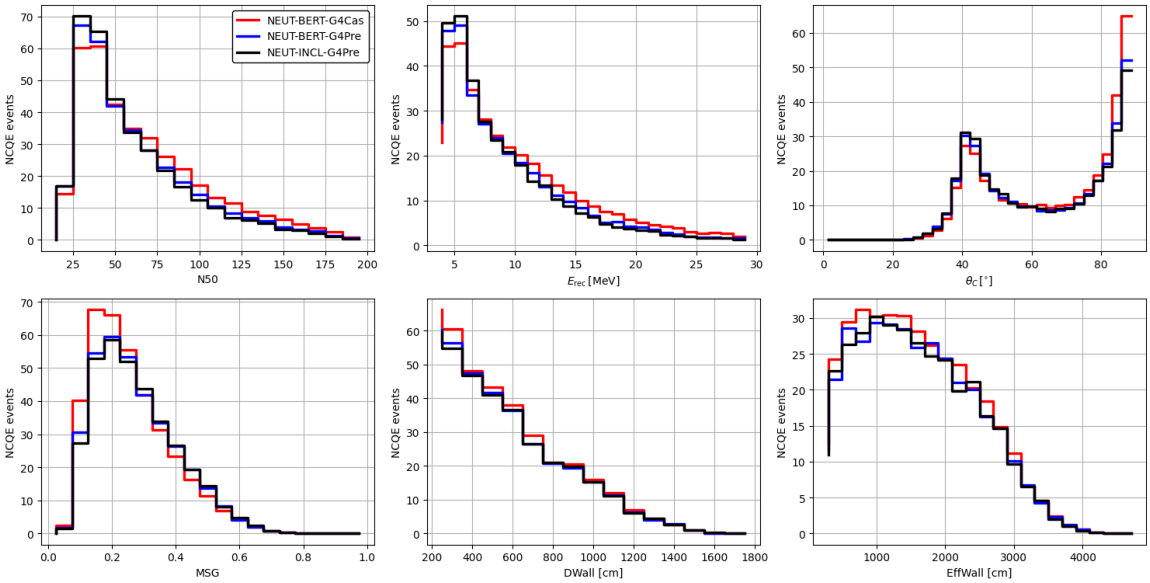

Figure 10.9: The features of T2K NCQE events (FHC, Run1-11) among BERT-G4Cas(red), BERT-G4Pre(blue), and INCL-G4Pre(black).

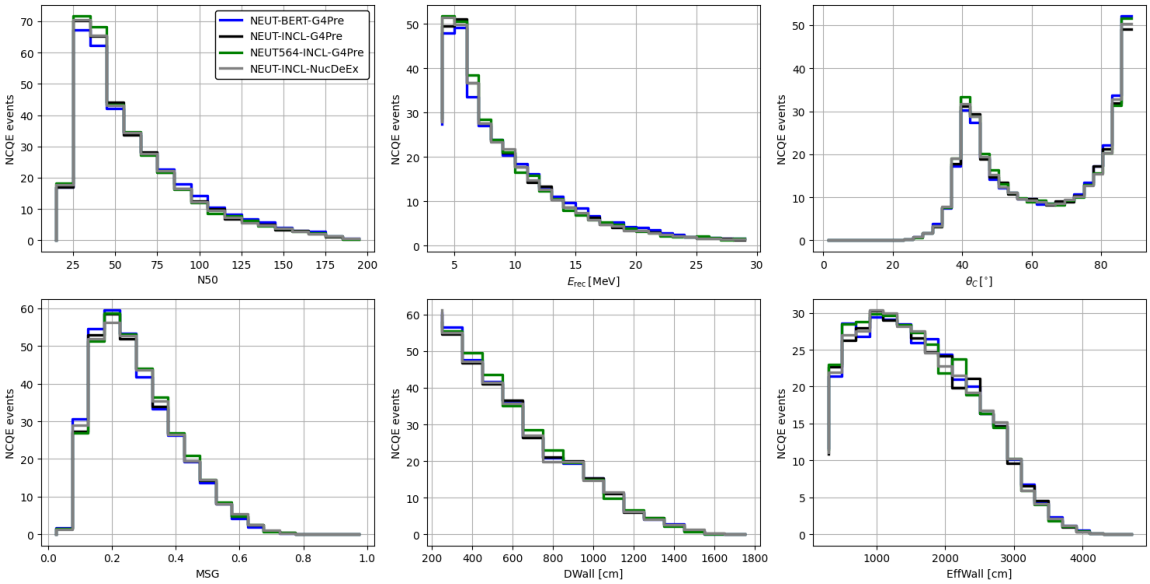

Figure 10.10: The features of T2K NCQE events (FHC, Run 1-11) among BERT-Pre, INCL-G4Pre, INCL-NucDeEx, and NEUT(564)-INCL-G4Pre.

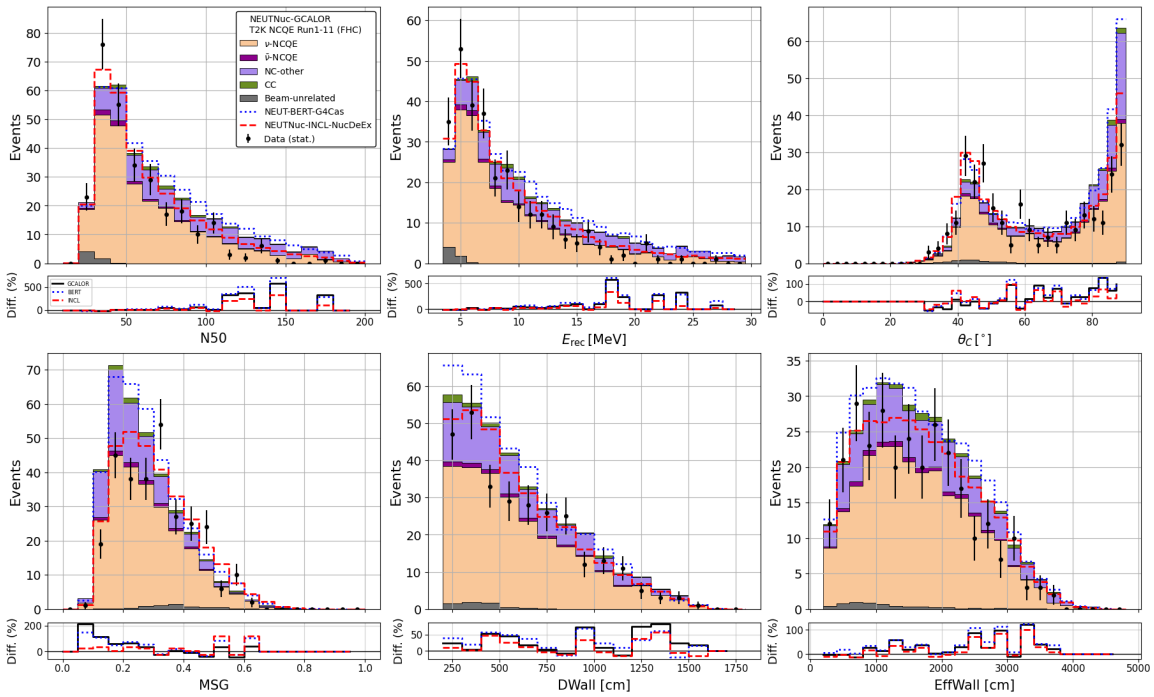

Figure 10.11: The features of T2K NCQE events (FHC) among Runs 1-11.

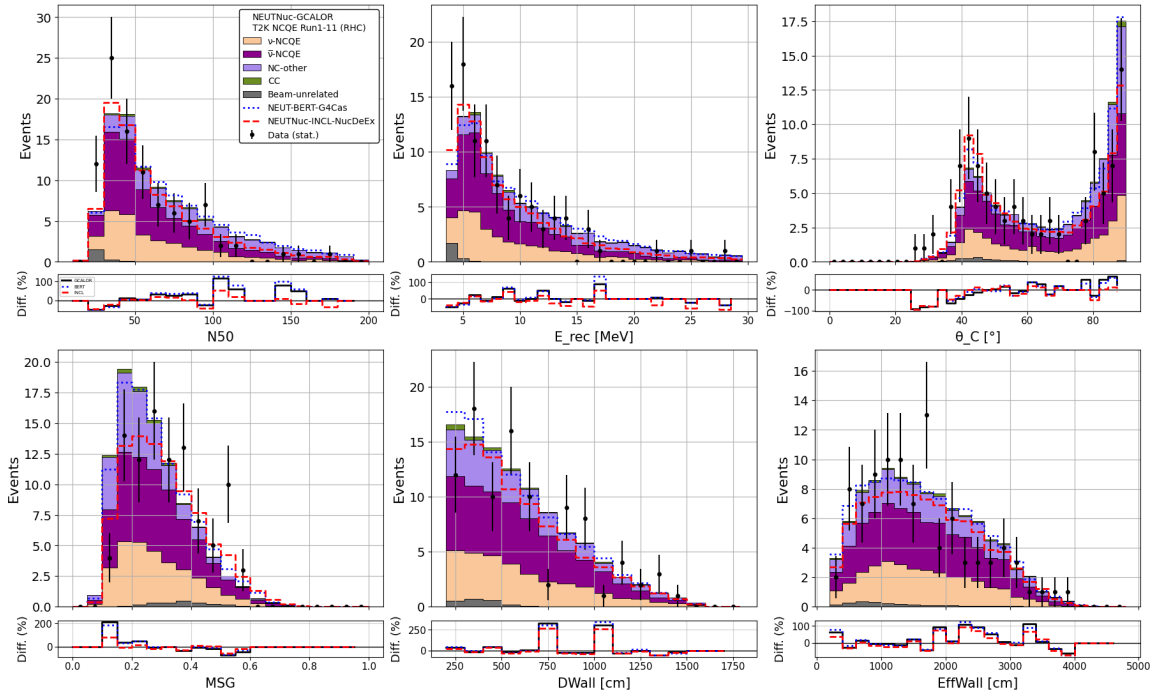

Figure 10.12: The features of T2K NCQE events (RHC) among Runs 1-9.

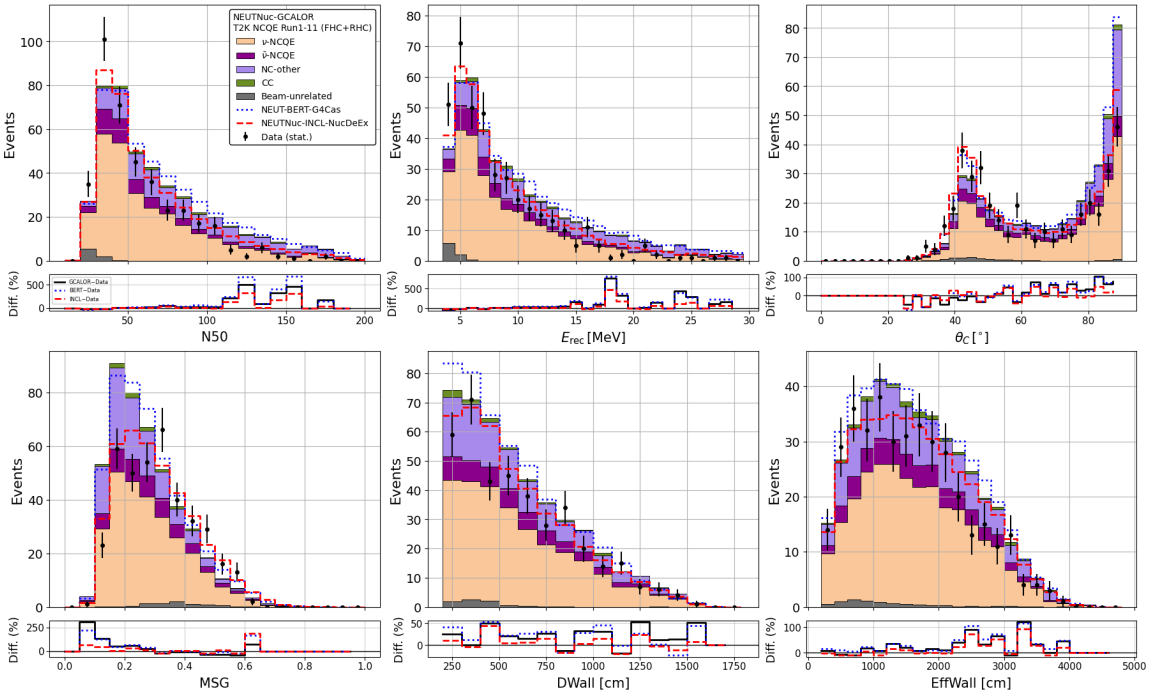

Figure 10.13: The features of T2K NCQE events (FHC+RHC) among Runs 1-11.

In summary, we carried out an assessment of de-excitation and intra-nuclear cascade models using both FHC and RHC MC and data sets. The results disfavor the G4Cascade and GCALOR configurations at a significance greater than 3σ with statistical error only. All examined observables, will be used in the next chapter to evaluate the systematic uncertainty on MC-to-data differences for NCQE interactions.

10.3 NCQE cross-section related systematic uncertainty

In the NCQE cross-section analysis, we omit "NEUTNuc–GCALOR" and "NEUT–BERT–G4Cas" due to discrepancies observed in Section 10.2.1. This decision is also supported by the MC truth γ in the detector simulation: "NEUT–BERT–G4Cas" lacks the nucleon de-excitation spectrum, making it an unsuitable choice for this low-energy study. All other MC settings were retained for the systematic uncertainty evaluation.

10.3.1 T2K flux

For T2K flux uncertainties, we use the values provided in the T2K flux release 21bv2 and reweight each event by neutrino flavor and energy. Figure 10.14 shows the uncertainties at SK in the ν_μ and $\bar{\nu_\mu}$ modes. The latest flux tuning file used in this study is plotted in solid black, and it improves upon the previous flux file shown as a dashed

black line. The dominant sources of flux uncertainty are the hadron interaction cross section and the proton beam profile. Further details are available in Ref. [162].

For NCQE events, we evaluate the impact of the T2K flux uncertainty after all selection cuts by comparing to the nominal prediction. Table 10.7 summarizes the channel-by-channel uncertainty breakdown.

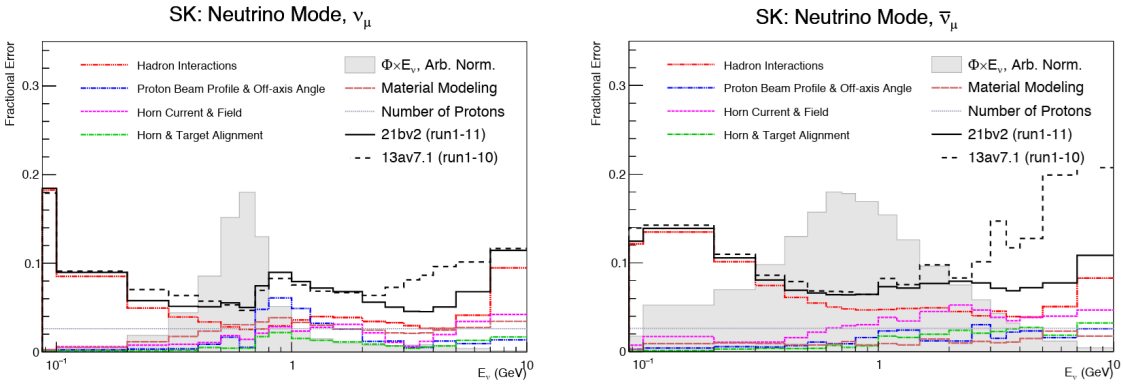

Figure 10.14: The previous (dashed black) T2K neutrino beam uncertainty and the updated one (solid black) in this study.

Table 10.7: Flux originated systematic uncertainties [%] for each interaction.

	ν-NCQE	$\bar{\nu}$-NCQE	NC-other	CC	Total (FHC+RHC)
FHC	5.6	6.2	6.0	5.7	6.2
RHC	6.6	7.2	7.1	8.2	

10.3.2 Neutrino interaction

T2KReWeight We evaluate uncertainties from neutrino interaction models by reweighting each MC event. For every event, model parameters within NEUT are shifted by their 1σ uncertainties using `T2KReWeight` version 24.12, and we adopt the package's default 1σ values.

Following Ref. [50], we do not assign uncertainties to the NCQE signal in neutrino interaction because the emitted γ rays are treated as isotropic and the detector is effectively 4π efficient. This choice is supported by the signal Q^2 distributions at each selection stage, which show no significant changes across the selections as shown in Figure 10.15 [4].

The resulting uncertainties are summarized in Table 10.8.

NC inelastic scattering In our MC, neutral-current (NC) inelastic scattering on oxygen without nucleon emission,

$$\nu\,(\bar{\nu}) + {}^{16}\mathrm{O} \rightarrow \nu\,(\bar{\nu}) + {}^{16}\mathrm{O}^{*}, \tag{10.2}$$

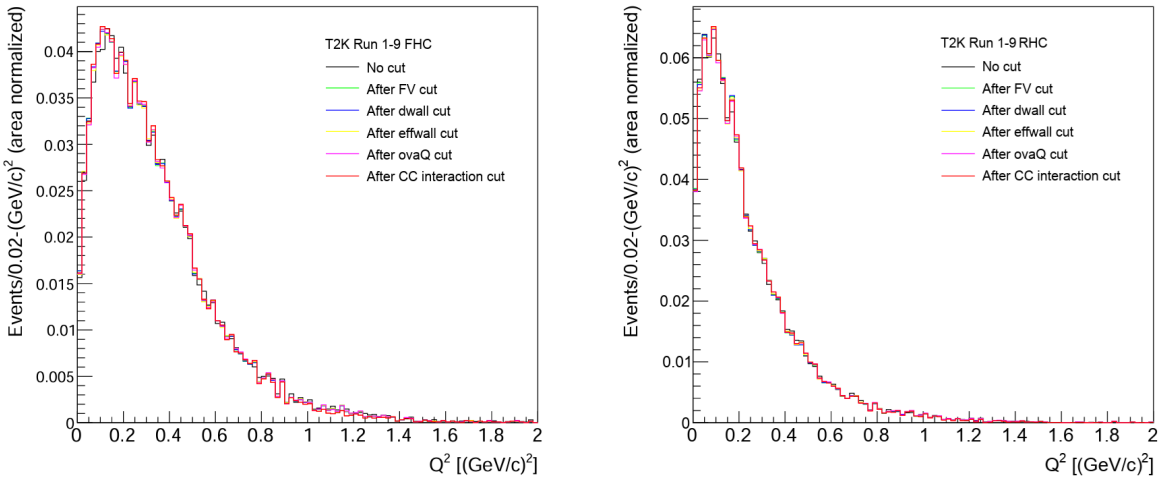

Figure 10.15: The Q^2 distributions of ν-NCQE in FHC (left) and $\bar{\nu}$-NCQE in RHC (right) each selection stage. Figure were taken from Ref. [4]

Table 10.8: Neutrino interaction related systematic uncertainties [%] for each interaction.

		ν-NCQE	$\bar{\nu}$-NCQE	NC-other	CC	Total (FHC+RHC)
FHC	T2KReWeight	—	—	4.8	10.2	3.9
	NC coherent inelastic	3.0	3.0	—	—	
RHC	T2KReWeight	—	—	5.5	12.2	
	NC coherent inelastic	3.0	3.0	—	—	

is not simulated because the associated γ-ray emission is not modeled. Nonetheless, our selection could still include such events. Therefore, we compare the NC (Left panel of Figure 10.16) and NCQE (Right panel of Figure 10.16) cross section.

Left panel of Figure 10.16 (from Ref. [164]) shows the NC cross sections on oxygen that populate the ground states (^{15}O, ^{15}N) and the excited states (^{15}O*, ^{15}N*), which arise from the decay of ^{16}O* after NC inelastic scattering with no nucleon knock-out. The summed cross section to ^{15}O* and ^{15}N* increases from 6.7×10^{-42} cm^2 at $E_\nu = 50$ MeV to 4.8×10^{-40} cm^2 at $E_\nu = 500$ MeV. Right panel of Figure 10.16 (from Ref. [26]) shows the NCQE cross sections. Comparing the two, NCQE dominates over NC inelastic without nucleon emission for $E_\nu \gtrsim 200$ MeV. At $E_\nu = 500$ MeV the NCQE cross section is about 40 times larger and becomes even more dominant at higher energies. Since the T2K sample is primarily from $E_\nu \sim 600$ MeV, and assuming the detectable γ-ray yield from the inelastic channel (without nucleon emission) is minor compared to that from NCQE, we assign a conservative 3% systematic uncertainty to cover this effect. The same assignment is used for antineutrinos. The resulting uncertainties are summarized in Table 10.8.

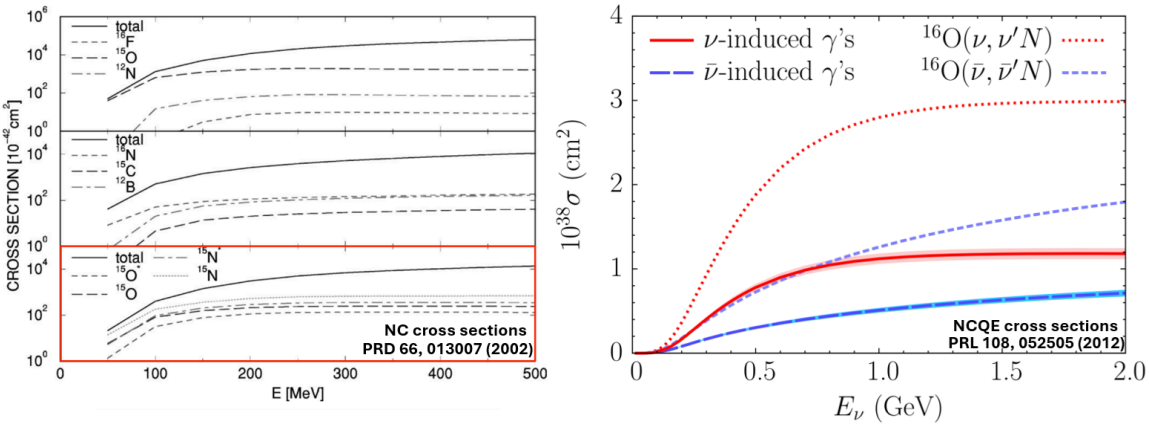

Figure 10.16: Comparison of NC inelastic (left) and NCQE cross sections on oxygen (right).

10.3.3 Primary-γ

Ref. [50] estimated primary-γ production using spectroscopic strengths for the $p_{1/2}$, $p_{3/2}$, $s_{1/2}$, and "other" states with probabilities

$$(p_{1/2},\ p_{3/2},\ s_{1/2},\ \text{others}) = (0.158,\ 0.3515,\ 0.1055,\ 0.385).$$

The nominal model folds the "others" component into $s_{1/2}$, whereas an extreme scenario assigns it to $(p_{1/2})^{-1}$, yielding (0.543, 0.3515, 0.1055), which dominates the primary-γ uncertainty. We adopt this treatment directly. The corresponding uncertainty is listed in Table 10.9.

This study also finds that the de-excitation model choice within NEUT (default vs. `NucDeEx`) introduces a noticeable primary-γ uncertainty. To quantify it, we compare MC configurations `NEUT-INCL-NucDeEx` and `NEUTNuc-INCL-NucDeEx`. The difference in the final NCQE event counts between these two settings is taken as the de-excitation model uncertainty within NEUT. The resulting values are reported in Table 10.9.

Table 10.9: Primary-γ originated systematic errors [%] for each interaction.

		ν-NCQE	$\bar{\nu}$-NCQE	NC-other	CC
FHC	$p_{3/2}$ changed	0.1	3.3	3.1	5.6
	others integrated into $(p_{1/2})^{-1}$	11.0	10.1	5.1	3.4
	De-excitation model	10.7	4.3	5.4	13.7
	Total	**15.2**	**11.4**	**8.0**	**15.2**
RHC	$p_{3/2}$ changed	0.8	1.8	2.6	< 0.1
	others integrated into $(p_{1/2})^{-1}$	12.2	11.3	2.3	0.5
	De-excitation model	11.7	5.2	0.7	2.0
	Total	**16.3**	**12.3**	**3.6**	**2.1**

10.3.4 Secondary-γ

This study updates the detector simulation and now enables switching between secondary-interaction models. Accordingly, we re-evaluate the associated uncertainty, replacing the "Secondary Cherenkov photons [50] (evaluate from γ spectrum from ^9Li measurement [165])" with "Secondary interaction models (evaluate from switching SI models in SKG4)". The systematic uncertainty is defined as the largest discrepancy observed among the following MC configurations: `NEUT_BERT_G4Pre`, `NEUT_INCL_G4Pre`, `NEUT_INCL_NucDeEx`, and `NEUT564_INCL_G4Pre`. For both FHC and RHC modes, the maximum deviation arises from the difference between `NEUT564_INCL_G4Pre` and `NEUT_INCL_G4Pre`. These configurations cover variations in the intra-nuclear cascade, nuclear de-excitation, and an updated NCQE model. The results, summarized in Table 10.10, show an improvement in the secondary-γ uncertainty compared with Ref. [50], consistent with the adoption of more precise physics models. The resulting values are reported in Table 10.10.

Following Ref. [50], we assess the impact of nucleon final-state interactions (FSI) on secondary γ production by varying the NEUT FSI cross sections by a conservative $\pm 30\%$ and comparing the resulting event yields. The selected sample changes by at most a few percent. Therefore, we assign a uniform 3.0% systematic uncertainty to all interaction channels in both modes.

Table 10.10: Secondary-γ originated systematic errors [%] for each interaction.

		ν-NCQE	$\bar{\nu}$-NCQE	NC-other	CC
FHC	Secondary interaction models	3.8	5.7	2.9	13.7
	nucleon FSI	3.0	3.0	3.0	3.0
	Total	**4.8**	**6.4**	**4.2**	**14.0**
RHC	Secondary interaction models	2.8	5.5	3.7	10.3
	nucleon FSI	3.0	3.0	3.0	3.0
	Total	**4.1**	**6.3**	**4.8**	**10.7**

10.3.5 Summary of uncertainty

In short, after updating the intranuclear and de-excitation modeling, our simulation is more reliable and yields a tighter constraint on the NCQE cross section uncertainty compared with Ref. [50]. The uncertainty from secondary γ's decreases by about 10%. The primary γ uncertainty increases by a few percent compared with Ref. [50] because we enabled the new de-excitation option `NucDeEx`. The flux uncertainty improves by a few percent thanks to updated NA61/SHINE measurements and refined simulation settings. The oscillation and detector response uncertainties are the same as in Ref. [50], since the oscillation parameter constraints and detector conditions are comparable.

Table 10.11 summarizes the revised NCQE cross-section systematic uncertainties. Original values taken from Ref. [50] are struck out where updated numbers are available. Unchanged entries are retained. Overall, the total uncertainty improves by about a few percent.

Table 10.11: Summary of systematic uncertainties (%) and event composition fractions (%) for the NCQE cross section. Struck-out entries indicate the values used in the Run 1–9 measurement [50]; updated values are given here.

		ν-NCQE	$\bar{\nu}$-NCQE	NC-other	CC	Acc.
FHC	Neutrino flux	~~6.7~~ 5.6	~~8.6~~ 6.2	~~7.3~~ 6.0	~~6.4~~ 5.7	–
	Neutrino interaction	3.0	3.0	~~8.2~~ 4.8	~~16.5~~ 10.2	–
	Primary-γ production	~~11.0~~ 15.2	~~10.6~~ 11.4	~~6.0~~ 8.0	~~6.6~~ 15.2	–
	Secondary-γ production	~~13.5~~ 4.8	~~13.4~~ 6.4	~~19.5~~ 4.2	~~17.6~~ 14.0	–
	Oscillation parameter	–	–	–	4.1	–
	Detector response	3.4	3.4	2.0	5.2	–
	Total error	~~19.2~~ 17.2	~~19.7~~ 14.9	~~23.3~~ 11.9	~~26.7~~ 24.6	3.0
RHC	Neutrino flux	~~7.0~~ 6.6	~~6.4~~ 7.2	~~7.0~~ 7.1	~~6.5~~ 8.2	–
	Neutrino interaction	3.0	3.0	~~10.8~~ 5.5	~~38.2~~ 12.2	–
	Primary-γ production	~~12.2~~ 16.3	~~11.4~~ 12.3	~~3.5~~ 3.6	~~0.5~~ 2.1	–
	Secondary-γ production	~~13.6~~ 4.1	~~13.1~~ 6.3	~~19.3~~ 4.8	~~21.4~~ 10.7	–
	Oscillation parameter	–	–	–	3.1	–
	Detector response	3.4	3.4	2.0	5.2	–
	Total error	~~20.1~~ 18.6	~~19.0~~ 16.2	~~23.4~~ 10.9	~~44.7~~ 19.2	3.0

10.4 NCQE cross-section measurement result

Notation We explain how the observed NCQE event numbers, combined with MC prediction and systematic uncertainty leads to the NCQE cross section results. The capital D refers to counts from *data* and a capital M refers to counts from *MC*. For each running mode, FHC or RHC, the observed data count can be modeled as

$$D^{\text{mode}}_{\text{obs}} = f_{\nu\text{-NCQE}}\, M^{\text{mode}}_{\nu\text{-NCQE}} + \bar{f}_{\nu\text{-NCQE}}\, M^{\text{mode}}_{\bar{\nu}\text{-NCQE}} + M^{\text{mode}}_{\text{NC-other}} + M^{\text{mode}}_{\text{CC}} + D^{\text{mode}}_{\text{beam-unrelated}},$$

with mode with FHC or RHC. Here $M^{\text{mode}}_{\nu\text{-NCQE}}$ and $M^{\text{mode}}_{\bar{\nu}\text{-NCQE}}$ are the NEUT-predicted numbers of neutrino and antineutrino NCQE events. The terms $M^{\text{mode}}_{\text{NC-other}}$, $M^{\text{mode}}_{\text{CC}}$, and $D^{\text{mode}}_{\text{beam-unrelated}}$ are backgrounds from other NC interactions, CC interactions, and non-beam sources, respectively. The scale factors $f_{\nu\text{-NCQE}}$ and $\bar{f}_{\nu\text{-NCQE}}$ are the parameters to be measured.

For each running mode, we subtract the known backgrounds and the non-NCQE MC contributions from the data to isolate the NCQE components :

$$D_{\text{obs}}^{\text{FHC}} - M_{\text{NC-other}}^{\text{FHC}} - M_{\text{CC}}^{\text{FHC}} - D_{\text{beam-unrelated}}^{\text{FHC}} = f_{\nu\text{-NCQE}}\, M_{\nu\text{-NCQE}}^{\text{FHC}} + \bar{f}_{\nu\text{-NCQE}}\, M_{\bar{\nu}\text{-NCQE}}^{\text{FHC}}, \tag{10.3}$$

$$D_{\text{obs}}^{\text{RHC}} - M_{\text{NC-other}}^{\text{RHC}} - M_{\text{CC}}^{\text{RHC}} - D_{\text{beam-unrelated}}^{\text{RHC}} = f_{\nu\text{-NCQE}}\, M_{\nu\text{-NCQE}}^{\text{RHC}} + \bar{f}_{\nu\text{-NCQE}}\, M_{\bar{\nu}\text{-NCQE}}^{\text{RHC}}. \tag{10.4}$$

Solving the two-equation system for the NCQE scale factors gives

$$f_{\nu\text{-NCQE}} = \frac{X\, M_{\bar{\nu}\text{-NCQE}}^{\text{RHC}} - Y\, M_{\nu\text{-NCQE}}^{\text{FHC}}}{M_{\nu\text{-NCQE}}^{\text{FHC}}\, M_{\bar{\nu}\text{-NCQE}}^{\text{RHC}} - M_{\bar{\nu}\text{-NCQE}}^{\text{FHC}}\, M_{\nu\text{-NCQE}}^{\text{RHC}}}, \tag{10.5}$$

$$f_{\bar{\nu}\text{-NCQE}} = \frac{X\, M_{\nu\text{-NCQE}}^{\text{RHC}} - Y\, M_{\bar{\nu}\text{-NCQE}}^{\text{FHC}}}{M_{\nu\text{-NCQE}}^{\text{FHC}}\, M_{\bar{\nu}\text{-NCQE}}^{\text{RHC}} - M_{\bar{\nu}\text{-NCQE}}^{\text{FHC}}\, M_{\nu\text{-NCQE}}^{\text{RHC}}}. \tag{10.6}$$

Here the inputs X and Y are defined as

$$X = D_{\text{obs}}^{\text{FHC}} - M_{\text{NC-other}}^{\text{FHC}} - M_{\text{CC}}^{\text{FHC}} - D_{\text{beam-unrelated}}^{\text{FHC}}, \tag{10.7}$$

$$Y = D_{\text{obs}}^{\text{RHC}} - M_{\text{NC-other}}^{\text{RHC}} - M_{\text{CC}}^{\text{RHC}} - D_{\text{beam-unrelated}}^{\text{RHC}}. \tag{10.8}$$

Given the observed quantities X and Y and the MC expectations M, these formulas directly yield the scale factors $f_{\nu\text{-NCQE}}$ and $f_{\bar{\nu}\text{-NCQE}}$. These factors are then applied to the predicted MC cross-section to derive the observed NCQE cross-section.

Scale factors and uncertainties With $D_{\text{obs}}^{\text{FHC}} = 289$ and $D_{\text{obs}}^{\text{RHC}} = 97$ and nominal MC inputs as in Table 10.5, the fitted scale factors are $f_{\nu\text{-NCQE}} = 0.82$ and $\bar{f}_{\nu\text{-NCQE}} = 1.10$. Uncertainties are evaluated using toy MC by varying the inputs with 1σ Gaussian fluctuations, as shown in Figure 10.17 and 10.18. We include statistical fluctuations for $D_{\text{obs}}^{\text{mode}}$ and systematic variations for $M_{\nu\text{-NCQE}}^{\text{mode}}$, $M_{\bar{\nu}\text{-NCQE}}^{\text{mode}}$, $M_{\text{NC-other}}^{\text{mode}}$, and $M_{\text{CC}}^{\text{mode}}$. Variations from different sources are drawn independently, except that primary and secondary γ-production uncertainties are treated as correlated across interaction types and modes. Flux and cross-section parameter correlations have negligible impact and are ignored. We obtain the following:

$$f_{\nu\text{-NCQE}} = 0.82 \pm 0.07\ (\text{stat.})\ ^{+0.20}_{-0.11}\ (\text{syst.}), \tag{10.9}$$

$$\bar{f}_{\nu\text{-NCQE}} = 1.10 \pm 0.20\ (\text{stat.})\ ^{+0.22}_{-0.15}\ (\text{syst.}). \tag{10.10}$$

The NEUT flux-averaged NCQE cross sections on oxygen are computed with MC and denoted $\langle\sigma^{\text{NEUT}}_{\nu\text{-NCQE}}\rangle$ and $\langle\sigma^{\text{NEUT}}_{\bar{\nu}\text{-NCQE}}\rangle$. For the calcualtion, we use the pure ϕ^{FHC}_{ν} spectrum for neutrinos and the pure $\phi^{\text{RHC}}_{\bar{\nu}}$ spectrum for antineutrinos. The sums run over muon and electron flavors, and the energy integrals extend to 10 GeV. The observed flux-averaged NCQE-like cross sections are then obtained by scaling the NEUT predictions with the fitted factors: $\langle\sigma^{\text{obs}}_{\nu\text{-NCQE}}\rangle = f_{\nu\text{-NCQE}} \cdot \langle\sigma^{\text{NEUT}}_{\nu\text{-NCQE}}\rangle$ and $\langle\sigma^{\text{obs}}_{\bar{\nu}\text{-NCQE}}\rangle = f_{\bar{\nu}\text{-NCQE}} \cdot \langle\sigma^{\text{NEUT}}_{\bar{\nu}\text{-NCQE}}\rangle$:

The predictions of the flux-averaged cross sections by NEUT for the neutrino and antineutrino NCQE interactions ($\langle\sigma^{\text{NEUT}}_{\nu\text{-NCQE}}\rangle$ and $\langle\sigma^{\text{NEUT}}_{\bar{\nu}\text{-NCQE}}\rangle$) are calculated as below:

$$\langle\sigma^{\text{NEUT}}_{\nu\text{-NCQE}}\rangle = \frac{\sum_{\nu=\nu_\mu,\nu_e}\int \sigma^{\text{NEUT}}_{\nu\text{-NCQE}}(E_\nu)\phi_\nu(E_\nu)dE_\nu}{\sum_{\nu=\nu_\mu,\nu_e}\int \phi_\nu(E_\nu)dE_\nu} = 2.11\times10^{-38}\ \text{cm}^2/\text{oxygen}, \tag{10.11}$$

$$\langle\sigma^{\text{NEUT}}_{\bar{\nu}\text{-NCQE}}\rangle = \frac{\sum_{\nu=\bar{\nu}_\mu,\bar{\nu}_e}\int \sigma^{\text{NEUT}}_{\bar{\nu}\text{-NCQE}}(E_\nu)\phi_\nu(E_\nu)dE_\nu}{\sum_{\nu=\bar{\nu}_\mu,\bar{\nu}_e}\int \phi_\nu(E_\nu)dE_\nu} = 0.90\times10^{-38}\ \text{cm}^2/\text{oxygen}. \tag{10.12}$$

$$\langle\sigma^{\text{obs}}_{\nu\text{-NCQE}}\rangle = \left(1.75 \pm 0.15\ (\text{stat.})^{+0.43}_{-0.23}\ (\text{syst.})\right)\times10^{-38}\ \text{cm}^2/\text{oxygen}, \tag{10.13}$$

$$\langle\sigma^{\text{obs}}_{\bar{\nu}\text{-NCQE}}\rangle = \left(0.97 \pm 0.16\ (\text{stat.})^{+0.19}_{-0.13}\ (\text{syst.})\right)\times10^{-38}\ \text{cm}^2/\text{oxygen}. \tag{10.14}$$

For comparison, the Run 1–9 flux-averaged NCQE cross sections were measured to be

$$\left\langle\sigma^{\text{Run 1–9}}_{\nu\text{-NCQE}}\right\rangle = \left(1.70 \pm 0.17\ (\text{stat.})^{+0.51}_{-0.38}\ (\text{syst.})\right)\times10^{-38}\ \text{cm}^2/\text{oxygen},$$

$$\left\langle\sigma^{\text{Run 1–9}}_{\bar{\nu}\text{-NCQE}}\right\rangle = \left(0.98 \pm 0.16\ (\text{stat.})^{+0.26}_{-0.19}\ (\text{syst.})\right)\times10^{-38}\ \text{cm}^2/\text{oxygen}.$$

Our updated results are consistent with these values and show a few-percent improvement in precision, in line with expectations from the revised systematic-uncertainty evaluation as shown in Figure 10.19.

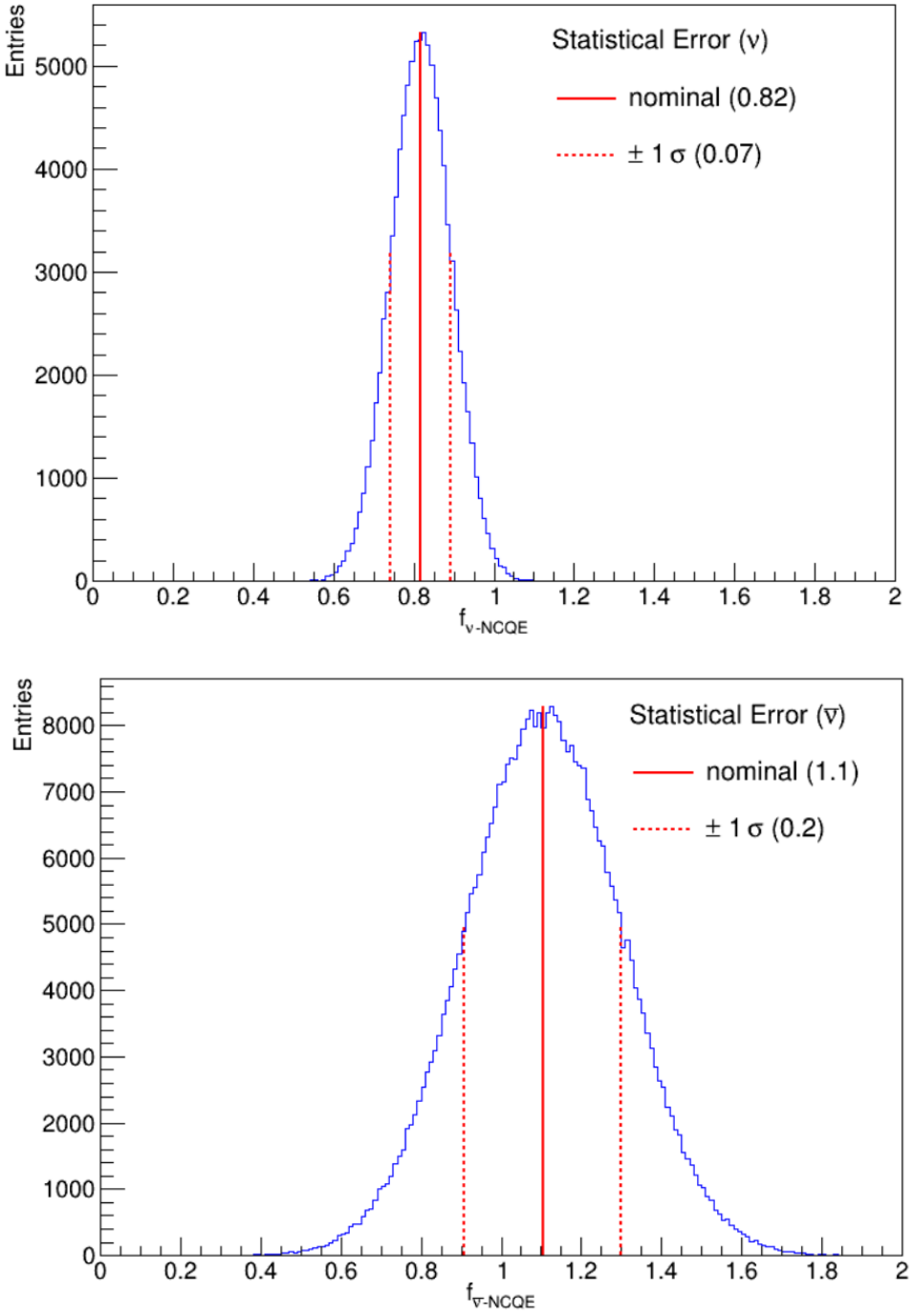

Figure 10.17: Scale factor results from pseudo-experiments, where observed event counts were fluctuated according to statistical uncertainties. The extracted values are $f_{\nu\text{-NCQE}} = 0.82 \pm 0.07$ and $f_{\bar{\nu}\text{-NCQE}} = 1.10 \pm 0.20$.

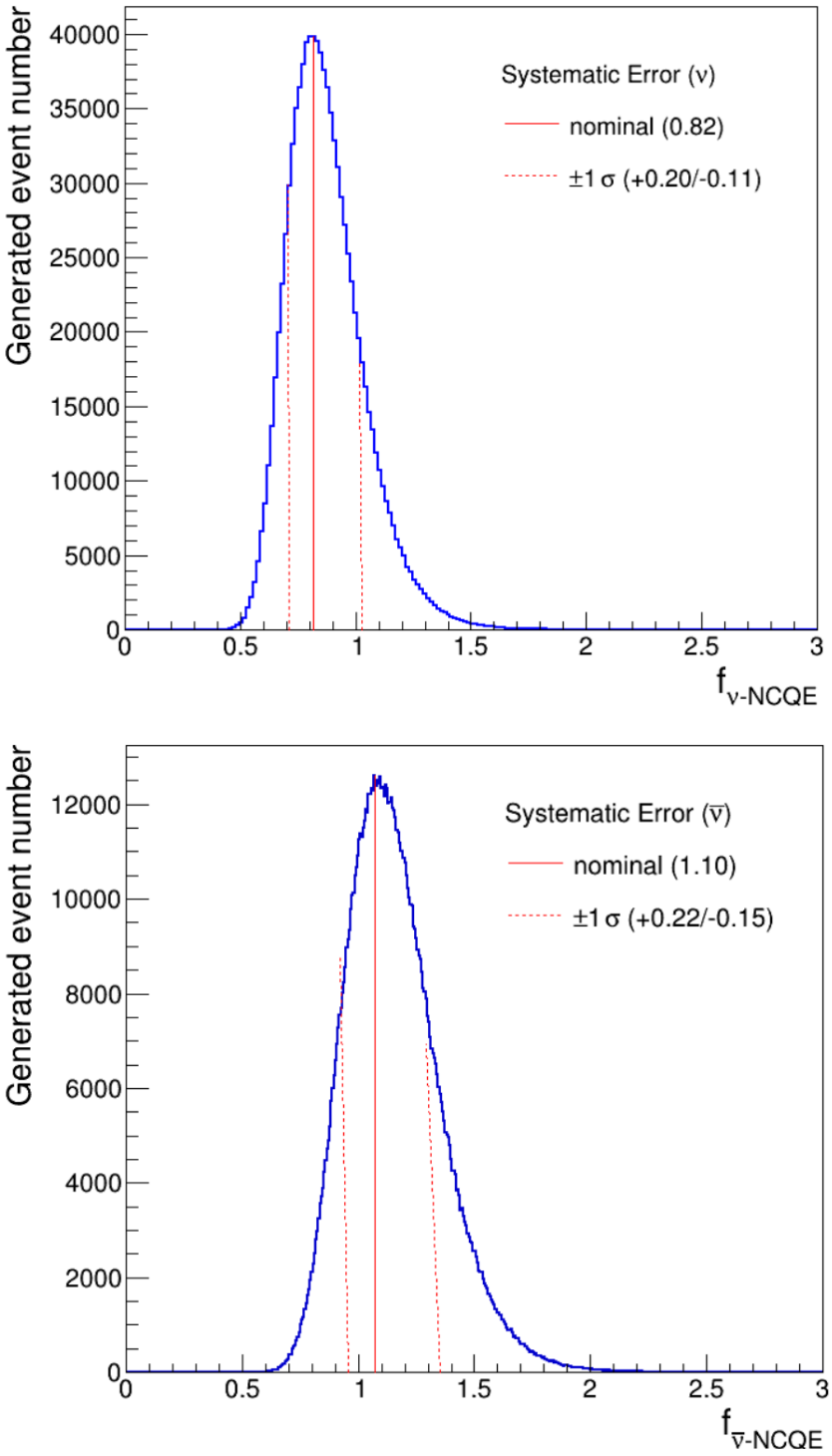

Figure 10.18: Systematic uncertainty evaluation of the scale factors via pseudo-experiment variations. The resulting values are $f_{\nu\text{-NCQE}} = 0.82^{+0.20}_{-0.11}$ and $f_{\bar{\nu}\text{-NCQE}} = 1.10^{+0.22}_{-0.15}$, with the secondary-$\gamma$ emission model identified as the primary source of uncertainty.

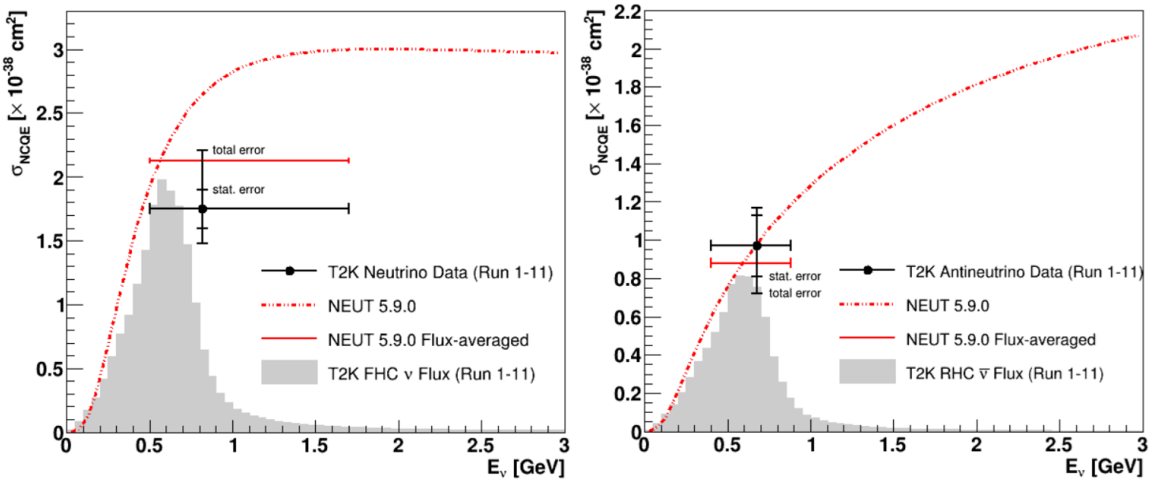

Figure 10.19: Measured Run 1-11 NCQE-like cross sections on ν–^{16}O (left) and $\bar{\nu}$–^{16}O (right), compared with the NEUT NCQE predictions. Data points are placed at the flux-mean energies: 0.82 GeV for neutrinos and 0.68 GeV for antineutrinos. Vertical bars show statistical uncertainties (shorter) and the total uncertainties (longer). Horizontal bars indicate the $\pm 1\sigma$ ranges for the T2K flux spectra.

This change reduces the systematic uncertainty in the predicted T2K NCQE event count used to determine the NCQE cross section. We describe the updated systematics below. Statistically, the added data from Runs 10 and 11 improves the FHC result. The RHC result is unchanged because these runs included no additional RHC data.

10.4.1 Systematic uncertainty improves other than SI models

In addition to improvements in SI models, the total systematic uncertainty for RHC CC events exhibits a reduction from 44.7% to 19.2%. This is primarily driven by a substantial decrease in neutrino interaction uncertainty (from 38.2% to 12.2%), which is likely attributable to updates in Deep Inelastic Scattering (DIS) and multi-pion production within NEUT version 5.6.2. Historically, these channels were assigned conservative systematic errors due to significant uncertainties in the RHC beam. However, modifications within NEUT version 5.6.2 have allowed for tighter constraints on their cross-sections. Furthermore, the implementation of binding energy corrections in the Nieves 1p1h model (CCQE) provides a more precise description of nuclear effects, while the introduction of the Dynamical Coupled Channels (DCC) model offers a more physically rigorous framework for resonant pion production than the legacy Rein-Sehgal model. Collectively, these refinements across the transition, resonance, and high-W regions could potentially be an explaination of the improvement in CC systematics.

10.4.2 Prospect of T2K NCQE Cross-section measurements

Following the update of the SI models in this study, the uncertainty associated with primary-γ production has emerged as the dominant source of systematic error in the NCQE cross-section measurement. To further improve the precision of the T2K NCQE result, two key developments are necessary. First, more precise spectroscopic strengths for the "other" states are required to replace the current conservative approach, where these components are assigned to the $(p_{1/2})^{-1}$ state. Second, a dedicated evaluation of the systematic uncertainty inherent to the `NucDeEx` model is essential to constrain the de-excitation modeling errors.

Overcoming these current limitations will depend heavily on future experimental programs. For example, inverse kinematics measurement, SAMURAI-79, conducted at the RIKEN Radioactive Isotope Beam Factory (RIBF) [158], is expected to yield high-precision measurements of de-excitation products and potentially resolve spectroscopic strengths. These data will be fundamental in constraining de-excitation model uncertainties and refining the neutrino-nucleus interaction frameworks employed in subsequent analyses.

Chapter 11

The DSNB selection in SK

The NCQE cross section uncertainty is a crucial factor in the search for the DSNB, as reducing this uncertainty helps lower the prediction level of the dominant atmospheric NCQE background. With simulation improvements offering more precise predictions of event features, we present how T2K data is used to optimize DSNB selection and constrain the uncertainties in NCQE selection efficiency in this chapter.

We use a step-by-step set of selection cuts in the DSNB search at SK to separate the DSNB signal from several backgrounds. At each stage, we describe the cut and specify which backgrounds it suppresses. We then show how these selections were improved and validated. Finally, we benchmark and compare the selection approaches. The overall procedure follows the DSNB search for SK-VI (Ref. [23]) and uses the higher neutron tagging efficiency from the (n, γ_s)Gd signal.

The 1st reduction, Pre-Cut :

- **Remove non-physical and invalid triggers**
  - Discard calibration, pedestal, periodic, and T2K-beam trigger events.
  - Omit bad or incomplete runs and runs with unresolved issues.
- **Cosmic-ray muon veto**
  Reject any event occurring $\leq 50\,\mu$s after an OD-triggered muon to remove through-going muons and short-lived spallation daughters.
- **Fiducial volume cut**
  Require the reconstructed vertex to be at least 200 cm from the inner wall to suppress radioactivity near the tank wall.
- **Fit-quality cut**

Keep events with vertex-fit goodness $g_{\rm vtx} > 0.5$, as defined at Part. II, chpater 4.2.1, to reject random noise (retains $> 99.9\%$ of signal MC above 8 MeV).

- **Trigger consistency**
  Events must fire the SHE trigger and a valid AFT trigger. Apply the energy-dependent AFT efficiency correction (63–100%).

The 2nd reduction, Spallation-Cut [166] :

- **1-ms cut**
  Remove hadronic cascades produced by a muon within [0, 1]ms time window of the candidate. Targets the most obvious muon-spallation secondaries.

- **Neutron-cloud cut**
  Reject muons accompanied by clusters of neutron captures ("clouds'') identified through multiplicity, timing (35–535, μs), and spatial clustering. This suppresses neutron-rich spallation isotopes.

- **Multiple-spallation cut**
  Discard SHE candidates that have an additional low-energy ([6, 25] MeV) event within $\pm$60 s and a vertex less than 4m from the candidate. This removes muons producing more than one radioactive daughter.

- **Spallation likelihood cut**
  Apply a multivariate log-likelihood based on time difference, transverse/longitudinal separation, and muon charge deposition ($\Delta t, \ell_\perp, \ell_\parallel, Q_\mu, Q_{\rm res}$) to reject residual correlated muons.

- **Spallation box cut**
  Impose stricter bounds on muon track goodness, timing variance, and spatial separation, especially for high energy ($E > 16$ MeV) events, to eliminate the hardest spallation backgrounds.

The 3rd cut, e^+ signal cut :

- **Effective distance cut ($d_{\rm eff}$)**
  Define the effective distance from the reconstructed vertex to the tank wall along the event direction, $d_{\rm eff}$. Require

$$d_{\rm eff} \;>\; \max[\,300\,{\rm cm},\; 500\,{\rm cm} - 50\,(E_{\rm vis} - 16\,{\rm MeV})\,]\,. \tag{11.1}$$

  to suppress residual wall radioactivity while preserving fiducial volume.

- **Additional PMT-activity vetoes**

  - *Pre-activity:* veto if the maximum number of hits in any 15ns sub-window before the main peak exceeds $N_{\text{pre}}^{\max} \geq 12$.

  - *Post-activity:* veto if any decay-electron–like cluster is found within the $35, \mu$s trigger window ($N_{\text{decay-}e} = 0$ required) [167].

- **Pion-likeness cut (Ring clearness, L_{pion})**
  Quantify ring "fuzziness'' with the ratio of three-hit combinations near the ring edge: $L_{\text{pion}} = N_{\text{triplets}}(\theta_c \pm 3^\circ)/N_{\text{triplets}}(\theta_c \pm 10^\circ)$. Require $L_{\text{pion}} < 0.37$ to eliminate multi-ring π/γ events that yield diffuse light patterns.

- **Charge–hit ratio cut ($q50/n50$)**
  In a 50 ns window around the main peak of tof-subtracted PMT hits, compute the ratio of total charge (q50) to number of PMT hits (n50). Select $q50/n50 < 2$ to remove energetic muons that deposit abnormally large charge on single tubes, while retaining low–energy positrons.

- **Cherenkov-angle cut (θ_{C})**
  Exploit the fact that true positrons have a reconstructed Cherenkov angle near the electron value of 42°. Require θ_{C} cut at $[38^\circ, 53^\circ]$ to suppress NC γ's, muons, and pions whose rings mis-reconstruct to larger or smaller angles.

- **Multiple–Scattering Goodness cut (MSG)**
  The Cherenkov-ring pattern of the PMT hits is encoded into a "multiple-scattering goodness (defined at Part. II, chapter 4.2.4)" variable, which was originally developed in solar-ν analyses to tag multiple scattered $e^{\pm}$. MSG values $\sim$0.5 correspond to a single cone (single-e^+) Cherenkov ring, where smaller MSG values indicate multi-cone (multiple-γ) topologies, which is a typical pattern of NCQE interactions. In the SK-VI&VII DSNB searches [36], MSG cuts were applied on a bin-by-bin basis with a threshold of around 0.38.

The 4th reduction, single neutron capture cut :
Several algorithms are used to tag the neutron-capture signal that follows the e^+ candidate. Here we introduce two approaches: a selection based on explicit cuts, used in the SK-VI DSNB search [23], and a neural network method, used in SK-VII DSNB search [36].

- **Cut-based neutron tagging**
  The cut-based neutron selection is based on neutron capture observables: capture time, travel distance, the typical number of PMT hits from the capture cascade, and event quality criteria that remove PMT hits from dark noise. The cut values and their efficiencies were determined using an AmBe calibration source within the 535 μs SHE/AFT window. The cuts are summarized in Ta-

ble 11.1.

Table 11.1: Cut based neutron selection variables.

Cut variables	**Criteria**
Capture time t	$t > 4$ μs
N_{200}	$N_{200} \geq 25$
Fiducial volume cut	$d_{\text{wall}} > 2$ m
Vertex reconstruction goodness g_{vtx}	$g_{\text{vtx}} > 0.4$
Direction reconstruction goodness g_{dir}	$g_{\text{dir}} < 0.4$
Distance from prompt vertex d_{prompt}	$d_{\text{prompt}} < 300$ cm
Reconstructed energy E	$E > 3$ MeV

- **Neural-net-based neutron tagging**
  Instead of applying separate cuts to neutron-capture observables, the neural network uses twelve observables that distinguish neutron captures from dark noise and outputs a neutron likelihood score optimized for tagging efficiency. Twelve inputs are used PMT hits, spatial and topological descriptors, timing RMS, distance to the inner detector wall, and related variables. Events from the AmBe serve as a neutron-capture calibration source, and T2K dummy triggers data serve as dark-noise input for training and validation. An event is classified as a neutron capture if the neutron likelihood score exceeds 0.99. This threshold was set using the AmBe calibration to achieve 99% neutron capture purity.

Whether we use the cut based or neural network method, we require $N_n = 1$: exactly one tagged neutron per event. This matches the DSNB signal (exactly one neutron) and suppresses atmospheric NCQE backgrounds, which usually produce more than one neutron.

11.1 Improving the 3rd cuts

This analysis improves the 3rd cuts by refining two event features cut: the Cherenkov-angle (θ_C) cut and the Multiple Scattering Goodness (MSG) cut. Both are designed to suppress atmospheric NCQE backgrounds while preserving the DSNB signal. Because the T2K neutrino flux is similar to the atmospheric flux, as shown in Figure 11.1, and provides a high-purity NCQE sample, the θ_C cut was previously validated with T2K Run 1–9 NCQE data [50]. In contrast, MSG had been evaluated only on a limited Run 11 sample in Part II, chapter 7.3.3. Here we revisit the θ_C and MSG settings and provide data-driven constrain on uncertainty using the combined Run 1–11 dataset. Our goal is to establish a new selection strategy that achieves better signal efficiency with lower uncertainty than the current one. We will benchmark both the existing and proposed third-reduction selections and use the T2K dataset as a control sample to validate these cut strategies.

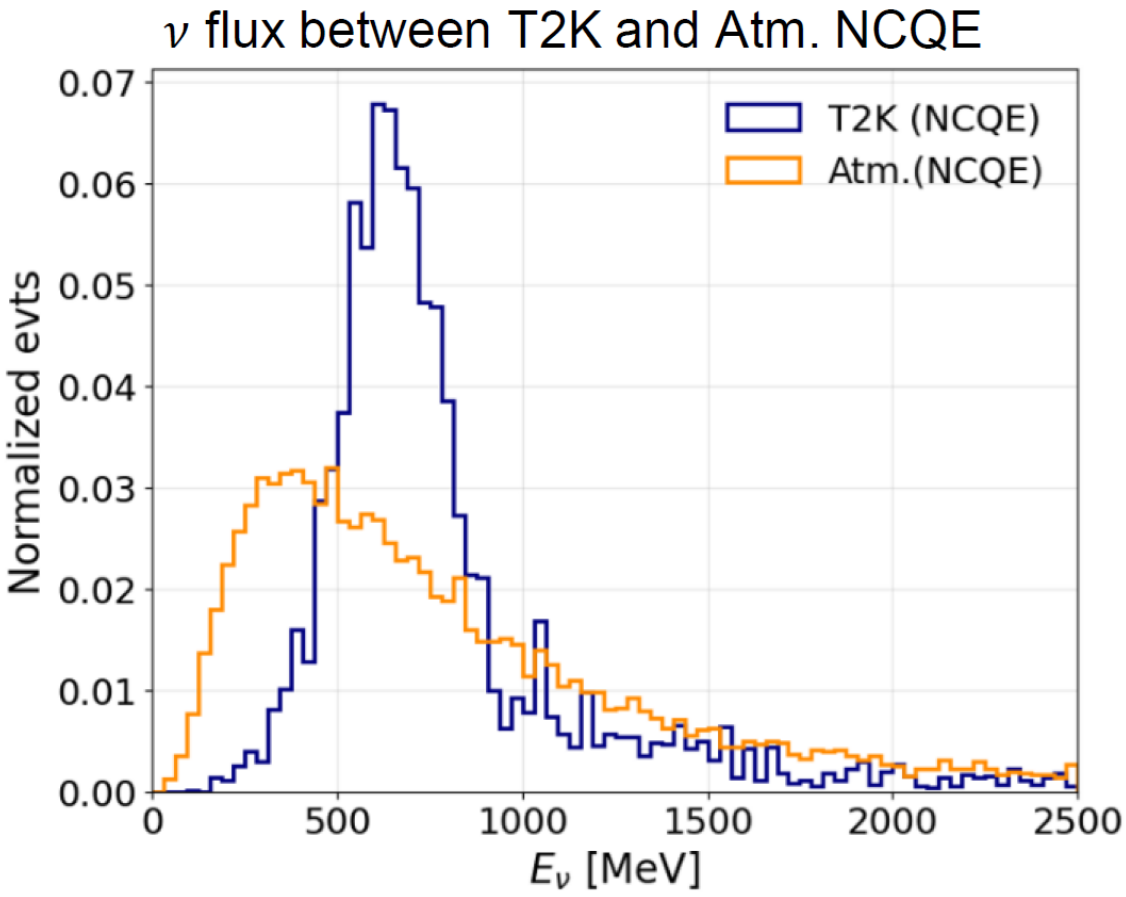

Figure 11.1: The T2K (blue) and atmospheric (yellow) neutrino fluxes, specifically for NCQE interactions.

11.1.1 MC samples for DSNB and atmospheric NCQE

The DSNB and atmospheric NCQE MC samples are taken from the SK-VI DSNB search [167]. For atmospheric NCQE, two configurations were used: BERT-G4Cascade and INCL-G4PreCompound. The BERT-G4Cascade sample provides the standard 500-year equivalent statistics, while the INCL-G4PreCompound sample provides 250 years. The INCL-G4PreCompound sample for atmospheric NCQE MC samples is adopted as the nominal setting in this study. Because the predicted neutron kinetic energy for DSNB is below 1 MeV, far lower than the $\mathcal{O}(100)$ MeV typical of atmospheric NCQE events, the impact of hadron–nucleus interactions on DSNB events is considered minor. Therefore, only the BERT-G4Cascade configuration was produced. The DSNB MC simulation is generated using a flat spectrum and subsequently reweighted to match the flux profile described in Horiuchi+09. Figure 11.2 illustrates the differences in event features among T2K, Atmospheric NCQE, and DSNB. These differences are primarily driven by γ and positron multiplicity. A schematic highlighting this distinction for DSNB and NCQE events is also included in the figure.

11.1.2 Cut strategies for DSNB and atmospheric NCQE

We begin by revisiting the previously applied θ_C and MSG cuts used to reduce atmospheric NCQE background, and we demonstrate how it can be improved in this study.
In general, the selection criteria used to suppress atmospheric NCQE events in the DSNB search can be summarized as follows:

- **θ_C cut within [38°, 53°] (used in DSNB SK-IV [35] and SK-VI [23])**
  This cut was first introduced in the DSNB search during the SK-IV phase, where a range of [38°, 50°] was applied. In the subsequent SK-VI phase, the upper bound was extended to [38°, 53°]. Figure 11.3 illustrates the distribution of relevant features before and after applying the θ_C cut. The brown and blue lines indicate the 95% containment regions for atmospheric NCQE and DSNB events, respectively.

- **θ_C + MSG discrete cut (used in DSNB SK-VII [36])**
  As shown in the center plot of Figure 11.3 (N50 vs. MSG distribution), a clear separation remains between atmospheric and DSNB events even after applying the θ_C cut. This indicates that MSG is a powerful discriminating variable and motivated its use as an additional cut. In the SK-VII phase of the DSNB study, an energy bin-by-bin MSG cut strategy was implemented, as shown in Figure 11.4.

  While the θ_C distribution has been validated with T2K data, the MSG variable

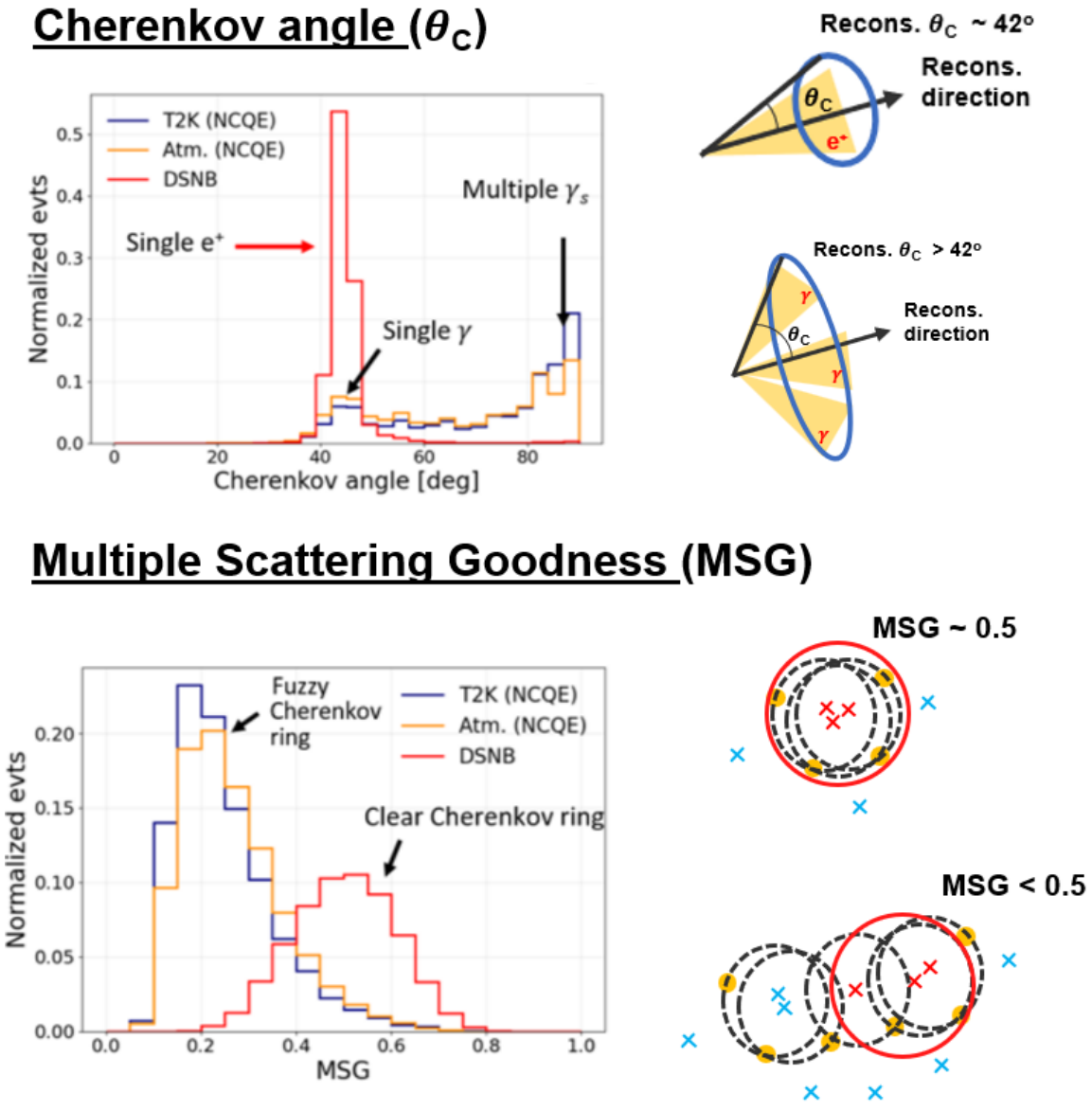

Figure 11.2: The T2K (blue) and atmospheric (yellow) neutrino NCQE event features, together with DSNB event feature (red).

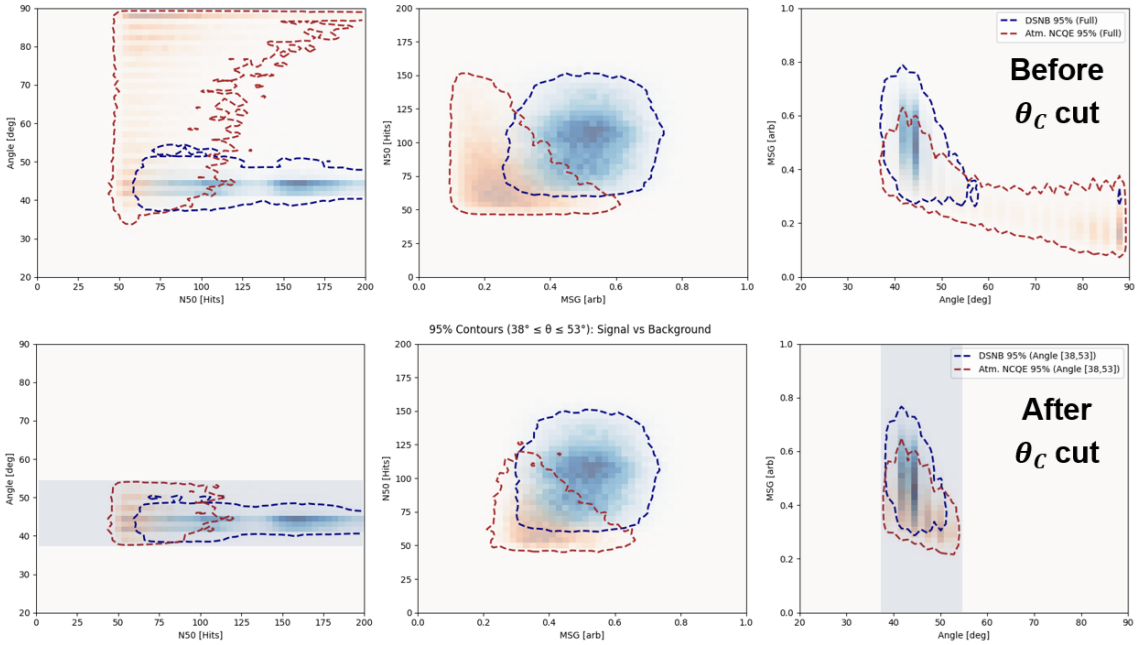

Figure 11.3: Feature distribution before and after applying the θ_C cut [38°, 53°]. Brown and blue lines mark the 95% containment for atmospheric NCQE and DSNB events, respectively.

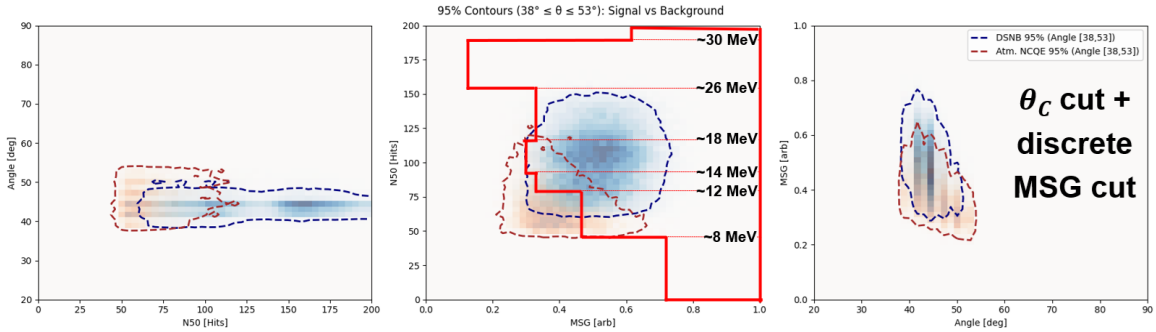

Figure 11.4: MSG cut strategy applied bin-by-bin in energy during the SK-VII DSNB search.

for NCQE events has not. As a result, the MSG discrete cut is currently adopted as a compromise. This study aims to explore advanced cut strategies and perform validation directly using the T2K NCQE sample.

- **θ_C + MSG linear cut (newly introduced in this study)**
  This study seeks to validate the MSG distribution in more depth, beginning with the MSG dependence on N50. This enables the formulation of a linear cut in the N50 versus MSG plane, as illustrated in the center plot of Figure 11.5. Here, S_{DSNB} denotes the expected number of signal events from the DSNB, and $B_{\mathrm{Atm.\,NCQE}}$ represents the expected number of background events arising from atmospheric NCQE interactions. The linear cuts were optimized by maximizing the opt value

  $$\mathrm{opt} = \frac{S_{\mathrm{DSNB}}}{\sqrt{S_{\mathrm{DSNB}} + B_{\mathrm{Atm.\,NCQE}}}}\,. \tag{11.2}$$

  Starting from the initial slope and intercept, $a_0 = 200$ and $b_0 = 160$, we performed 100,000 random trials varying a_0 and b_0 by $\pm 100\%$, and selected the parameters that yielded the highest opt value. The optimized parameters are $(a_0, b_0) = (-163.84,\ 146.48)$ for the linear cut with equation

  $$N_{50} = a_0 \cdot \mathrm{MSG} + b_0\,. \tag{11.3}$$

  When compared to the existing discrete MSG cut (left plot of Figure 11.5), the proposed linear cut shows improved signal efficiency in the [8, 12] MeV range, a region where the discrete cut performs poorly.

- **Neural Network (NN) cut (newly introduced in this study)**
  To further refine background suppression, we examine the correlations among N50, θ_C, and MSG distributions. Validating these dependencies allows for the development of a neural network (NN) classifier. The NN cut functions as a multivariate, MC-based shape selector, the details of which are provided in Chapter 11.1.3.

  As shown by the solid lines in the right plot of Figure 11.5, the NN-selected background closely overlaps with the signal MC shape, suggesting that the NN approach can suppress more background while retaining higher signal efficiency compared to the linear MSG cut.

11.1.3 Neural network for feature classification

A neural network is a function approximator that maps input features to output predictions. In a fully connected feed-forward layer (see Figure 11.6), each neuron

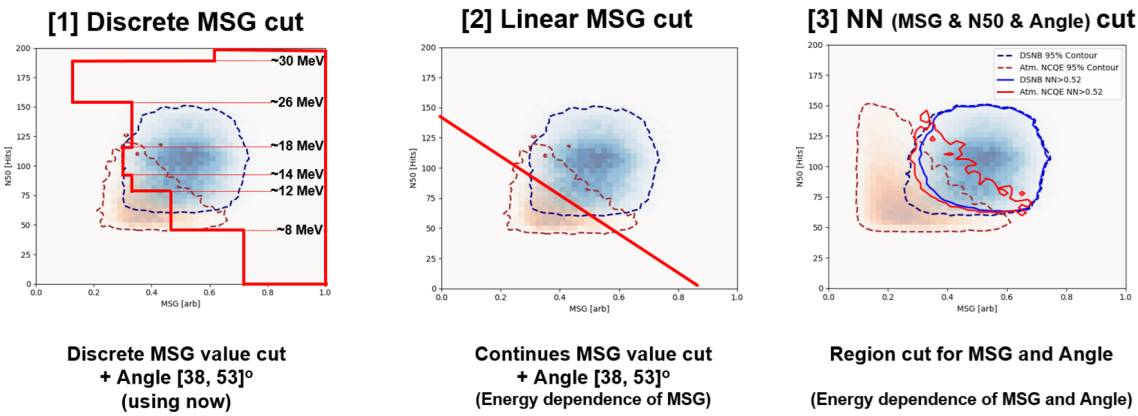

Figure 11.5: Comparison of different cut strategies using MSG and N50 distributions. The plots illustrate how the proposed linear and NN cuts perform relative to the traditional discrete approach.

performs the following computation:

$$\text{output} \;=\; \sigma\left(\sum_i w_i x_i + b\right), \tag{11.4}$$

where w_i are the weights, b is the bias, and σ is a nonlinear activation function. In this study, we use either the sigmoid function or the ReLU function, defined as $\max(0, x)$. These nonlinearities enable the model to learn complex, non-linear relationships between input features and target outputs.

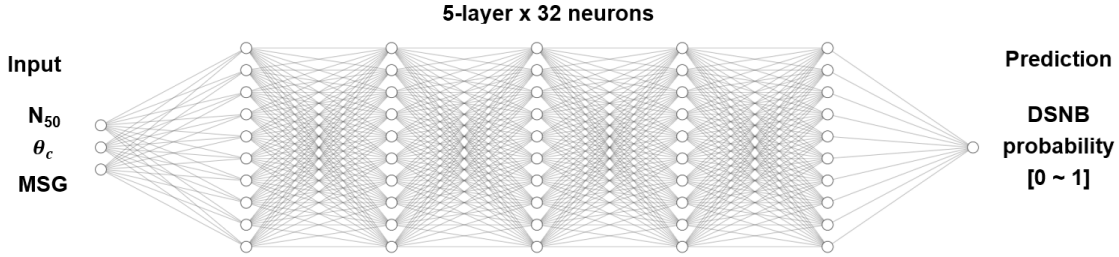

Figure 11.6: Schematic of the neural network structure used in this analysis.

Training involves optimizing the weights W and biases B by minimizing a loss function $L(X, W, B)$. This is achieved using mini-batch gradient descent, where parameters are iteratively updated according to:

$$(W, B) \;\leftarrow\; (W, B) \;-\; \alpha\,(\nabla_W L,\; \nabla_B L)\,, \tag{11.5}$$

where α denotes the learning rate, and $\nabla_W L$ and $\nabla_B L$ represent the gradients of the loss function L with respect to the weights and biases, respectively.

For the classification task distinguishing DSNB signal from atmospheric NCQE

background, we employ a fully connected neural network consisting of three input features (N50, θ_C, and MSG), five hidden layers with 64 ReLU-activated nodes each, and a final output layer with a single sigmoid activation.[1] The complete architecture is summarized in Table 11.2.

For neural-network training, we used DSNB (signal) and atmospheric NCQE (background) features (N50, θ_C, and MSG) from MC samples generated with SKG4 for the SK-VI phase of the DSNB study, as shown in Figure 11.2 (1D) and Figure 11.3 (2D). We note that the MC setting for atmospheric NCQE that is used for training is NEUT 5.6.4 with the INCL–G4PreCompound. Both signal and background samples followed the 1st, and 2nd reduction routines defined in the DSNB analysis. The 3rd cut, applied prior to the Cherenkov angle cut, was applied to both signal and background events. After applying these selections, a total of 50,000 DSNB events and 32,000 atmospheric NCQE events were retained and used for training the neural network in this study. We used all generated MC samples for training, even though the number of signal and background events was unbalanced.

Training seeks to minimize a loss function. The selection of the loss function is based on the specific goals of the task. In our case, we use the binary cross entropy loss function, which is particularly well-suited for a binary classification problem for two reasons:

1. **Exact negative log-likelihood under a Bernoulli model.** For binary classification, we model the probability of an event belonging to the signal class as:

$$p(y_i = 1 \mid x_i, \theta) = \hat{p}_i, \quad p(y_i = 0 \mid x_i, \theta) = 1 - \hat{p}_i, \tag{11.6}$$

where x_i denotes the input feature vector for the i-th sample, θ represents the trainable model parameters, and $\hat{p}_i$ is the network's predicted probability. So that the joint likelihood over all N samples is

$$\mathcal{L}(\theta) = \prod_{i=1}^{N} \hat{p}_i^{\,y_i^{\text{true}}} \, (1 - \hat{p}_i)^{1 - y_i^{\text{true}}}. \tag{11.7}$$

Taking the negative logarithm yields exactly the binary cross entropy in Eq. 11.9, guaranteeing that minimizing the loss is equivalent to maximizing the likelihood.

2. **Smooth gradients without vanishing issues.** The gradient

$$\frac{\partial L}{\partial \hat{p}_i} = -\frac{1}{N}\left(\frac{y_i^{\text{true}}}{\hat{p}_i} - \frac{1 - y_i^{\text{true}}}{1 - \hat{p}_i}\right) \tag{11.8}$$

remains well-behaved even as $\hat{p}_i$ approaches 0 or 1, avoiding the saturation

[1] Implemented using `TensorFlow`.

problems encountered with squared-error losses on bounded outputs [168].

These features make binary cross entropy the ideal loss function for "background vs. signal" (or any binary) classification task, outperforming other loss functions, such as Mean Squared Error or Mean Absolute Error, and margin-based losses in both theory and practice.

The binary cross entropy loss function used in this technical note is defined as:

$$L = -\frac{1}{N}\sum_{i=1}^{N}\Big(y_i^{\text{true}}\log y_i + (1-y_i^{\text{true}})\log(1-y_i)\Big). \tag{11.9}$$

where $y_i \in [0,1]$ is the network's predicted DSNB probability and $y_i^{\text{true}} \in \{0,1\}$ is the true label (0 for background, 1 for signal).

Weights were initialized using the He initialization [169] scheme and optimized using the Adam algorithm [170] (mini-batch size of 32, learning rate $\alpha = 10^{-4}$). A 50:50 split was used for training and validation. Hyperparameters were tuned heuristically, and training was terminated early if the validation set signal efficiency did not improve for three consecutive epochs. The full configuration is summarized in Table 11.2.

Option	**Settings**
Layer architecture	3-64-64-64-64-64-1
Hidden-layer activation	ReLU
Output-layer activation	Sigmoid
Train:validation split	50 % : 50 %
Mini-batch size	32
Input scaling	Standardised
Weight initialisation	He [169]
Loss	Binary cross-entropy
Optimiser	Adam [170]
Initial learning rate	10^{-4}

Table 11.2: Neural-network configuration and training settings.

Figure 11.7 shows the training history, including the evolution of loss (left panel) and accuracy (right panel) over epochs.

The NN classification cut threshold was optimized by scanning the NN output distribution and maximizing the following figure of merit (FOM):

$$FOM = \frac{S_{\text{DSNB}}}{\sqrt{S_{\text{DSNB}} + B_{\text{INCL-G4Pre}} + |\,B_{\text{BERT-G4Cas}} - B_{\text{INCL-G4Pre}}\,|}}. \tag{11.10}$$

Here, S_{DSNB} denotes the number of DSNB events surviving a given NN output cut,

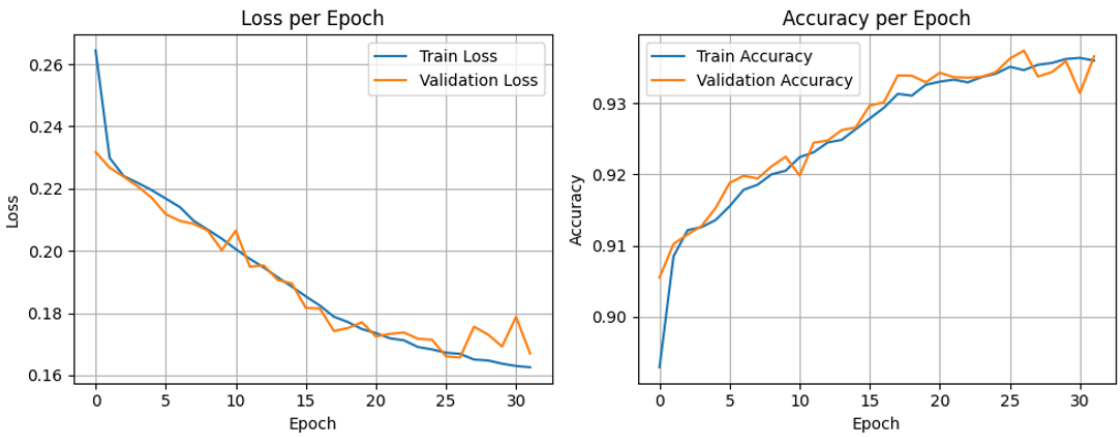

Figure 11.7: Training loss (left) and accuracy (right) versus epoch.

while $B_{\mathrm{BERT-G4Cas}}$ and $B_{\mathrm{INCL-G4Pre}}$ are the atmospheric NCQE MC backgrounds after a given NN output cut with two different MC settings. We take $B_{\mathrm{INCL-G4Pre}}$ as the nominal background prediction and include a penalty term, $|B_{\mathrm{BERT-G4Cas}} - B_{\mathrm{INCL-G4Pre}}|$, to cover MC systematics in the input features.

The optimal NN output threshold is found to be 0.52 and is indicated in the left panel of Figure 11.8. We also provide the receiver operating characteristic (ROC) curve, obtained by scanning the NN output and recording the corresponding signal and background efficiencies. The optimal point is marked with a star. The two MC configurations (BERT-G4Cas and INCL-G4Pre) yield similar NN output and ROC distributions, demonstrating the robustness of the NN method, with areas under the curve (AUCs) of 0.976 and 0.975, respectively. Compared with the θ_C-only selection (black star) and the combined θ_C+MSG selection (grey star), the neural network achieves clearly better background rejection while maintaining higher signal efficiency.

11.2 Performance and benchmarking

We present a comprehensive comparison of existing selection strategies: θ_C only (black star), an MSG threshold at 0.38 (gray star), a discrete MSG cut (green star), a linear MSG cut (red star), and a neural-network (NN) classifier (blue star). Their performance is evaluated using ROC curves, as shown in Figure 11.9. The traditional θ_C-only cut retains the most atmospheric NCQE events but also has the best DSNB efficiency, as shown in Table 11.3. Adding MSG as an additional variable significantly suppresses atmospheric NCQE backgrounds, with the linear MSG cut providing a further improvement. The NN classifier achieves background rejection comparable to the linear MSG cut while further increasing the signal efficiency.

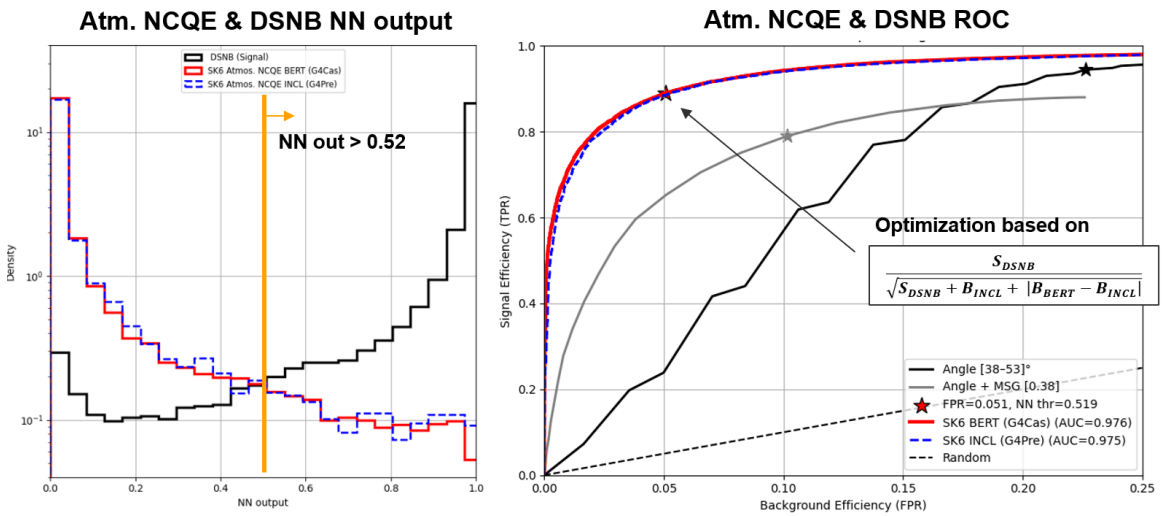

Figure 11.8: Optimization of the NN output threshold (left) and corresponding ROC curves (right).

Each selection strategy has trade-offs. Discrete and linear cuts are simple and may be more robust to systematic uncertainties. In contrast, the neural network offers a feature-based, physically interpretable classifier that preserves more signal, which is important for rare DSNB searches, though its complexity may introduce larger systematics. The final selection method for the DSNB search at SK will be chosen after analyzing the T2K data sample to quantify MC–data differences and the associated uncertainties for each approach, as in Chapter 12 and 13.

Cut method	**DSNB (%)**	**Atm. NCQE (%)**
θ_C [38°, 53°]	95.3	22.7
θ_C+MSG$_{0.38}$	79.5	10.1
θ_C+MSG$_{dis}$	81.8	7.2
θ_C+MSG$_{lin}$	80.8	5.1
NN	89.3	5.0

Table 11.3: Selection methods on DSNB and atmospheric NCQE efficiency.

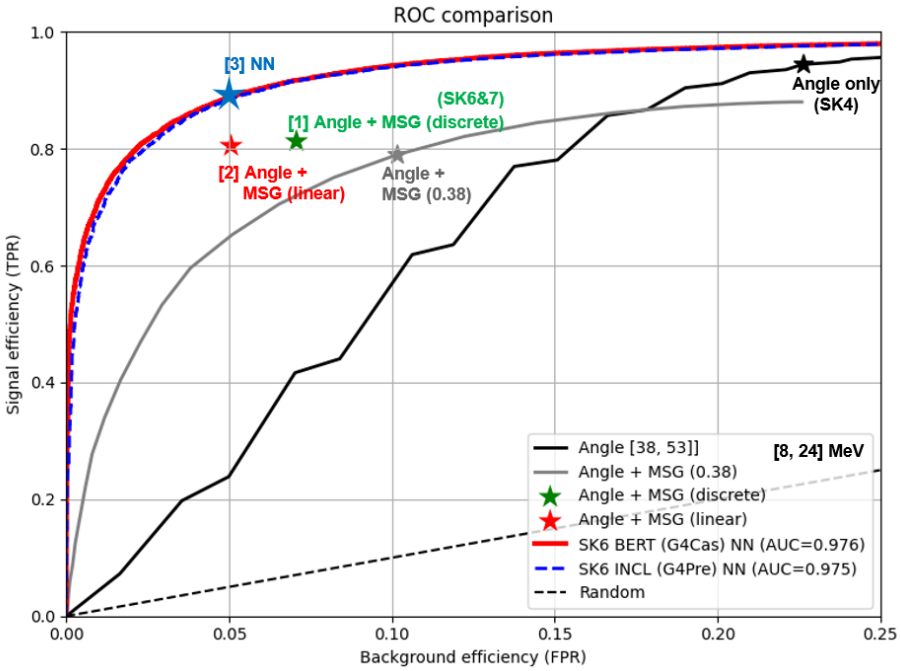

Figure 11.9: ROC comparison of the θ_C-only cut, discrete MSG, linear MSG, and NN classifier.

Chapter 12

LINAC validation

The event features used as inputs to the cuts must be calibrated with real data, and the resulting uncertainties should be propagated to the selection criteria proposed in Chapter 11.1. To estimate the uncertainties of the cuts applied on DSNB signal, we use the linear accelerator (LINAC) as a proxy. Its electron beam mimics DSNB positrons in SK detector and covers the same energy range, making it a suitable benchmark for validating our DSNB event features. Although the LINAC and DSNB energy spectra are not identical, operating the LINAC at multiple detector positions and energies provides sufficient statistics to quantify the systematic uncertainties in DSNB observables after all selection cuts.

The August 2021 LINAC calibration is used to model the SK-VI phase (SK with Gd-loaded), while the August 2017 campaign represents the SK-IV phase (SK with pure water). Table 12.1 lists the specific runs analyzed.

Z position	**Energy**	**Run (SK6)**	**Run (SK4)**	**Run (SK4)**
12 m	8 MeV	086119	076430	076347
	12 MeV	086126	076435	076350
	15 MeV	086129	076422	076361
0 m	8 MeV	086135	076471	076367
	12 MeV	086138	076474	076370
	15 MeV	086142	076453	076373
-12 m	8 MeV	086154	076501	076393
	12 MeV	086157	076504	076399
	15 MeV	086160	076483	076390
		Note: Side (X,Y): (-12,0)m	Note: Center (X,Y): (0,0)m	Note: Side (X,Y): (-12,0)m

Table 12.1: LINAC Runs by Period and Position

12.1 Features from LINAC

We focus on three event features (N50, θ_C, and MSG) and test whether their MC predictions are consistent with the calibration data. Figure 12.1 overlays the MC distributions of these variables for LINAC, DSNB, and atmospheric NCQE samples. 95% density contours highlight the two-dimensional feature space SK-VI period. The rows correspond to LINAC beam energies of 8 MeV (top), 12 MeV (middle), and 15 MeV (bottom). The 12 MeV setting matches the DSNB spectral peak, while the 8 MeV and 15 MeV settings probe the lower and upper edges of the DSNB energy spectra.

Energy dependence of the MSG distribution is a key focus of this study. Using single electron source as a proxy for single positrons, we examine how the MSG distribution changes with energy (central column of Figure 12.1). Despite the rise in N50, the distribution stays centered near 0.5 with a nearly constant width, indicating a weak energy dependency for a single electron.

Energy dependence of the Cherenkov-angle distribution is another key aspect we probe. We examine how this distribution evolves with energy. As seen in the left column of Figure 12.1, the Cherenkov-angle distribution from the LINAC becomes narrower and more peaked as N50 increases. The same trend appears in the right column, where events with larger LINAC energy settings exhibit a tighter Cherenkov-angle spread. Although the mean angle remains near 42^o, these results show that the Cherenkov angle is more sensitive to energy for a single electron.

12.2 Neural network validation

Each event's N50, θ_C, and MSG are inputted into a trained neural network introduced in Chapter 11.1 that yields a score (NN output) representing how DSNB-like the event appears. Because the DSNB and LINAC samples differ in energy spectra, their NN output distributions need not match perfectly, though they should resemble each other. The crucial test is the comparison between LINAC MC and LINAC Data: if the correlations among N50, θ_C, and MSG are modeled accurately, their NN-output distributions should align closely.

We then evaluate the NN output distributions for LINAC MC and LINAC Data across SK run periods, injection positions, and energy settings. Figure 12.2 focuses on the SK-VI period at "side position": each row corresponds to a LINAC energy setting, and each column to a electron-injection position (top, middle, or bottom). The LINAC data (purple points with statistical error bars) agree well with the LINAC-MC prediction (solid blue line).

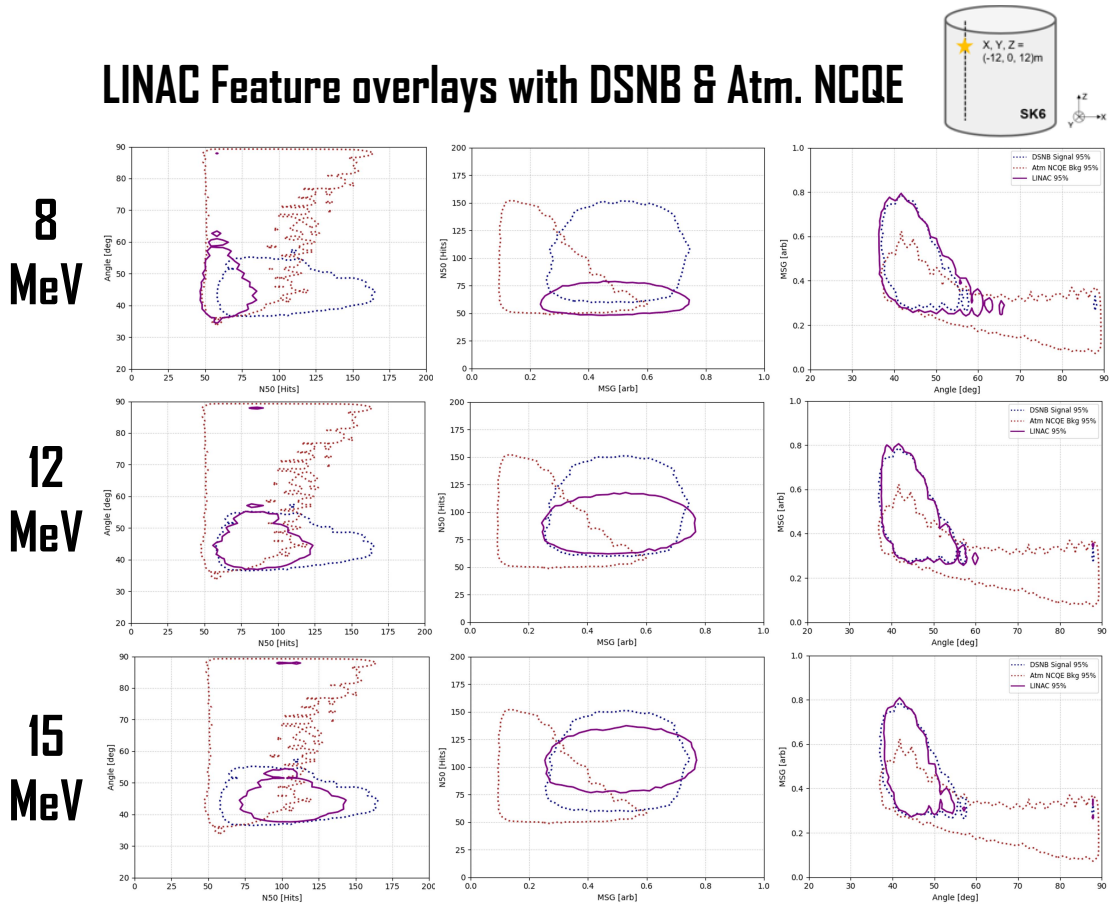

Figure 12.1: LINAC features (purple) overlays with DSNB (dash blue) and Atm. NCQE (dash brown). Rows indicate 8, 12, 15 MeV LINAC e^- beams. Columns plot θ_C-N50, N50-MSG, and N50-θ_C.

For context, Figure 12.2 also overlays the expected NN output shapes for DSNB events (red dashed) and atmospheric NCQE backgrounds (black dashed). At 12 MeV (middle row), the LINAC NN output distribution overall matches the DSNB because their spectrum peaks overlap most in this region. At 8 MeV (top row), the LINAC spectrum differs from the DSNB spectrum, resulting in a different NN output distribution. However, the consistency between LINAC MC and LINAC data in the 8 MeV setup provides a useful low-energy boundary check. We also took the 15 MeV setting (bottom row) as a high-energy boundary check of the DSNB.

This analysis spans both the pure-water phase and the Gd-loaded phase of Super-K. Therefore, we also include LINAC calibrations from SK-IV (pure-water), shown for "edge (X = -12m)" (Figure 12.3) and "center (X = 0m)" (Figure 12.4) injections. The SK-IV distributions match those of SK-VI periods, indicating that changes in water status or PMT conditions have little effect on the signal features.

Although the NN-output distributions are largely consistent between LINAC MC and LINAC data, a small MC–data discrepancy emerges in the low-energy, lower-edge region. This deviation is visible in both the SK-IV data set (Figure 12.3 and Figure 12.4) and the SK-VI period (Figure 12.2). When we focus on events with a high NN score (e.g. 0.9), the mismatch becomes clearer: as illustrated in Figure 12.5, the LINAC data extend to $N50 \approx 125$, whereas the MC prediction peaks at $N50 \approx 75$, corresponding to 8 MeV.

The LINAC data excess relative to MC is most obvious in the SK-VI period, appearing across the detector's top, center, and bottom regions (Figure 12.6). In the SK-IV period, the LINAC data excess is weaker but still visible at the lower-edge position for the 8 MeV setting. A summary is provided in Figure 12.7. Although the final NN cut will be set to a milder value (NN Output$\approx$ 0.52, Figure 12.8) rather than the extreme 0.9 taken as demonstration here, the dominant MC–data discrepancy, and hence the primary contribution to the systematic uncertainty, arises in this high NN output MC-data mismatchment region, necessitates a special focused examination presented here.

The systematic uncertainty assigned to the NN cut for single-electron events is obtained from the cumulative NN output distributions. Specifically, the largest separation between the LINAC MC and LINAC data integrals is adopted as the systematic uncertainty. A representative portion of these cumulative curves is shown in Figure 12.9. Figure 12.10 and Table 12.2 summarizes the LINAC MC–data differences in the cumulative NN-output curves for various SK periods and injection positions. The largest fractional discrepancy, 2.72%, occurs for the 8 MeV LINAC run at the lower-edge position during the SK-VI period. We adopt this most conservative value as the systematic uncertainty on the NN-based selection for single-electron events.

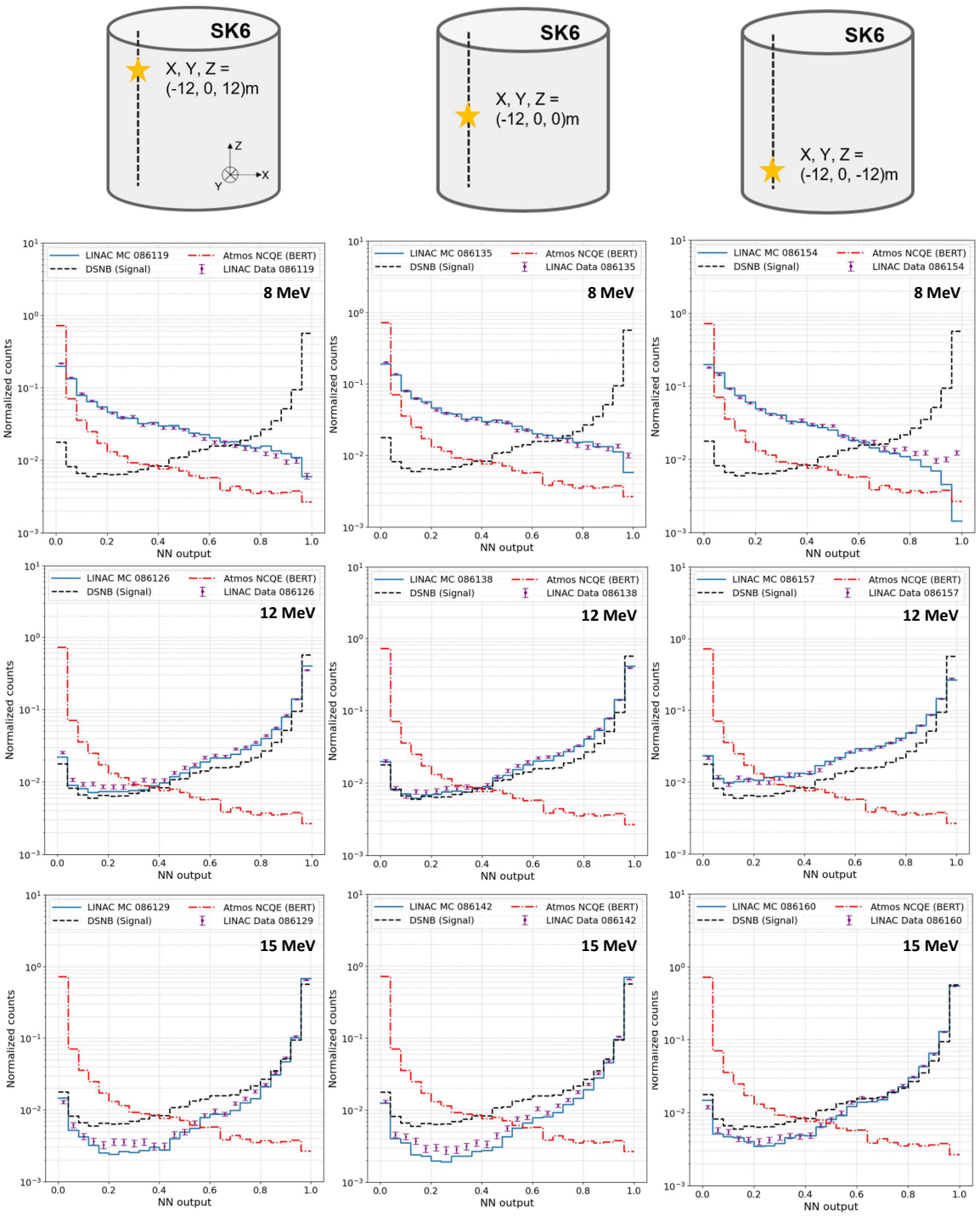

Figure 12.2: NN-output distributions for LINAC electrons in SK6 (Run 11). Rows: 8, 12, 15 MeV. Columns: injection positions. LINAC Data (purple) vs. LINAC MC (blue). DSNB (black dashed) and Atm. NCQE (red dashed) overlaid.

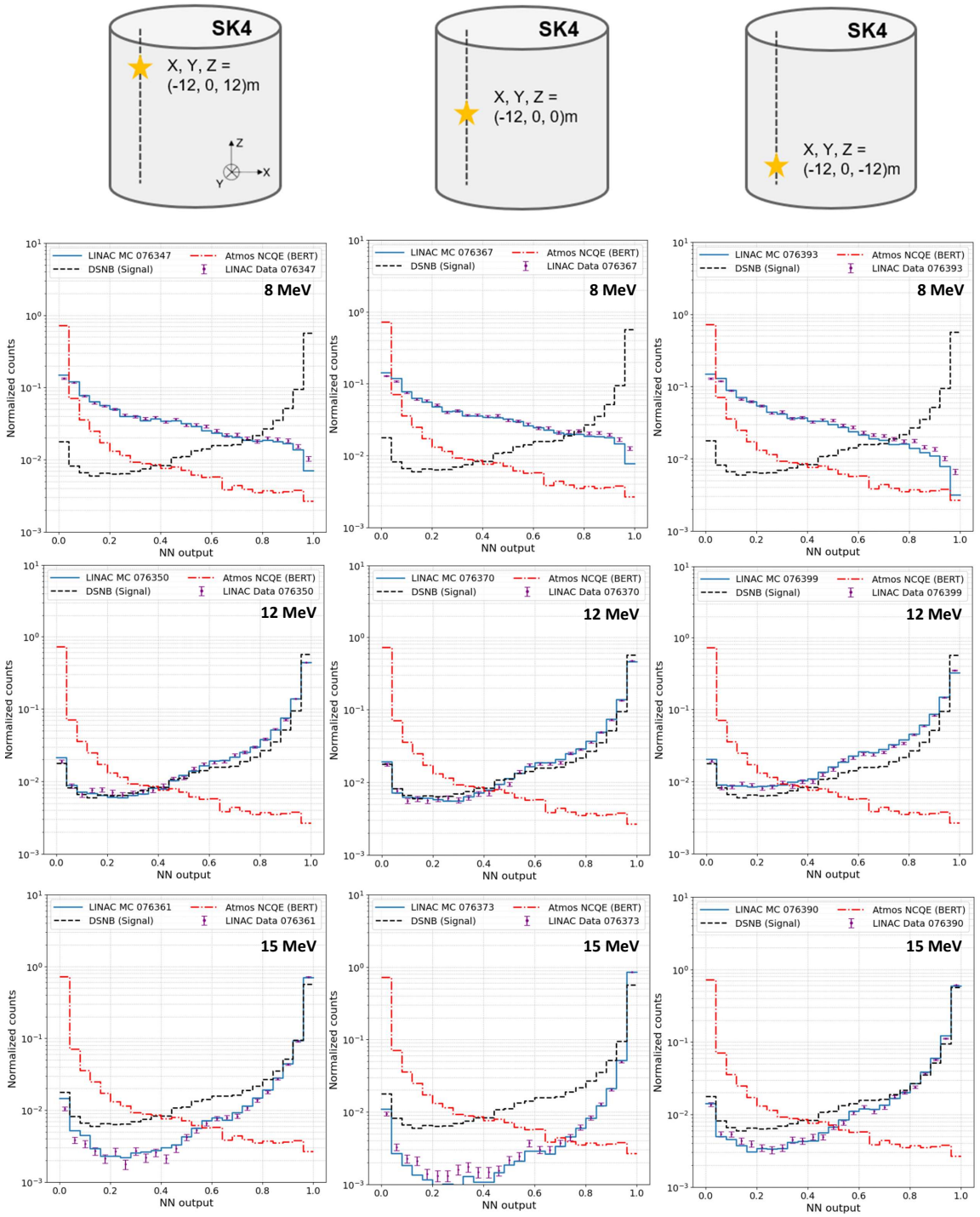

Figure 12.3: NN-output distributions for LINAC electrons in SK-IV (pure water), "edge" injections. Rows: 8, 12, 15 MeV. Columns: injection positions. LINAC Data (purple) vs. LINAC MC (blue). DSNB (black dashed) and Atm. NCQE (red dashed) templates overlaid.

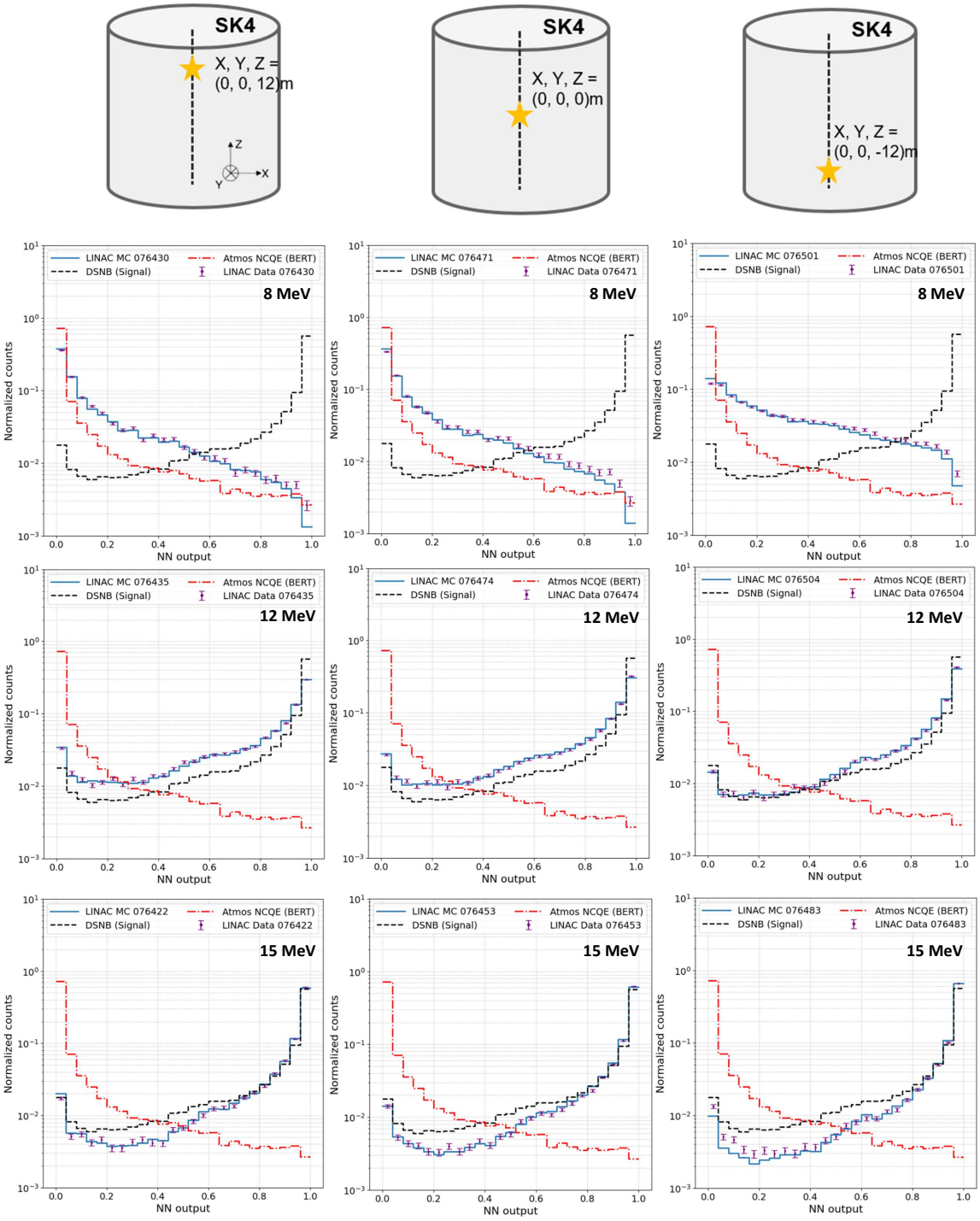

Figure 12.4: NN-output distributions for LINAC electrons in SK-IV (pure water), "center" injections. Rows: 8, 12, 15 MeV. columns: injection positions. LINAC Data (purple) vs. LINAC MC (blue). DSNB (black dashed) and Atm. NCQE (red dashed) templates overlaid.

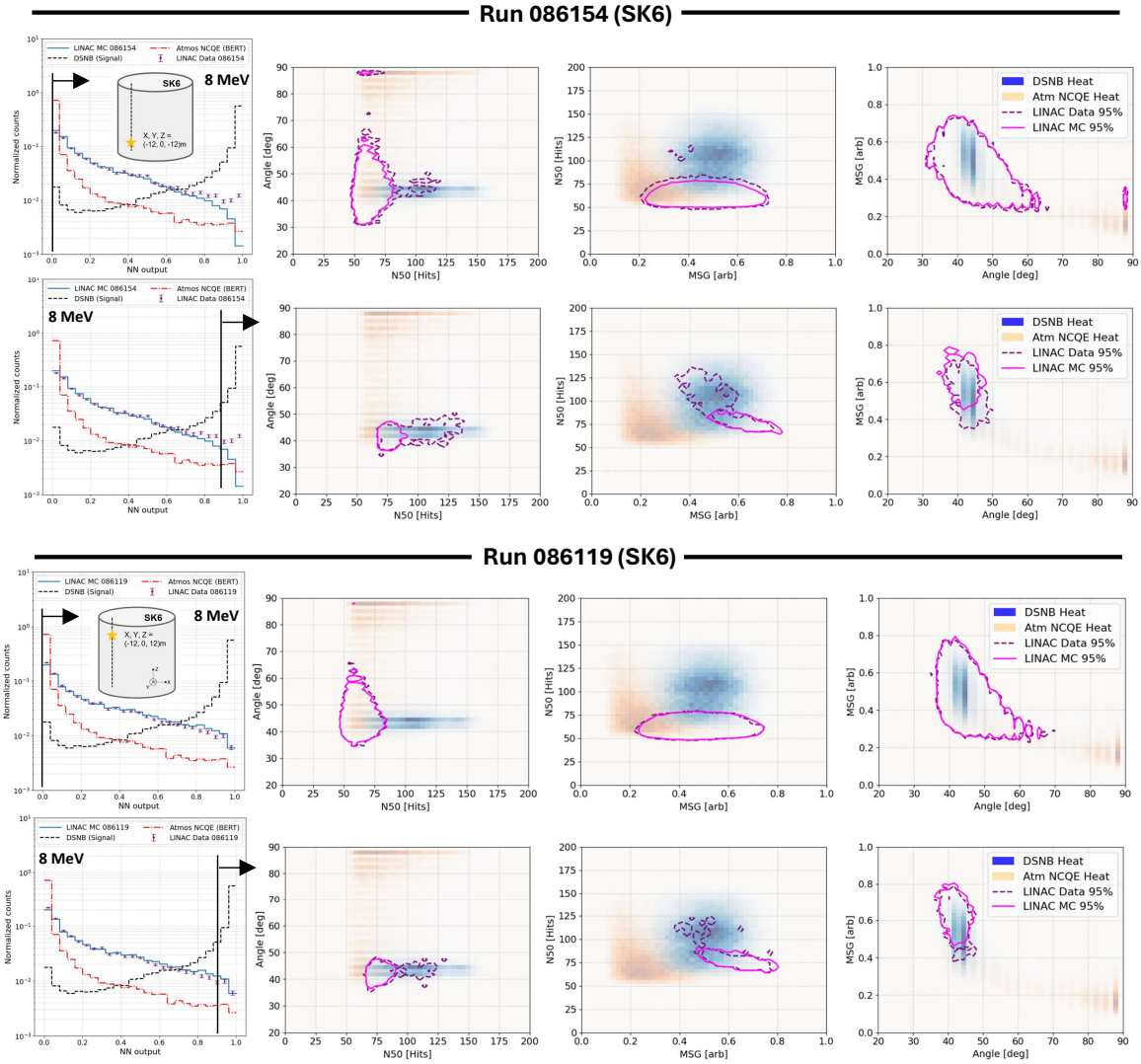

Figure 12.5: SK-VI, 8 MeV LINAC run: comparison of NN output and related features for data and MC, shown both all and with NN output higher than 0.9. The data (purple dashed) have a sub-cluster at $N50 \approx 100$, whereas the MC (magenta solid) confines at $N50 \approx 75$.

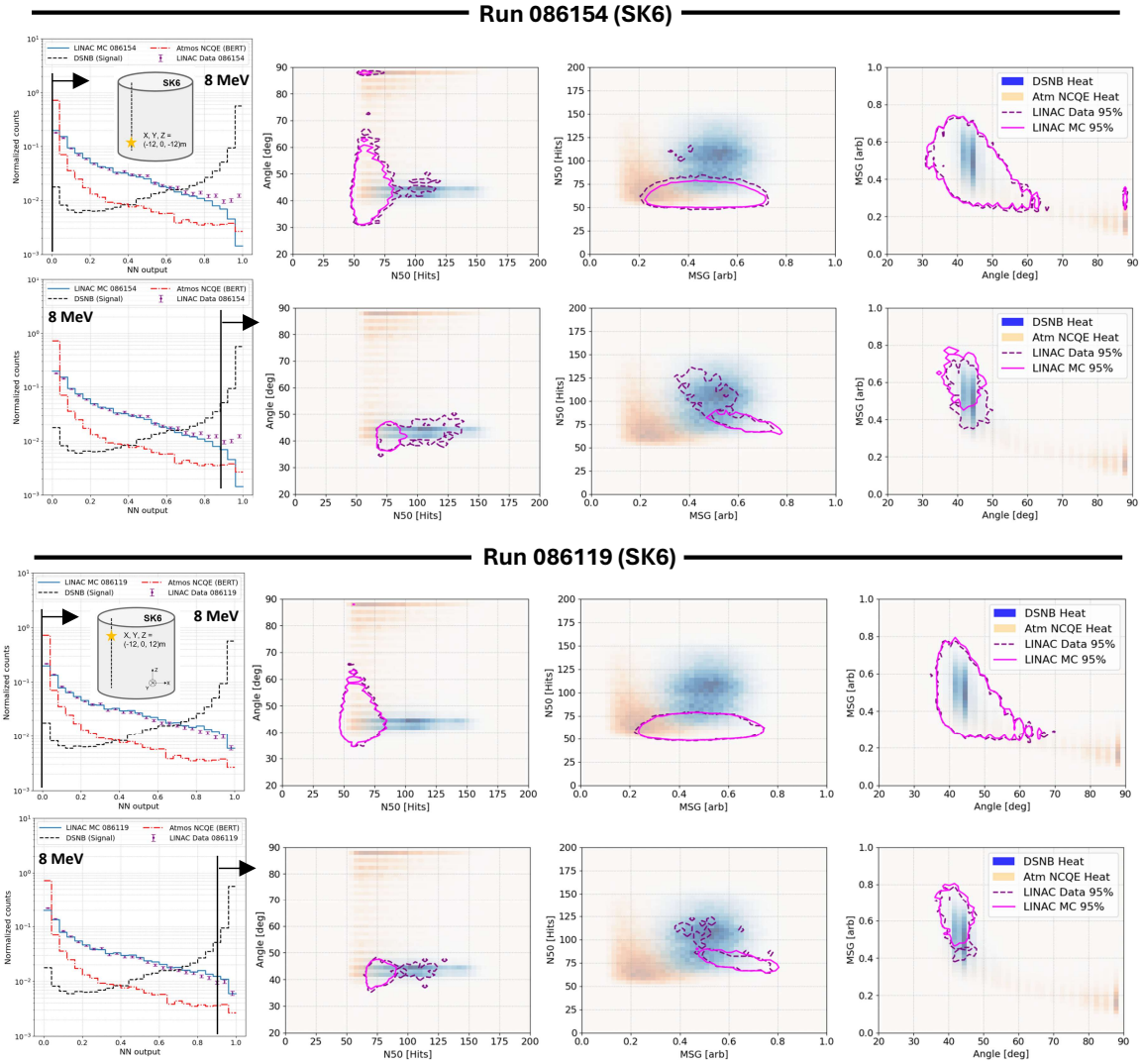

Figure 12.6: SK-VI period, 8 MeV LINAC run. For events with a high NN output larger than 0.9, the LINAC data (purple dashed) show a clear excess over MC (magenta) across the detector's top, center, and bottom regions.

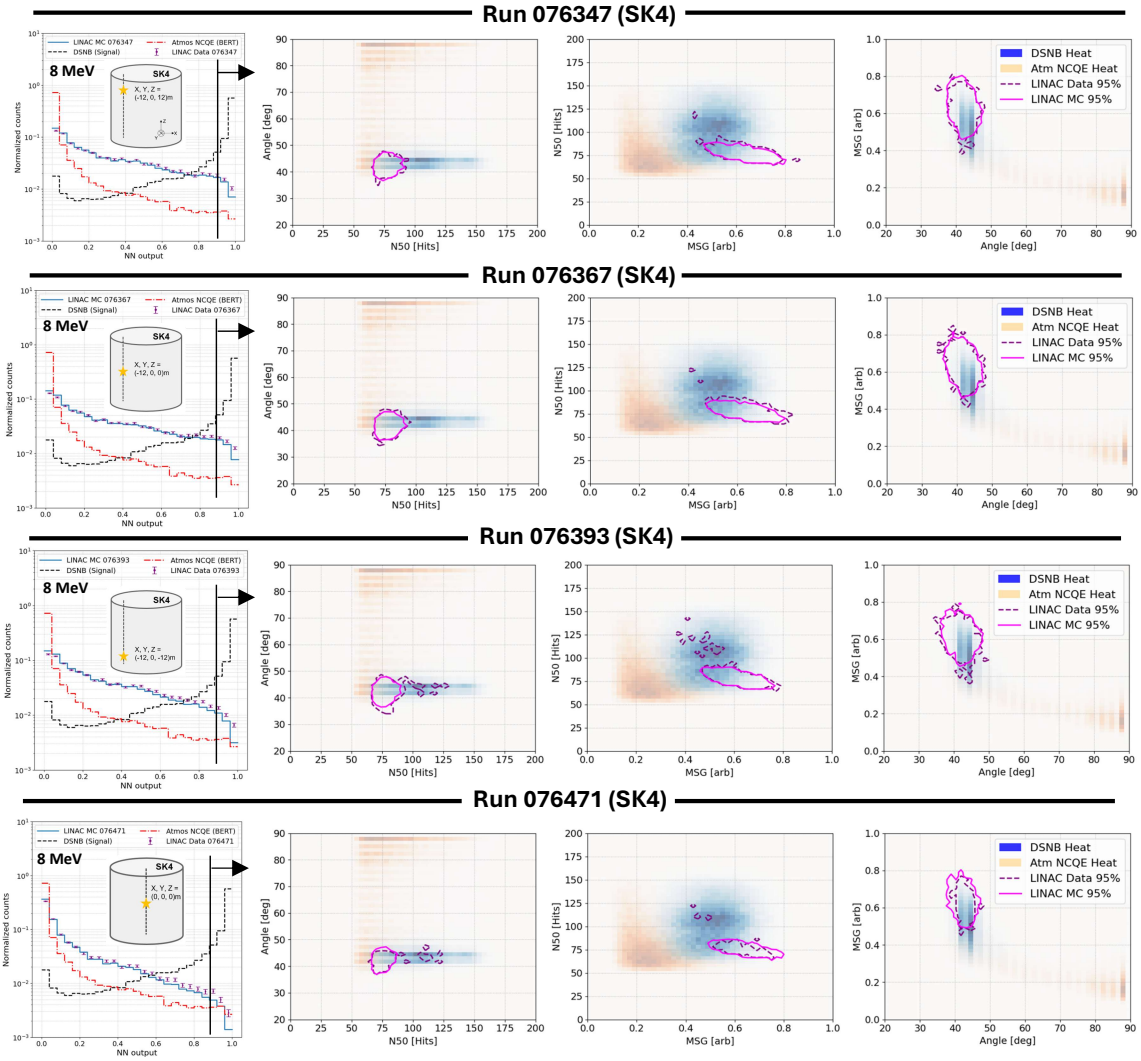

Figure 12.7: SK-IV period, 8 MeV LINAC run. For events with a high NN output larger than 0.9, the LINAC data (purple dashed) show a clear excess over MC (magenta) across the detector's top, center, and bottom regions. The LINAC data excess is weaker than in SK-IV but remains visible at the lower-edge position for events with NN output larger than 0.9.

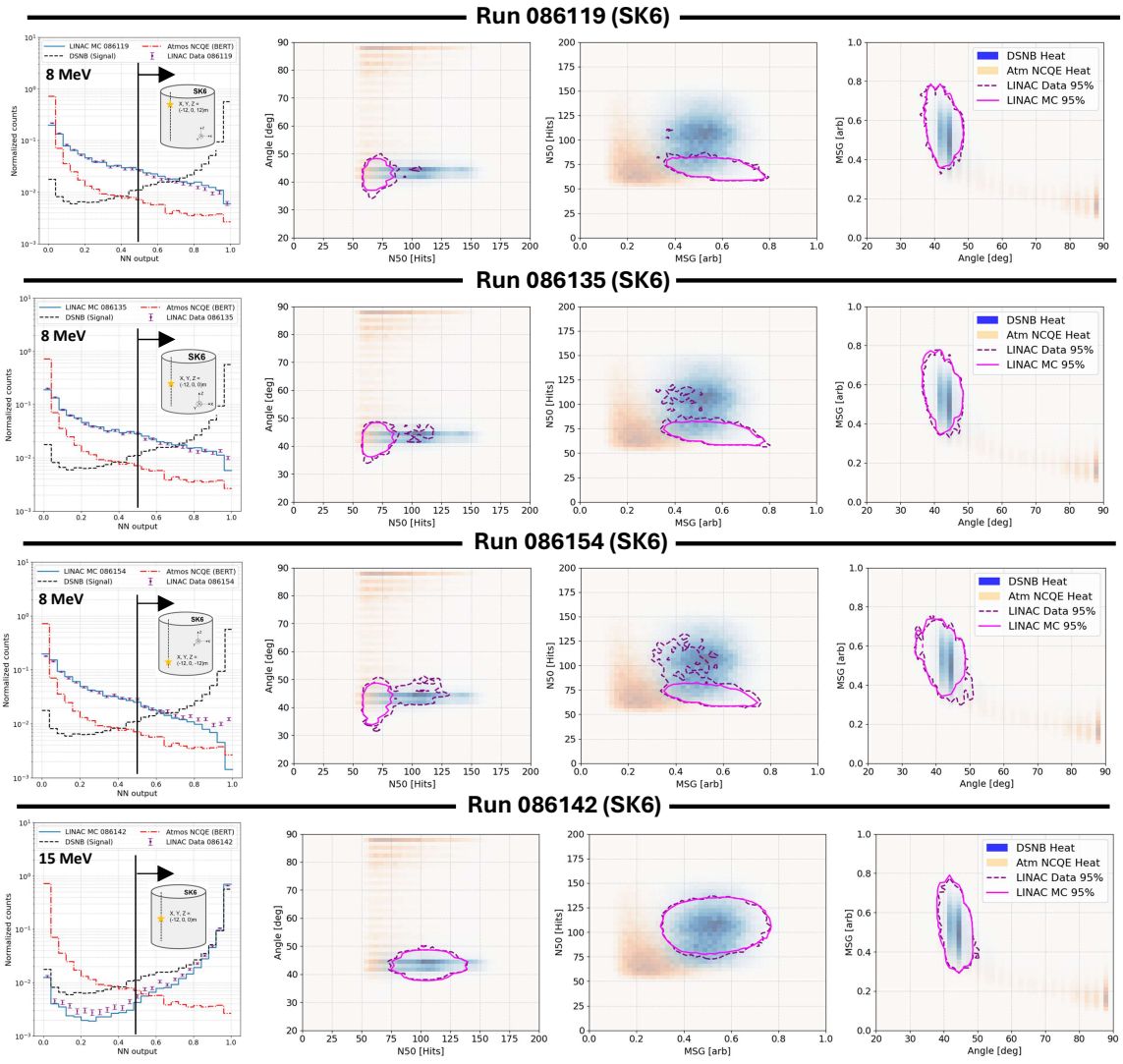

Figure 12.8: SK-VI period, 8 MeV LINAC run. For events with a high NN output larger than 0.52, the LINAC data (purple dashed) show a clear excess over MC (magenta) across the detector's top, center, and bottom regions. Also a 15 MeV LINAC run for reference.

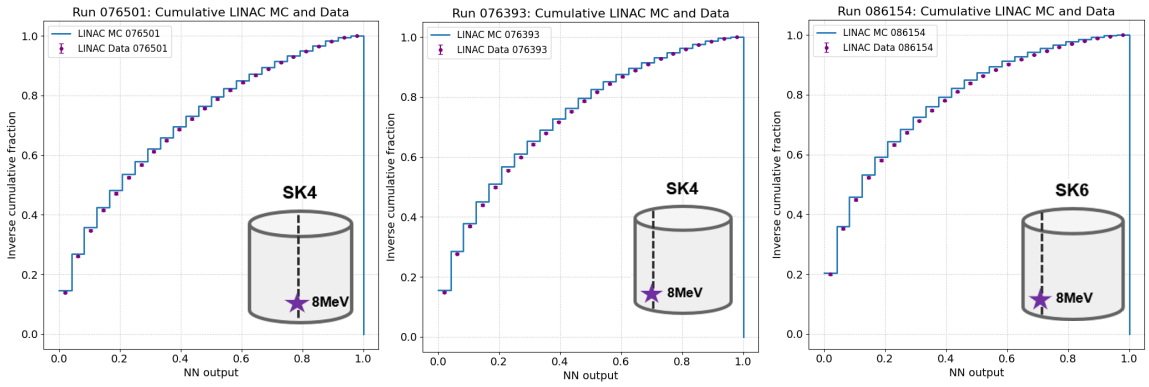

Figure 12.9: Cumulative NN-output distributions for single-electron LINAC events. The LINAC data (purple dot) and LINAC MC (blue line) are integrated from high to low NN score. The largest difference between them is adopted as the systematic uncertainty on the NN cut for DSNB (single electron-like) source.

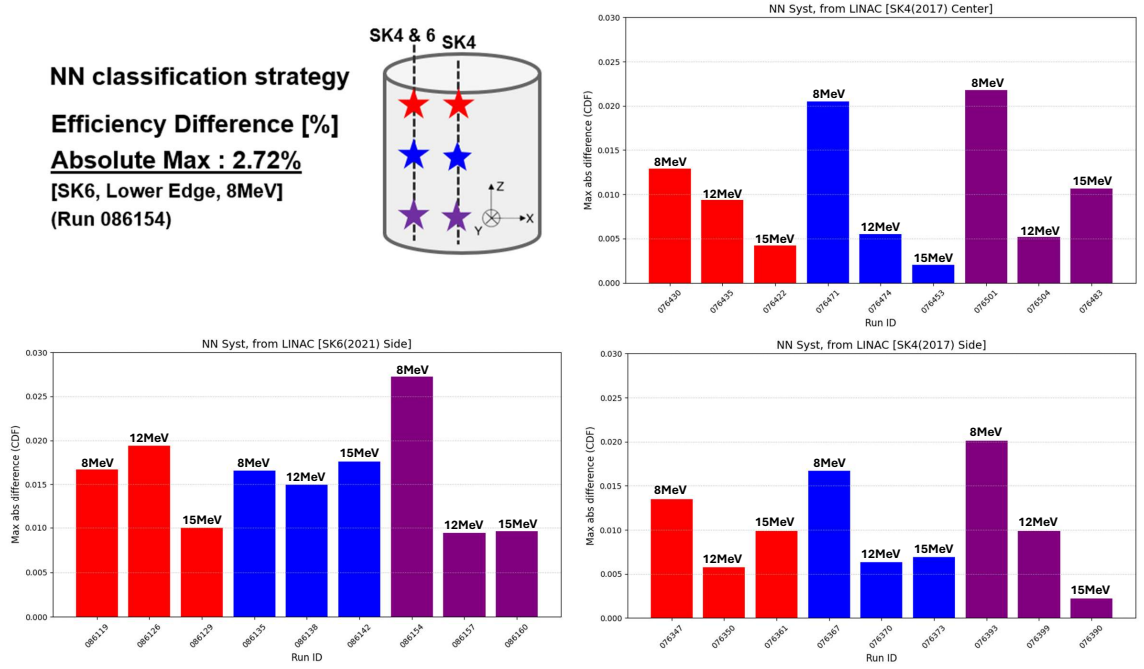

Figure 12.10: LINAC MC–data separation in cumulative NN-output curves for LINAC runs across SK periods and injection positions. The maximum gap, 2.72%, occurs for the 8 MeV lower-edge sample in SK-VI period and is taken as the NN-cut systematic uncertainty.

NN Syst. From LINAC [SK6 (2021) Side]						
	Run ID	$\epsilon_{\texttt{8MeV}}$ (%)	Run ID	$\epsilon_{\texttt{12MeV}}$ (%)	Run ID	$\epsilon_{\texttt{15MeV}}$ (%)
Z = +12 m	086119	1.66	086126	1.94	086129	0.99
Z = 0 m	086135	1.65	086138	1.49	086142	1.75
Z = -12 m	086154	2.72	086157	0.95	086160	0.96
NN Syst. From LINAC [SK4 (2017) Center]						
	Run ID	$\epsilon_{\texttt{8MeV}}$ (%)	Run ID	$\epsilon_{\texttt{12MeV}}$ (%)	Run ID	$\epsilon_{\texttt{15MeV}}$ (%)
Z = +12 m	076430	1.29	076435	0.94	076422	0.42
Z = 0 m	076471	2.04	076474	0.55	076453	0.2
Z = -12 m	076501	2.18	076504	0.52	076483	1.06
NN Syst. From LINAC [SK4 (2017) Side]						
	Run ID	$\epsilon_{\texttt{8MeV}}$ (%)	Run ID	$\epsilon_{\texttt{12MeV}}$ (%)	Run ID	$\epsilon_{\texttt{15MeV}}$ (%)
Z = +12 m	076347	1.35	076350	0.57	076361	0.99
Z = 0 m	076367	1.67	076370	0.64	076373	0.69
Z = -12 m	076393	2.01	076399	0.99	076390	0.23

Table 12.2: NN Systematic uncertainty from LINAC for SK6 and SK4.

12.3 Discrete MSG cut strategy validation

We revisit the discrete MSG cut used in the SK-VI and SK-VII DSNB analyses to evaluate its uncertainty, enabling a direct comparison with the multivariate neural network method. The accepted MSG region is shown in green in Figure 12.11.

We compare the selection efficiency, defined as the ratio of events passing the discrete MSG cut to the total sample between LINAC data and MC. The efficiency differences for various SK periods, LINAC energy setup, and injection positions are summarised in Figure 12.12 and Table 12.3. A consistent pattern emerges: the 8 MeV samples exhibit the largest MC–data discrepancies, leading to higher systematic uncertainties than the 12 or 15 MeV settings in both the SK-IV and SK-VI periods. Adopting the most conservative case, we assign a 2.76% systematic uncertainty to the discrete-MSG selection for single-electron events. The NN-based selection, despite its more complex decision boundary, shows a comparable level of uncertainty.

12.4 Linear MSG cut strategy validation

To examine whether a simpler selection boundary changes the systematic uncertainty, we also test a linear MSG cut. This approach simplifies the discrete MSG cut while achieving a better performance for DSNB search. The accepted region is highlighted in green in Figure 12.13. We quantify the selection efficiency passing the linear MSG cut divided by the total sample for both LINAC data and MC, and plot their differences in Figure 12.14 and Table 12.4. As before, the lowest-energy (8 MeV) samples exhibit the largest MC–data mismatches. The maximal discrepancy reaches 3.22%, which

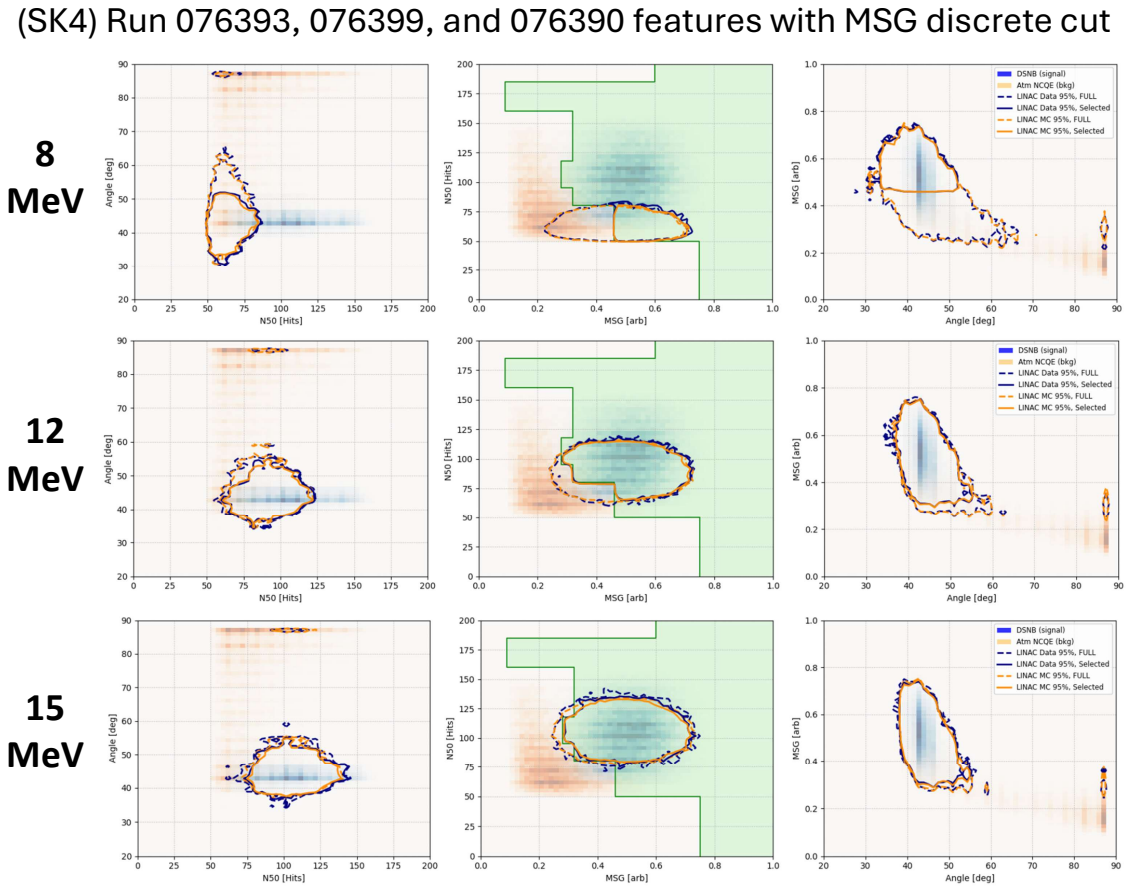

Figure 12.11: LINAC calibration of the discrete MSG cut employed in the SK-VI/VII DSNB analyses. LINAC data (blue) and MC (orange) for the 8, 12, and 15 MeV SK-IV period sample are shown. The green band denotes the accepted MSG range used, providing a baseline for comparison with the NN multivariate selection.

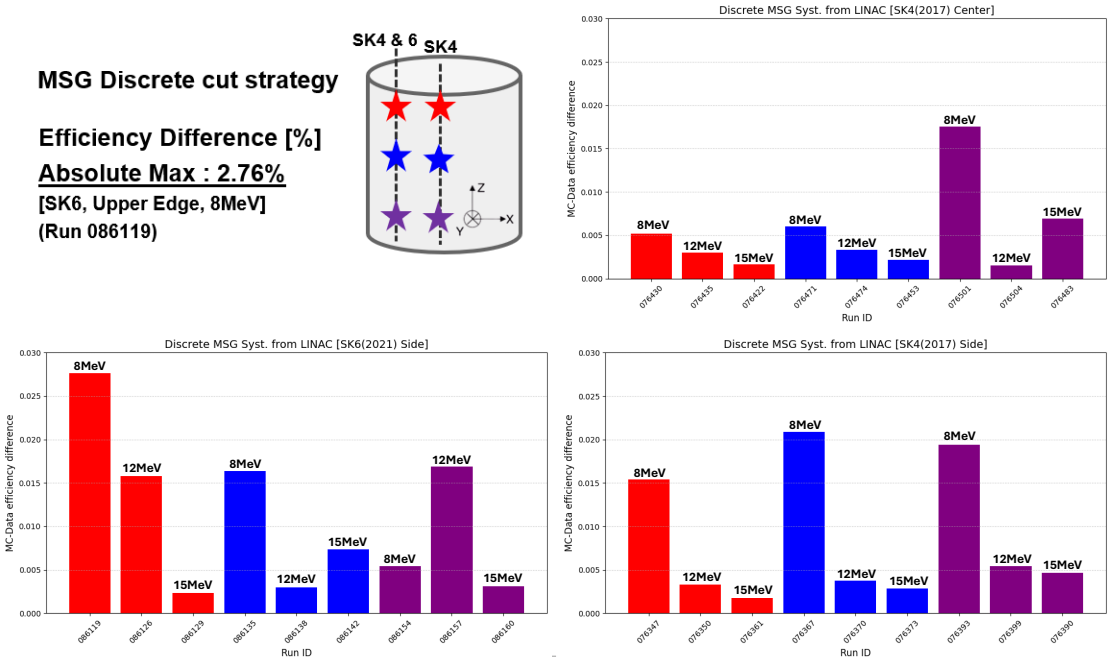

Figure 12.12: MC–data efficiency differences for the discrete MSG cut, evaluated with LINAC calibration runs at 8, 12, and 15 MeV during SK4 and SK6. The largest discrepancy (2.76%) occurs for the 8 MeV lower-edge sample in SK6 and is adopted as the systematic uncertainty for the discrete MSG cut on DSNB (single electron-like).

Discerte MSG Syst. From LINAC [SK6 (2021) Side]						
	Run ID	$\epsilon_{8\mathrm{MeV}}$ (%)	Run ID	$\epsilon_{12\mathrm{MeV}}$ (%)	Run ID	$\epsilon_{15\mathrm{MeV}}$ (%)
Z = +12 m	086119	2.76	086126	1.58	086129	0.23
Z = 0 m	086135	1.64	086138	0.3	086142	0.73
Z = -12 m	086154	0.54	086157	1.68	086160	0.31
Discerte MSG Syst. From LINAC [SK4 (2017) Center]						
	Run ID	$\epsilon_{8\mathrm{MeV}}$ (%)	Run ID	$\epsilon_{12\mathrm{MeV}}$ (%)	Run ID	$\epsilon_{15\mathrm{MeV}}$ (%)
Z = +12 m	076430	0.52	076435	0.3	076422	0.17
Z = 0 m	076471	0.61	076474	0.33	076453	0.22
Z = -12 m	076501	1.76	076504	0.15	076483	0.69
Discerte MSG Syst. From LINAC [SK4 (2017) Side]						
	Run ID	$\epsilon_{8\mathrm{MeV}}$ (%)	Run ID	$\epsilon_{12\mathrm{MeV}}$ (%)	Run ID	$\epsilon_{15\mathrm{MeV}}$ (%)
Z = +12 m	076347	1.54	076350	0.33	076361	0.18
Z = 0 m	076367	2.09	076370	0.38	076373	0.29
Z = -12 m	076393	1.94	076399	0.54	076390	0.46

Table 12.3: Discrete MSG Systematic uncertainty from LINAC for SK6 and SK4.

we assign as the systematic uncertainty associated with the linear-MSG selection for single-electron events.

In summary, we use the LINAC single electron beam as a proxy source to assess DSNB systematic uncertainties for three selection strategies: the current discrete MSG cut (MSG_{dis}), a new proposed linear MSG cut (MSG_{lin}), and a new proposed

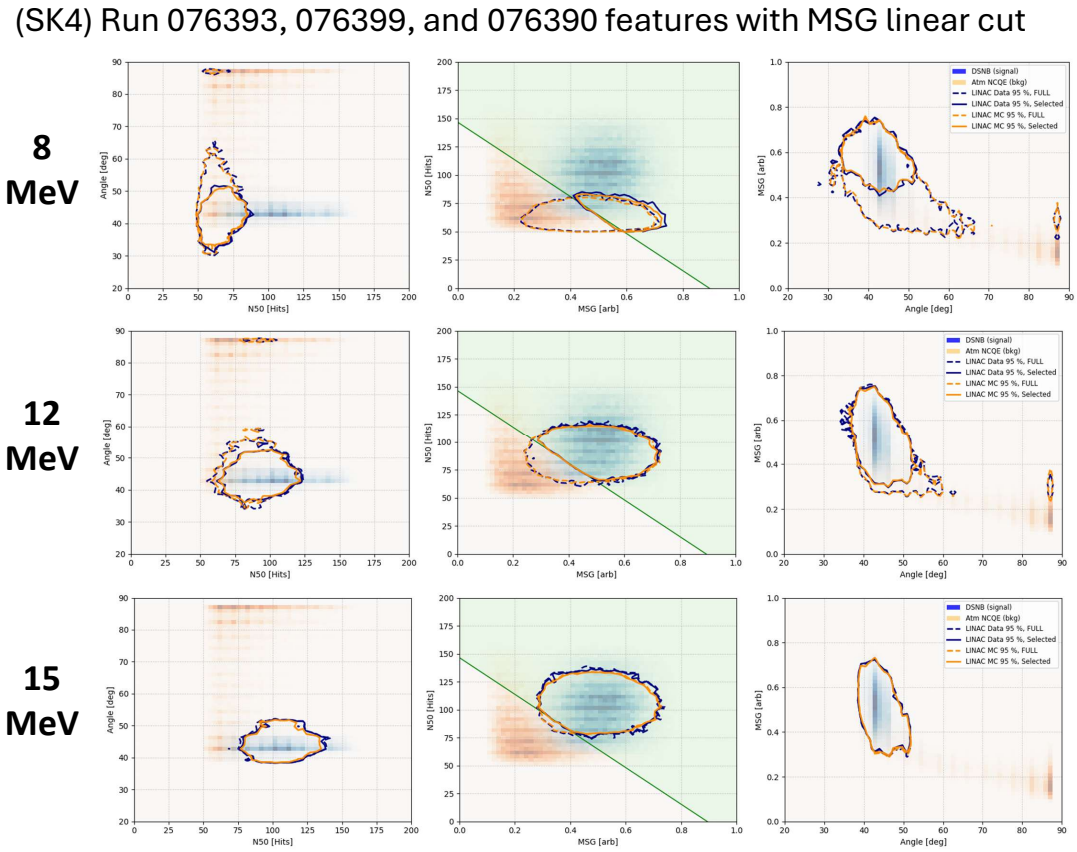

Figure 12.13: SK-IV LINAC calibration for linear MSG cut. LINAC data (blue) and MC (orange) for the 8, 12, and 15 MeV LINAC sample are shown. The green band denotes the linearly defined acceptance region, showing a simplified alternative to the discrete MSG selection.

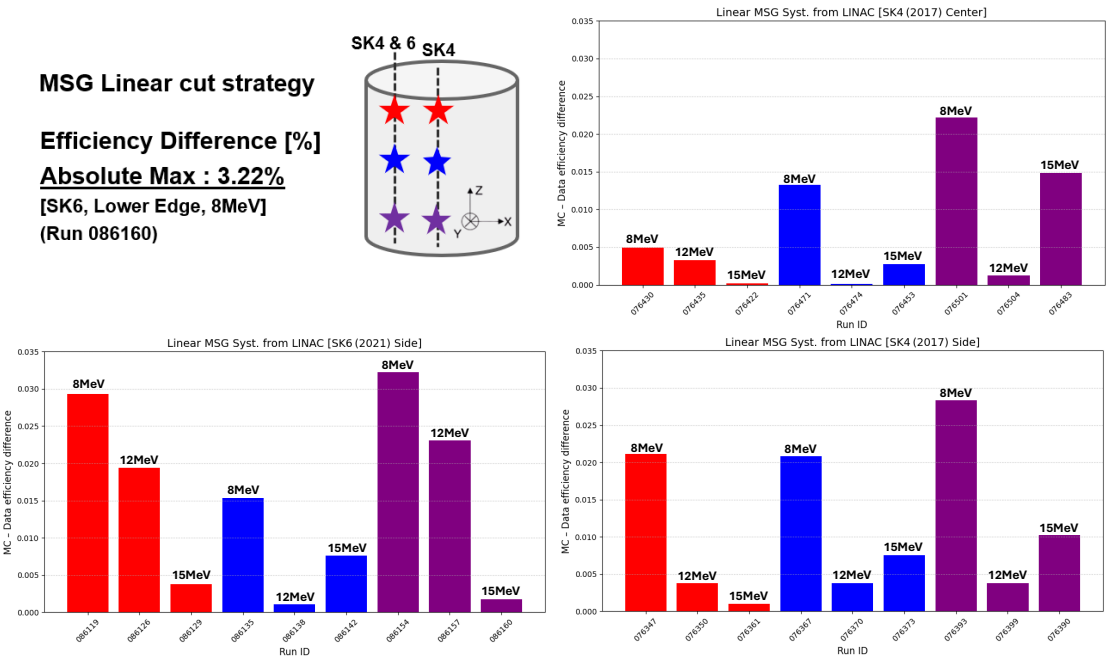

Figure 12.14: LINAC MC–data efficiency differences for the linear MSG cut, evaluated with LINAC runs at 8, 12, and 15 MeV among SK-IV and SK-VI period. The largest discrepancy, 3.22%, occurs for the 8 MeV sample in SK-VI period and is taken as the systematic uncertainty for the linear-MSG selection for DSNB (single electron-like source).

NN-based cut (NN cut). The resulting uncertainties are 2.76%, 2.72%, and 3.22%, respectively. These values are driven largely by the excess of LINAC data over MC in the 8 MeV edge sample, an effect most pronounced during the SK-VI period.

Linear MSG Syst. From LINAC [SK6 (2021) Side]						
	Run ID	$\epsilon_{\texttt{8MeV}}$ (%)	Run ID	$\epsilon_{\texttt{12MeV}}$ (%)	Run ID	$\epsilon_{\texttt{15MeV}}$ (%)
$Z = +12$ m	086119	2.93	086126	1.94	086129	0.38
$Z = 0$ m	086135	1.53	086138	0.10	086142	0.75
$Z = -12$ m	086154	3.22	086157	2.31	086160	0.17
Linear MSG Syst. From LINAC [SK4 (2017) Center]						
	Run ID	$\epsilon_{\texttt{8MeV}}$ (%)	Run ID	$\epsilon_{\texttt{12MeV}}$ (%)	Run ID	$\epsilon_{\texttt{15MeV}}$ (%)
$Z = +12$ m	076430	0.49	076435	0.32	076422	0.02
$Z = 0$ m	076471	1.32	076474	0.02	076453	0.27
$Z = -12$ m	076501	2.22	076504	0.12	076483	1.48
Linear MSG Syst. From LINAC [SK4 (2017) Side]						
	Run ID	$\epsilon_{\texttt{8MeV}}$ (%)	Run ID	$\epsilon_{\texttt{12MeV}}$ (%)	Run ID	$\epsilon_{\texttt{15MeV}}$ (%)
$Z = +12$ m	076347	2.11	076350	0.37	076361	0.10
$Z = 0$ m	076367	2.09	076370	0.37	076373	0.75
$Z = -12$ m	076393	2.84	076399	0.36	076390	1.02

Table 12.4: Linear MSG Systematic uncertainty from LINAC for SK6 and SK4.

Chapter 13

T2K validation

The event features used as inputs to the cuts must be calibrated with real data, and the resulting uncertainties should be propagated to the selection criteria proposed here. To estimate the uncertainties of the cuts applied on atmospheric NCQE signal, we use the T2K NCQE as a proxy as introduced in Chapter 11.1.1. Although the T2K sample has only a few hundred events and its flux still differs from that of atmospheric neutrinos (see Figure 11.2), its precise beam timing and use of the same detector provide the most reliable available reference for validating atmospheric NCQE event event features within SK.

Despite the similarity between T2K and atmospheric NCQE events, we account for uncertainties when comparing their visible energy spectra. The main sources are:

1. Flux uncertainties for atmospheric neutrinos (15.0%) [171] and for T2K itself (6.2%).

2. Neutrino interaction uncertainties other than NCQE, estimated using T2KReWeight and NC coherent scattering (3.9%).

3. NCQE energy spectrum differences due to imperfect flux matching after reweighting T2K to the atmospheric MC sample (8.0%).

4. NCQE cross-section models, evaluated using relative ratios of flux-averaged event counts (7.0%).

Sections 10.3.1 and 10.3.2 describe the evaluation of uncertainties in the T2K flux and neutrino interactions. The remainder of this section introduces additional uncertainties relevant to using T2K as an atmospheric NCQE sample.

Next, we use the T2K NCQE sample from Runs 1–11 to check both the

existing and newly proposed DSNB third cut settings. To keep events within the DSNB signal window, we first select those with visible energy in [7.5, 29.5] MeV before applying any further selections. We then test three cut strategies from Chapter 11.1 in each mode: discrete MSG, linear MSG, and a neural network cut. Finally, we estimate the overall systematic uncertainty.

In short, though the MC agrees well with the data, the data sample after cuts is small (∼10 events), resulting in a statistical uncertainty of roughly 30%. Furthermore, the MC adds an additional ∼ 15% systematic uncertainty, and neutron tagging contributes another ∼ 15%. Combining these gives a total uncertainty of about 45% for the cut strategies used in this study. The following sections explain each contribution in detail.

13.1 Feature difference between T2K and atmospheric neutrino flux.

For atmospheric flux uncertainties, we assign a 15% uncertainty based on Refs. [171, 172].

Besides of the flux uncertainty it self from atmospheric or T2K, the flux differences between them also propagate to event features distribution differences between T2K and atmospheric NCQE events. Figure 13.1 shows the atmospheric neutrino flux (orange or green curve) after the 1st, 2nd and 3rd DSNB cuts, just before the Cherenkov-angle and MSG cuts. Compared with the atmospheric flux, the T2K flux (blue curve) is slightly higher and narrower in neutrino energy, shifting the visible-energy (and N_{50}) distributions and producing a modest high-energy tail in the T2K NCQE spectrum. Consequently, the T2K sample contains a larger fraction of higher-energy NCQE events, characterized by lower MSG and larger Cherenkov angles values, than the atmospheric sample (right panel of Figure 13.1). This observable difference between T2K and atmospheric NCQE is larger than the SI model variations within the atmospheric sample [43], motivating a check of how well T2K can resemble the atmospheric NCQE sample, especially in visible energy.

We reweight the T2K NCQE sample to the atmospheric NCQE reference (both INCL-G4PreCompound) to compare visible energy spectra between the "reweighted T2K NCQE" and "atmospheric NCQE" samples. Because the T2K flux is narrowly peaked, few T2K events fall in the atmospheric peak region, which would cause large fluctuations if we directly reweighted based on the neutrino flux. Instead, we reweight using the Cherenkov-angle distribution because (i) our primary goal is to demonstrate the energy dependence of MSG, (ii) the Cherenkov angle is well validated in Ref. [50] and correlates with both E_{vis} and E_ν, and (iii) its distribution in the T2K sample

is broader than the flux peak, providing good statistical coverage of the atmospheric NCQE phase space.

Figure 13.2 shows the reweighted T2K features (light blue), the original T2K sample (blue), and the atmospheric NCQE sample (orange). After reweighting, the MSG and visible energy spectra agree. From this study we assign an 8% uncertainty on the visible energy spectrum, representing the dominant difference between the reweighted T2K and atmospheric NCQE samples.

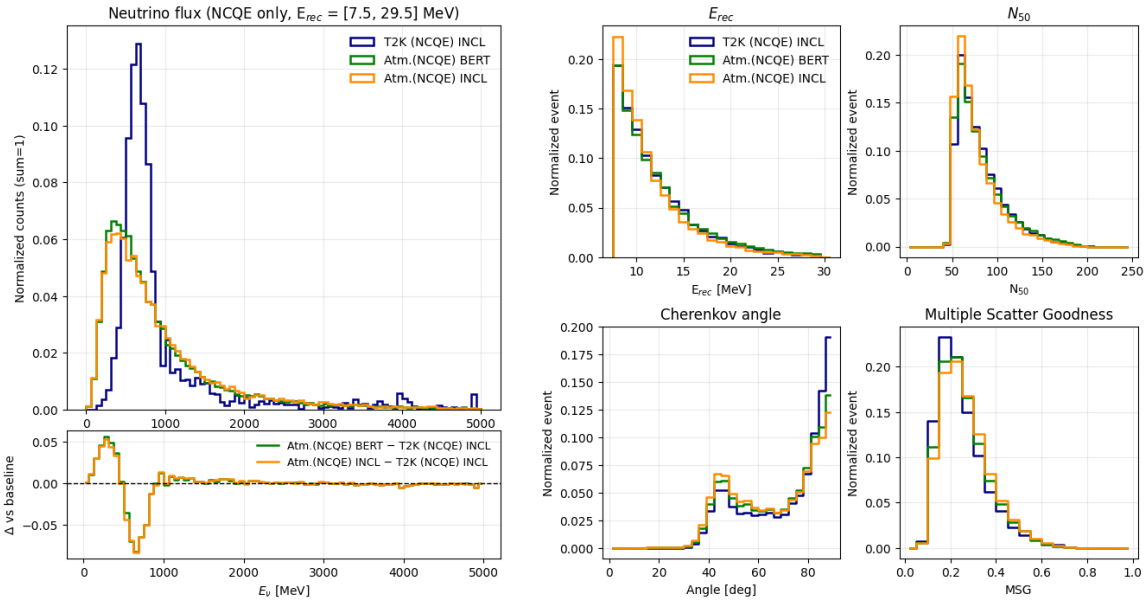

Figure 13.1: T2K FHC (blue) vs atmospheric NCQE (orange or green) neutrino flux after the 1st–3rd DSNB cuts. T2K's narrower, higher flux yields a slightly high energy tail and larger Cherenkov angles with lower MSG.

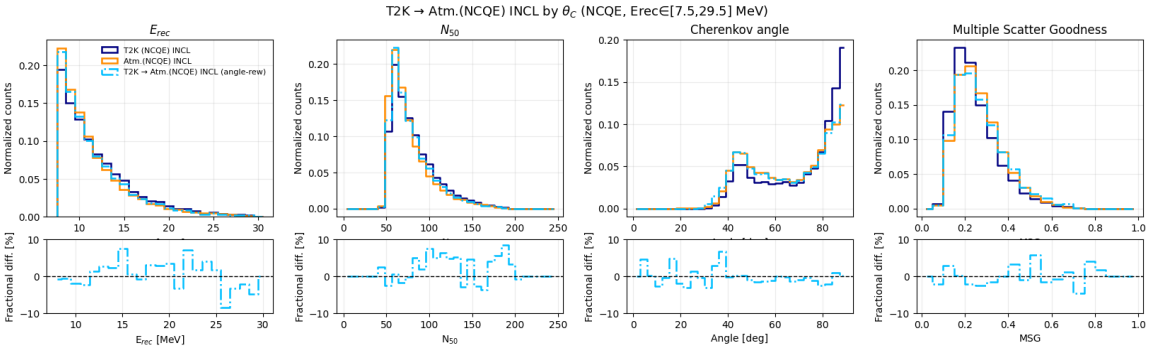

Figure 13.2: Cherenkov angle reweighting of T2K to atmospheric NCQE. Reweighted T2K (light blue) matches the atmospheric E_{vis} and MSG. Ratio panels show residuals (at most ∼8% on the energy spectrum).

Differences among NCQE models

Following Ref. [50], we estimate the NCQE cross-section modeling uncertainty by comparing, for each NCQE model i, the flux-averaged event ratios between the T2K

and atmospheric fluxes:

$$R_{\nu}^{i} = \frac{\int \phi_{\nu}^{\mathrm{T2K}}\, \sigma_{\nu\text{-NCQE}}^{i}\, dE_{\nu}}{\int \phi_{\nu}^{\mathrm{ATM}}\, \sigma_{\nu\text{-NCQE}}^{i}\, dE_{\nu}}, \tag{13.1}$$

$$R_{\bar{\nu}}^{i} = \frac{\int \phi_{\bar{\nu}}^{\mathrm{T2K}}\, \sigma_{\bar{\nu}\text{-NCQE}}^{i}\, dE_{\bar{\nu}}}{\int \phi_{\bar{\nu}}^{\mathrm{ATM}}\, \sigma_{\bar{\nu}\text{-NCQE}}^{i}\, dE_{\bar{\nu}}}. \tag{13.2}$$

Here, ϕ^{T2K} and ϕ^{ATM} are the T2K and atmospheric fluxes, and $\sigma^{i}_{\nu\text{-NCQE}}$ and $\sigma^{i}_{\bar{\nu}\text{-NCQE}}$ are the oxygen NCQE cross sections for model i. Ratios relative to the nominal NEUT model are given in Table 13.1. The largest deviation, 7%, is taken as the systematic uncertainty.

Table 13.1: Relative ratios of flux-averaged events from T2K to atmospheric flux for six models, normalized to NEUT. Table taken from Ref. [50]

Model (i)	$R_{\nu}^{i}/R_{\nu}^{\mathrm{NEUT}}$	$R_{\bar{\nu}}^{i}/R_{\bar{\nu}}^{\mathrm{NEUT}}$
NEUT	1.00	1.00
SF	1.03	1.03
RMF	1.05	1.07
SuSA	0.96	0.98
RGF, EDAI	1.04	1.04
RGF, Democratic	1.05	1.06
RPWIA	0.98	0.96

13.2 The three cut strategies validation

The cut strategies to validation are detailed in Sec. 11.1.2. Three approaches are examined: (1) *Discrete MSG*, (2) *Linear MSG*, and (3) *Neural Network cut*, each employing event features to distinguish NCQE from DSNB events.

For both the *Discrete MSG* and *Linear MSG* methods, a Cherenkov angle requirement of $\theta_c = [38°, 53°]$ is applied, treating the Cherenkov angle and MSG as independent observables. The primary difference lies in the MSG implementation: fixed cut value for each visible energy bins (discrete) versus a linear PMT hits-dependent function (linear) case. Consequently, validating the *Linear MSG* approach necessitates testing the energy dependence of MSG. In contrast, the *Neural Network* method simultaneously exploits correlations among visible energy (N50), Cherenkov angle, and MSG.

To evaluate the robustness of these cut strategies, the T2K NCQE sample is used as a validation dataset. The analysis in this study focuses on two aspects: (1) systematic uncertainties in the MC, including variations in de-excitation models, and (2) discrepancies between MC predictions and experimental data. We first

demonstrate that, for all three cut strategies, the MC-predicted samples after selection remain dominated by neutral current events, as summarized in Table 13.2. The NCQE channel fraction decreases progressively with each cut, while the CC channel fraction increases, consistent with expectations since the cuts are designed to retain DSNB (CC-like) events while suppressing NCQE events. It is also worth noting that T2K CC events exhibit low selection efficiency in this context, as the optimization was tuned for the DSNB signal (but not T2K CC events). This is largely due to the T2K CC energy spectrum peaking around 6 MeV, in contrast to the DSNB spectrum, which peaks near 12 MeV.

NCQE Run 1–11 (FHC) expectation (NEUTNuc-GCALOR)						
Selection	ν-NCQE	$\bar{\nu}$-NCQE	NC-other	CC	Total$_{MC}$	Total$_{Data}$
NCQE selection	241.0(69.6%)	7.8(2.3%)	89.8(25.9%)	7.8(2.3%)	346.5(100%)	289
E_{vis} [7.5, 29.5]MeV	122.1(61.4%)	3.7(1.9%)	67.3(33.8%)	5.7(2.9%)	198.8(100%)	125
E_{vis} + θ_C	17.3(66.2%)	0.7(2.6%)	6.8(26.0%)	1.4(5.2%)	26.1(100%)	24
E_{vis} + θ_C + MSG$_{\mathrm{dis}}$	4.8(57.8%)	0.2(2.6%)	2.6(31.7%)	0.7(7.9%)	8.3(100%)	11
E_{vis} + θ_C + MSG$_{\mathrm{lin}}$	3.7(56.2%)	0.1(1.6%)	2.2(33.0%)	0.6(9.2%)	6.6(100%)	7
E_{vis} + NN cut	3.3(50.1%)	0.1(1.5%)	2.4(35.5%)	0.9(13.0%)	6.7(100%)	6
NCQE Run 1–9 (RHC) expectation (NEUTNuc-GCALOR)						
NCQE selection	30.6(30.5%)	42.9(42.9%)	24.8(24.8%)	1.9(1.9%)	100.2(100%)	96
E_{vis} [7.5, 29.5]MeV	15.8(26.8%)	22.5(38.1%)	19.1(32.5%)	1.5(2.6%)	58.9(100%)	40
E_{vis} + θ_C	2.1(25.6%)	3.7(45.4%)	2.2(26.6%)	0.2(2.4%)	8.2(100%)	11
E_{vis} + θ_C + MSG$_{\mathrm{dis}}$	0.6(22.6%)	0.9(35.2%)	1.0(37.0%)	0.1(5.3%)	2.6(100%)	2
E_{vis} + θ_C + MSG$_{\mathrm{lin}}$	0.5(22.7%)	0.6(28.4%)	0.9(43.0%)	0.1(5.9%)	2.0(100%)	3
E_{vis} + NN cut	0.4(17.6%)	0.7(35.8%)	0.8(41.1%)	0.1(5.5%)	2.0(100%)	4

Table 13.2: Expected event yields after successive selection cuts for NCQE Runs 1–11 FHC and RHC modes. Percentages in parentheses give the fractional contribution of each component to the total MC expectation at the corresponding stage.

We next summarize the event predictions and cut efficiencies for each MC configuration after applying the selection cuts. As shown in Table 13.3, a sequence of additional cuts is applied, including the "NCQE selection" described in Chapter 10.1. Results are provided for both FHC and RHC modes. The feature distributions, including E_{vis}, N50, θ_C, MSG, and OvaQ after each cut, are shown in Figures 13.3(FHC-E_{vis}), 13.4(FHC-N_{50}), 13.5(FHC-θ_C), 13.6(FHC-MSG), 13.7(FHC-OvaQ), 13.8(RHC-E_{vis}), 13.9(RHC-N_{50}), 13.10(RHC-θ_C), 13.11(RHC-MSG), and 13.12(RHC-OvaQ). In these figures, the histograms represent the SKDETSIM predictions, while the SKG4 predictions with settings NEUT-BERT-G4Cas (blue dashed) and NEUTNuc-INCL-NucDeEx (red dashed) are overlaid, respectively.

We then present the evaluation of systematic uncertainties in the MC. In this study, systematic uncertainties are assessed by comparing the cut efficiencies across different MC configurations, which reflect feature differences while normalizing the total event counts. The comparison focuses on cut efficiencies rather than absolute event yields, since the event scale will be included in the Flux, neutrino interaction, and NCQE models. The MC systematic uncertainties are summarized as follows:

Table 13.3: Summary of Run 1–11 event predictions for FHC and RHC. Columns correspond to cuts; rows correspond to different MC settings. Numbers in parentheses indicate the fraction relative to the "NCQE selection" sample.

NCQE Run 1–11 FHC						
MC setting (FHC)	NCQE selection	E_{vis} [7.5, 29.5]MeV	$E_{\text{vis}} + \theta_C$	$E_{\text{vis}} + \theta_C$+MSG$_{\text{dis}}$	$E_{\text{vis}} + \theta_C$+MSG$_{\text{lin}}$	E_{vis}+NN
NEUT-BERT-G4Cas	370.3 (100.0%)	220.4 (59.5%)	32.6 (8.8%)	11.8 (3.2%)	9.4 (2.5%)	8.9 (2.4%)
NEUT-BERT-G4Pre	348.6 (100.0%)	188.5 (54.1%)	33.5 (9.6%)	11.8 (3.5%)	9.4 (2.7%)	8.7 (2.5%)
NEUT-INCL-G4Pre	343.3 (100.0%)	177.6 (51.7%)	32.9 (9.6%)	12.6 (3.7%)	9.9 (2.9%)	9.2 (2.7%)
NEUT564-INCL-G4Pre	352.1 (100.0%)	185.3 (52.6%)	36.6 (10.4%)	13.4 (3.8%)	10.4 (2.9%)	9.8 (2.8%)
NEUT-INCL-NucDeEx	345.1 (100.0%)	181.2 (52.5%)	33.0 (9.6%)	12.3 (3.6%)	9.4 (2.7%)	9.3 (2.7%)
NEUTNuc-INCL-NucDeEx	315.5 (100.0%)	163.1 (51.7%)	31.6 (10.0%)	12.8 (4.1%)	10.1 (3.2%)	9.5 (3.0%)
NEUTNuc-GCALOR	346.5 (100.0%)	198.8 (57.4%)	26.1 (7.5%)	8.3 (2.4%)	6.6 (1.9%)	6.7 (1.9%)
Data (FHC)	289 (100.0%)	125 (43.3%)	24 (8.3%)	11 (3.8%)	7 (2.4%)	6 (2.1%)
NCQE Run 1–9 RHC						
MC setting (RHC)	NCQE selection	E_{vis} [7.5, 29.5]MeV	$E_{\text{vis}} + \theta_C$	$E_{\text{vis}} + \theta_C$+MSG$_{\text{dis}}$	$E_{\text{vis}} + \theta_C$+MSG$_{\text{lin}}$	E_{vis}+NN
NEUT-BERT-G4Cas	101.0 (100.0%)	59.1 (58.6%)	9.1 (9.0%)	3.3 (3.3%)	2.6 (2.6%)	2.5 (2.5%)
NEUT-BERT-G4Pre	95.1 (100.0%)	50.3 (52.9%)	9.2 (9.7%)	3.4 (3.6%)	2.5 (2.7%)	2.5 (2.6%)
NEUT-INCL-G4Pre	93.4 (100.0%)	46.8 (50.1%)	8.6 (9.2%)	3.4 (3.6%)	2.7 (2.9%)	2.6 (2.8%)
NEUT564-INCL-G4Pre	96.0 (100.0%)	48.5 (50.5%)	9.4 (9.8%)	3.3 (3.5%)	2.8 (2.9%)	2.9 (3.0%)
NEUT-INCL-NucDeEx	93.9 (100.0%)	47.5 (50.6%)	9.0 (9.6%)	3.2 (3.4%)	2.5 (2.6%)	2.5 (2.7%)
NEUTNuc-INCL-NucDeEx	89.3 (100.0%)	44.2 (49.5%)	8.8 (9.9%)	3.5 (3.9%)	2.7 (3.0%)	2.6 (2.9%)
NEUTNuc-GCALOR	100.2 (100.0%)	56.8 (56.7%)	8.0 (8.0%)	2.9 (2.9%)	2.2 (2.2%)	2.1 (2.0%)
Data (RHC)	96 (100.0%)	40 (41.7%)	11 (11.5%)	2 (2.1%)	3 (3.1%)	4 (4.2%)

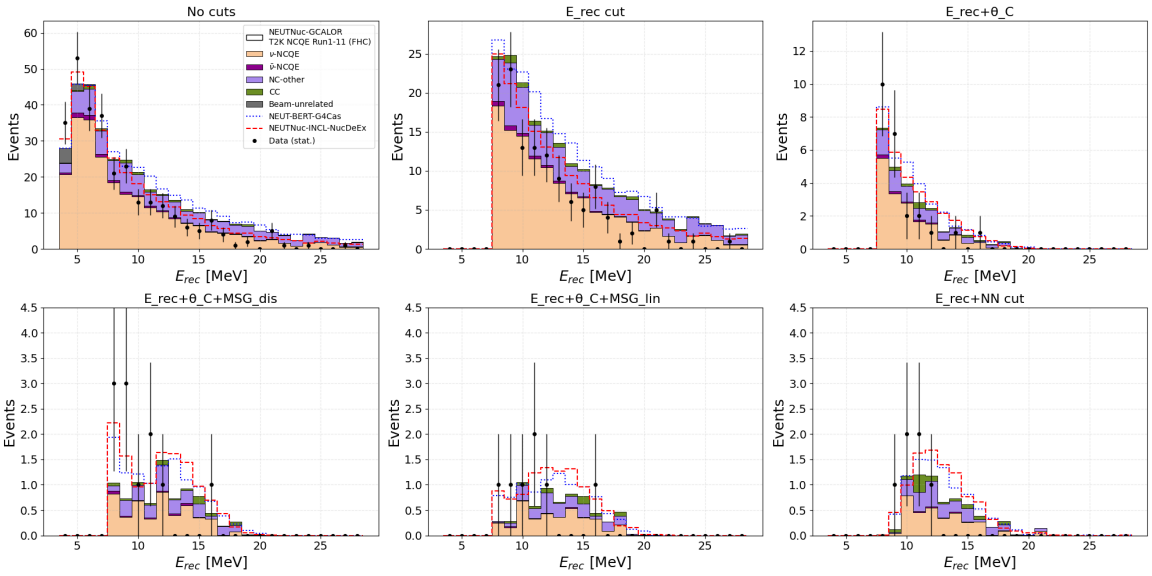

Figure 13.3: T2K FHC: visible energy E_{vis} after each cumulative cut (SKDETSIM histograms, SKG4 with BERT-G4Cascade (blue) and INCL-NucDeEx (red) overlays.).

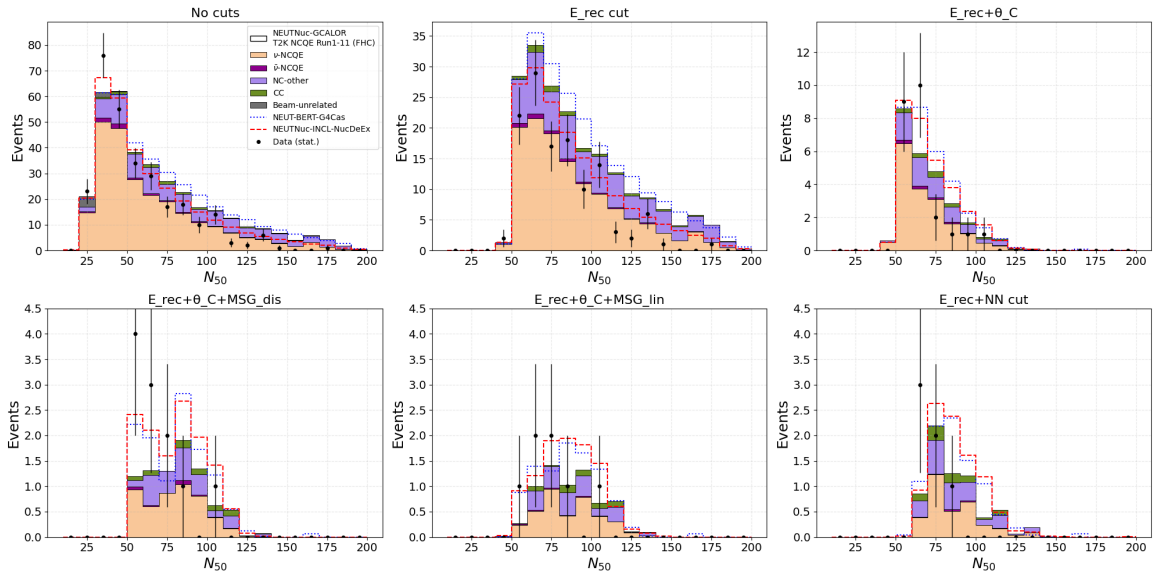

Figure 13.4: T2K FHC: N_{50} after each cumulative cut (SKDETSIM histograms, SKG4 with BERT-G4Cascade (blue) and INCL-NucDeEx (red) overlays.)

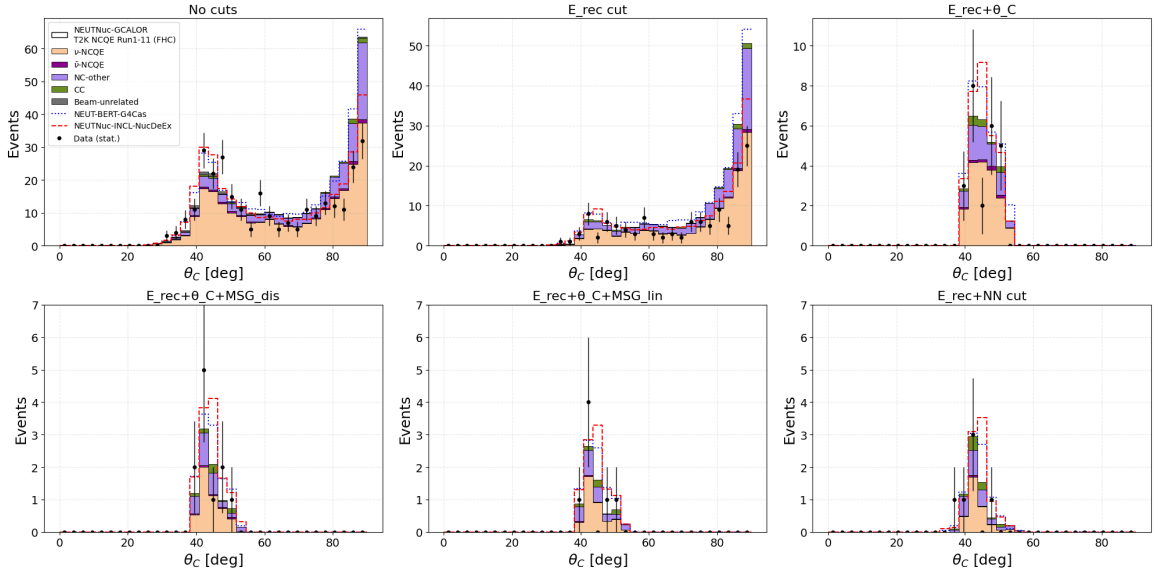

Figure 13.5: T2K FHC: θ_C after each cumulative cut (SKDETSIM histograms, SKG4 with BERT-G4Cascade (blue) and INCL-NucDeEx (red) overlays.)

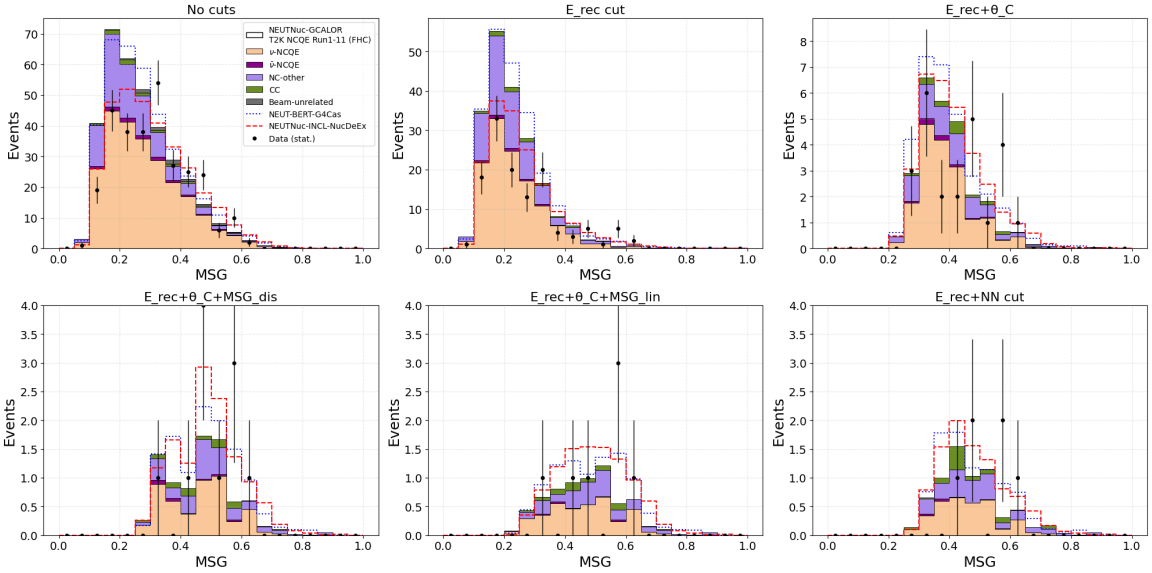

Figure 13.6: T2K FHC: MSG after each cumulative cut (SKDETSIM histograms, SKG4 with BERT-G4Cascade (blue) and INCL-NucDeEx (red) overlays.)

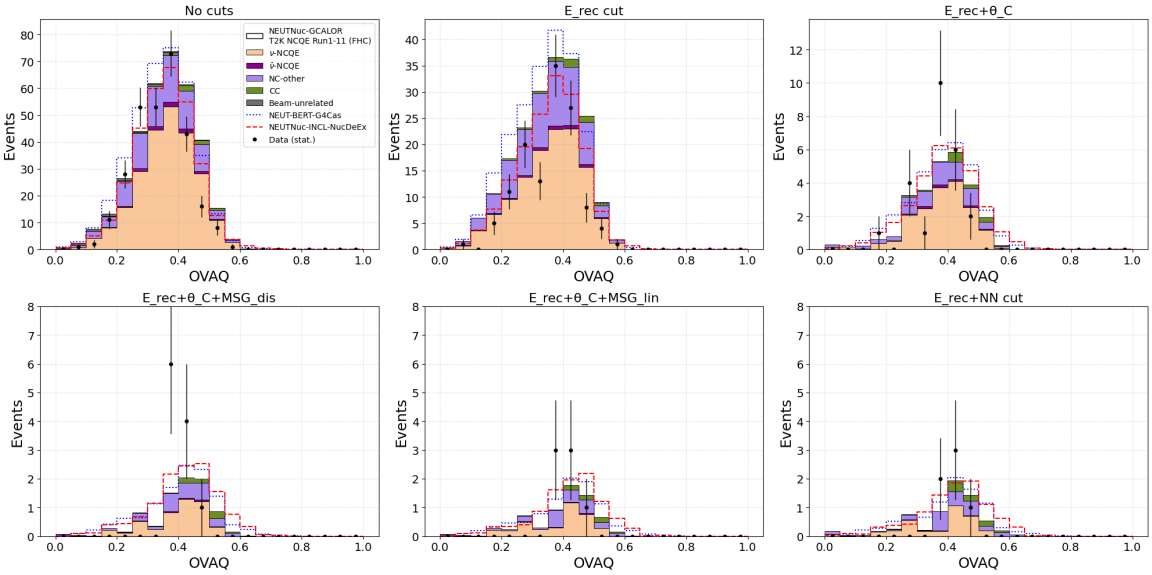

Figure 13.7: T2K FHC: OvaQ after each cumulative cut (SKDETSIM histograms, SKG4 with BERT-G4Cascade (blue) and INCL-NucDeEx (red) overlays.)

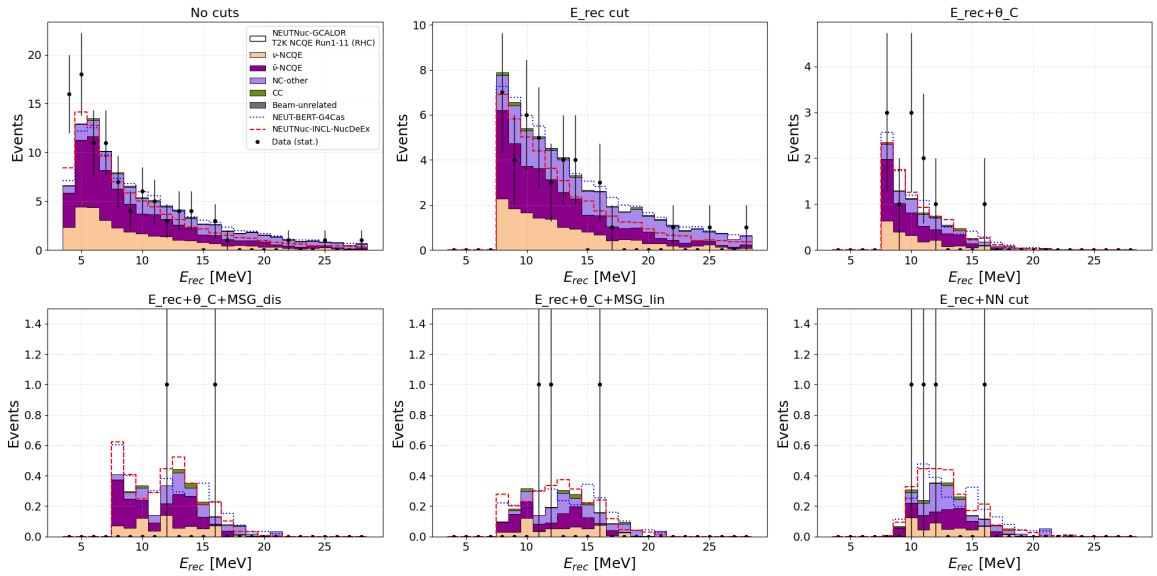

Figure 13.8: T2K RHC: visible energy E_{vis} after each cumulative cut (SKDETSIM histograms, SKG4 with BERT-G4Cascade (blue) and INCL-NucDeEx (red) overlays.)

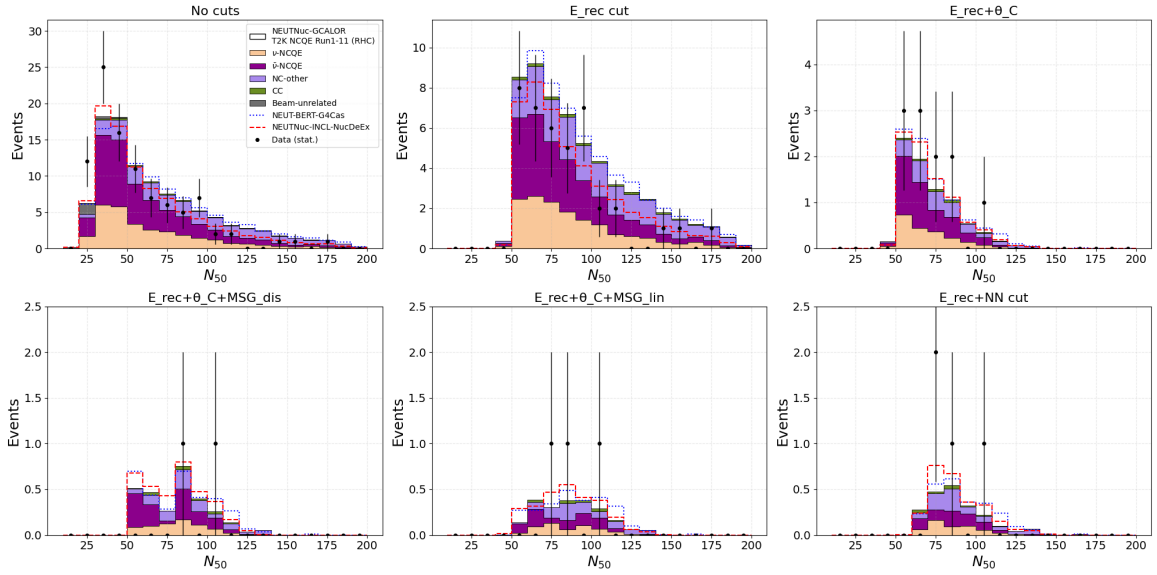

Figure 13.9: T2K RHC: N_{50} after each cumulative cut (SKDETSIM histograms, SKG4 with BERT-G4Cascade (blue) and INCL-NucDeEx (red) overlays.)

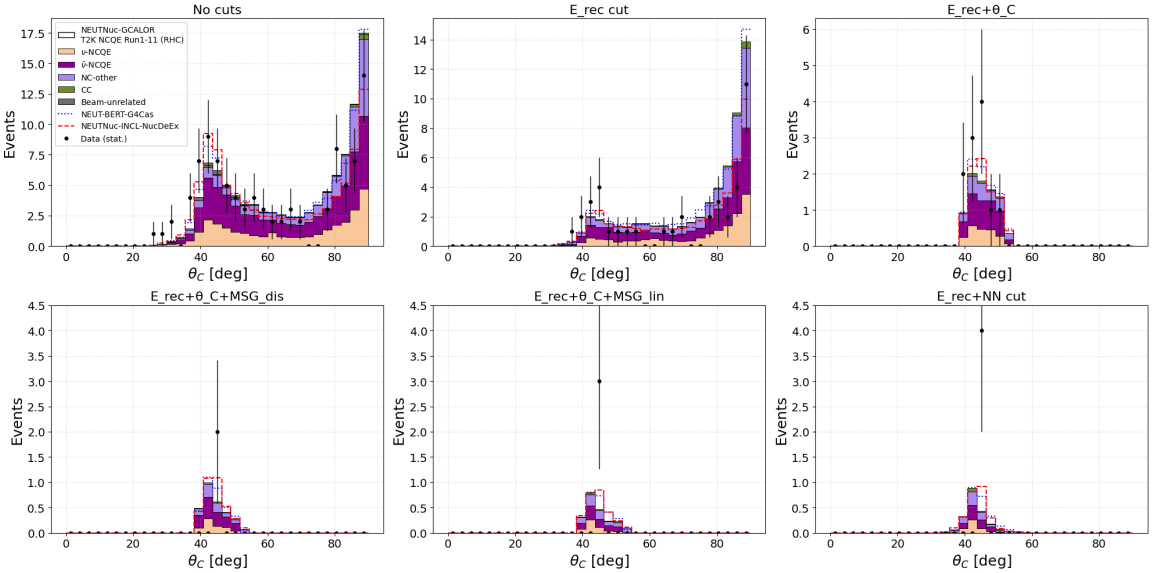

Figure 13.10: T2K RHC: Cherenkov angle θ_C after each cumulative cut (SKDETSIM histograms, SKG4 with BERT-G4Cascade (blue) and INCL-NucDeEx (red) overlays.)

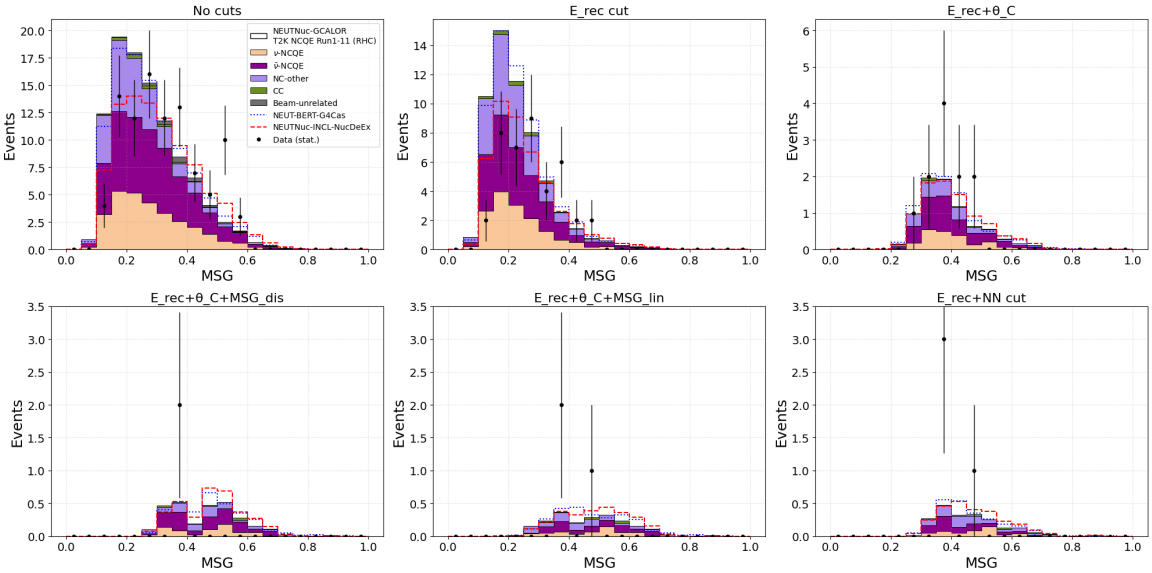

Figure 13.11: T2K RHC: MSG after each cumulative cut (SKDETSIM histograms, SKG4 with BERT-G4Cascade (blue) and INCL-NucDeEx (red) overlays.)

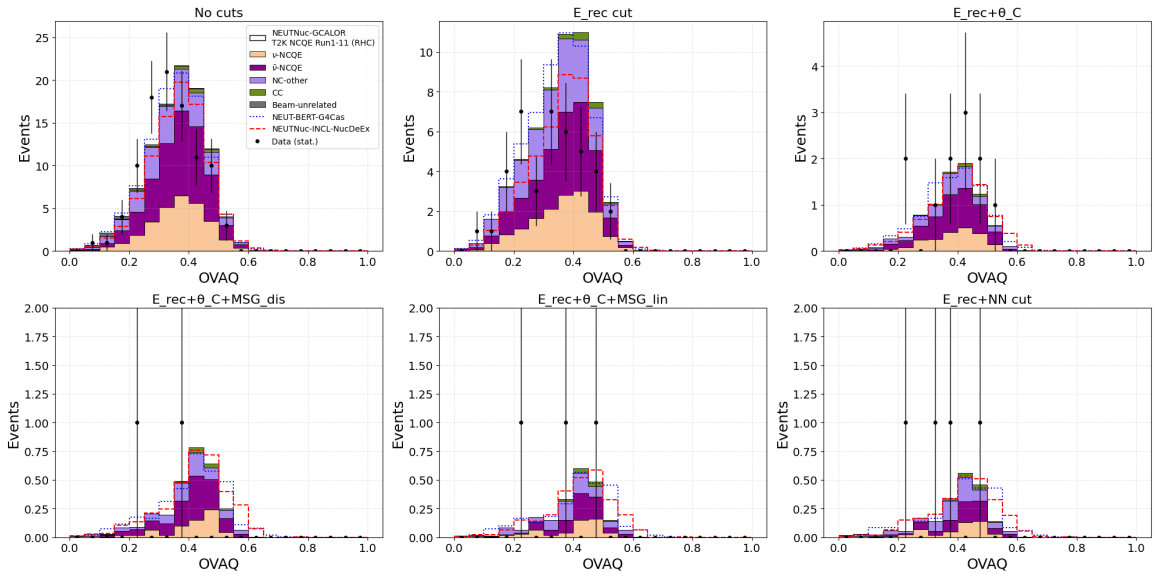

Figure 13.12: T2K RHC: OvaQ after each cumulative cut (SKDETSIM histograms, SKG4 with BERT-G4Cascade (blue) and INCL-NucDeEx (red) overlays.)

- **NEUT version (5.6.4 and 5.9.0)**
  NEUT 5.9.0 will be used in the upcoming DSNB search for SK IV–VIII, whereas the previous SK VI–VII DSNB search [36] and the cut optimization in Part. III were based on NEUT 5.6.4. We therefore compare the performance of the cut strategies between the "NEUT564-INCL-G4Pre" and "NEUT(590)-INCL-G4Pre" configurations. Since the MC truth information for γ production differs only slightly between NEUT 5.6.4 and NEUT 5.9.0, the systematic uncertainties across the three cut strategies remain at a low level of below 3.5%. However, we observe a relatively large efficiency difference, about 8%, at the $E_{\text{vis}} + \theta_C$ cut stage. The uncertainty is reduced when the MSG cut is applied or when switching to the NN cut strategy, suggesting that the MSG parameter constrains part of the Cherenkov angle distribution and thereby reduces the uncertainty to Cherenkov-angle only cuts. A summary is provided in Table 13.5.

- **NEUT de-excitation model(NucDeEx vs. Default)**
  NEUT 5.9.0 with NuDeEx will be used in the upcoming DSNB search for SK IV–VIII, whereas the SK VI–VII DSNB search [36] and the cut optimization in Part III employed NEUT with its default de-excitation model. We therefore compare the cut strategy performance between "NEUT-INCL-NucDeEx" and "NEUTNuc-INCL-NucDeEx". The MC truth information for γ production shows clear differences in both spectrum and multiplicity between NEUT's default and NuDeEx, suggesting a larger systematic uncertainty on primary interaction de-excitation models is reasonable in this case. Overall, the estimated systematic uncertainties are 12.5% for MSG_{dis}, 15.6% for MSG_{lin}, and 10.0% for NN. A summary is provided in Table 13.5.

- **SKG4 de-excitation model (NucDeEx vs. G4PreCompound)**
  The de-excitation model NuDeEx will be implemented not only in NEUT but also in the detector simulation, SKG4, for the upcoming DSNB search in SK IV–VIII, whereas the SK VI–VII DSNB search [36] and the cut optimization in Part III employed G4PreCompound (with INCL++) with its default de-excitation model. We therefore compare the systematic uncertainties between the "NEUT-INCL-G4Pre" and "NEUT-INCL-NucDeEx" configurations. The MC truth information for γ production shows only minor differences in both spectrum and multiplicity between the de-excitation models in the detector simulation, leading to a relatively small systematic uncertainty. Overall, we estimate at most a $\sim 5.3\%$ systematic uncertainty associated with the choice of de-excitation model between G4PreCompound and NucDeEx in SKG4. A summary is provided in Table 13.5.

- **SKG4 BERT physics list issue (BERT-G4Pre vs. INCL-G4Pre)**
  The legacy de-excitation model implemented in SKG4, also employed in the SK VI DSNB search [23] as well as in numerous previous DSNB, atmospheric (and T2K) NCQE and CCQE studies, was "NEUT-BERT-G4Cas." The primary limitation of "NEUT-BERT-G4Cas" lies in its inaccurate oxygen de-excitation gamma spectrum and multiplicity. This issue has been thoroughly investigated both within the simulation code itself and through comparisons with observed NCQE-induced gamma production in T2K measurements, as well as NCQE-induced neutron production in T2K mentioned in Part II, and atmospheric events at SK [105, 129]. The present work further shows the insufficiency of using the native de-excitation model in Bertini cascade (G4Cascade) in SKG4 for DSNB analyses. Consequently, G4Cascade will be excluded from the MC systematic evaluation. Instead, we will compare the uncertainties arising from the intra-nuclear cascades themselves. To be intra-nuclear cascade-specific, we connect the Bertini cascade with G4PreCompound, aligning it with the INCL cascade, and evaluate the impact on cut strategy efficiencies under these MC configurations. We compare the efficiencies of three cut strategies between "NEUT-BERT-G4Pre" and "NEUT-INCL-G4Pre," finding a maximum difference of $\sim$7%, a level comparable to that observed when comparing "G4PreCompound" with "NucDeEx." This result is reasonable, as the MC truth information for gamma production is largely identical between BERT and INCL once they adopt the same de-excitation model.

- **SKG4 (NucDeEx vs. G4Cascade)**
  Although G4Cascade will not be included in the evaluation of systematic uncertainties, it is still valuable to perform a cross-check with previous results. In this study, we estimate the uncertainty associated with G4Cascade by com-

Table 13.4: Summary of NCQE event predictions combining Run 1–11 FHC and Run 1–9 RHC (FHC+RHC). Columns correspond to cuts; rows correspond to different MC settings. Numbers in parentheses indicate the fraction relative to the combined "NCQE selection" sample.

NCQE Run 1–11 FHC + Run 1–9 RHC (FHC+RHC)						
MC setting	NCQE selection	E_{vis} [7.5, 29.5] MeV	$E_{\mathrm{vis}} + \theta_C$	$E_{\mathrm{vis}} + \theta_C$+MSG$_{\mathrm{dis}}$	$E_{\mathrm{vis}} + \theta_C$+MSG$_{\mathrm{lin}}$	E_{vis}+NN
NEUT-BERT-G4Cas	471.3 (100.0%)	279.5 (59.3%)	41.7 (8.8%)	15.1 (3.2%)	12.0 (2.5%)	11.4 (2.4%)
NEUT-BERT-G4Pre	443.7 (100.0%)	238.8 (53.8%)	42.7 (9.6%)	15.2 (3.4%)	11.9 (2.7%)	11.2 (2.5%)
NEUT-INCL-G4Pre	436.7 (100.0%)	224.4 (51.4%)	41.5 (9.5%)	16.0 (3.7%)	12.6 (2.9%)	11.8 (2.7%)
NEUT564-INCL-G4Pre	448.1 (100.0%)	233.8 (52.2%)	46.0 (10.3%)	16.7 (3.7%)	13.2 (2.9%)	12.7 (2.8%)
NEUT-INCL-NucDeEx	439.0 (100.0%)	228.7 (52.1%)	42.0 (9.6%)	15.5 (3.5%)	11.9 (2.7%)	11.8 (2.7%)
NEUTNuc-INCL-NucDeEx	404.8 (100.0%)	207.3 (51.2%)	40.4 (10.0%)	16.3 (4.0%)	12.8 (3.2%)	12.1 (3.0%)
NEUTNuc-GCALOR	446.7 (100.0%)	255.6 (57.2%)	34.1 (7.6%)	11.2 (2.5%)	8.8 (2.0%)	8.8 (2.0%)
Data (FHC+RHC)	385 (100.0%)	165 (42.9%)	35 (9.1%)	13 (3.4%)	10 (2.6%)	10 (2.6%)

paring it to NucDeEx in SKG4, thereby enabling a direct comparison with earlier analyses. The DSNB SK-VII [36] analysis assigned an uncertainty of approximately 20% to the θ_C and MSG differences arising from G4Cascade and G4PreCompound. Since G4PreCompound has been shown to produce predictions similar to those of NucDeEx in SK, we re-evaluated the uncertainty between "NucDeEx" and "G4Cascade" for the three cut strategies, comparing "NEUT-BERT-G4Cas" with "NEUTNuc-INCL-NucDeEx." This analysis yields an uncertainty of approximately 25%, consistent with the estimation of the previous study.

- **SKG4 and SKDETSIM (BERT-G4Casade vs. GCALOR)**
  Although the DSNB analysis will be fully performed in SKG4, which does not require evaluation with SKDETSIM, we comment on differences between SKG4 and SKDETSIM in this study. For the physics list used in SKDETSIM(GCALOR), since it also employs a Bertini-like de-excitation model and exhibits similar feature predictions to G4Cascade, we consider it reasonable to compare with G4Cascade in order to reflect these two detector simulation systematics. While G4Cascade is not identical to GCALOR, it is the most similar option available for this comparison. We evaluated the uncertainty between "NEUT-BERT-G4Cas" and "NEUTNuc-GCALOR" for the three cut strategies, finding a maximum uncertainty of approximately 35%. It should be noted that this value may include contributions from both the NucDeEx systematic and the default de-excitation model in NEUT.

We treat the NEUT version, the de-excitation models in both the neutrino generator and the detector simulator, as well as the intra-nuclear cascade model in the detector simulation, as sources of systematic uncertainty for the three cut strategies. We summarize the MC systematic fractional uncertainties for Run 1-11 FHC plus RHC as the final estimate. The MC systematic uncertainties for the three cut strategies are 14.9%, 17.4%, and 12.9% for "Discrete MSG," "Linear MSG," and "NN cut," respectively. Overall, the three methods exhibit a similar level of uncertainty.

We next estimate the systematic uncertainty arising from the MC–Data difference. Owing to the limited statistics of the T2K NCQE sample, the uncertainty is evaluated using the combined Run 1-11 FHC plus RHC sample set, as summarized in Table 13.4. The MC–Data systematic uncertainty is determined by comparing the exact event numbers between "Data" and "NEUTNuc-INCL-NucDeEx" in Table 13.5. The resulting MC–Data systematic uncertainties for the three cut strategies are 20.2%, 21.9%, and 17.4% for "Discrete MSG," "Linear MSG," and "NN cut," respectively. The T2K NCQE Run 1-11 data itself also includes statistical uncertainties, which are 27.7%, 31.6%, and 31.6% for "Discrete MSG," "Linear MSG," and "NN cut," respectively. It is clear that the statistical uncertainty is the dominant uncertainty when compared to systematic uncertainties in MC, MC-Data difference, or other sources of uncertainty. The uncertainties discussed in this study are summarized in Table 13.5.

Table 13.5: Summary of MC systematic uncertainties for FHC and RHC from different sources.

MC settings	$E_{\text{vis}} + \theta_C$+MSG$_{\text{dis}}$	$E_{\text{vis}} + \theta_C$+MSG$_{\text{lin}}$	E_{vis}+NN
	FHC + RHC	FHC + RHC	FHC + RHC
NEUT (ver 5.9.0 vs. 5.6.4)	1.4%	1.7%	3.5%
NEUT (NucDeEx vs. Default)	12.5%	15.6%	10.0%
SKG4 (NucDeEx vs. G4PreCompound)	4.1%	5.3%	1.9%
SKG4 (BERT-G4Pre vs. INCL-G4Pre)	6.8%	5.3%	5.7%
MC systematic uncertainty	14.9%	17.4%	12.9%
MC systematic uncertainty	14.9%	17.4%	12.9%
MC-Data difference in #events	20.2%	21.9%	17.4%
Data stat.	27.7%	31.6%	31.6%
Total uncertainty for 3rd cut	**37.4%**	**42.2%**	**38.3%**
Reference			
SKG4 (NucDeEx vs G4Cascade)	25.4%	28.7%	25.1%
SKG4-G4Cas vs. SKDETSIM-GCALOR	36.8%	37.1%	33.5%

Finally, we present the feature distributions at these cut stages. The visible energy (E_{vis}), PMT hits within 50 ns (N_{50}), Cherenkov angle (θ_C), MSG, and OvaQ are shown in Figures 13.13 (Run 1-11 E$_{vis}$), 13.14 (Run 1-11 N50), 13.15 (Run 1-11 θ_C), 13.16 (Run 1-11 MSG), and 13.17 (Run 1-11 OvaQ), corresponding to Table 13.4. The plotting style follows that of the FHC and RHC breakdowns, where the histograms represent the predictions from SKDETSIM and SKG4 with configure NEUT-BERT-G4Cas (blue dashed) and NEUTNuc-INCL-NucDeEx (red dashed), respectively.

Figures 13.18, and 13.19 show the 2D distributions of N_{50}, θ_C, and MSG, with DSNB signal selection regions highlighted in light green. The T2K NCQE MC is shown as a brown heat map. Selected (red) and non-selected (black) data points are overlaid, with circles denoting FHC and triangles denoting RHC.

Figures 13.20 and 13.21 present the T2K NCQE MC broken down by γ multiplicity: Figure 13.20 applies only the E_{rec} cut at [7.5, 29.5] MeV, whereas Figure 13.21 applies both the E_{rec} and Cherenkov-angle cut at $38° \leq \theta_C \leq 53°$. From Figure 13.21,

we observe that even within the MSG_{lin} or NN selected regions, some T2K NCQE events with multiple γ's persist, suggesting that more sophisticated selection criteria could further suppress this background.

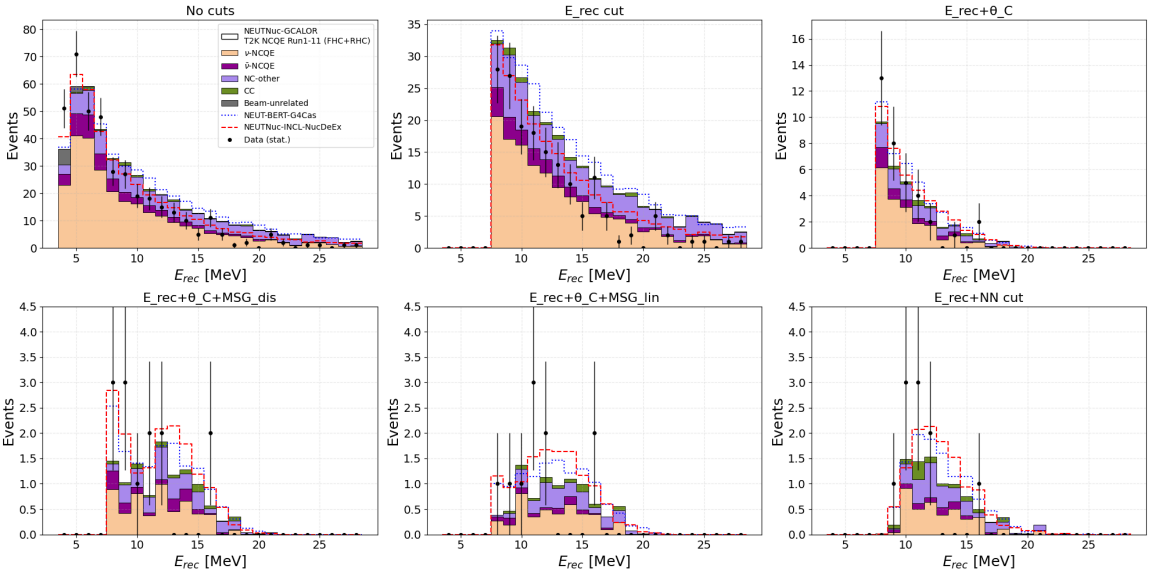

Figure 13.13: T2K NCQE (FHC+RHC, Runs 1–11): visible energy E_{vis} after each cumulative cut. SKDETSIM histograms. SKG4 overlays in blue(BERT-G4Cascade) / red(INCL-NucDeEx)).

We demonstrate that the systematic uncertainty in MC could be reduced from approximately 30% (as reported in the SK-VII DSNB study [36]) to about 14.9% in this study, primarily due to a detailed examination of the de-excitation model. However, the final uncertainty includes contributions from MC systematics, MC-Data systematics, and the statistical uncertainty of the data. The renewed total uncertainty has a statistical uncertainty of approximately 30%, shifting the study from systematics-limited to statistics-limited. Nevertheless, we demonstrate that, given the existing data statistics, the past uncertainty estimates are reasonable, thereby supporting the validity of the previous analysis.

13.3 Summary of systematic uncertainty

We summarize the renewed 3rd cuts uncertainties for the DSNB signal (Table 13.6, from LINAC) and the atmospheric NCQE background (Table 13.8, from T2K NCQE).

13.3.1 Updated 3rd cuts uncertainty for DSNB

The updated 3rd cuts increase the systematic for DSNB from the previous θ_c (1.3% [23]) and MSG (1.7% [23]) selections to about 3% for all cut choices in this study. Another major uncertainty for signal is neutron tagging: about 7% [129] in SK-IV and about

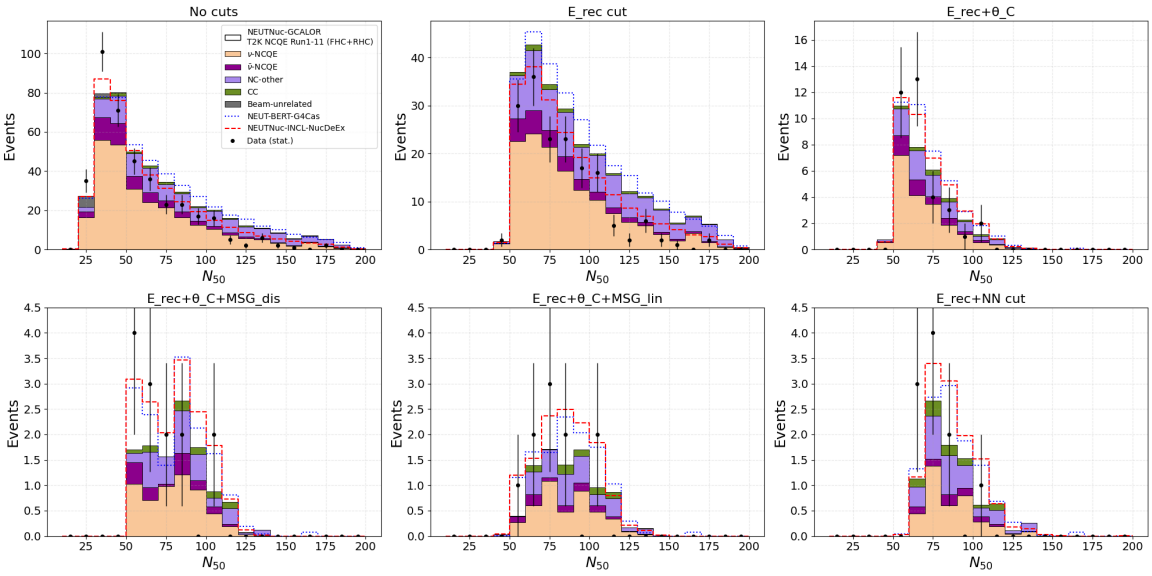

Figure 13.14: T2K NCQE (FHC+RHC): PMT hits N_{50} after each cumulative cut. SKDETSIM histograms, SKG4 with BERT-G4Cascade (blue) and INCL-NucDeEx (red) overlays.

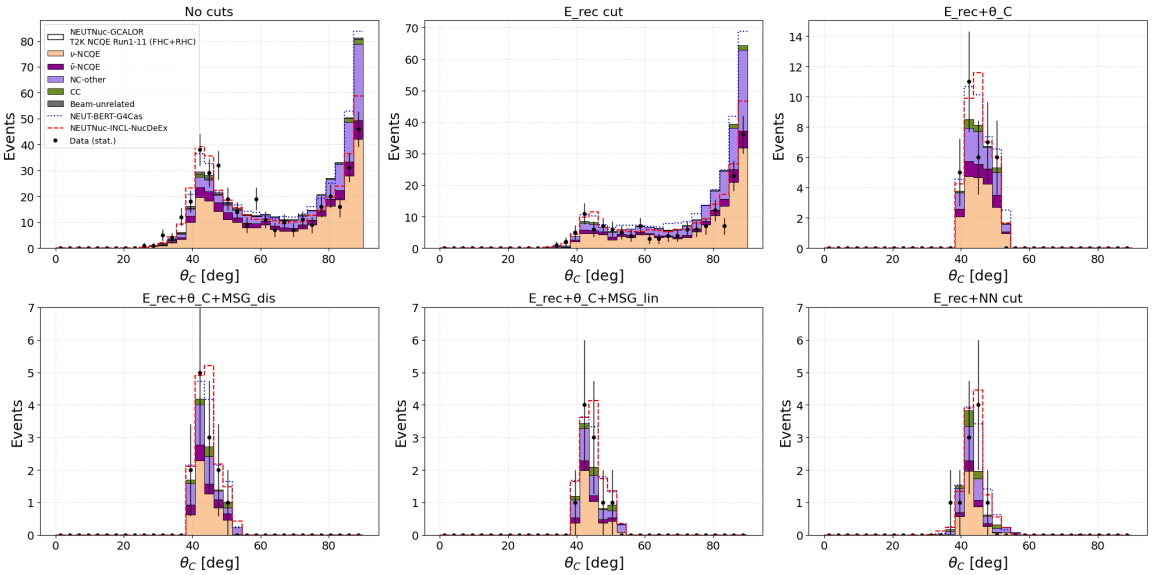

Figure 13.15: T2K NCQE (FHC+RHC): Cherenkov angle θ_C after each cumulative cut. SKDETSIM histograms, SKG4 with BERT-G4Cascade (blue) and INCL-NucDeEx (red) overlays.

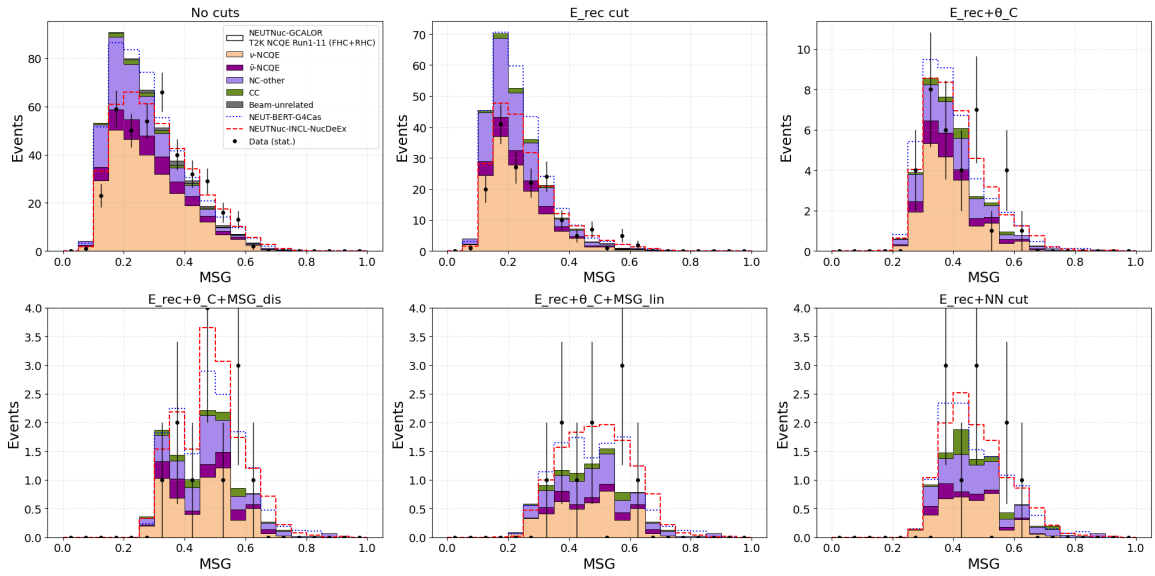

Figure 13.16: T2K NCQE (FHC+RHC): MSG after each cumulative cut. SKDETSIM histograms, SKG4 with BERT-G4Cascade (blue) and INCL-NucDeEx (red) overlays.

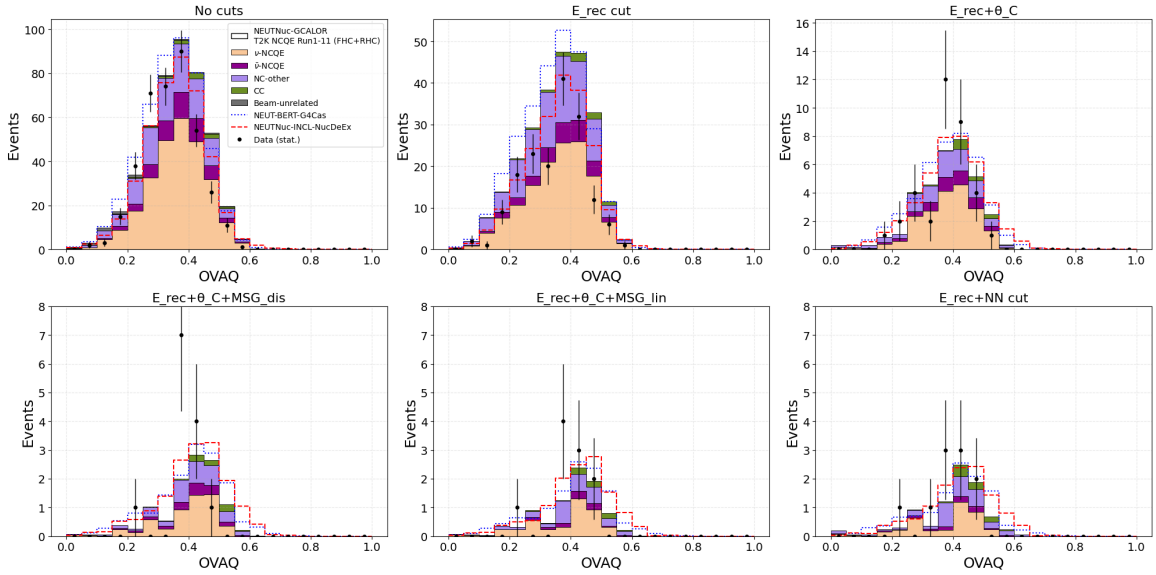

Figure 13.17: T2K NCQE (FHC+RHC): OvaQ after each cumulative cut. SKDETSIM histograms, SKG4 with BERT-G4Cascade (blue) and INCL-NucDeEx (red) overlays.

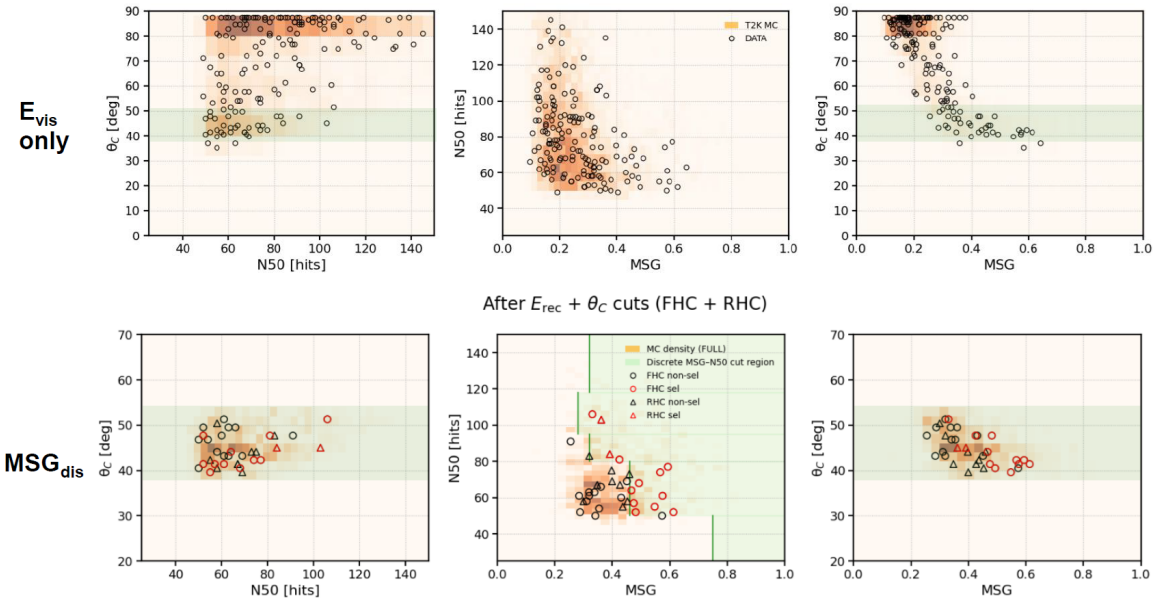

Figure 13.18: Distributions of θ_C–N50 (left), N50–MSG (center), and θ_C–MSG (right). The top row shows events passing only the E_{vis} [7.5, , 29.5] MeV cut. The bottom row shows MC after applying the E_{vis} and θ_C cuts, with events selected by the MSG_{dis} cut highlighted. T2K MC is shown as a brown heatmap. T2K data are plotted in black (non-selected) and red (selected). FHC points are circles, and RHC points are triangles. The selected region (MSG_{dis}) is shaded light green.

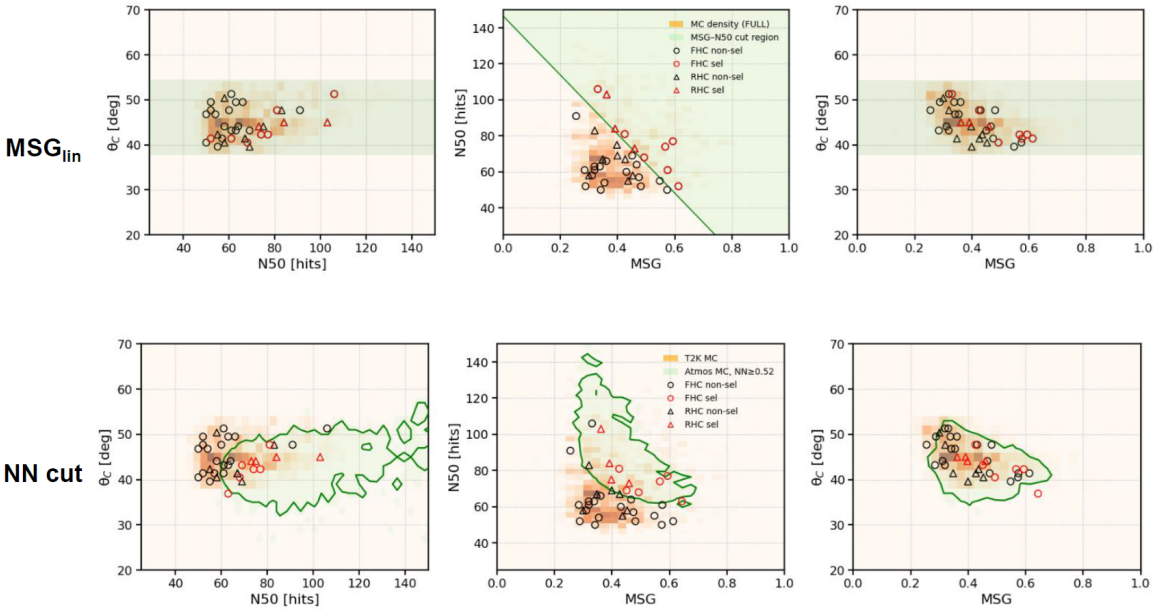

Figure 13.19: Distributions of θ_c–N50 (left), N50–MSG (center), and θ_c–MSG (right). The top row shows events after the MSG_{lin} selection. The bottom row shows events after the NN selection. T2K MC is shown as a brown heatmap. T2K data are plotted in black (non-selected) and red (selected). FHC points are circles and RHC points are triangles. Selected regions are shaded light green.

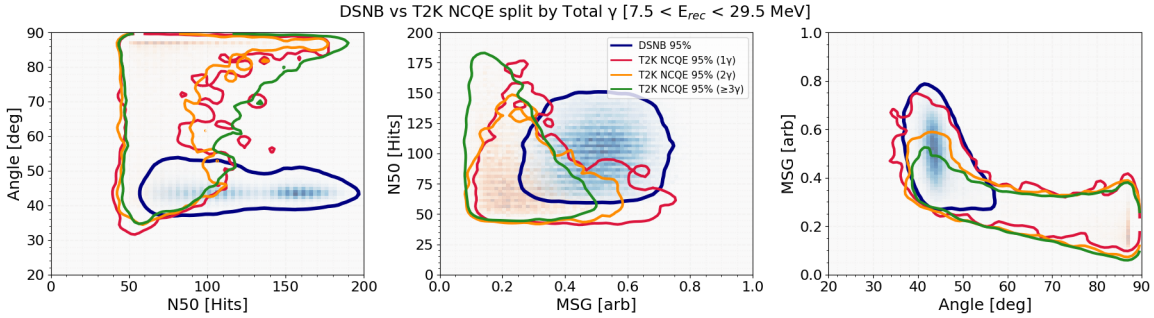

Figure 13.20: Distributions of θ_c–N50 (left), N50–MSG (center), and θ_c–MSG (right) with visible-energy selection. T2K MC (brown) and DSNB MC (blue) are rendered as heatmaps. The 95% contours are shown for both samples. T2K MC are further categorized by γ multiplicity: single (red), double (orange), and ≥ 3 (green).

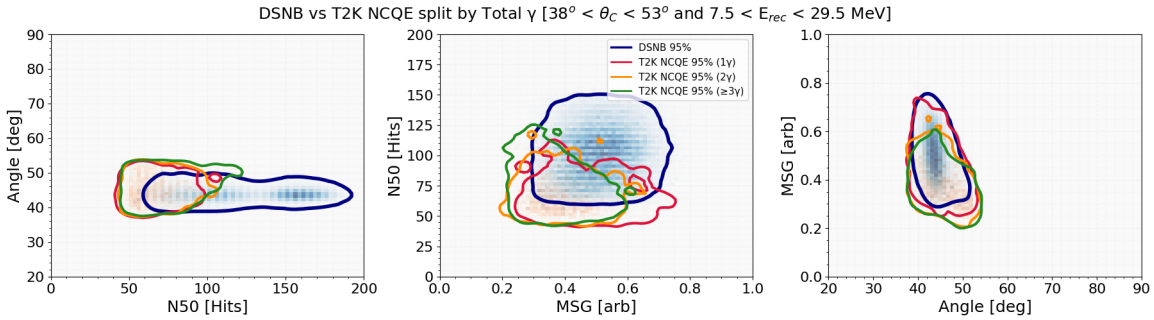

Figure 13.21: Distributions of θ_c–N50 (left), N50–MSG (center), and θ_c–MSG (right) with visible-energy and cherenkov angle selection. T2K MC (brown) and DSNB MC (blue) are rendered as heatmaps. The 95% contours are shown for both samples. T2K MC are further categorized by γ multiplicity: single (red), double (orange), and ≥ 3 (green).

Table 13.6: Systematic uncertainties on the DSNB signal due to event reduction cuts (mentioned in Chapter 11) as estimated with LINAC data and MC.

	Relative systematic uncertainty		
Cut	SK-IV	SK-VI	SK-VII
Spallation cut	0.1% [35]	-%	-%
d_{eff} cut	0.1% [35]	< 0.1% [167]	-%
L_{clear} cut	0.2% [35]	-%	-%
q_{50}/n_{50} cut	1.2% [35]	0.20% [36]	0.25% [36]
New 3rd cuts (This study)	**2.7% (MSG_{dis}) or 3.2% (MSG_{lin}) or 2.7% (NN cut)**		
Neutron tagging with NN (BDT)	7.3% [129] (12.5% [35])	8.4% (5.0%) [36]	3.4% (6.0%) [36]

3.4% [36] in SK-VII. In SK-IV the new 3rd cuts uncertainty is relatively minor because water-based neutron tagging dominates the signal uncertainty. However, after Gd loading and extensive calibration works, the neutron-tagging systematic drops to a level comparable to the new 3rd cuts. Further reduction of the "new 3rd cut" uncertainty should be possible with a detailed study of LINAC-calibration MC and data, since MC–data mismatches near 8 MeV and at lower-edge positions drive the current uncertainty. The uncertainties are summarized in Table 13.6.

13.3.2 Updated 3rd cut uncertainty for atmospheric NCQE

The updated "New 3rd cuts" yield an atmospheric NCQE background uncertainty better than the previous estimation from DSNB SK-VII search [36]. Removing the inappropriate de-excitation model, "G4Cascade", from the detector simulation reduces MC systematics to current $\sim$ 15% and leads to a good MC-data agreement (Figure 13.13,13.14,13.15,13.16, and 13.17), which is $\sim$ 20%. However, the stricter θ_c plus MSG selection lowers NCQE efficiency, leaving only $\sim$10 events in the T2K validation data sample, which make the statistical uncertainty now dominant over the total uncertainty. The current statistical uncertainty is about 30%, achieving $\sim$15% (comparable to other uncertainties) would require roughly five times more data.

Neutron related efficiency : For the atmospheric NCQE background, this study also updates two neutron-related uncertainties: neutron tagging efficiency and neutron multiplicity.

Neutron tagging efficiency : The previous neutron-tagging efficiency uncertainty was discussed in Part II, with detector response identified as the dominant contributor (Table 13.7). Detector responsce to neutron capture was calibrated using a ^{241}Am–Be source, which we assess the uncertainty of neutron capture, dominated by the H–Gd capture ratio r_H (with $r_{\mathrm{Gd}} = 1 - r_H$). Following a recent ^{241}Am–Be recalibration to address the MC simulation correction [130], the results shows a $\sim$ 6%

Table 13.7: Each uncertainty value from the original table divided by 43.1 and reported in percent.

Taken from TN-475	**Fractional uncertainty of neutron tagging on NCQE events**
Detector response to delayed signal	~~+12.3% / − 18.9% [129]~~ **6**%
Nucleon SI	+0.0% / − 2.0%
Prompt signal selection	+1.2% / − 1.2%
MC statistics	±1.2%
ν beam flux	±0.2%
ν oscillation	±0.02%
ν interaction	±0.9%
π capture on ^{16}O	+0.0% / − 3.4%
μ capture on ^{16}O	+0.0% / − 1.2%
PMT gain	Negligible
Water status	Negligible
Total	~~**+12.5**%~~ / ~~**− 19.5**%~~ **7.5**%

fraction discrepancy between calibration data and MC, so we update the neutron-tagging uncertainty from 21% to 7.5%. The latest neutron tagging calibration results is summarized in Figure 13.22: the lower-right panel compares MC with data, and the lower-left panel shows the fractional difference.

Neutron multiplicity : The previous uncertainty on neutron multiplicity was approximately 40% based on Ref. [127], driven mainly by uncertainties from secondary-interaction neutrons in CCQE interactions in T2K. Secondary-interaction effects for neutron prediction have been discussed extensively, both for NCQE at T2K (Left panel in Figure 13.23) and for CCQE in atmospheric-neutrino at SK [122] (Center panel in Figure 13.23). Rather than relying on the native de-excitation model in the BERTINI physics list, a more appropriate approach is to compare BERT and INCL using the same de-excitation model. We therefore adopt the neutron-multiplicity result from Ref. [129], which is based on extensive SK data collected from 2009 to 2021. As shown in the right panel of Figure 13.23, the difference between BERT and INCL with the same de-excitation model, when compared to data, is about 15%. Accordingly, we update the neutron-multiplicity uncertainty from 40% [50] to 15% [122].

Summary of atmospheric NCQE uncertainty for DSNB search : The final total uncertainty for 3rd cut on the atmospheric NCQE background is 45.6% for MSG_{dis}, 49.6% for MSG_{lin}, and 43.4% for NN cut. The dominant uncertainty contributions arise from the T2K data statistics. Opening additional datasets in the future should bring the possibility to examine physics models in more detail. In summary, this study validates the N50, angle, and MSG with T2K NCQR Run 1-11 data sample and provides updated systematic uncertainties for both signal and background.

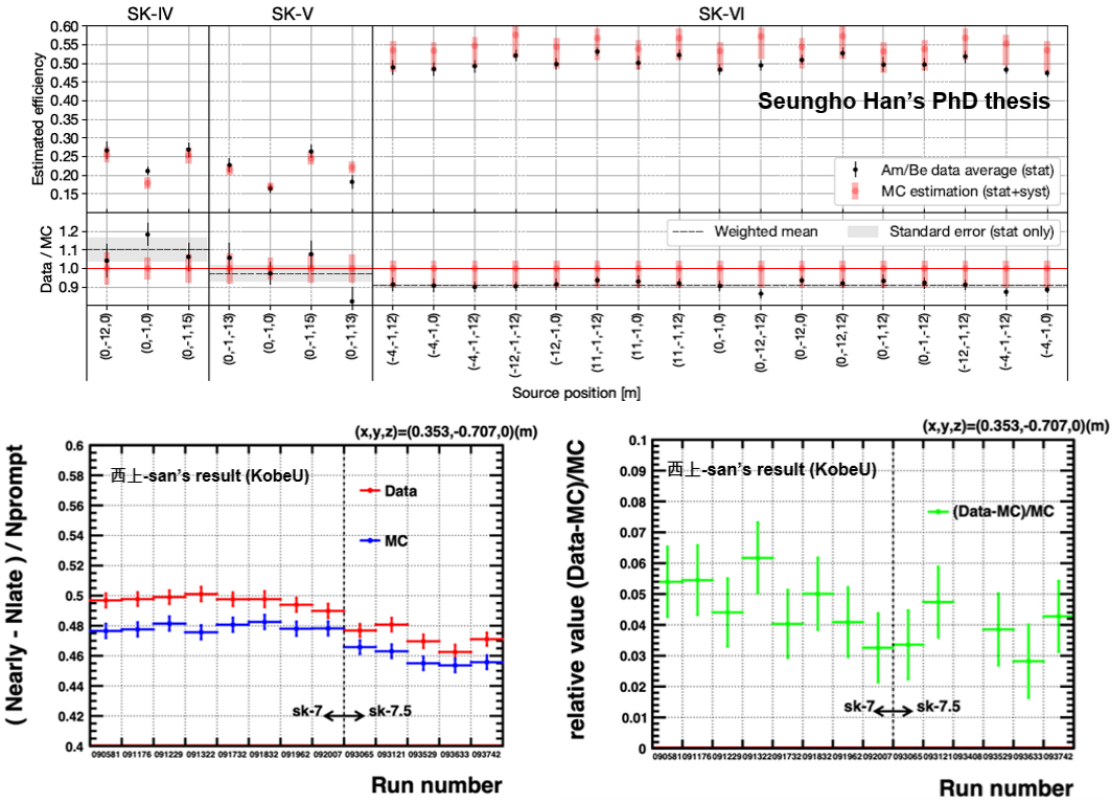

Figure 13.22: Neutron tagging efficiency calibration with a ^{241}Am-Be source. Top panel shows pre-correction results [129]. Bottom left shows the corrected calibration, and bottom-right shows the data/MC ratio. Fixing the MC H–Gd capture ratio achieves ∼6% data–MC agreement and reduces the neutron tagging uncertainty on NCQE events from 21% to 7.5%.

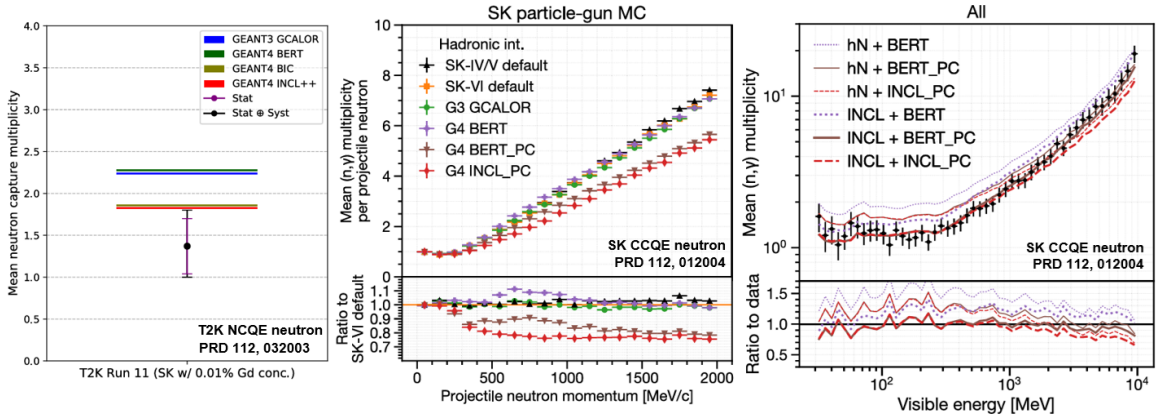

Figure 13.23: Update to the neutron-multiplicity systematic. **Left:** mean neutron multiplicity form T2K NCQE [161]. **Center:** atmospheric-neutrino CCQE with different de-excitation models at SK [129]. **Right:** Comparison of BERT and INCL with the same de-excitation model to SK data. The ratio to data spread between "INCL + BERT_PC" and "INCL + INCL_PC" is ∼15%, which is adopted as the revised neutron multiplicity uncertainty, replacing the previous 40% estimate [50].

Table 13.8: Systematic uncertainties on the atmospheric NCQE for DSNB search.

	Relative systematic uncertainty		
SK period	SK IV-VI, (Energy [7.49-29.49] MeV)		
T2K-ν flux	6.2%		
atmospheric-ν flux	15.0% [171]		
ν interaction	3.9%		
NCQE models	7.0%[161]		
Feature difference due to flux	8.0%		
Spallation cut	3.0% [23]		
New 3rd cuts options	**MSG$_{dis}$**	**MSG$_{lin}$**	**NN cut**
MC systematic	14.9%	17.4%	12.9%
MC-Data difference	20.2%	21.9%	17.4%
Data statistics	27.7%	31.6%	31.6%
Other third reduction	3.0% [23]		
Neutron tagging efficiency	7.5% [50]		
Neutron multiplicity	15.0% [129]		
Total uncertainty	**45.6%**	**49.6%**	**43.4%**

Chapter 14

Other background Estimation

In addition to the atmospheric NCQE background, several other sources can also produce events that mimics DSNB signals in the energy range of interest, [8, 30] MeV. In the following, we discuss background contributions from atmospheric CCQE interactions, Lithium-9, reactor neutrinos, and accidental coincidences.

14.1 Atmospheric CCQE Interactions

Atmospheric neutrinos can also undergo charged current interactions and create background events that mimic the DSNB signal. In particular, decay electrons from "invisible" muons, produced together with neutrons, form the dominant background above 20 MeV. Since the Michel spectrum from muon decay has been precisely measured using cosmic-ray muon data, we determine the size of this background by fitting a scaling factor between data and MC in the 30–80 MeV side-band region. For the SK-VI period, the best-fit scaling factor from the χ^2 minimization is 0.846. [23] Uncertainties in the production rates of muons, pions, and neutrons affect only the overall normalization of the Michel spectrum. The resulting uncertainty from the 1σ region of the χ^2 distribution is 17%. Including additional uncertainties from neutron multiplicity and neutron tagging efficiency, the total uncertainty on the non-NCQE interaction rate is taken to be 36%.

14.2 Lithium-9

The isotope ^{9}Li, produced by cosmic-ray muons, can undergo $\beta + n$ decay and mimic DSNB events. The expected number of ^{9}Li background events is calculated as

$$N^{^9\mathrm{Li}} = Rate^{^9\mathrm{Li}} \times \mathrm{Br}[^9\mathrm{Li} \rightarrow \beta + n] \times \epsilon_{\mathrm{reduc}} \times T_{\mathrm{live}}[\mathrm{day}] \times 22.5\ [\mathrm{kton}], \tag{14.1}$$

where $Rate^{^9\mathrm{Li}}$ is the spallation production rate of ^{9}Li, measured to be 0.86±0.12 (stat.)± 0.15 (sys.) kton^{-1} day^{-1} [165]. The term T_{live} is the live time (552.2 days), Br[^{9}Li $\rightarrow$ $\beta + n$] is the branching ratio (50.8%), and $\epsilon_{\mathrm{reduc}}$ is the reduction efficiency for DSNB search.

The uncertainty on $Rate^{^9\mathrm{Li}}$ corresponds to 22%. The ^{9}Li selection efficiency, evaluated using spallation cuts and cosmic muon simulation, is assigned a conservative 50% uncertainty, following the previous SK-IV analysis [34]. An additional 10% is included for neutron-related effects. Combining these contributions, the total uncertainty on the ^{9}Li background, $N^{^9\mathrm{Li}}$, is taken to be 55%.

14.3 Reactor Neutrinos

Electron antineutrinos produced in nearby nuclear reactors can enter SK and create IBD events that mimic DSNB signals. The expected flux of these reactor neutrinos is calculated using the reactor neutrino model [173], which takes into account the operating status of Japanese reactors during the SK-Gd observation period and neutrino oscillations over the distances from the reactors. A conservative 100% systematic uncertainty is assigned to the predicted number of reactor neutrino events. Because their rate in the DSNB signal energy region is relatively small and they contribute only to the lowest energy bin, their impact on the final result is negligible.

14.4 Accidental Coincidences

The accidental background mainly comes from noise that are incorrectly tagged as neutron capture event. The accidental coincidence background, N_{acc}, is calculated as

$$N_{\mathrm{acc}} = \varepsilon_{\mathrm{mis}} \times N^{\mathrm{data}}_{\text{pre-ntag}}, \tag{14.2}$$

where $\varepsilon_{\mathrm{mis}}$ is the neutron mis-tagging rate($\sim$1%), and $N^{\mathrm{data}}_{\text{pre-ntag}}$ is the number of remaining data events after the first to third reduction steps. The contribution from events with multiple misidentifications is negligible and can be ignored. The uncertainty, dominated by the estimation of $\varepsilon_{\mathrm{mis}}$, is taken to be 5% [23].

Chapter 15

DSNB sensitivity with new cuts

15.1 Expected Spectrum and Upper Limit Extraction

We calculate upper limits on the DSNB $\bar{\nu}_e$ flux in certain energy bins. First, we compile the background estimates, as each of the component is introduced in Chapter 14 and Chapter 11.1.1, and their systematic uncertainties for four selection settings: θ_C only (Table 15.1), MSG_{dis} (Table 15.2), MSG_{lin} (Table 15.3), and NN (Table 15.4), as introduced in Chapter 11.1.2. The spectrum distribution for four different cut settings were also shown in Figure 15.1.

We calculate independent upper limits for each energy bin individually. While incorporating the bin-to-bin correlations established in previous chapters would strictly yield tighter constraints by leveraging the full spectral shape, treating bins independently provides a more model-independent result that characterizes the sensitivity in specific energy ranges. For each energy bin, the total expected background is used to compute the 90% confidence level upper limit on the number of signal events, $N_{90\%}^{\text{sig}}$, using pseudo experiments. In each toy data set, the expected number of background events $N_{\text{bkg}}^{\text{MC}}$ is generated 10^6 times from a Gaussian distribution whose width reflects the systematic uncertainty on total background, $N_{\text{bkg}}^{\text{MC}}$.

For a given bin, $N_{90\%}^{\text{sig}}$ is defined such that the integral of the resulting distribution from zero to $N_{90\%}^{\text{sig}}$ contains 90% of the total probability for $N_{\text{bkg}}^{\text{MC}}$. Figure 15.2 shows the distribution of background-subtracted distributions and indicates the corresponding $N_{90\%}^{\text{sig}}$ for each energy bin, with the NN selection used as an example.

Table 15.1: Background by energy bin for the θ_C cut, including systematic uncertainties and 90% C.L. limits.

$E_{\rm rec}$ [MeV] (θ_C cut)	7.49–9.49	9.49–11.49	11.49–15.49	15.49–23.49	23.49–29.49
non-NCQE	0.287 ± 0.103	0.252 ± 0.091	0.407 ± 0.147	0.753 ± 0.271	0.938 ± 0.338
NCQE	1.789 ± 1.218	1.259 ± 0.856	0.962 ± 0.654	0.306 ± 0.208	0.052 ± 0.035
^{9}Li	3.553 ± 1.954	2.135 ± 1.174	0.242 ± 0.133	0.0 ± 0.0	0.0 ± 0.0
Reactor	0.257 ± 0.257	0.001 ± 0.001	0.0 ± 0.0	0.0 ± 0.0	0.0 ± 0.0
Accidental	1.336 ± 0.067	0.915 ± 0.046	0.349 ± 0.017	0.011 ± 0.001	0.0 ± 0.0
Total background	7.22 ± 2.32	4.56 ± 1.46	1.96 ± 0.68	1.07 ± 0.34	0.99 ± 0.34
$N_{90\%}^{\rm sig}$	3.94	4.70	3.59	3.09	1.75
Live time T			552.2 days		
Number of Target N_p			1.5×10^{33} protons		
DSNB efficiency	13.7%	21.3%	26.1%	26.3%	30.8%
$\phi_{90}^{\rm MC}$ [/cm^2/sec/MeV]	48.3	16.4	2.69	0.52	0.32

Table 15.2: Background by energy bin for the MSG$_{dis}$ cut, including systematic uncertainties and 90% C.L. limits.

$E_{\rm rec}$ [MeV] (MSG_{dis} cut)	7.49–9.49	9.49–11.49	11.49–15.49	15.49–23.49	23.49–29.49
non-NCQE	0.053 ± 0.019	0.067 ± 0.024	0.296 ± 0.107	0.721 ± 0.259	0.856 ± 0.308
NCQE	0.350 ± 0.161	0.197 ± 0.091	0.569 ± 0.261	0.280 ± 0.129	0.048 ± 0.022
^{9}Li	1.991 ± 1.095	1.388 ± 0.763	0.220 ± 0.212	0.0 ± 0.0	0.0 ± 0.0
Reactor	1.360 ± 1.360	0.001 ± 0.001	0.0 ± 0.0	0.0 ± 0.0	0.0 ± 0.0
Accidental	0.852 ± 0.043	0.423 ± 0.021	0.235 ± 0.012	0.010 ± 0.0	0.0 ± 0.0
Total background	4.61 ± 1.75	2.08 ± 0.77	1.32 ± 0.35	1.01 ± 0.29	0.90 ± 0.31
$N_{90\%}^{\rm sig}$	4.55	2.69	1.98	1.72	1.65
Live time T			552.2 days		
Number of Target N_p			1.5×10^{33} protons		
DSNB efficiency	7.1%	13.4%	25.0%	22.7%	30.8%
$\phi_{90}^{\rm MC}$ [/cm^2/sec/MeV]	72.1	16.5	2.16	0.58	0.31

Table 15.3: Background by energy bin for the MSG$_{lin}$ cut, including systematic uncertainties and 90% C.L. limits.

$E_{\rm rec}$ [MeV] (MSG_{lin} cut)	7.49–9.49	9.49–11.49	11.49–15.49	15.49–23.49	23.49–29.49
non-NCQE	0.015 ± 0.005	0.062 ± 0.022	0.252 ± 0.091	0.750 ± 0.270	0.856 ± 0.308
NCQE	0.131 ± 0.064	0.153 ± 0.075	0.389 ± 0.190	0.302 ± 0.147	0.048 ± 0.023
^{9}Li	1.563 ± 0.859	1.411 ± 0.776	0.209 ± 0.115	0.0 ± 0.0	0.0 ± 0.0
Reactor	0.080 ± 0.080	0.001 ± 0.001	0.0 ± 0.0	0.0 ± 0.0	0.0 ± 0.0
Accidental	0.406 ± 0.020	0.408 ± 0.020	0.185 ± 0.009	0.010 ± 0.0	0.0 ± 0.0
Total background	2.19 ± 0.88	2.04 ± 0.78	1.04 ± 0.24	1.06 ± 0.31	0.90 ± 0.31
$N_{90\%}^{\rm sig}$	2.82	2.69	1.98	1.72	1.65
Live time T			552.2 days		
Number of Target N_p			1.5×10^{33} protons		
DSNB efficiency	5.9%	14.0%	24.4%	22.8%	30.8%
$\phi_{90}^{\rm MC}$ [/cm^2/sec/MeV]	53.7	21.6	2.22	0.58	0.31

Table 15.4: Background by energy bin for the NN cut, including systematic uncertainties and 90% C.L. limits.

E_{rec} [MeV] (NN cut)	7.49–9.49	9.49–11.49	11.49–15.49	15.49–23.49	23.49–29.49
non-NCQE	0.009 ± 0.003	0.105 ± 0.038	0.273 ± 0.098	0.753 ± 0.271	0.909 ± 0.327
NCQE	0.044 ± 0.019	0.297 ± 0.128	0.385 ± 0.165	0.223 ± 0.096	0.048 ± 0.021
^{9}Li	0.622 ± 0.342	2.059 ± 1.132	0.406 ± 0.223	0.0 ± 0.0	0.0 ± 0.0
Reactor	0.054 ± 0.054	0.001 ± 0.001	0.0 ± 0.0	0.0 ± 0.0	0.0 ± 0.0
Accidental	0.165 ± 0.008	0.618 ± 0.031	0.231 ± 0.012	0.010 ± 0.0	0.0 ± 0.0
Total background	0.89 ± 0.35	3.08 ± 1.14	1.29 ± 0.29	0.99 ± 0.29	0.96 ± 0.33
$N_{90\%}^{\mathrm{sig}}$	1.65	3.74	1.93	1.71	1.70
Live time T			552.2 days		
Number of Target N_p			1.5×10^{33} protons		
DSNB efficiency	4.5%	16.5%	24.7%	26.2%	30.8%
ϕ_{90}^{MC} [/cm^2/sec/MeV]	41.2	23.4	2.13	0.49	0.31

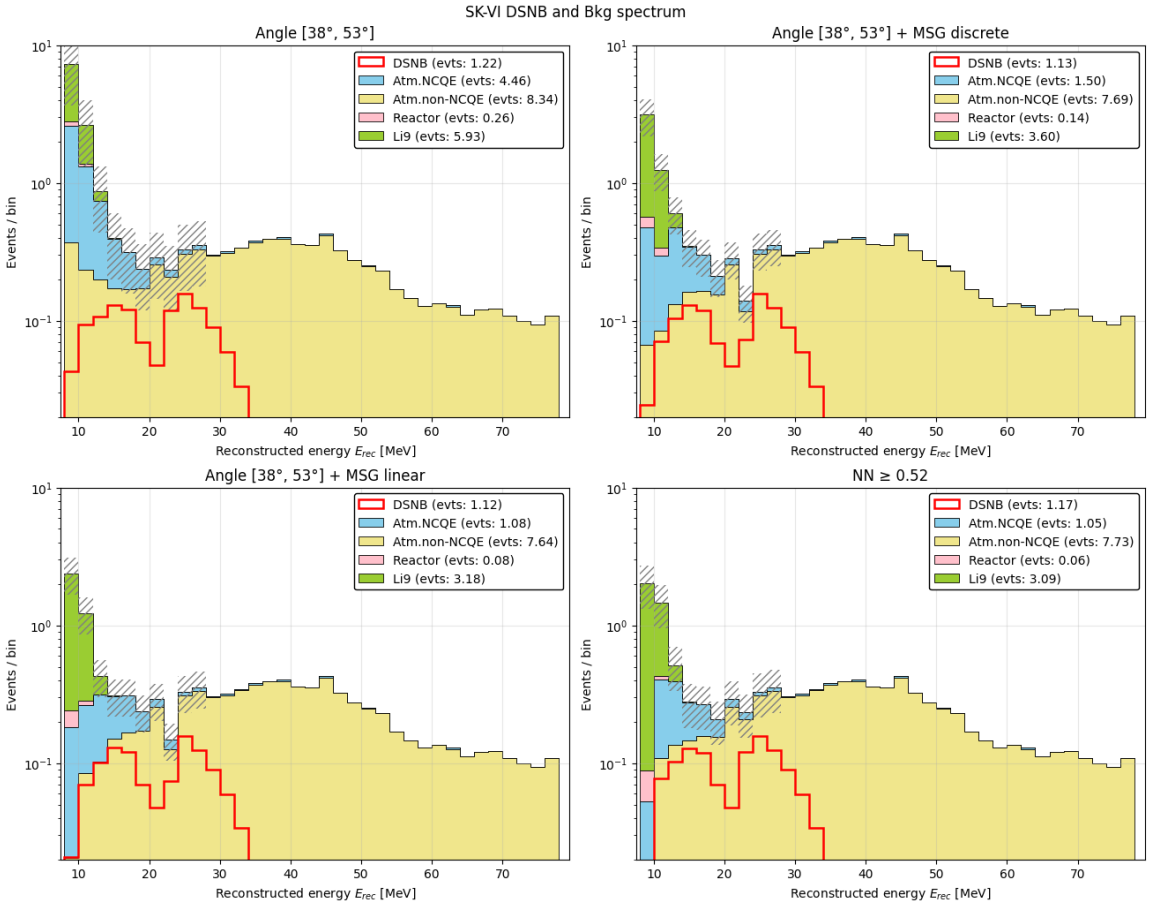

Figure 15.1: Expected background spectra for the DSNB search under four selection settings: θ_C only, $\mathrm{MSG_{dis}}$, $\mathrm{MSG_{lin}}$, and NN. The DSNB signal shape is modeled assuming the flux predictions of Horiuchi+09 [17].

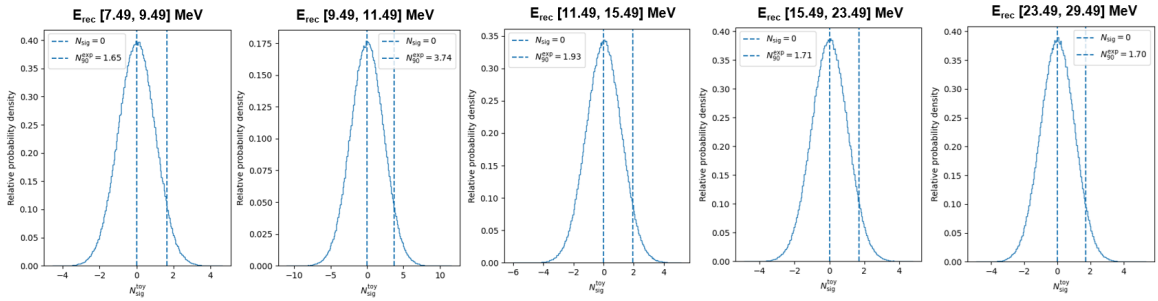

Figure 15.2: Distribution of background subtracted distributions from 10^6 pseudo-experiments in each energy bin using the NN selection. The vertical marker indicates the 90% C.L. upper limit on the signal yield, $N^{\mathrm{sig}}_{90\%}$.

We compute the 90% C.L. flux upper limit $\phi^{\mathrm{MC}}_{90\%}$ [$\mathrm{cm}^{-2}\,\mathrm{s}^{-1}\,\mathrm{MeV}^{-1}$] as

$$\phi^{\mathrm{MC}}_{90\%} = \frac{N^{\mathrm{sig}}_{90\%}}{\bar{\sigma}_{\mathrm{IBD}}\, N_p\, T\, \varepsilon_{\mathrm{sig}}}\,, \tag{15.1}$$

where $\bar{\sigma}_{\mathrm{IBD}}$ [cm^2] is the IBD cross section averaged at the mean neutrino energy E_ν for the bin, N_p is the number of target protons, $1.5{\cdot}10^{33}$, in SK, T is the SK-VI live time in second (552.2 days $\approx 4.77 \times 10^7$ s), and $\varepsilon_{\mathrm{sig}}$ is the signal efficiency. For IBD interactions, the neutrino energy is related to the reconstructed energy by $E_\nu = E_{\mathrm{rec}} + 1.8$ MeV. Figure 15.3 summarizes the expected DSNB $\bar{\nu}_e$ flux limits for the four selection settings (θ_C only, $\mathrm{MSG}_{\mathrm{dis}}$, $\mathrm{MSG}_{\mathrm{lin}}$, and NN), with numerical values listed in Tables 15.1, 15.2, 15.3, and 15.4.

15.2 Future Prospect

Our significance projection assumes an SK livetime extending to a tentative end date of March 31, 2031 (approximately one year after the 2028 Japanese fiscal year). To assess the discovery potential, we calculate the overall significance by combining the signal and background expectations across above energy bins 11.49 MeV. Figure 15.4 displays three scenarios. In the first two, the background efficiency is fixed at 5% while the overall systematic uncertainty is set to 68% (blue soild) and 43% with NN (red soild). In the third, at the same systematic level, we illustrate the gain from additional T2K data that would permit a 2% background efficiency (purple dashed) relative to the current 5% projection. Under the most optimistic DSNB flux model (Kaplinghat+00), all scenarios reach 3σ before 2032. Background rejection and its associated systematics largely determine the timescale to the first 3σ DSNB observation.

However, DSNB flux predictions vary, Figure 15.5 shows the DSNB flux 3σ sensitivity alongside modern DSNB models. The figure further illustrates how con-

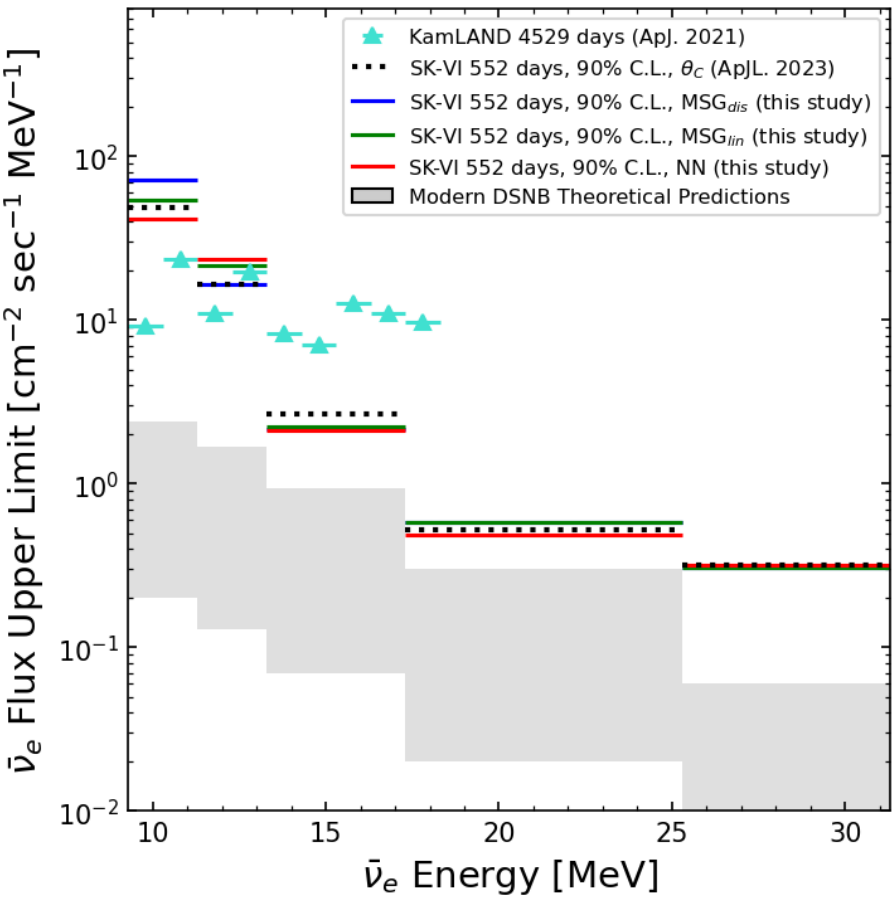

Figure 15.3: 90% C.L. upper limits on the DSNB $\bar{\nu}_e$ flux versus energy for selections θ_C (black dashed), MSG$_{\text{dis}}$ (blue), MSG$_{\text{lin}}$ (green), and NN (red). The KamLAND limit (cyan) [38] is shown for comparison.

straints on systematics and stronger background suppression enhance the discovery reach. Although achieving 3σ remains challenging, several actions could strengthen the prospects: a larger T2K NCQE data sample, refined modeling of nucleon nucleus interactions, and additional rejection using features such as the neutron travel distance.

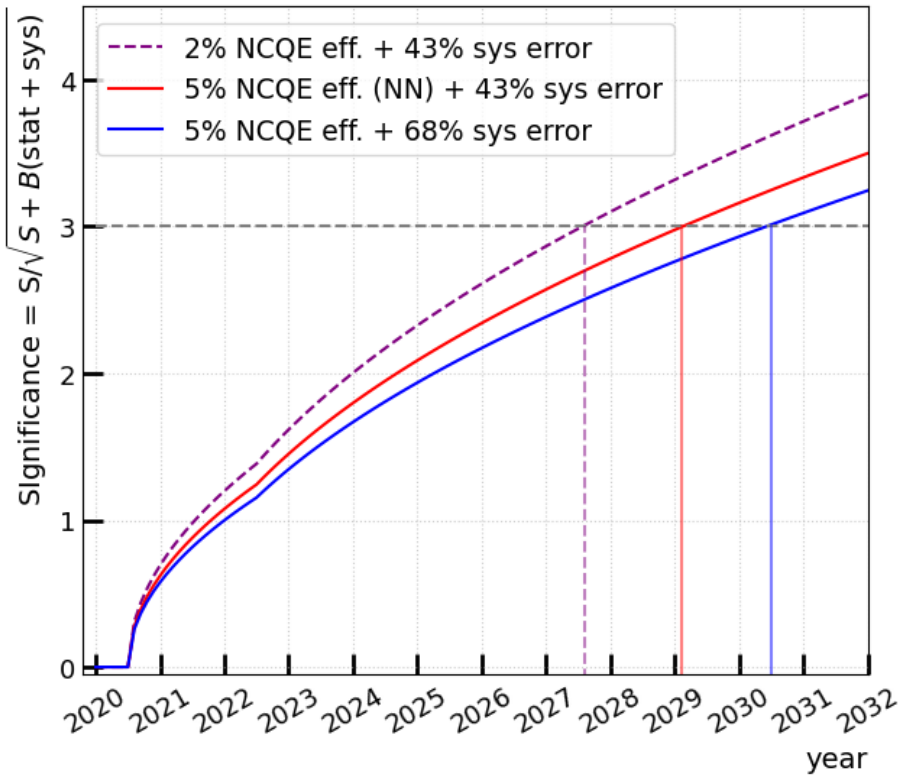

Figure 15.4: Projected DSNB significance versus time [23] up to 2032. Curves show 5% background efficiency with 68% (blue soild) and 43% (red soild) systematics, and a 2% background efficiency enabled by additional T2K data (purple dashed). Under the the most optimistic DSNB flux model (Kaplinghat+00), all scenarios reach 3σ before SK ends.

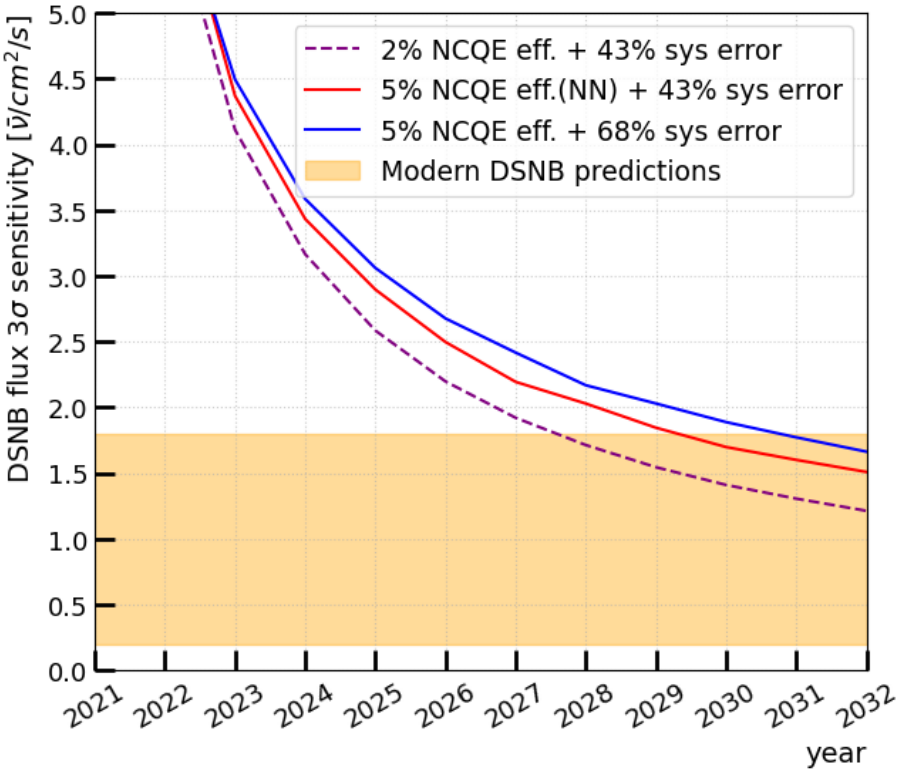

Figure 15.5: DSNB 3σ flux sensitivity compared with modern model predictions.

Part IV

Summary

Chapter 16

Conclusion

The Diffuse Supernova Neutrino Background (DSNB), if observed, would provide important information about how supernovae explode and how stars have formed over the history of the Universe. A major background in DSNB searches at water Cherenkov detectors comes from atmospheric neutrino neutral-current quasielastic-like (NCQE-like) interactions. In this thesis, we have measured neutron and gamma-ray production from NCQE-like interactions using T2K neutrino and antineutrino beams, and we have demonstrated how these results enhance the DSNB search at Super-Kamiokande.

We introduced the latest GEANT4-based detector simulation, SKG4, to study how nucleon–nucleus interactions affect neutron and gamma-ray production in NCQE-like interactions. Using a data set corresponding to 1.76×10^{20} protons on target (POT) from the T2K neutrino beam, we measured the neutron-capture multiplicity from ν-^{16}O NCQE-like interactions using the Gd-loaded Super-Kamiokande detector for the first time. The observed mean multiplicity is

$$1.37 \pm 0.33 \text{ (stat.)}^{+0.17}_{-0.27} \text{ (syst.)}.$$

This result deviates from the NEUT prediction using the Bertini-based secondary interaction model (2.28±0.01), whereas the INCL++ (1.87±0.01) and BIC (1.84±0.01) models show better agreement with the data. We also updated the T2K NCQE cross section measurement using SKG4 with exposures of 21.42×10^{20} POT for neutrinos and 16.35×10^{20} POT for antineutrinos. The resulting flux-averaged NCQE-like cross sections are

$$\langle \sigma_{\nu \text{NCQE}} \rangle = \left(1.75 \pm 0.15 \text{ (stat.)}^{+0.43}_{-0.23} \text{ (syst.)}\right) \times 10^{-38} \text{ cm}^2/\text{oxygen},$$

$$\langle \sigma_{\bar{\nu} \text{NCQE}} \rangle = \left(0.97 \pm 0.16 \text{ (stat.)}^{+0.19}_{-0.13} \text{ (syst.)}\right) \times 10^{-38} \text{ cm}^2/\text{oxygen},$$

with flux-averaged energies of 0.82 GeV for neutrinos and 0.68 GeV for antineutrinos.

We carried out a detailed study of how primary and secondary γ rays are produced at the Monte Carlo truth level, and we examined event features such as the Cherenkov angle and Multiple Scatter Goodness, including how these quantities depend on energy. Based on these studies, we developed an optimized event selection for DSNB searches at Super-K and provided uncertainty estimation using T2K NCQE data from Runs 1–11. At present, the leading source of uncertainty is the limited statistics of the T2K NCQE data. To reduce the total uncertainty to the level of the Monte Carlo systematic uncertainty (about 15%), a larger detector such as Hyper-Kamiokande and an upgraded T2K beam would be required.

Finally, we carried out a DSNB sensitivity study assuming 552.1 days of Super-Kamiokande VI data. The updated estimate of the atmospheric NCQE-like background, constrained by the T2K measurements, reduces the associated uncertainty from 71% to 43%, leading to an improvement in the search sensitivity. This study indicates that Super-Kamiokande has the potential to reach a 3σ detection of the DSNB flux. The methods developed in this thesis can be directly applied to current and future DSNB searches at Super-Kamiokande.

Bibliography

[1] Alexei V. Filippenko. "Optical spectra of supernovae". In: *Ann. Rev. Astron. Astrophys.* 35 (1997), pp. 309–355. DOI: 10.1146/annurev.astro.35.1.309.

[2] Hans-Thomas Janka. "Explosion Mechanisms of Core-Collapse Supernovae". In: *Ann. Rev. Nucl. Part. Sci.* 62 (2012), pp. 407–451. DOI: 10.1146/annurev-nucl-102711-094901. arXiv: 1206.2503 [astro-ph.SR].

[3] J. M. Lattimer and M. Prakash. "The Physics of Neutron Stars". In: *Science* 304.5670 (2004), pp. 536–542. DOI: 10.1126/science.1090720. eprint: https://www.science.org/doi/pdf/10.1126/science.1090720. URL: https://www.science.org/doi/abs/10.1126/science.1090720.

[4] Y. Ashida. "Measurement of Neutrino and Antineutrino Neutral-Current Quasielastic-like Interactions and Applications to Supernova Relic Neutrino Searches". In: *Ph.D. thesis, Kyoto University* (2020). URL: https://www-sk.icrr.u-tokyo.ac.jp/sk/_pdf/articles/thesis_ashida_ver6.0.pdf.

[5] Adam Burrows and James M. Lattimer. "The birth of neutron stars". In: *Astrophys. J.* 307 (1986), pp. 178–196. DOI: 10.1086/164405.

[6] Roland Diehl et al. "Radioactive Al-26 and massive stars in the galaxy". In: *Nature* 439 (2006), pp. 45–47. DOI: 10.1038/nature04364. arXiv: astro-ph/0601015.

[7] K. Hirata et al. "Observation of a Neutrino Burst from the Supernova SN 1987a". In: *Phys. Rev. Lett.* 58 (1987). Ed. by K. C. Wali, pp. 1490–1493. DOI: 10.1103/PhysRevLett.58.1490.

[8] R. M. Bionta et al. "Observation of a Neutrino Burst in Coincidence with Supernova SN 1987a in the Large Magellanic Cloud". In: *Phys. Rev. Lett.* 58 (1987), p. 1494. DOI: 10.1103/PhysRevLett.58.1494.

[9] E.N. Alexeyev et al. "Detection of the neutrino signal from SN 1987A in the LMC using the INR Baksan underground scintillation telescope". In: *Phys. Lett. B* 205.2 (1988), pp. 209–214. ISSN: 0370-2693. DOI: https://doi.org/10.1016/0370-2693(88)91651-6. URL: https://www.sciencedirect.com/science/article/pii/0370269388916516.

[10] K. S. Hirata et al. “Observation in the Kamiokande-II Detector of the Neutrino Burst from Supernova SN 1987a”. In: *Phys. Rev. D* 38 (1988), pp. 448–458. DOI: 10.1103/PhysRevD.38.448.

[11] Ken’ichiro Nakazato et al. “Spectrum of the Supernova Relic Neutrino Background and Metallicity Evolution of Galaxies”. In: *Astrophys. J.* 804.1 (2015), p. 75. DOI: 10.1088/0004-637X/804/1/75. arXiv: 1503.01236 [astro-ph.HE].

[12] D. H. Hartmann and S. E. Woosley. “The cosmic supernova neutrino background”. In: *Astropart. Phys.* 7 (1997), pp. 137–146. DOI: 10.1016/S0927-6505(97)00018-2.

[13] R. A. Malaney. “Evolution of the cosmic gas and the relic supernova neutrino background”. In: *Astropart. Phys.* 7 (1997), pp. 125–136. DOI: 10.1016/S0927-6505(97)00012-1. arXiv: astro-ph/9612012.

[14] M. Kaplinghat, G. Steigman, and T. P. Walker. “The Supernova relic neutrino background”. In: *Phys. Rev. D* 62 (2000), p. 043001. DOI: 10.1103/PhysRevD.62.043001. arXiv: astro-ph/9912391.

[15] S. Ando, K. Sato, and T. Totani. “Detectability of the supernova relic neutrinos and neutrino oscillation”. In: *Astropart. Phys.* 18 (2003), pp. 307–318. DOI: 10.1016/S0927-6505(02)00152-4. arXiv: astro-ph/0202450.

[16] Cecilia Lunardini. “Diffuse neutrino flux from failed supernovae”. In: *Phys. Rev. Lett.* 102 (2009), p. 231101. DOI: 10.1103/PhysRevLett.102.231101. arXiv: 0901.0568 [astro-ph.SR].

[17] Shunsaku Horiuchi, John F. Beacom, and Eli Dwek. “The Diffuse Supernova Neutrino Background is detectable in Super-Kamiokande”. In: *Phys. Rev. D* 79 (2009), p. 083013. DOI: 10.1103/PhysRevD.79.083013. arXiv: 0812.3157 [astro-ph].

[18] Sebastien Galais et al. “Shockwaves in Supernovae: New Implications on the Diffuse Supernova Neutrino Background”. In: *Phys. Rev. D* 81 (2010), p. 053002. DOI: 10.1103/PhysRevD.81.053002. arXiv: 0906.5294 [hep-ph].

[19] Shunsaku Horiuchi et al. “Diffuse supernova neutrino background from extensive core-collapse simulations of 8–100 $M_\odot$ progenitors”. In: *Monthly Notices of the Royal Astronomical Society* 475.1 (Dec. 2017), pp. 1363–1374. ISSN: 0035-8711. DOI: 10.1093/mnras/stx3271. eprint: https://academic.oup.com/mnras/article-pdf/475/1/1363/23585266/stx3271.pdf. URL: https://doi.org/10.1093/mnras/stx3271.

[20] Daniel Kresse, Thomas Ertl, and Hans-Thomas Janka. “Stellar Collapse Diversity and the Diffuse Supernova Neutrino Background”. In: *Astrophys. J.* 909.2 (2021), p. 169. DOI: 10.3847/1538-4357/abd54e. arXiv: 2010.04728 [astro-ph.HE].

[21] Zahra Tabrizi and Shunsaku Horiuchi. "Flavor triangle of the diffuse supernova neutrino background". In: *JCAP* 2021.05 (May 2021), p. 011. DOI: 10.1088/1475-7516/2021/05/011. URL: https://dx.doi.org/10.1088/1475-7516/2021/05/011.

[22] Shunsaku Horiuchi et al. "Impact of binary interactions on the diffuse supernova neutrino background". In: *Phys. Rev. D* 103.4 (2021), p. 043003. DOI: 10.1103/PhysRevD.103.043003. arXiv: 2012.08524 [astro-ph.HE].

[23] M. Harada et al. "Search for Astrophysical Electron Antineutrinos in Super-Kamiokande with 0.01% Gadolinium-loaded Water". In: *Astrophys. J. Lett.* 951.2 (2023), p. L27. DOI: 10.3847/2041-8213/acdc9e. arXiv: 2305.05135 [astro-ph.HE].

[24] Alessandro Strumia and Francesco Vissani. "Precise quasielastic neutrino/nucleon cross-section". In: *Phys. Lett. B* 564 (2003), pp. 42–54. DOI: 10.1016/S0370-2693(03)00616-6. arXiv: astro-ph/0302055.

[25] J. Nieves, I. Ruiz Simo, and M. J. Vicente Vacas. "Inclusive charged-current neutrino-nucleus reactions". In: *Phys. Rev. C* 83 (2011), p. 045501. DOI: 10.1103/PhysRevC.83.045501. URL: https://doi.org/10.1103/PhysRevC.83.045501.

[26] Artur M. Ankowski et al. "Analysis of γ-ray production in neutral-current neutrino-oxygen interactions at energies above 200 MeV". In: *Phys. Rev. Lett.* 108 (2012), p. 052505. DOI: 10.1103/PhysRevLett.108.052505. arXiv: 1110.0679 [nucl-th].

[27] R. Bradford et al. "A New Parameterization of the Nucleon Elastic Form Factors". In: *Nucl. Phys. B* 159 (2006), pp. 127–132. DOI: 10.1016/j.nuclphysbps.2006.08.028. URL: https://doi.org/10.1016/j.nuclphysbps.2006.08.028.

[28] B. Pontecorvo. "Mesonium and Antimesonium". In: *Sov. Phys. JETP* 6 (1958), pp. 429–431.

[29] Ziro Maki, Masami Nakagawa, and Shoichi Sakata. "Remarks on the unified model of elementary particles". In: *Prog. Theor. Phys.* 28 (1962), pp. 870–880. DOI: 10.1143/PTP.28.870.

[30] Claudio Giganti, Stéphane Lavignac, and Marco Zito. "Neutrino oscillations: The rise of the PMNS paradigm". In: *Prog. Part. Nucl. Phys.* 98 (2018), pp. 1–54. DOI: 10.1016/j.ppnp.2017.10.001. arXiv: 1710.00715 [hep-ex].

[31] Hiroshi Nunokawa, Stephen J. Parke, and Jose W. F. Valle. "CP Violation and Neutrino Oscillations". In: *Prog. Part. Nucl. Phys.* 60 (2008), pp. 338–402. DOI: 10.1016/j.ppnp.2007.10.001. arXiv: 0710.0554 [hep-ph].

[32] M. Malek et al. “Search for supernova relic neutrinos at SUPER-KAMIOKANDE”. In: *Phys. Rev. Lett.* 90 (2003), p. 061101. DOI: 10.1103/PhysRevLett.90.061101. arXiv: hep-ex/0209028.

[33] K. Bays et al. “Supernova Relic Neutrino Search at Super-Kamiokande”. In: *Phys. Rev. D* 85 (2012), p. 052007. DOI: 10.1103/PhysRevD.85.052007. arXiv: 1111.5031 [hep-ex].

[34] H. Zhang et al. “Supernova Relic Neutrino search with neutron tagging at Super-Kamiokande-IV”. In: *Astroparticle Physics* 60 (2015), pp. 41–46. ISSN: 0927-6505. DOI: https://doi.org/10.1016/j.astropartphys.2014.05.004. URL: https://www.sciencedirect.com/science/article/pii/S0927650514000681.

[35] K. Abe et al. “Diffuse supernova neutrino background search at Super-Kamiokande”. In: *Phys. Rev. D* 104.12 (2021), p. 122002. DOI: 10.1103/PhysRevD.104.122002. arXiv: 2109.11174 [astro-ph.HE].

[36] K. Abe et al. “Search for Diffuse Supernova Neutrino Background with 956.2 days of Super-Kamiokande Gadolinium Dataset”. In: *arXiv* (Nov. 2025). arXiv: 2511.02222 [astro-ph.HE].

[37] A. Gando et al. “A study of extraterrestrial antineutrino sources with the KamLAND detector”. In: *Astrophys. J.* 745 (2012), p. 193. DOI: 10.1088/0004-637X/745/2/193. arXiv: 1105.3516 [astro-ph.HE].

[38] S. Abe et al. “Limits on Astrophysical Antineutrinos with the KamLAND Experiment”. In: *Astrophys. J.* 925.1 (2022), p. 14. DOI: 10.3847/1538-4357/ac32c1. arXiv: 2108.08527 [astro-ph.HE].

[39] B. Aharmim et al. “A Search for Neutrinos from the Solar hep Reaction and the Diffuse Supernova Neutrino Background with the Sudbury Neutrino Observatory”. In: *Astrophys. J.* 653 (2006), pp. 1545–1551. DOI: 10.1086/508768. arXiv: hep-ex/0607010.

[40] B. Aharmim et al. “Search for *hep* solar neutrinos and the diffuse supernova neutrino background using all three phases of the Sudbury Neutrino Observatory”. In: *Phys. Rev. D* 102.6 (2020), p. 062006. DOI: 10.1103/PhysRevD.102.062006. arXiv: 2007.08018 [hep-ex].

[41] M. Agostini et al. “Search for low-energy neutrinos from astrophysical sources with Borexino”. In: *Astropart. Phys.* 125 (2021), p. 102509. DOI: 10.1016/j.astropartphys.2020.102509. arXiv: 1909.02422 [hep-ex].

[42] L. Wan et al. “Measurement of the neutrino-oxygen neutral-current quasielastic cross section using atmospheric neutrinos at Super-Kamiokande”. In: *Phys. Rev. D* 99.3 (2019), p. 032005. DOI: 10.1103/PhysRevD.99.032005. arXiv: 1901.05281 [hep-ex].

[43] S. Sakai et al. “Measurement of the neutrino-oxygen neutral-current quasielastic cross section using atmospheric neutrinos in the SK-Gd experiment”. In: *Phys. Rev. D* 109.1 (2024), p. L011101. DOI: 10.1103/PhysRevD.109.L011101. arXiv: 2311.03842 [hep-ex].

[44] S. Abe et al. “First measurement of the strange axial coupling constant using neutral-current quasielastic interactions of atmospheric neutrinos at KamLAND”. In: *Phys. Rev. D* 107.7 (2023), p. 072006. DOI: 10.1103/PhysRevD.107.072006. arXiv: 2211.13911 [hep-ex].

[45] L. A. Ahrens et al. “Measurement of Neutrino - Proton and anti-neutrino - Proton Elastic Scattering”. In: *Phys. Rev. D* 35 (1987), p. 785. DOI: 10.1103/PhysRevD.35.785.

[46] G. T. Garvey, W. C. Louis, and D. H. White. “Determination of proton strange form-factors from neutrino p elastic scattering”. In: *Phys. Rev. C* 48 (1993), pp. 761–765. DOI: 10.1103/PhysRevC.48.761.

[47] A. A. Aguilar-Arevalo et al. “Measurement of the Neutrino Neutral-Current Elastic Differential Cross Section on Mineral Oil at $E_\nu \sim 1$ GeV”. In: *Phys. Rev. D* 82 (2010), p. 092005. DOI: 10.1103/PhysRevD.82.092005. arXiv: 1007.4730 [hep-ex].

[48] J. Kameda. “Observation of de-excitation gamma rays from nuclei in 1-kton detector in K2K experiment”. In: *Nucl. Phys. B Proc. Suppl.* 159 (2006). Ed. by F. Cavanna, J. G. Morfin, and T. Nakaya, pp. 44–49. DOI: 10.1016/j.nuclphysbps.2006.08.076.

[49] K. Abe et al. “Measurement of the neutrino-oxygen neutral-current interaction cross section by observing nuclear deexcitation γ rays”. In: *Phys. Rev. D* 90.7 (2014), p. 072012. DOI: 10.1103/PhysRevD.90.072012. arXiv: 1403.3140 [hep-ex].

[50] K. Abe et al. “Measurement of neutrino and antineutrino neutral-current quasielasticlike interactions on oxygen by detecting nuclear deexcitation γ rays”. In: *Phys. Rev. D* 100.11 (2019), p. 112009. DOI: 10.1103/PhysRevD.100.112009. arXiv: 1910.09439 [hep-ex].

[51] Koh Ueno. “Study of neutral-current de-excitation gamma-rays with the T2K neutrino beam”. PhD thesis. Tokyo U., 2012.

[52] Fabio Iacob. “Measurement of neutral current quasielastic interaction neutron multiplicity by detecting radiative captures on hydrogen at the T2K far detector”. PhD thesis. Universita’ Di Padova, Padua U., 2020.

[53] Pruthvi Mehta. “NCQE interactions as a background to DSNB events with neutron tagging at SK-Gd.” PhD thesis. U. Liverpool (main), 2023. DOI: 10.17638/03171334.

[54] Y. Hino et al. “A simulation model investigation of neutron-oxygen inelastic scattering and subsequent nucleus deexcitation based on experimental data”. In: *Preprint* (June 2025). arXiv: 2506.14388.

[55] K. Abe et al. “The T2K Experiment”. In: *Nucl. Instrum. Meth. A* 659 (2011), pp. 106–135. DOI: 10.1016/j.nima.2011.06.067. arXiv: 1106.1238 [physics.ins-det].

[56] Giuseppe Battistoni et al. “The FLUKA code: Description and benchmarking”. In: *AIP Conf. Proc.* 896.1 (2007). Ed. by M. Albrow and R. Raja, pp. 31–49. DOI: 10.1063/1.2720455.

[57] R. Brun et al. “GEANT –Detector Description and Simulation Tool”. In: *CERN, Report No. CERNW5013* (1994). URL: https://cds.cern.ch/record/1082634/files/geantall_CERN-W5013.pdf.

[58] N. Abgrall et al. “Measurements of $\pi^{\pm}$, $K^{\pm}$ and proton double differential yields from the surface of the T2K replica target for incoming 31 GeV/c protons with the NA61/SHINE spectrometer at the CERN SPS”. In: *Eur. Phys. J. C* 79.2 (2019), p. 100. DOI: 10.1140/epjc/s10052-019-6583-0. arXiv: 1808.04927 [hep-ex].

[59] N Abgrall et al. “Measurements of Cross Sections and Charged Pion Spectra in Proton-Carbon Interactions at 31 GeV/c”. In: *Phys. Rev. C* 84 (2011), p. 034604. DOI: 10.1103/PhysRevC.84.034604. arXiv: 1102.0983 [hep-ex].

[60] N. Abgrall et al. “Measurement of Production Properties of Positively Charged Kaons in Proton-Carbon Interactions at 31 GeV/c”. In: *Phys. Rev. C* 85 (2012), p. 035210. DOI: 10.1103/PhysRevC.85.035210. arXiv: 1112.0150 [hep-ex].

[61] N. Abgrall et al. “Measurements of $\pi^{\pm}$, $K^{\pm}$, K^0_S , Λ and proton production in proton–carbon interactions at 31 GeV/c with the NA61/SHINE spectrometer at the CERN SPS”. In: *Eur. Phys. J. C* 76.2 (2016), p. 84. DOI: 10.1140/epjc/s10052-016-3898-y. arXiv: 1510.02703 [hep-ex].

[62] K. Abe et al. “Measurements of neutrino oscillation parameters from the T2K experiment using 3.6×10^{21} protons on target”. In: *Eur. Phys. J. C* 83.9 (2023), p. 782. DOI: 10.1140/epjc/s10052-023-11819-x. arXiv: 2303.03222 [hep-ex].

[63] P. A. Amaudruz et al. “The T2K Fine-Grained Detectors”. In: *Nucl. Instrum. Meth. A* 696 (2012), pp. 1–31. DOI: 10.1016/j.nima.2012.08.020. arXiv: 1204.3666 [physics.ins-det].

[64] N. Abgrall et al. “Time Projection Chambers for the T2K Near Detectors”. In: *Nucl. Instrum. Meth. A* 637 (2011), pp. 25–46. DOI: 10.1016/j.nima.2011.02.036. arXiv: 1012.0865 [physics.ins-det].

[65] D. Allan et al. "The Electromagnetic Calorimeter for the T2K Near Detector ND280". In: *JINST* 8 (2013), P10019. DOI: 10.1088/1748-0221/8/10/P10019. arXiv: 1308.3445 [physics.ins-det].

[66] S. Assylbekov et al. "The T2K ND280 Off-Axis Pi-Zero Detector". In: *Nucl. Instrum. Meth. A* 686 (2012), pp. 48–63. DOI: 10.1016/j.nima.2012.05.028. arXiv: 1111.5030 [physics.ins-det].

[67] S. Aoki et al. "The T2K Side Muon Range Detector (SMRD)". In: *Nucl. Instrum. Meth. A* 698 (2013), pp. 135–146. DOI: 10.1016/j.nima.2012.10.001. arXiv: 1206.3553 [physics.ins-det].

[68] Y. Fukuda et al. "The Super-Kamiokande detector". In: *Nucl. Instrum. Meth. A* 501 (2003). Ed. by V. A. Ilyin, V. V. Korenkov, and D. Perret-Gallix, pp. 418–462. DOI: 10.1016/S0168-9002(03)00425-X.

[69] S. Fukuda et al. "Solar B-8 and hep neutrino measurements from 1258 days of Super-Kamiokande data". In: *Phys. Rev. Lett.* 86 (2001), pp. 5651–5655. DOI: 10.1103/PhysRevLett.86.5651. arXiv: hep-ex/0103032.

[70] Y. Fukuda et al. "Evidence for oscillation of atmospheric neutrinos". In: *Phys. Rev. Lett.* 81 (1998), pp. 1562–1567. DOI: 10.1103/PhysRevLett.81.1562. arXiv: hep-ex/9807003.

[71] R. Wendell et al. "Atmospheric neutrino oscillation analysis with sub-leading effects in Super-Kamiokande I, II, and III". In: *Phys. Rev. D* 81 (2010), p. 092004. DOI: 10.1103/PhysRevD.81.092004. arXiv: 1002.3471 [hep-ex].

[72] K. Abe et al. "Solar neutrino results in Super-Kamiokande-III". In: *Phys. Rev. D* 83 (2011), p. 052010. DOI: 10.1103/PhysRevD.83.052010. arXiv: 1010.0118 [hep-ex].

[73] K. Abe et al. "Evidence for the Appearance of Atmospheric Tau Neutrinos in Super-Kamiokande". In: *Phys. Rev. Lett.* 110.18 (2013), p. 181802. DOI: 10.1103/PhysRevLett.110.181802. arXiv: 1206.0328 [hep-ex].

[74] A. Renshaw et al. "First Indication of Terrestrial Matter Effects on Solar Neutrino Oscillation". In: *Phys. Rev. Lett.* 112.9 (2014), p. 091805. DOI: 10.1103/PhysRevLett.112.091805. arXiv: 1312.5176 [hep-ex].

[75] K. Abe et al. "Atmospheric neutrino oscillation analysis with external constraints in Super-Kamiokande I-IV". In: *Phys. Rev. D* 97.7 (2018), p. 072001. DOI: 10.1103/PhysRevD.97.072001. arXiv: 1710.09126 [hep-ex].

[76] K. Abe et al. "Search for proton decay via $p \to e^+\pi^0$ and $p \to \mu^+\pi^0$ in 0.31 megaton · years exposure of the Super-Kamiokande water Cherenkov detector". In: *Phys. Rev. D* 95.1 (2017), p. 012004. DOI: 10.1103/PhysRevD.95.012004. arXiv: 1610.03597 [hep-ex].

[77] K. Abe et al. “First gadolinium loading to Super-Kamiokande”. In: *Nucl. Instrum. Meth. A* 1027 (2022), p. 166248. DOI: 10.1016/j.nima.2021.166248. arXiv: 2109.00360 [physics.ins-det].

[78] K. Abe et al. “Second gadolinium loading to Super-Kamiokande”. In: *Nucl. Instrum. Meth. A* 1065 (2024), p. 169480. DOI: 10.1016/j.nima.2024.169480. arXiv: 2403.07796 [physics.ins-det].

[79] Ll. Marti et al. “Evaluation of gadolinium’s action on water Cherenkov detector systems with EGADS”. In: *Nucl. Instrum. Meth. A* 959 (2020), p. 163549. DOI: 10.1016/j.nima.2020.163549. arXiv: 1908.11532 [physics.ins-det].

[80] John F. Beacom and Mark R. Vagins. “GADZOOKS! Antineutrino Spectroscopy with Large Water Cherenkov Detectors”. In: *Phys. Rev. Lett.* 93 (2004), p. 171101. DOI: 10.1103/PhysRevLett.93.171101. arXiv: hep-ph/0309300.

[81] R. L. Workman et al. “Review of Particle Physics”. In: *PTEP* 2022 (2022), p. 083C01. DOI: 10.1093/ptep/ptac097.

[82] H. Kume et al. “20-INCH DIAMETER PHOTOMULTIPLIER”. In: *Nucl. Instrum. Meth.* 205 (1983), pp. 443–449. DOI: 10.1016/0167-5087(83)90007-8.

[83] R. Becker-Szendy et al. “IMB-3: A Large water Cherenkov detector for nucleon decay and neutrino interactions”. In: *Nucl. Instrum. Meth. A* 324 (1993), pp. 363–382. DOI: 10.1016/0168-9002(93)90998-W.

[84] H. Nishino et al. “High-speed charge-to-time converter ASIC for the Super-Kamiokande detector”. In: *Nucl. Instrum. Meth. A* 610 (2009), pp. 710–717. DOI: 10.1016/j.nima.2009.09.026. arXiv: 0911.0986 [physics.ins-det].

[85] K. Abe et al. “Calibration of the Super-Kamiokande Detector”. In: *Nucl. Instrum. Meth. A* 737 (2014), pp. 253–272. DOI: 10.1016/j.nima.2013.11.081. arXiv: 1307.0162 [physics.ins-det].

[86] Y. Nakano et al. “Measurement of the radon concentration in purified water in the Super-Kamiokande IV detector”. In: *Nucl. Instrum. Meth. A* 977 (2020), p. 164297. DOI: 10.1016/j.nima.2020.164297. arXiv: 1910.03823 [physics.ins-det].

[87] M. Shinoki et al. “Measurement of the cosmogenic neutron yield in Super-Kamiokande with gadolinium loaded water”. In: *Phys. Rev. D* 107.9 (2023), p. 092009. DOI: 10.1103/PhysRevD.107.092009. arXiv: 2212.10801 [hep-ex].

[88] M. Nakahata et al. “Calibration of Super-Kamiokande using an electron linac”. In: *Nucl. Instrum. Meth. A* 421 (1999), pp. 113–129. DOI: 10.1016/S0168-9002(98)01200-5. arXiv: hep-ex/9807027.

[89] E. Blaufuss et al. “N-16 as a calibration source for Super-Kamiokande”. In: *Nucl. Instrum. Meth. A* 458 (2001), pp. 638–649. DOI: 10.1016/S0168-9002(00)00900-1. arXiv: hep-ex/0005014.

[90] Y. Hayato and L. Pickering. “The NEUT neutrino interaction simulation program library”. In: *Eur. Phys. J. Spec. Top.* 230 (Oct. 2021), pp. 4469–4481. DOI: 10.1140/epjs/s11734-021-00287-7. URL: https://doi.org/10.1140/epjs/s11734-021-00287-7.

[91] T. Golan, J. Sobczyk, and J. Żmuda. “Nuwro: the wroclaw monte carlo generator of neutrino interactions”. In: *Nuclear Physics B- Proceedings Supplements* 499 (2012), pp. 229–232. DOI: https://doi.org/10.1016/j.nuclphysbps.2012.09.136. URL: https://doi.org/10.1016/j.nuclphysbps.2012.09.136.

[92] C. Andreopoulos et al. “The genie neutrino monte carlo generator”. In: *Nuclear Instruments and Methods in Physics Research Section A: Accelerators, Spectrometers, Detectors and Associated Equipment* 614 (2010), pp. 87–104. DOI: https://doi.org/10.1016/j.nima.2009.12.009. URL: https:%20//doi.org/10.1016/j.nima.2009.12.009.

[93] O. Benhar et al. “Spectral function of finite nuclei and scattering of GeV electrons”. In: *Nucl. Phys. A* 24 (1994), pp. 493–517. DOI: 10.1016/0375-9474(94)90920-2. URL: https://doi.org/10.1016/0375-9474(94)90920-2.

[94] A. Rodriguez et al. “Measurement of single charged pion production in the charged-current interactions of neutrinos in a 1.3-GeV wide band beam”. In: *Phys. Rev. D* 78 (2008), p. 032003. DOI: 10.1103/PhysRevD.78.032003. arXiv: 0805.0186 [hep-ex].

[95] M. Glück, E. Reya, and A. Vogt. “Dynamical parton distributions revisited”. In: *Eur. Phys. J. C* 5 (1998), pp. 461–470. DOI: 10.1007/s100529800978. URL: https://doi.org/10.1007/s100529800978.

[96] A. Bodek, U. K. Yang, and Y. Xu. “Inelastic Axial and Vector Structure Functions for Lepton-Nucleon Scattering 2021 Update”. In: *arXiv:2108.09240 [hep-ph]* (2021). URL: https://arxiv.org/abs/2108.09240.

[97] C. Berger and L. M. Sehgal. “Partially conserved axial vector current and coherent pion production by low energy neutrinos”. In: *Phys. Rev. D* 79 (2009), p. 053003. DOI: 10.1103/PhysRevD.79.053003.. URL: https://doi.org/10.1103/PhysRevD.79.053003.

[98] H. W. Bertini. “Nonelastic interactions of nucleons and π mesons with complex nuclei at energies below 3 Gev”. In: *Phys. Rev. C* 6 (Aug. 1972), pp. 631–659.

DOI: 10.1103/PhysRevC.6.631. URL: https://doi.org/10.1103/PhysRevC.6.631.

[99] E. S. Pinzon et al. "Using world $\pi^{\pm}$-nucleus scattering data to constrain an intranuclear cascade model". In: *Phys. Rev. D* 99 (Mar. 2019), p. 052007. DOI: 10.1103/PhysRevD.99.052007. URL: https://doi.org/10.1103/PhysRevD.99.052007.

[100] K. M. Graczyk and J. T. Sobczyk. "Form factors in the quark resonance model". In: *Phys. Rev. D* 77 (2008), p. 053001. DOI: 10.1103/PhysRevD.77.053001. URL: https://doi.org/10.1103/PhysRevD.77.053001.

[101] K. Kobayashi et al. "De-excitation gamma-rays from the s-hole state in N-15 associated with proton decay in O-16". In: *Preprint* (Apr. 2006). arXiv: nucl-ex/0604006.

[102] M. Leuschner et al. "Quasielastic proton knockout from O-16". In: *Phys. Rev. C* 49 (1994), pp. 955–967. DOI: 10.1103/PhysRevC.49.955.

[103] F. Ajzenberg-Selove. "Energy levels of light nuclei A = 13-15". In: *Nucl. Phys. A* 523 (1991), pp. 1–196. DOI: 10.1016/0375-9474(91)90446-D.

[104] S. Abe. "Nuclear deexcitation simulator for neutrino interactions and nucleon decays of 12C and 16O based on TALYS". In: *Phys. Rev. D* 109 (2024), p. 036009. DOI: 10.1103/PhysRevD.109.036009. URL: https://doi.org/10.1103/PhysRevD.109.036009.

[105] S. Sakai. "Measurement of the neutrino-oxygen neutral-current quasielastic cross section and study of nucleon-nucleus interaction model using atmospheric neutrino data in the SK-Gd experiment". In: *Ph.D. thesis, Okayama University* (2024). URL: https://www-sk.icrr.u-tokyo.ac.jp/sk/_pdf/articles/2024/2024_Sakai_PhD_v240324.pdf.

[106] J. Allison et al. "Recent developments in Geant4". In: *Nucl. Instrum. Meth. A* 835 (2016), p. 186. DOI: 10.1016/j.nima.2016.06.125. URL: https://doi.org/10.1016/j.nima.2016.06.125.

[107] C. Zeitnitz and T.A. Gabriel. "The GEANT-CALOR interface and benchmark calculations of ZEUS test calorimeters". In: *Nucl. Instrum. Meth. A* 349 (1994), pp. 106–111. DOI: 10.1016/0168-9002(94)90613-0. URL: https://doi.org/10.1016/0168-9002(94)90613-0.

[108] Edited by R. Kinsey. "ENDF-102, Data Formats and Procedures for the Evaluated Nuclear Data File, ENDF". In: *BNL-NCS 50496, 2nd Edition* (1979). URL: https://www.oecd-nea.org/dbdata/data/manual-endf/endf102_2001.pdf.

[109] D. H. Wright and M. H. Kelsey. "The Geant4 Bertini Cascade". In: *Nucl. Instrum. Meth. A* 88 (6 Dec. 2013), p. 065501. DOI: 10.1103/PhysRevC.88.065501. URL: https://link.aps.org/doi/10.1103/PhysRevC.88.065501.

[110] J. Cugnon, C. Volant, and S. Vuillier. "Improved intranuclear cascade model for nucleon-nucleus interactions". In: *Nucl. Phys. A* 620 (1997), pp. 475–509. DOI: 10.1016/S0375-9474(97)00186-3. URL: https://doi.org/10.1016/S0375-9474(97)00186-3.

[111] A. Boudard et al. "Intranuclear cascade model for a comprehensive description of spallation reaction data". In: *Phys. Rev. D* 66 (2002), p. 044615. DOI: 10.1103/PhysRevC.66.044615. URL: https://link.aps.org/doi/10.1103/PhysRevC.66.044615.

[112] G. Folger, V.N. Ivanchenko, and J.P. Wellischa. "The Binary Cascade - Nucleon nuclear reactions". In: *Eur. Phys. J. A* 21 (2004), pp. 407–417. DOI: 10.1140/epja/i2003-10219-7. URL: https://doi.org/10.1140/epja/i2003-10219-7.

[113] M. J. Kobra. "Intranuclear Cascade Model for Deuteron- and Alpha-induced Reactions at Intermediate Energies". In: *Ph.D. Thesis, Kyushu University* (2017).

[114] https://geant4-userdoc.web.cern.ch/UsersGuides/PhysicsReferenceManual/fo/PhysicsReference "Physics Reference Manual". In: *CERN Website* (2018).

[115] J. J. Griffin. "Energy dependence of average direct reaction cross sections and partial nuclear level densities". In: *Phys. Lett. B* 24 (1 1967), pp. 5–7. DOI: 10.1016/0370-2693(67)90319-X. URL: https://doi.org/10.1016/0370-2693(67)90319-X.

[116] M. Bleicher et al. "Relativistic hadron-hadron collisions in the ultra-relativistic quantum molecular dynamics model". In: *J. Phys. G: Nucl. Part. Phys.* 25 (1999), p. 1859. DOI: 10.1088/0954-3899/25/9/308. URL: https://doi.org/10.1088/0954-3899/25/9/308.

[117] S. Leray et al. "Improved modelling of helium and tritium production for spallation targets". In: *Nucl. Instrum. Meth. B* 268 (2010), pp. 581–586. DOI: 10.1016/j.nimb.2009.12.003. arXiv: 0911.4062 [nucl-ex].

[118] V. F. Weisskopf and D. H. Ewing. "On the Yield of Nuclear Reactions with Heavy Elements". In: *Phys. Rev.* 57.6 (1940), p. 472. DOI: 10.1103/PhysRev.57.472.

[119] I. Dostrovsky, Z. Fraenkel, and G. Friedlander. "Monte Carlo Calculations of Nuclear Evaporation Processes. 3. Applications to Low-Energy Reactions". In: *Phys. Rev.* 116 (1959), pp. 683–702. DOI: 10.1103/PhysRev.116.683.

[120] National Nuclear Data Center. *Evaluated Nuclear Structure Data File (ENSDF)*. http://www.nndc.bnl.gov/ensdf/. Brookhaven National Laboratory. Accessed: Jan. 2026. 2026.

[121] J. Allison et al. "Recent developments in Geant4". In: *Nucl. Instrum. Meth. A* 835 (2016), pp. 186–225. DOI: 10.1016/j.nima.2016.06.125.

[122] S. Han et al. "Measurement of neutron production in atmospheric neutrino interactions at Super-Kamiokande". In: *Phys. Rev. D* 112.1 (2025), p. 012004. DOI: 10.1103/4d71-d69k. arXiv: 2505.04409 [hep-ex].

[123] K. Hagiwara et al. "Gamma-ray spectrum from thermal neutron capture on gadolinium-157". In: *Prog. Theor. Phys.* 2019 (2019), p. 023D01. DOI: 10.1093/ptep/ptz002. URL: https://doi.org/10.1093/ptep/ptz002.

[124] K. Abe et al. "Search for CP Violation in Neutrino and Antineutrino Oscillations by the T2K Experiment with 2.2×10^{21} Protons on Target". In: *Phys. Rev. Lett.* 121.17 (2018), p. 171802. DOI: 10.1103/PhysRevLett.121.171802. arXiv: 1807.07891 [hep-ex].

[125] M. Smy. "Low Energy Event Reconstruction and Selection in Super-Kamiokande-III". In: *Proceedings, 30th International Cosmic Ray Conference* 5 (2007), pp. 1279–1282.

[126] François Chollet et al. *Keras*. https://keras.io. 2015.

[127] R. Akutsu. "A Study of Neutrons Associated with Neutrino and Antineutrino Interactions on the Water Target at the T2K Far Detector". In: *Ph.D. thesis, University of Tokyo* (2019). URL: http://www-rccn.icrr.u-tokyo.ac.jp/pub/files/thesis/akutsu_dthesis.pdf.

[128] Zhenzhou Liu et al. "The 4.438MeV gamma to neutron ratio for the Am–Be neutron source". In: *Applied Radiation and Isotopes* 65.12 (2007), pp. 1318–1321. ISSN: 0969-8043. DOI: https://doi.org/10.1016/j.apradiso.2007.04.007. URL: https://www.sciencedirect.com/science/article/pii/S0969804307001200.

[129] S. Han. "Measurement of neutrons produced in atmospheric neutrino interactions at Super-Kamiokande". In: *Doctor thesis, The University of Tokyo* (2024). URL: https://www-sk.icrr.u-tokyo.ac.jp/sk/%5C_pdf/articles/2024/han%5C_dthesis.pdf.

[130] Y. Hino et al. "Modification on Thermal Motion in Geant4 for Neutron Capture Simulation in Gadolinium Loaded Water". In: *PTEP* 2025.1 (2025), p. 013C01. DOI: 10.1093/ptep/ptae193. arXiv: 2412.04186 [hep-ex].

[131] M. V. Kossov. "Chiral-invariant phase space model. I: Masses of hadrons". In: *Eur. Phys. J. A* 14 (2002), pp. 265–269. DOI: 10.1140/epja/i2001-10211-3.

[132] Tomasz Golan, Cezary Juszczak, and Jan T. Sobczyk. "Final State Interactions Effects in Neutrino-Nucleus Interactions". In: *Phys. Rev. C* 86 (2012), p. 015505. DOI: 10.1103/PhysRevC.86.015505. arXiv: 1202.4197 [nucl-th].

[133] A. Bodek, H. S. Budd, and M. E. Christy. "Neutrino quasielastic scattering on nuclear targets". In: *The European Physical Journal C* 71.9 (2011), p. 1726. DOI: 10.1140/epjc/s10052-011-1726-y.

[134] J. Ashmanetal et al. "An investigation of the spin structure of the proton in deep inelastic scattering of polarised muons on polarised protons". In: *Nucl. Phys* B328 (1989), p. 1. DOI: 10.1016/0550-3213(89)90089-8. URL: https://doi.org/10.1016/0550-3213(89)90089-8.

[135] W. Alberico, S. Bilenky, and C. Maieron. "Strangeness in the nucleon: neutrino–nucleon and polarized electron–nucleon scattering". In: *Phys. Rep.* 358 (2002), p. 227. DOI: 10.1016/S0370-1573(01)00058-8. URL: https://doi.org/10.1016/S0370-1573(01)00058-8.

[136] A. Airapetianetal and others (HERMES Collaboration). "Precise determination of the spin structure function g 1 of the proton, deuteron, and neutron". In: *Phys. Rev. D* 75 (2007), p. 012007. DOI: 10.1103/PhysRevD.75.01200. URL: https://doi.org/10.1103/PhysRevD.75.012007.

[137] V. Alexakhinetal and others (COMPASS Collaboration). "The deuteron spin-dependent structure function and its first moment". In: *Phys. Lett. B* 647 (2007), p. 8. DOI: 10.1016/j.physletb.2006.12.076. URL: https://doi.org/10.1016/j.physletb.2006.12.076.

[138] T. Golan et al. "Extraction of axial mass and strangeness values from the MiniBooNE neutral current elastic cross section measurement". In: *Phys. Rev. C* 88 (2013), p. 024612. DOI: 10.1103/PhysRevC.88.024612. URL: https://doi.org/10.1103/PhysRevC.88.024612.

[139] A. Koning, S. Hilaire, and S. Goriely. "TALYS: modeling of nuclear reactions". In: *Eur. Phys. J. A* 59 (2023), p. 131.

[140] W. Hauser and H. Feshbach. "The Inelastic Scattering of Neutrons". In: *Phys. Rev.* 87 (1952), p. 366.

[141] Omar Benhar and Davide Meloni. "Total neutrino and antineutrino nuclear cross-sections around 1-GeV". In: *Nucl. Phys. A* 789 (2007), pp. 379–402.

[142] Michael Thomas Nieslony. "Towards a neutron multiplicity measurement with the Accelerator Neutrino Neutron Interaction Experiment". PhD thesis. Mainz U., Nov. 2022. DOI: 10.25358/openscience-8530.

[143] M. Elkins et al. "Neutron measurements from antineutrino hydrocarbon reactions". In: *Phys. Rev. D* 100.5 (2019), p. 052002. DOI: 10.1103/PhysRevD.100.052002. arXiv: 1901.04892 [hep-ex].

[144] B. Aharmim et al. "Measurement of Neutron Production in Atmospheric Neutrino Interactions at the Sudbury Neutrino Observatory". In: *Phys. Rev. D* 99.11 (2019), p. 112007. DOI: 10.1103/PhysRevD.99.112007. arXiv: 1904.01148 [hep-ex].

[145] J.M. Quesada et al. "Recent Developments in Pre-Equilibrium and De-Excitation Models in Geant4". In: *Progress in Nuclear Science and Technology* 2 (2011), p. 936. DOI: 10.15669/pnst.2.936. URL: https://doi.org/10.15669/pnst.2.936.

[146] S. Furihata et al. "The GEM Code- A Simulation Program for the Evaporation and Fission Process of an Excited Nucleus". In: *JAERI-Data/Code 2001-015* (2001), Japan Atomic Energy Research Institute (JAERI). URL: https://inis.iaea.org/records/y787f-04m04.

[147] K. Abe et al. "Hyper-Kamiokande Design Report". In: *Preprint* (May 2018). arXiv: 1805.04163 [physics.ins-det].

[148] Fengpeng An et al. "Neutrino Physics with JUNO". In: *J. Phys. G* 43.3 (2016), p. 030401. DOI: 10.1088/0954-3899/43/3/030401. arXiv: 1507.05613 [physics.ins-det].

[149] Patrick deNiverville, David McKeen, and Adam Ritz. "Signatures of sub-GeV dark matter beams at neutrino experiments". In: *Phys. Rev. D* 86 (2012), p. 035022. DOI: 10.1103/PhysRevD.86.035022. arXiv: 1205.3499 [hep-ph].

[150] Patrick deNiverville et al. "Light dark matter in neutrino beams: production modelling and scattering signatures at MiniBooNE, T2K and SHiP". In: *Phys. Rev. D* 95.3 (2017), p. 035006. DOI: 10.1103/PhysRevD.95.035006. arXiv: 1609.01770 [hep-ph].

[151] P. Adamson et al. "Active to sterile neutrino mixing limits from neutral-current interactions in MINOS". In: *Phys. Rev. Lett.* 107 (2011), p. 011802. DOI: 10.1103/PhysRevLett.107.011802. arXiv: 1104.3922 [hep-ex].

[152] P. Adamson et al. "Search for active-sterile neutrino mixing using neutral-current interactions in NOvA". In: *Phys. Rev. D* 96.7 (2017), p. 072006. DOI: 10.1103/PhysRevD.96.072006. arXiv: 1706.04592 [hep-ex].

[153] K. Abe et al. "Search for light sterile neutrinos with the T2K far detector Super-Kamiokande at a baseline of 295 km". In: *Phys. Rev. D* 99.7 (2019), p. 071103. DOI: 10.1103/PhysRevD.99.071103. arXiv: 1902.06529 [hep-ex].

[154] Ko Abe et al. "Proposal for an Extended Run of T2K to 20×10^{21} POT". In: *Preprint* (Sept. 2016). arXiv: 1609.04111 [hep-ex].

[155] Y. Ashida et al. "Measurement of γ-ray production via the neutron-^{16}O reaction using a 77 MeV quasimonoenergetic neutron beam". In: *Phys. Rev. C* 109.1

(2024), p. 014620. DOI: 10.1103/PhysRevC.109.014620. arXiv: 1902.08964 [nucl-ex].

[156] T. Tano et al. "Measurement of γ-Rays Generated by Neutron Interaction with ^{16}O at 30 MeV and 250 MeV". In: *PTEP* 2024.11 (2024), p. 113D01. DOI: 10.1093/ptep/ptae159. arXiv: 2405.15366 [nucl-ex].

[157] D. Chiesa et al. "Measurements of Neutron Fields in a Wide Energy Range Using Multi-Foil Activation Analysis". In: *IEEE Trans. Nucl. Sci.* 69.7 (2022), pp. 1659–1666. DOI: 10.1109/TNS.2021.3138636. arXiv: 2110.05073 [physics.ins-det].

[158] Y. Shimizu et al. "SAMURAI project at RIBF". In: *J. Phys. Conf. Ser.* 312 (2011). Ed. by Jens Dilling and Jana Thomson, p. 052022. DOI: 10.1088/1742-6596/312/5/052022.

[159] A. Hiramoto et al. "First measurement of $\overline{\nu}_\mu$ and ν_μ charged-current inclusive interactions on water using a nuclear emulsion detector". In: *Phys. Rev. D* 102.7 (2020), p. 072006. DOI: 10.1103/PhysRevD.102.072006. arXiv: 2008.03895 [hep-ex].

[160] M. Khachatryan et al. "Electron-beam energy reconstruction for neutrino oscillation measurements". In: *Nature* 599.7886 (2021), pp. 565–570. DOI: 10.1038/s41586-021-04046-5.

[161] K. Abe et al. "First measurement of neutron capture multiplicity in neutrino-oxygen neutral-current quasielasticlike interactions using an accelerator neutrino beam". In: *Phys. Rev. D* 112.3 (2025), p. 032003. DOI: 10.1103/qh28-4znk. arXiv: 2505.22547 [hep-ex].

[162] A. Acharya et al. "Measurement of the production cross section of 31 GeV/c protons on carbon via beam attenuation in a 90-cm-long target". In: *Phys. Rev. D* 103.1 (2021), p. 012006. DOI: 10.1103/PhysRevD.103.012006. arXiv: 2010.11819 [hep-ex].

[163] Seisho Abe. "Implementation and investigation of electron-nucleus scattering in the neut neutrino event generator". In: *Phys. Rev. D* 111.3 (2025), p. 033006. DOI: 10.1103/PhysRevD.111.033006. arXiv: 2412.07466 [hep-ph].

[164] E. Kolbe, K. Langanke, and P. Vogel. "Estimates of weak and electromagnetic nuclear decay signatures for neutrino reactions in Super-Kamiokande". In: *Phys. Rev. D* 66 (2002), p. 013007. DOI: 10.1103/PhysRevD.66.013007.

[165] Yang Zhang and Shaomin Chen. "First measurement of radioactive isotope production through cosmic-ray muon spallation in Super-Kamiokande IV". In: *PoS* ICHEP2016 (2017), p. 1014. DOI: 10.22323/1.282.1014.

[166] S. Locke et al. "New methods and simulations for cosmogenic induced spallation removal in Super-Kamiokande-IV". In: *Phys. Rev. D* 110.3 (2024), p. 032003. DOI: 10.1103/PhysRevD.110.032003. arXiv: 2112.00092 [hep-ex].

[167] M. Harada. "Development of Neutron Tagging Algorithm and Search for Supernova Relic Neutrino in SK-Gd Experiment". In: *Ph.D. thesis, Okayama University* (2023). URL: https://www-sk.icrr.u-tokyo.ac.jp/sk/_pdf/articles/2023/Harada_PhDThesis_v5.0.pdf.

[168] Ian Goodfellow, Yoshua Bengio, and Aaron Courville. *Deep Learning*. http://www.deeplearningbook.org. MIT Press, 2016.

[169] Kaiming He et al. "Delving Deep into Rectifiers: Surpassing Human-Level Performance on ImageNet Classification". In: *Proceedings of the IEEE International Conference on Computer Vision (ICCV)*. Dec. 2015, pp. 1026–1034.

[170] Diederik P. Kingma and Jimmy Ba. "Adam: A Method for Stochastic Optimization". In: *Proceedings of the 3rd International Conference on Learning Representations (ICLR)*. arXiv:1412.6980. San Diego, CA, USA, 2015. URL: https://arxiv.org/abs/1412.6980.

[171] M. Honda et al. "Improvement of low energy atmospheric neutrino flux calculation using the JAM nuclear interaction model". In: *Phys. Rev. D* 83 (2011), p. 123001. DOI: 10.1103/PhysRevD.83.123001. arXiv: 1102.2688 [astro-ph.HE].

[172] Morihiro Honda et al. "Calculation of atmospheric neutrino flux using the interaction model calibrated with atmospheric muon data". In: *Phys. Rev. D* 75 (2007), p. 043006. DOI: 10.1103/PhysRevD.75.043006. arXiv: astro-ph/0611418.

[173] Marica Baldoncini et al. "Reference worldwide model for antineutrinos from reactors". In: *Phys. Rev. D* 91.6 (2015), p. 065002. DOI: 10.1103/PhysRevD.91.065002. arXiv: 1411.6475 [physics.ins-det].